Computational Fluid Dynamics (CFD) of Turbulent Flows: Direct Numerical Simulation and Large Eddy Simulation

Pieter Plehiers

Supervisor: Prof. dr. ir. Kevin Van Geem
Counsellor: Pieter Reyniers

Master's dissertation submitted in order to obtain the academic degree of
Master of Science in Chemical Engineering

Department of Chemical Engineering and Technical Chemistry
Chair: Prof. dr. ir. Guy Marin
Faculty of Engineering and Architecture
Academic year 2015-2016

UNIVERSITEIT
GENT

Acknowledgements

This work would not be what it is, without the guidance, advice and support of several people. I would like to thank everyone who has been – directly or indirectly – involved in this work.

First of all, I would like to thank my promoter prof. dr. ir. Kevin Van Geem and the director of the Laboratory for Chemical Technology prof. dr. ir. Guy Marin for giving me the opportunity to work on this subject. I am even more grateful that they have allowed me to continue my academic career at the LCT and for the prospect of visiting MIT.

I could not have wished for a better coach than ir. Pieter Reyniers. Thank you for the unrelenting support and advice during the past year. Whether it was looking for pesky errors in the code for hours at a time, or reviewing my poster, presentations and writings for a fifth time to eventually comment on changes you made yourself, I am genuinely grateful for the amount of effort you put into me as thesis student. Special thanks also to ir. David Van Cauwenberghe who often joined the debugging sessions and expertly showed me around OpenFOAM.

Thank you to Laurien, Alexander and Jens for tolerating my presence in their office. I have enjoyed sharing an office with you and hope that the upcoming personnel relocations in building 918 don't ship me off to somewhere else.

For the recreational moments – in the breaks and after hours – I wish to thank Andres, Lennert and Michiel. Thanks for suffering my complaints when I probably should not have been complaining. Congratulations to Andres for hauling in the most card playing victories. I am also glad to be part of the newly instated LCT running club: Moreno, Nick, Thomas and Michiel, thanks for helping me stay active during the final months of the year.

Last but most definitely not least, I would like to thank my parents. Not only for the genes they gave me 23 year ago, but for always giving me every possible chance in my personal development and education.

Pieter Plehiers

May 31st 2016

Computational Fluid Dynamics (CFD) of Turbulent Flows: Direct Numerical Simulation and Large Eddy Simulation

Pieter P. Plehiers

Master's dissertation submitted in order to obtain the academic degree of
Master of Science in Chemical Engineering

Academic year 2015-2016

Promotor: Prof. dr. ir. Kevin M. Van Geem
Coach: ir. Pieter A. Reyniers

GHENT UNIVERSITY
Faculty of Engineering and Architecture

Department of Chemical Engineering and Technical Chemistry
Laboratory for Chemical Technology
Chairman: Prof. dr. ir. Guy B. Marin

Abstract

Turbulence is a natural phenomenon, which is present in a myriad of industrial processes. In the reactor section of a steam cracking, turbulence is used to a benefit. By promoting turbulence, more uniform temperature profiles are achieved, increasing heat transfer. In ribbed tubes, turbulence is promoted through periodic break-up of the boundary layer. Large Eddy Simulations (LES) show that the ribbed tube significantly reduces coke formation compared to a bare tube. Finned tubes perform comparably. Coke formation is slightly faster than in the ribbed tube, but the pressure drop is lower.

Contrarily, turbulence is a nuisance in vortex-based natural gas dehydration technologies. Turbulence increases the overall pressure drop, requiring repressurisation of the natural gas after dehydration. Based on Reynolds Averaged Navier-Stokes (RANS) simulations, the existing geometry of the SUSTOR2 natural gas dehydration device is further optimised.

Keywords: Steam cracking, computational fluid dynamics, turbulence, LES, RANS, DNS, enhanced coil geometries, natural gas dehydration, OpenFOAM, FLUENT

Computational Fluid Dynamics (CFD) of Turbulent Flows: Direct Numerical Simulation and Large Eddy Simulation

Pieter Plehiers

Promotor: prof. dr. ir. Kevin M. Van Geem
Coach: ir. Pieter A. Reyniers

***Abstract*: Turbulence is a natural phenomenon, present in a myriad of industrial processes. In steam cracking, the most important process for the production of valuable light olefins such as ethene and propene, turbulence is used to a benefit. By promoting turbulence via internal elements (e.g. helicoidal ribs), higher heat transfer rates and more uniform temperature profiles are achieved. The heat transfer can also be augmented by increasing the heat transfer surface in the tube (e.g. internal fins). Large eddy simulations (LES) of butane steam cracking are used to predict temperature and species profiles at Reynolds numbers around 65,000 to eventually predict coking rates in a bare reactor, an internally finned reactor and a ribbed reactor.**

Contrarily, turbulence is a nuisance in swirl-flow-based natural gas dehydration technologies. Turbulence increases the pressure drop, requiring repressurisation of the natural gas after dehydration. Based on Reynolds averaged Navier-Stokes (RANS) simulations, the existing geometry of the SUSTOR2 natural gas dehydration device is further optimised. Via 2D simulations, optimal nozzle throat diameter and axial length are determined. The influence of a profiled end wall (PEW) is also investigated. A 3D simulation of the optimised geometry is performed to provide an *in silico* proof of concept for the novel technology.

***Keywords*: Steam cracking, computational fluid dynamics, turbulence, LES, RANS, DNS, enhanced coil geometries, natural gas dehydration, SUSTOR2, OpenFOAM, FLUENT**

I. Introduction

Light olefins such as ethene and propene are among the most important building blocks in the petrochemical industry [1]. Both products are mainly used in the polymer industry for the manufacturing of polyolefins. While in recent years, some attention has been devoted to alternative olefin production routes [2], steam cracking remains by far the predominant process for the production of light olefins.

The concept of steam cracking is over 150 years old, having been devised in 1855. Today, world scale facilities annually produce over 1.5 million tonnes of ethene and 600,000 tonnes of propene. The furnaces of a typical world scale plant have a combined heat output of around 800 MW. Due to the scale of the production, even minor improvements can deliver considerable operational and economic benefits.

Small enhancements can still be made in various aspects of the process. In the current work, the focus is on the reactor tubes and more specifically on the influence of their geometry on the product yields and coking rate. Coke formation [3] in the cracking coils results in the formation of an insulating layer, deteriorating the heat transfer and increasing the energy consumption of the process. Also, the coke layer reduces the cross-sectional area for flow, increasing the pressure drop. Enhanced coil geometries make use of different types of internal elements to augment the heat transfer [4-6]. The internally finned tube achieves this mainly by increasing the available surface for heat transfer. The helicoidally ribbed tube on the other hand promotes turbulence by interrupting the laminar boundary layer via impingement on the rib. In both cases, the trade-off is an increased pressure drop.

The second part of this work is situated in the field of natural gas processing. Raw natural gas generally contains substantial amounts of water. Even small amounts of water can damage pipelines by corrosion or abrasion (ice formation or hydrate formation). Different technologies are available for natural gas dehydration, e.g. adsorption, absorption and membrane technology [7]. The main disadvantages of these technologies are their high cost, high complexity and bulkiness. Several novel technologies, all based on the Joule-Thomson effect in swirling flows, have been developed in recent years [8-10], of which the Twister® Supersonic Separator is the most important example. The major drawback of these technologies is their high pressure drop (up to 50 % of the inlet pressure). The SUSTOR2 technology claims to have a pressure drop of only 5 % [9].

The aim of this work is twofold. Firstly, the turbulent flow in three tubular geometries for steam cracking coils is investigated (bare, internally finned and helicoidally ribbed). Large eddy simulations are performed in OpenFOAM, implementing detailed kinetics. The differences between the three geometries are discussed and the results are compared to the relevant data from the work of M. Zhu [11], executed in AVBP. Secondly, the SUSTOR2 device is investigated. Using 2D Reynolds averaged Navier-Stokes simulations, the initial geometry is optimised. The developed geometry is then further investigated in a more detailed 3D simulation.

II. Literature study: DNS Codes

A. Introduction

Direct numerical simulation (DNS) is a powerful tool for the fundamental study of turbulence. DNS has several specific characteristics, demanding dedicated codes to perform the simulations. Due to the fundamental nature of DNS, it is paramount that numerical errors are kept at a minimum [12]. An important aspect of the code is the selection of the discretisation method. There are three major categories, namely finite differencing, finite volume and spectral methods. In the first two, the domain is divided into a discrete number of cells and the equations are solved to determine a single value for the flow parameters in each cell. The approach is different in the spectral methods; instead of solving the equations in a large number of

cells, the solution in the entire domain is represented as a weighted sum of base functions [13]. The greatest drawback of the spectral methods is their incapability to simulate complex domains (the finned and ribbed tubes qualify as complex in this context). The spectral elements methods (SEM) combine the strengths of the cell-based discretisation methods and the domain-based spectral methods. In the SEM, the domain is sub-divided into several smaller elements. In each of these elements a different set of weighting coefficients is imposed, rather than one set for the entire domain. Spectral-based methods by far outperform the finite volume and finite differencing methods in accuracy and grid demands. On the other hand, their computational cost is considerably higher.

Table 1: Overview of the analysed DNS codes.

Code	*Spatial Discreti-sation*	*Temporal Discretisation*	*Open Source*	*Main application*
OpenFOAM	FVM	Cash-Carp Runge-Kutta, 5th order	YES	Not dedicated to DNS, very broad applicability
Nek5000	SEM	BDS, 3rd order	YES	Wall-bounded flows
S3D	High-order FDM	Explicit Runge-Kutta, 4th order	NO	Reactive flows (combustion) in large numerical domains
SIMSON	Fourier-Chebyshev SM	Crank-Nicolson, 2nd order	YES	Wall-bounded flows
Gerris	FVM, octree structured, adaptive mesh	Fractional-step projection, 2nd order	YES	Atmospheric and aquatic research

B. Comparison of Different Codes

Five of the most frequently used codes for DNS are compared. Each code is tailored for certain types of flow. OpenFOAM is not a DNS-dedicated code. However, within its wide range of solvers, the dnsFoam solver is capable of performing DNS. The low order discretisation of OpenFOAM is a major drawback, though accurate results have been achieved [14]. Nek5000 is based on the SEM and is a widely used open-source code for a variety of wall-bounded flows [15]. SIMSON is a purely spectral code and is found to have the best single-core performance of all compared codes [16], it too is open-source. S3D is a commercial code owned by Sandia National Laboratories [17]. Using high (12^{th}) order finite differencing methods, this code has been developed for GPU accelerated computations of turbulent combustion. This code allows the simulation of very large domains comprising in the order of 10^9 grid points. Gerris is specialised in multiphase flow simulations and minimises the computational cost by automatically refining the grid in the region of the fluid interface, via octree refinement [18]. Table 1 summarises the most important characteristics of the codes. For direct numerical simulations, the Nek5000 code is proposed. It combines the best of the FVM and spectral methods to provide excellent accuracy for an acceptable computational cost. It also has a broad user base and is well supported and documented.

III. Large Eddy Simulation of Butane Cracking

A. Numerical Methods

The non-isothermal, reactive flow in a steam cracking tube is described by four conservation equations, namely conservation of global mass (eq. (1)), momentum (eq. (2)), energy (eq. (3)) and species (eq. (4)). The concept of LES implies filtering the conservation equations based on a certain cut-off length. All turbulent phenomena with a length scale smaller than this cut-off length are modelled rather than resolved. In the finite volume approach, the filter and cut-off are determined implicitly, based on the cube root of the local cell volume. In this work, the wall adaptive local eddy viscosity (WALE) model is used to compute the sub-grid scale stresses. The turbulent diffusion coefficient and thermal conductivity are determined based on the turbulent viscosity, but corrected by respectively the turbulent Schmidt and Prandtl numbers.

$$\frac{\partial \rho}{\partial t} + \nabla \cdot (\rho \boldsymbol{v}) = 0 \quad (1)$$

$$\frac{D\rho \boldsymbol{v}}{Dt} = \rho \boldsymbol{g} + \nabla \cdot \boldsymbol{\tau} \quad (2)$$

$$\nabla \cdot (\lambda \nabla T) + \dot{q} + \Lambda = \nabla \cdot (P\boldsymbol{v}) + \frac{\rho}{2}\frac{Dv^2}{Dt} + \rho \frac{Du}{Dt} + \rho \frac{D(gy)}{Dt} \quad (3)$$

$$\frac{\partial C_i}{\partial t} + v_j \frac{\partial C_i}{\partial x_j} = D_{mol,i} \frac{\partial^2 C_i}{\partial x_j \partial x_j} + R_i(C_j) \quad (4)$$

The kinetic model describing butane steam cracking comprises 20 components and 149 reactions. The reaction network was generated using RMG [19]. The pseudo-steady state assumption is applied to the reactive, radical species to reduce the stiffness of the problem and reduce the number of species equations that have to be solved.

The inlet conditions for each of the three geometries are identical. Butane is diluted with water to a hydrocarbon content of 69 wt%. The geometries are designed such that the cross-sectional flow area is equal for all three cases. All grids consist of structured, hexahedral cells and have an initial cell spacing at the wall corresponding to $y^+ < 1$, *i.e.*, wall-resolved LES is performed. The meshes of respectively the bare, finned and ribbed geometry comprise a total of ± 4.0 10^6, ± 6.2 10^6 and ± 14.2 10^6 cells.

Table 2: Inlet conditions for all geometries.

Parameter	*Mass flow rate [kg s-1]*	*Pressure [Pa]*	*Temperature [K]*	*Reactor length [m]*	*Butane mass fraction*
Value	0.0655	235680	909.15	10	0.69

B. Results and Discussion

1) Comparison to 1D Simulations

The results are compared to 1D simulations made in CHEMKIN as a basic validation. The full validation of the QSSAPipeFoam solver for reactive RANS simulations will be published by Van Cauwenberge et al. [20]. Overall, the qualitative agreement is found to be very good. Quantitatively the differences between the 1D simulations and 3D LES can amount to quite large values. For example differences in bulk temperature of up to 30 K are observed (Figure 1). These differences are to be expected as the flow in all three geometries is intrinsically three dimensional with radial and azimuthal gradients that are not accounted for in 1D simulation.

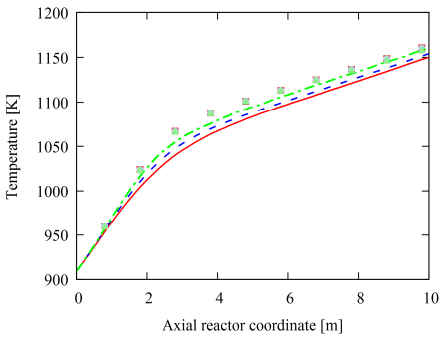

Figure 1: Bulk temperature profiles as simulated in CHEMKIN: bare tube (■), finned tube (●) and ribbed tube (▲); and LES: bare tube (———), finned tube (— —) and ribbed tube (— - —).

2) *Heat Transfer*

The effect of the improved heat transfer is seen in Figure 2 by the difference between the wall and bulk temperatures. The bulk temperatures are highest in the ribbed and lowest in the bare reactor. Both the finned and ribbed tubes have a significantly lower tube inner wall temperature, reducing the temperature difference between the fluid and the wall.

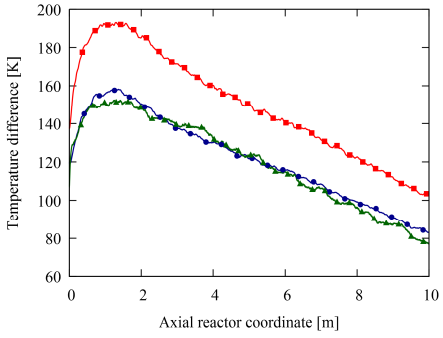

Figure 2: Difference between wall and bulk temperatures as function of the axial reactor coordinate in the bare (——■——), finned (——●——) and ribbed (——▲——) geometries.

The improved heat transfer is also expressed in the Nusselt numbers and corresponding heat transfer coefficients. The comparison of Nusselt numbers is not entirely relevant as the hydraulic diameters of the different cases are not equal. Comparing the average heat transfer coefficients however clearly shows that the heat transfer coefficient is highest in the ribbed reactor and lowest in the bare reactor. The heat transfer characteristics are summarised in Table 3.

Table 3: Summary of the heat transfer characteristics of the different geometries.

Geometry	*Average Nusselt number*	*Average heat transfer coefficient [W m⁻² K⁻¹]*	*Improvement factor*
Bare	163.5	691.5	1.0
Finned	160.7	672.7	1.25
Ribbed	217.0	917.8	1.33

3) *Pressure Drop*

The difference in pressure drop is clearly observed in Figure 3. It is also a result of both the increased tube inner wall surface area and the increased turbulence. Table 4 summarises the pressure drop characteristics in the different cases. Care should be taken with a one-on-one comparison of the bare and finned cases. The average Reynolds number in the bare tube is 66,641, while for the finned tube this is 52,206 and in the ribbed tube it is 67,158. The difference arises from the different hydraulic diameters in the cases. Therefore, while the mass flow rates and velocities in both cases are the same, the increased surface area implies a less turbulent flow. At equal Reynolds numbers, the pressure drop ratio for the finned tube will be even higher.

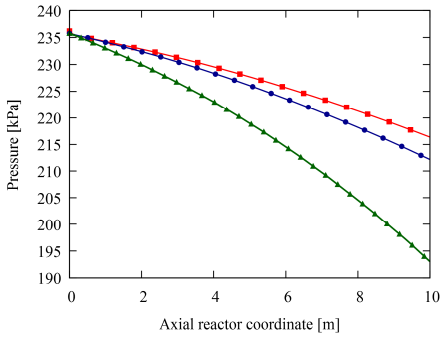

Figure 3: Pressure profiles in the bare (——■——), finned (——●——) and ribbed (——▲——) geometries.

Table 4: Summary of the pressure drop characteristics of the geometries.

Geometry	*Total pressure drop [Pa]*	*Average Fanning friction factor*	*Pressure drop ratio*
Bare	19.8	0.0082	1.0
Finned	23.6	0.0074	1.19
Ribbed	42.7	0.0157	2.15

4) *Selectivities and Yields*

The enhanced coil geometries affect the product yields by the modified flow structures and hence the changed temperature profiles. The combined yield of ethene and propene is shown in Figure 4. In the initial stages, there is some difference between the yields in the different geometries. The outlet yields are approximately equal. The enhanced geometries have a slightly higher selectivity towards propene due to the lower average cracking temperatures. Consequentially, the reactor outlet has a lower propene to ethene ratio in the bare reactor (0.451) compared to the finned (0.466) and ribbed reactors (0.467).

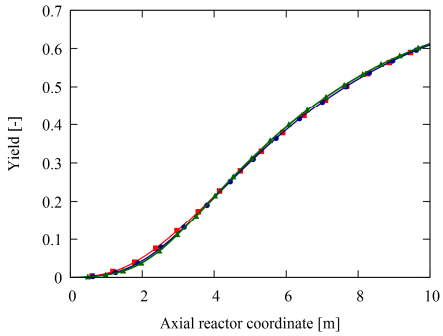

Figure 4: Combined yield of ethene and propene in the bare (——■——), finned (——●——) and ribbed (——▲——) geometries.

5) *Coking Rates*

Next to improving the selectivities and yields, the enhanced coils must prolong the run length of a steam cracking furnace. This run length is determined by the coking rate at the tube walls. An assessment of the coking rates is made based on the coking model of Plehiers [21].

$$R_{coke} = f_c \left(k_{coke,1} \frac{C_{ethene}^{\ 2}}{C_{propene}} + k_{coke,2} C_{ethene} + k_{coke,3} C_{propene} \right) \quad (5)$$

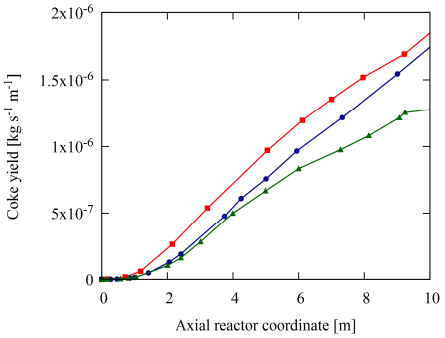

Figure 5: Average coke yields as function of the axial reactor coordinate in the bare (—■—), finned (—●—) and ribbed (—▲—) geometries.

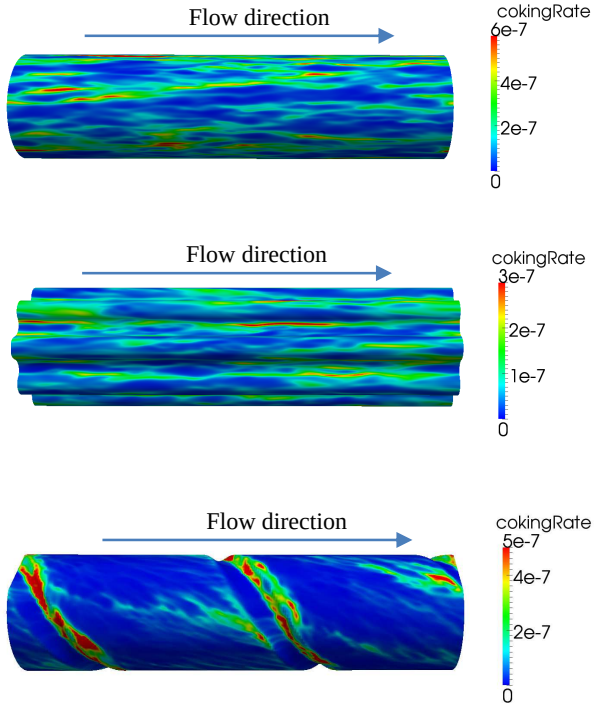

Figure 6: Instantaneous coking rate [kg s^{-1} m^{-2}] in the bare (top), finned (middle) and ribbed (bottom) tubes, for a section of the tube centred around an axial position of around 0.8 m.

Figure 5 proves that both enhanced geometries succeed at reducing the average coke yield in the reactor. Figure 6 represents the instantaneous coking rates in a section of the tube centred around an axial position around 0.8 m. The finned tube is observed to have a distribution of the coking rates along the tube wall. Similarly as in the bare tube, there is no indication of coke being formed preferentially at certain locations. This is the case in the ribbed tube. Nearly all coking takes place on the trailing edge of the rib. Elevated coking rates are also found on the tube wall directly in front of the leading edge of the rib. At these locations, the coking rates in the ribbed tube are even higher than in the bare tube. However, in the rest of the ribbed tube, coke formation takes place at minimal rates. The finned reactor has a higher coke yield than the ribbed reactor due to the higher inner wall surface area. The intrinsic coking rate of the finned tube is lower. This is the result of a lower average wall temperature originating from small differences in heat flux profiles. The local character of the coke formation in the ribbed tube can potentially affect the run-length of the reactor in a negative way. However, to truly assess the effects of the non-uniform coking rate, run-length simulations accounting for the growth of the coke layer are required.

C. *Comparison to AVBP*

Similar simulations have been performed in a bare and ribbed geometry by M. Zhu, using AVBP [11]. Contrary to OpenFOAM, AVBP uses unstructured grids. This simplifies the mesh of the ribbed geometry, but results in an inhomogeneous spread of the cell volumes. Additionally, for the OpenFOAM cases, wall-resolved LES (WRLES) has been performed ($y^+ = 1$), compared to wall-modelled LES (WMLES, $y^+ \sim 20$) in AVBP. A second geometric difference in that the length of the AVBP cases is only a single pitch (69.11 mm, 138.22 mm in OpenFOAM). This is below the advised length to radius ratio of 2π [22] to prevent resonance effects from the periodic boundary conditions.

In the bare geometry, the differences between the simulated average temperatures are quite high, resulting from a different averaging procedure. In AVBP, volume-weighted averaging is used, while in OpenFOAM the averages are mass-weighted. The volume-weighting gives comparatively more weight to the cells at high temperature near the wall, resulting in a higher average temperature. The higher conversion predicted by AVBP indicates that the AVBP mass-weighted average temperature is higher than in the OpenFOAM case as well. The higher temperature results in a higher selectivity towards ethene. In the ribbed tube, the volume-weighted average temperature is only slightly higher in the AVBP case. The conversion is lower, as is the ethene selectivity. This indicates that the mass-weighted average temperature is lower, though differences between WRLES – WMLES also contribute to the lower selectivity.

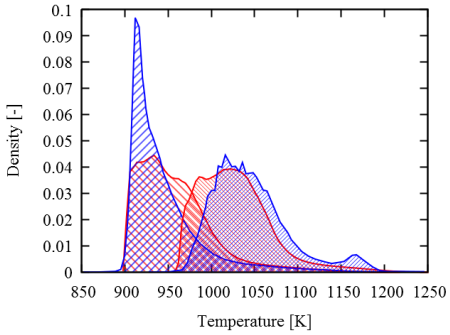

Figure 7: Temperature distribution in the bare tube. OpenFOAM: 0.013 s (▨) and 0.03675 s (▨) AVBP: 0.010 s (▨) and 0.040 s (▨)

An important difference is also seen in the temperature distributions, shown in Figure 7 for the bare case. Volume-weighted distributions are used in both cases. At a residence time of about 0.04 s the distributions match well, apart from the secondary peak in the AVBP case. This peak is linked to the combination of high cell density and low mass density near the wall. At a residence time of around 0.01 s, there is a significant difference in the variance of the distribution. This is a result of the pre-simulations. For the AVBP cases, only the turbulent velocity field has been developed, while for OpenFOAM, both velocity and temperature fields have been developed. Similar observations are made for the ribbed geometry, but due to the

improved heat transfer, the variation decreases much more rapidly.

IV. Supersonic Swirling Flows

A. *Supersonic Nozzle Flow*

The supersonic flow in nozzles is described by the same equations as given in section III, though in this section, the Reynolds averaging concept is used for turbulence modelling. In subsonic flows, the flow rate through a nozzle is determined by both up- and downstream pressures. Contrarily, in choked flow, *i.e.* flow where the Mach number is unity in the throat, the flow rate is independent of the downstream pressure as the pressure in the throat is determined by purely thermodynamic quantities (eq. (6)).

$$\frac{P^*}{P_0} = \left(\frac{2}{1+\gamma}\right)^{\frac{\gamma}{\gamma-1}} \quad \textbf{(6)}$$

In a converging-diverging nozzle, the flow accelerates towards the throat. If a Mach number equal to unity is attained in the throat, the flow will accelerate in the diverging section as well. At a certain point, it is impossible to comply with all conservation equations and a shockwave develops, significantly affecting the pressure drop. However, according to the inventors of SUSTOR2, this is not the case for swirling flows of which the axial velocity component is subsonic [9]. This idea is exploited in the SUSTOR2 device.

B. *2-D Simulations: Geometry Optimisation*

Two dimensional simulations are used to optimise the geometry. The base case consists of the geometry provided in US patent 8790455 B2 [9]. It has axial symmetry around a horizontal axis and planar symmetry over the left end of the computational domain. The mass flow rate through half the geometry is 0.14 kg s^{-1}. The inlet temperature is 293 K and the outlet pressure is 202.6 kPa. Due to convergence issues typical for supersonic flows, first order discretisation schemes are used. In this initial geometry, the highest Mach number that is attained is only 0.87 (Figure 8). This means that the flow does not expand sufficiently after passing through the nozzle and hence the Joule-Thomson effect is not strong, only lowering the temperature to a minimum of 263 K. This is too high to fulfil the dew point specification on the natural gas of 233 K. A low velocity zone is observed near the axis of symmetry. Here the axial velocity is negative, indicating backflow. The large difference in velocity between the backflow zone and the high-velocity zone near the wall contributes to a high pressure drop.

A first parameter that is varied is the diameter of the nozzle throat. Decreasing this results in an overall increase in the fluid velocity in the region downstream of the nozzle. In the original geometry with a throat diameter of 40 mm, the flow was subsonic at all positions. Figure 9 indicates that supersonic flow is achieved when reducing the throat diameter. With a radius of 5 mm, the nozzle has now become so narrow that a Mach number of unity is reached in the entire cross section of the nozzle throat. The axial velocity component is also supersonic, resulting in shockwave development. In the case with a nozzle radius of 10 mm, the central backflow region no longer extends through the throat, it is pushed downstream by the accelerating flow.

A second optimisation is the addition of the profiled end wall, which should shift the end of the backflow region even farther upstream. The conic backflow zone extends through the nozzle again, until it hits the PEW. Due to the lower axial velocity in the backflow zone and the higher proximity of the flow to the wall, the pressure drop over the device is reduced by 0.2 bar. Additionally, the low-temperature zone is significantly larger when the PEW is present, enhancing the condensation capacity of this geometry.

The third part of the geometry optimisation concerns the axial length of the SUSTOR2 device. The Mach number increases with decreasing axial length, resulting in greater fluid expansion and lower minimum temperatures, as illustrated in Figure 10. The flow pattern changes significantly when reducing the axial length in the presence of a PEW. Upon reducing the length sufficiently, the axial acceleration, which was virtually non-existent in the initial geometry with PEW, becomes important. This results in an axial flow which prevents the backflow region from penetrating through the nozzle. This axial flow already occurs in the longest geometry when no PEW is present and therefore no significant change in flow pattern is observed.

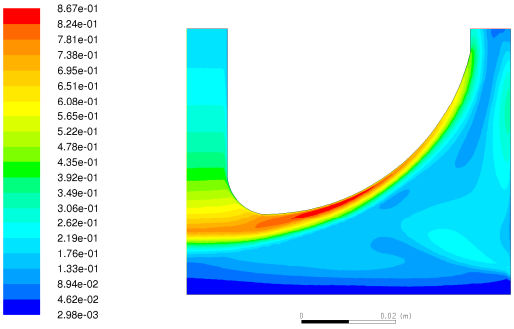

Figure 8: Mach number in the SUSTOR2 base case.

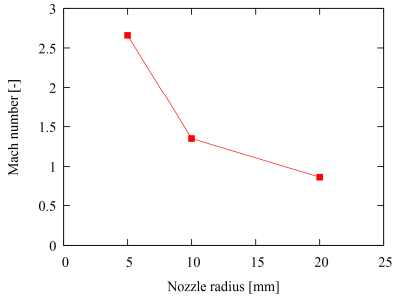

Figure 9: Maximal Mach number as function of the nozzle radius.

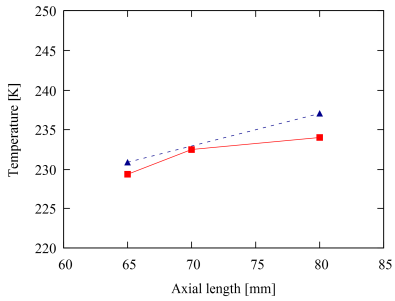

Figure 10: Temperature as function of the axial domain length with (-■-) and without PEW (-▲-).

The initial geometry is not suited to serve as dehydration device. Feasible condensation conditions are achieved for a

similar device with a nozzle diameter of 20 mm. The performance is further enhanced via the addition of a profiled end wall and a reduction of the axial length to 65 mm. This geometry is used as starting point for a full three dimensional simulation of the device.

C. 3-D Simulations

The central part of the three dimensional simulations is the geometry proposed in the previous section. Both the inlet and outlet are extended, to simulate the swirling flow in the device more accurately. The mass flow rate is still 0.14 kg s^{-1}.

Contrary to what the two dimensional, axisymmetric simulations predict, shockwave flow does occur in the 3D simulation. The important flow characteristics in the nozzle are illustrated in Figure 11. Due to the asymmetric character of the inlet and outlet extensions, the flow in the nozzle is not axisymmetric. A Mach number above 2 is attained, the corresponding gas expansion results in a minimum temperature of 179 K. However, due to the loss of swirl flow in the transition to supersonic flow, the correct working of the device is impaired. Simulations with lower mass flow rates (0.1, 0.07 and 0.035 kg s^{-1}) are consequentially performed to determine the onset of shockwave flow. At all lower flow rates, the shockwave has been eliminated. At 0.1 kg s^{-1}, the flow is unstable and highly asymmetric. The two lowest mass flow rates indicate feasible operation, with a minimum temperature below 230 K and a pressure drop of 175 kPa.

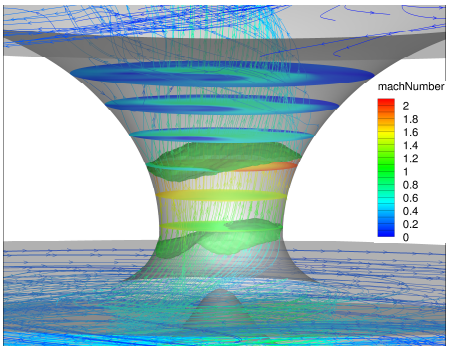

Figure 11: Stream lines and y-plane slices coloured by Mach number, iso-surface for unity Mach numbers.

V. Conclusions and Future Work

Two types of turbulent flows have been investigated: steam cracking of butane in an industrial coil and natural gas dehydration in the novel SUSTOR2 device.

LES of butane steam cracking shows that improving the heat transfer via longitudinal fins or helicoidal ribs strongly affects the wall temperature of the reactor. Consequentially reaction rates, selectivities and coking rates are altered. The heat transfer in the finned coil is 25 % higher than in the bare. This becomes 33 % in the ribbed coil. Nonetheless, the wall temperature is lowest in the finned reactor as a result of differences in the imposed heat flux profile, resulting in the lowest coking rates. On the trailing edge of the rib, coking rates can be up to 70 times as high as the average, though. These extremes are not observed in the other two geometries. The trade-off for the increased heat transfer is the increased pressure drop. The pressure drop is 19 % higher over the finned reactor than over the bare and 115 % higher over the ribbed reactor. Altering the mass flow rates to obtain equal Reynolds numbers could be of interest for the theoretical comparison of heat transfer and pressure drops, while changing the inlet pressure to match the outlet pressures could be of interest for industrial comparison.

2D RANS of swirling trans- and supersonic flows in the SUSTOR2 device are used to optimise the geometry described in US patent 8790455 B2. A device with a nozzle diameter of 20 mm, an axial length of 65 mm and a profiled end wall is found to display the greatest potential. 3D simulations including inlet and outlet predict the formation of a shockwave. Stable flows with a minimal temperature below 230 K and a pressure drop of 175 kPa are achieved for mass flow rates below 0.07 kg s^{-1}. Further refinement of the inlet and outlet is required, *e.g.* by adding vanes. Optimising the curvature of the nozzle wall could also result in performance enhancement. Finally, performing the simulations at a realistic operating pressure of 100 bar could reduce the relative pressure drop to the acclaimed 5 %.

Acknowledgements

The author acknowledges the aid and support from the members of the Laboratory for Chemical Technology, in particular from my coach, ir. Pieter A. Reyniers, from ir. David J. Van Cauwenberge and from my promotor prof. dr. ir. Kevin M. Van Geem.

This work was carried out using the STEVIN Supercomputer Infrastructure at Ghent University, funded by Ghent University, the Flemish Supercomputer Center (VSC), the Research Foundation Flanders (FWO) and the Flemish Government – department EWI.

List of Symbols

C_i	Concentration of component i	$mol\ m^{-3}$
$D_{mol,i}$	Molecular diffusion coefficient	$mol\ m^{-2}\ s^{-1}$
M	Mach number	$-$
P^*	Pressure in nozzle throat	Pa
P_0	Pressure at nozzle inlet	Pa
$\dot{q}$	Heat generation	$W\ m^{-2}$
R_i	Reaction rate of component i.	$mol\ m^{-3}\ s^{-1}$
$\boldsymbol{v}$	Velocity vector	$m\ s^{-1}$
y^+	Dimensionless wall distance	$-$
γ	Ratio of specific heats	$-$
λ	Conductivity of the fluid	$W\ m^{-1}\ K^{-1}$
Λ	Viscous energy transfer	$W\ m^{-2}$
$\boldsymbol{\tau}$	Viscous stress tensor	Pa

References

1. Zimmermann, H.; Walzl, R., In *Ullmann's Encyclopedia of Industrial Chemistry*, Wiley-VCH Verlag GmbH & Co. KGaA: 2000.
2. Dijkmans, T., et al., *Green Chemistry* **2013,** 15, (11), 3064-3076.
3. Muñoz Gandarillas, A. E., et al., *Industrial & Engineering Chemistry Research* **2014,** 53, (35), 13644-13655.
4. Schietekat, C. M., et al., *AIChE Journal* **2014,** 60, (2), 794-808.
5. Schietekat, C. M., et al., *Chemical Engineering Journal* **2014,** 238, 56-65.
6. Van Geem, K. M., et al., In *AIChE Spring Meeting*, San Antonio, Texas, 2013.
7. Wang, X.; Economides, M., In *Advanced Natural Gas Engineering*, Gulf Publishing Company: Houston, Texas, 2009; pp 115-170.
8. Alferov, V. I., et al. WO2000/023757 (A1), 2000.
9. Borissov, A., et al. 2014.
10. Tjeenk, W. C. A. WO0040834 (A1), 2000.
11. Zhu, M. Université de Toulouse, 2015.
12. Moin, P.; Mahesh, K., *Annual review of fluid mechanics* **1998,** 30, (1), 539-578.
13. Canuto, C., et al., In *Spectral methods : fundamentals in single domains*, Springer-Verlag: 2006; pp 117-165.
14. van Haren, S. W. Delft University of Technology, 2011.
15. El Khoury, G. K., et al., *Journal of Physics: Conference Series* **2014,** 506, (1), 012010.
16. Ohlsson, J., et al., In *Spectral and High Order Methods for Partial Differential Equations: Selected papers from the ICOSAHOM '09 conference, June 22-26, Trondheim, Norway*, Hesthaven, S. J.; Rønquist, M. E., Eds. Springer Berlin Heidelberg: Berlin, Heidelberg, 2011; pp 459-467.
17. Chen, J. H., et al., *Computational Science & Discovery* **2009,** 2, (1), 015001.
18. Popinet, S., *Journal of Computational Physics* **2003,** 190, (2), 572-600.
19. Gao, C. W., et al., *Computer Physics Communications* **2016,** 203, 212-225.
20. Van Cauwenberge, D. J., et al., *AIChE Journal* **2016,** In preparation.
21. Plehiers, P. M. Rijksuniversiteit Gent, 1989.
22. Chin, C., et al., *Physics of Fluids* **2010,** 22, (11), 115107.

Table of contents

Nomenclature

Acronyms

0D	Zero Dimensional (e.g. maxima and minima, pressure drop)
1D	One Dimensional
2D	Two Dimensional
3D	Three Dimensional
BD(S)	Backward Differencing (Scheme)
c.s.	Control Surface
c.v.	Control Volume
CERFACS	Centre Européen de Recherche et de Formation Avancée en Calcul Scientifique European Centre for Research and Advanced Training in Scientific Computation
CD(S)	Central Differencing (Scheme)
CFD	Computational Fluid Dynamics
CFL	Courant (Flow) Number
CIP	Coil Inlet Pressure
CIT	Coil Inlet Temperature
CN	Crank-Nicholson
CPU	Central Processing Unit
CPU-s	CPU seconds, equals the actual wall time multiplied by the number of CPUs
COP	Coil Outlet Pressure
COT	Coil Outlet Temperature

DES	Detached Eddy Simulation
DNS	Direct Numerical Simulation
DOF	Degrees Of Freedom
FD(M)	Forward Differencing (Method)
FEM	Finite Element Method
FFT	Fast Fourier Transform
FVM	Finite Volume Method
GPU	Graphics Processing Unit
HPC	High Performance Computing
IBR	Inner Butterfly Region
LES	Large Eddy Simulation
MERT	Mixing Element Radiant Tube
MPI	Message Passing Interface
MTO	Methanol-to-Olefins
OBR	Outer Butterfly Region
PEW	Profiled End Wall
PDF	Probability Density Function
PDH	Propane Dehydrogenation
PISO	Pressure Implicit with Splitting of Operators
PIMPLE	Merged PISO-SIMPLE
PSS(A)	Pseudo-Steady-State (Assumption)
RANS	Reynolds-Averaged Navier-Stokes
RK	Runge-Kutta
RKE	Realizable k-epsilon model

RMS	Root-Mean-Square
RNG	RNG-k-epsilon turbulence model
RSM	Reynolds Stress Model
S(E)M	Spectral (Element) Method
SFT	Swirl Flow Tube®
SGS	Sub-Grid Stress models
SIMPLE	Semi-Implicit Pressure Linked Equations
SIMPLEC	Semi-Implicit Pressure Linked Equations – Consistent
SRK	Soave-Redlich-Kwong equation of state
SIMPLER	Semi-Implicit Pressure Linked Equations – Revised
TBLE	Thin Boundary Layer Equations
TKE	Turbulent Kinetic Energy
TLE	Transfer Line Exchanger
TLM	Two Layer Model
WALE	Wall Adaptive Local Eddy viscosity
WMLES	Wall-Modelled Large Eddy Simulation
WRLES	Wall-Resolved Large Eddy Simulation

Roman Symbols

A	Surface area	m^2
$B[i]$	Backward reaction rate of reaction i	$mol\ s^{-1}$
C_i , $Conc[i]$	Concentration of component i	$mol\ m^{-3}$
C_κ	Proportionality constant in Kolmogorov's spectrum law	$-$
C_w	Model parameter in the WALE model for LES	$-$
c	Speed of sound (propagation velocity of a pressure wave)	$m\ s^{-1}$
c_v	Specific heat capacity at constant volume	$J\ kg^{-1}\ K^{-1}$
c_p	Specific heat capacity at constant pressure	$J\ kg^{-1}\ K^{-1}$
D	(Hydraulic) Diameter	m
$D_{mol,i}$	Molecular diffusion constant of component i	$m^2\ s^{-1}$
D^k	Viscous diffusion of turbulent kinetic energy	$m^2\ s^{-3}$
E	Energy spectrum	$m^3\ s^{-2}$
e	Specific energy	$J\ kg^{-1}$
e	Absolute wall roughness	m
err	Truncation error	
$\boldsymbol{F}$	Force vector	N
F_n	Distribution function of the velocity	$-$
$F[i]$	Forward reaction rate of reaction i	$mol\ s^{-1}$
f	Friction factor	$-$

$\hat{f}$	Expansion coefficient of the function f, in a continuous domain	
$\check{f}$	Expansion coefficient of the function f, in a discrete domain	
g	Gravitational constant	$m\ s^{-2}$
g_{ij}	Derivative of velocity component i to spatial coordinate j.	s^{-1}
H	Height of a channel	m
$\mathcal{H}$	Function grouping the advective and viscous terms of the momentum equation	$kg\ s^{-2}\ m^{-2}$
h	Enthalpy	$J\ kg^{-1}$
h	Heat transfer coefficient	$W\ m^{-2}\ K^{-1}$
k	(Turbulent) Kinetic energy	$m^2\ s^{-2}$
k_{coke}	Reaction rate coefficient for coking reactions	$kg_{coke} m^3_{reactor} m^{-2}_{wall} mol^{-1} s^{-1}$
$kb[i]$	Backwards reaction rate coefficient of reaction i	$s^{-1}/m^3 mol^{-1} s^{-1}$
$kf[i]$	Forwards reaction rate coefficient of reaction i	$s^{-1}/m^3 mol^{-1} s^{-1}$
L	Length	m
M	Mach Number	$-$
m_i	Mass fraction of component i	$-$
$\dot{m}$	Mass flow rate	$kg\ s^{-1}$
MM	Molar mass	$kg\ mol^{-1}$
$\boldsymbol{N}$	Vector of flux of φ	$[\varphi]\ s^{-1}\ m^{-2}$

n_i	Number of moles of component i	mol
$\boldsymbol{n}$	Normal vector of a surface	
P	Pressure	Pa
P	Wetted perimeter of a tube	m
P^k	Production of turbulent kinetic energy	$m^2\ s^{-3}$
Pr	Prandtl number	$-$
Q	Volumetric flow rate	$m^3\ s^{-1}$
$\dot{q}$	Heat transfer rate per unit area	$W\ m^{-2}$
$\boldsymbol{q_\varphi}$	Diffusive flux of parameter φ (e.g. diffusion, conduction)	$[\varphi]\ s^{-1}\ m^{-2}$
R	Radius	m
R_i	Net rate of formation of component i	$mol\ m^{-3}\ s^{-1}$
R_{ij}	Correlation of quantities I and J	$-$
$R[i]$	Production rate of component i	$mol\ m^{-3}\ s^{-1}$
$R[i+9]$	Consumption rate of component i	$mol\ m^{-3}\ s^{-1}$
r	Radial coordinate in a tubular geometry	m
Re	Reynolds number	$-$
S	Strain rate tensor	s^{-1}
S^d	Traceless, symmetric part of the square of the velocity gradient tensor	s^{-2}
S_i	Selectivity towards component i	$-$
S_φ	Integrated source term for φ over a control volume	
s_φ	Source term for φ	
Sc	Schmidt number	$-$

T	Absolute Temperature	K
T^k	Turbulent, velocity related diffusion of turbulent kinetic energy	$m^2\ s^{-3}$
T_l	Energy transfer at scale l	$m^2\ s^{-3}$
t	Time	s
u	Specific Internal Energy	$J\ kg^{-1}$
V	Volume	m^3
v	Velocity	$m\ s^{-1}$
$\boldsymbol{v}$	Velocity vector	$m\ s^{-1}$
X_i	Conversion of component i	$-$
x_i	Coordinate (x,y,z)	m
Y_i	Yield of component i	$-$
y	Space variable	m
y^+	Dimensionless wall distance (perpendicular to the wall)	$-$
z	Axial coordinate in a tubular geometry	m

Greek Symbols

α	Under-relaxation coefficient	$-$
γ	Ratio of heat capacities	$-$
γ	Parameter in Gaussian filter	$-$
δ_{ij}	Kronecker Delta: $\delta_{ij} = \begin{cases} 1 & if \ \ i = j \\ 0 & if \ \ i \neq j \end{cases}$	
Δ	Difference	$-$
Δ	Cut-off width	m
ε	(Viscous) dissipation rate of turbulent kinetic energy	$m^2\ s^{-3}$
η	Kolmogorov length scale	m
θ	Alternative notation time	s
θ	Tangential coordinate in tubular geometry	$-$
κ	Wavenumber	m^{-1}
λ	Thermal conductivity	$W\ m^{-1}\ K^{-1}$
Λ	Viscous energy transfer	$W\ m^{-2}$
μ	Dynamic viscosity	$kg\ m^{-1}\ s^{-1}$
ν	Kinematic viscosity	$m^2\ s^{-1}$
Π^k	Pressure related diffusion of turbulent kinetic energy	$m^2\ s^{-3}$
ρ	Density	$kg\ m^{-3}$
τ	Stress tensor, off-diagonal elements represent shear stresses, diagonal elements normal stresses	Pa
φ	Transported scalar	

ϕ	Basis function	
Φ	Integral of $\rho\varphi$ over the control volume	
Ψ	Dissipation function	$W\ m^{-2}$
Ω	Control Volume Surface	$-$
$\boldsymbol{\Omega}$	Surface ($\boldsymbol{n}\Omega$)	$-$

Mathematical

	Gradient	
$\nabla(f)$	$\left(\frac{\partial f}{\partial x}, \frac{\partial f}{\partial y}, \frac{\partial f}{\partial z}\right)$	m^{-1}
	$(cartesian)$	
	Divergence	
$\nabla \cdot (\boldsymbol{f})$	$\frac{\partial f_x}{\partial x} + \frac{\partial f_y}{\partial y} + \frac{\partial f_z}{\partial z}$	m^{-1}
	$(cartesian)$	
	Laplacian	
$\Delta(f)$	$\frac{\partial^2 f_x}{\partial x^2} + \frac{\partial^2 f_y}{\partial y^2} + \frac{\partial^2 f_z}{\partial z^2}$	m^{-2}
	$(cartesian)$	
	Substantial derivative	
$\frac{D}{Dt}$	$\frac{\partial}{\partial t} + v_x \frac{\partial}{dx} + v_y \frac{\partial}{dy} + v_z \frac{\partial}{dz}$	s^{-1}
	$(cartesian)$	
	Expected value over time of φ	
$\langle \varphi \rangle$	$\frac{1}{\Delta t} \int_t^{t+\Delta t} \varphi(t) dt$	
$\{\phi_k\}$	Orthogonal set of base functions	
$\mathcal{F}(x)$	Any (linear or non-linear) function of x	
#	Number of	

Sub- and Superscripts

l_0	Characteristic of the large turbulent scales
l	Characteristic of the turbulent scale l
η	Characteristic of the Kolmogorov scale
H	Hydraulic
th	Property at the throat of the nozzle
eff	Effective (taking into account an increase of the base value due to turbulence
C,i	Carbon atoms in component i
0	Base value (in laminar flow)
w	Property at the wall
$bulk$	Property in the bulk
$'$	Deviation from average
$\overline{\ }$	Average (time)
$\sim$	Filtered value
SGS	Sub-Grid-Stress
RS	Reynolds Stress
$\bullet$	Radical

1

Introduction

1.1. Light Olefins

Light olefins such as ethene and propene are some of the most important building blocks in the (petro)chemical industry. They can be used both as monomer or as base chemical as illustrated in Figure 1-1 and Figure 1-2, though the majority of both olefins is consumed in the production of their polymers.

As of 2012, the annual production of ethene amounted to 156 million tonnes [1], of which 19 million tonnes were produced in Western Europe [2], giving Europe a market share of approximately 12 %. The European share in the propene market is significantly larger (14.3 million tonnes in an 80 million tonne market [3], or 18 %, in the year 2012). This higher market share in propene is related to naphtha being the dominant feedstock in Europe, while in other countries shale gas is being exploited increasingly [4]. The main component of shale gas is methane, but considerable amounts of ethane (20 wt%) and propane (5 wt%) can be present as well [5]. Before using it as a feed stock in a steam cracking unit, the methane, ethane and propane are separated. The shale gas ethane is used as feedstock, yielding only very low amounts of propene.

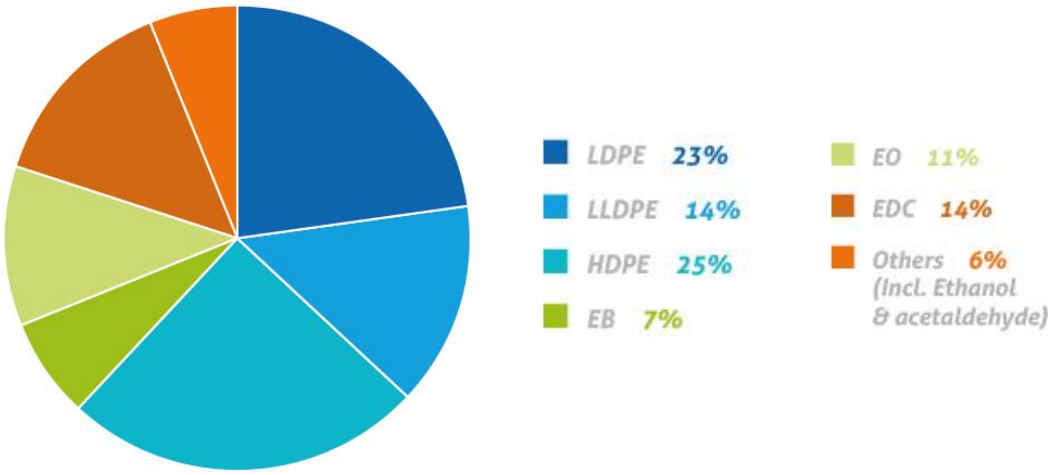

Figure 1-1: Western European ethene consumption by derivative 2014 [2].

Ample production methods are available for ethene and propene. Thermal cracking of hydrocarbons is the most important source of olefins. The light olefins (mainly propene) can also be recovered from the gas fraction of the (fluid) catalytic cracking process [6]. Propane dehydrogenation (PDH) is another alternative route to produce propene [6, 7]. Also, in the context of sustainable chemistry, several "green" routes are being or have been developed [7, 8]. The Methanol-to-Olefins (MTO) process is one of the most promising of these alternative methods [9]. One can distinguish between on-purpose propene production, e.g. PDH and MTO, and processes which have propene as by-product, e.g. (fluid) catalytic cracking. Due to the increased importance of shale gas, especially in the USA, there is an increasing supply-demand gap in the propene market. Therefore more and more on-purpose production methods for propene are being devised [10]. Nonetheless, for the foreseeable future, steam cracking will remain the predominant production route for propene, with significant amounts also being produced elsewhere in refineries, see Figure 1-3.

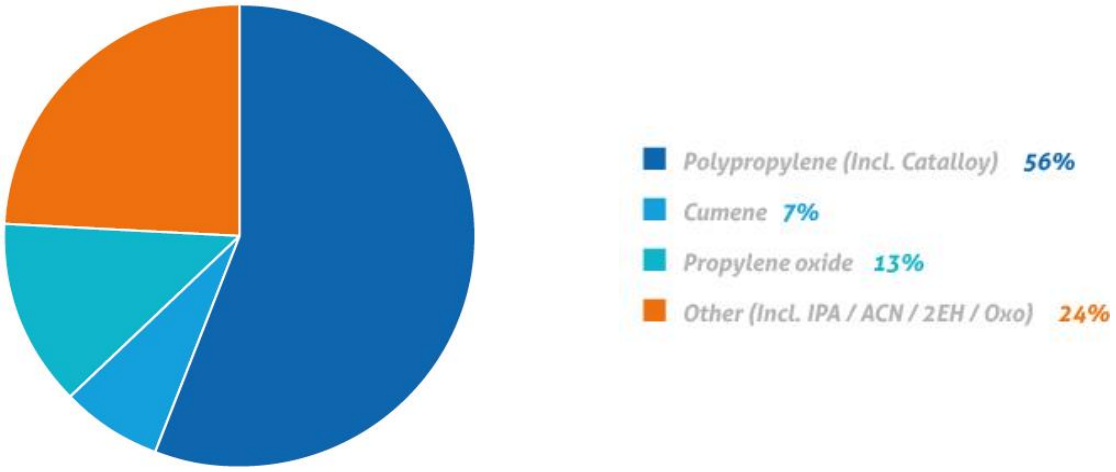

Figure 1-2: Western European propylene consumption by derivative 2014 [2].

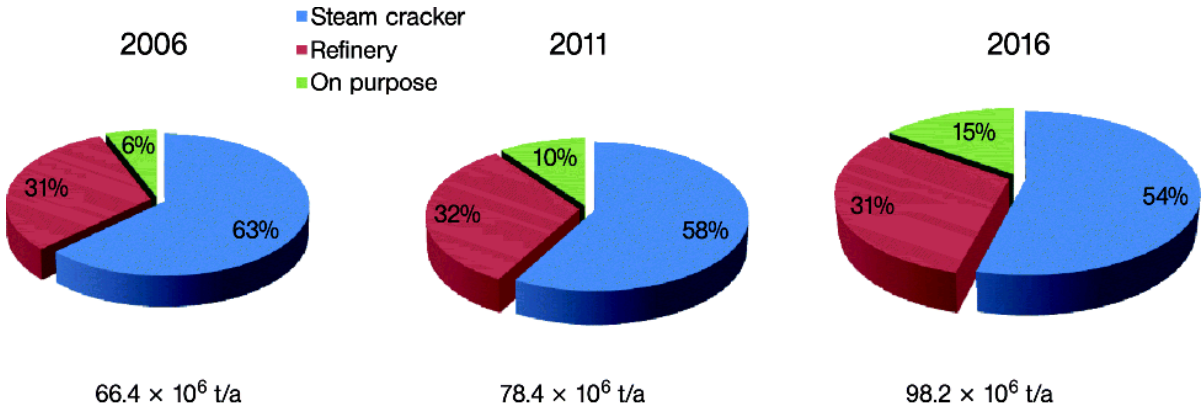

Figure 1-3: Evolution of the importance of different sources of propene and of the total annual propene production in the year 2006, 2011 and 2016 (projection) [10].

1.2. Steam Cracking

As stated in the previous paragraph, steam cracking has been the most important production route for light olefins for quite some time and it is expected to maintain this position in the foreseeable future. The concept of thermally decomposing heavy hydrocarbons was first devised by prof. Benjamin Silliman in 1855 [11], but it was only in 1912 that a useful process was invented by William Burton of the Standard Oil Co. [12]. Thermal cracking of heavy feeds was used to increase the gasoline production in refineries. The idea for purposefully producing ethene through thermal cracking of hydrocarbons originates from the 1930's, with patents issued in the early 1940's [13, 14]. Throughout the years the steam cracking process has been further optimized and scaled-up, making it a very mature technology at the moment. As of today, a world-scale steam cracker produces up to 1.5 million tonnes of ethene and 600,000 tonnes of propene per year [15].

A steam cracking plant comprises two main sections, the hot section (furnaces and quenches) and the cold section (separation train). In the first section, the feed is preheated and mixed with dilution steam. This takes place in the convection section of the furnaces. The heat duty in this part is delivered by the hot flue

gases from the radiant section. The hydrocarbon-steam mixture then enters the radiant section, where reactor coils are vertically suspended in the furnace. The tubes are heated via floor and/or wall mounted burners with combustion of predominantly natural gas providing the necessary heat duty. Residence times in the reactor coils in the radiant section are kept as low as possible (lower than 0.5 s) to improve selectivity to the lower olefins [16]. The reactor effluent is subsequently quenched in the Transfer Line Exchanger (TLE) to stop any reactions and maintain the selectivity towards light olefins. The energy is used to produce high pressure steam. These furnaces are very energy intensive equipment. A world-scale plant producing 1.5 million tonnes of ethene per year requires a heat input to the furnaces exceeding 800 MW [15]. Such a world-scale plant has several furnaces operating in parallel. A typical furnace consisting of two radiant sections and one shared convection section has an annual capacity of approximately 120,000-150,000 tonnes of ethene [17, 18], though the largest furnaces can produce nearly 200,000 tonnes of ethene per year for liquid feedstocks (e.g. naphtha) and even more for gas feedstocks (e.g. ethane) [19, 20].

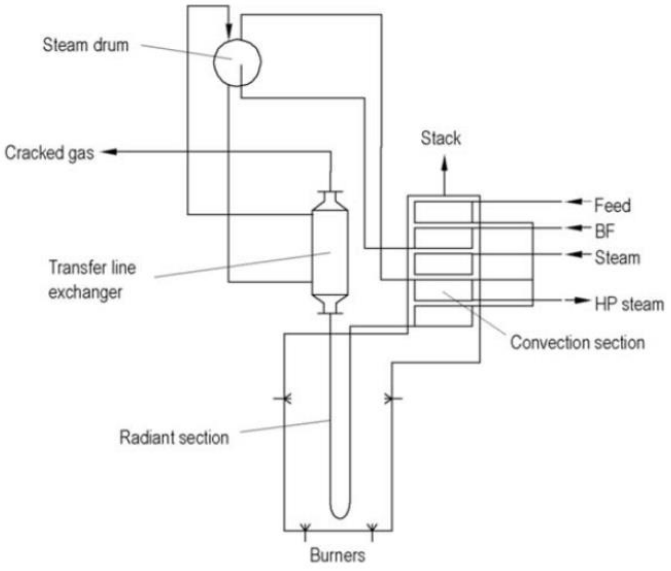

Figure 1-4: Simplified process flow diagram of a steam cracking furnace [21].

Once the process gasses have been cooled in the TLE, they are further cooled in an oil quench column and a water quench column, where heavy hydrocarbons are also (partially) removed. Organic acids that have formed due to contact of CO_2 with water [22], are removed in the caustic scrubber. This column is the final step in the hot section. The process gas the enters the cold section, where it is first compressed to around 36 bar [15]. The high pressure, while reducing the separation efficiency, increases the boiling points of all components. This allows light gasses such as ethene and propene to be condensed at temperatures above their normal boiling point (the normal boiling point of ethene is -103.7 °C [23]). In the separation train, methane/hydrogen, ethane, ethene, propane, propene, C_4 and C_{5+} are separated into different streams. The C_{5+} fraction is recycled to the furnaces.

1.3. Enhanced Coil Geometries

Although the steam cracking technology has been around for several decades and is considered to be quite mature, it is still further developed. At these scales, any minor reduction of energy consumption or improvement to selectivity corresponds to a significant increase in profit. Energy consumption is strongly affected by coke formation. Coke is a carbonaceous deposit on the internal surface of the tubes. The formation of the coke layer proceeds in different steps [24]. The first step is the catalytic formation of an initial layer of carbon on the metal surface of tube. Once this layer is formed, growth of the coke layer happens via radical hydrogen abstractions and additions of unsaturated compounds. Coke has a low thermal conductivity and therefore the formed layer of coke insulates the process gasses from the furnace, resulting in a decreased heat transfer to the process gas. The layer of coke also reduces the cross sectional flow area of the tube, increasing the pressure drop. The decreased heat transfer and increased pressure drop both negatively impact operations. Coke formation can be reduced in several ways, such as changing the tube surface [25], using different alloys for the tube wall [24, 26, 27], introducing chemical additives to the feed [24, 28-30] or changing the reactor geometry [31-35]. In this work the effect of altering the (internal) coil geometry will be investigated.

Changing the internal coil geometry has an effect on several aspects of the process. Most changes to the geometry include the addition of internal fins to the tubes. Using fins has several advantages as well as some important disadvantages. The fins increase the surface area that is available for heat transfer. As a result, the heat transfer to the process gas is increased, lowering temperature gradients in the tube wall. The final result is a lower outer tube wall temperature for a given furnace duty or the possibility to increase the flow through the tube (and thus the required furnace duty) without exceeding the tube material specifications. The higher temperature of the tube wall, the higher the rate of coking will be. One drawback of introducing fins is that the internal surface area of the tube is increased. This increases the amount of friction at the wall and consequently the pressure drop. Straight fins mainly influence the heat transfer, but other fin geometries are possible as well [36]. Helicoidally finned tubes affect the flow pattern besides increasing the heat transfer surface area. Additional turbulence is introduced in the flow, which improves mixing in the fluid. Improved mixing leads to a general increase in uniformity, decreasing gradients. Considering temperature, this means that heat transfer is further improved. The increased turbulence implies a further increase in pressure drop though [37]. Figure 1-5 combines temperature profiles for different coil geometries. The helicoidally finned tubes clearly have the smallest radial temperature gradients. The low inner wall temperatures mean that these tubes will also have the lowest coking rates. Besides the finned tubes, ribbed geometries also exist. Two examples hereof are shown in Figure 1-6.

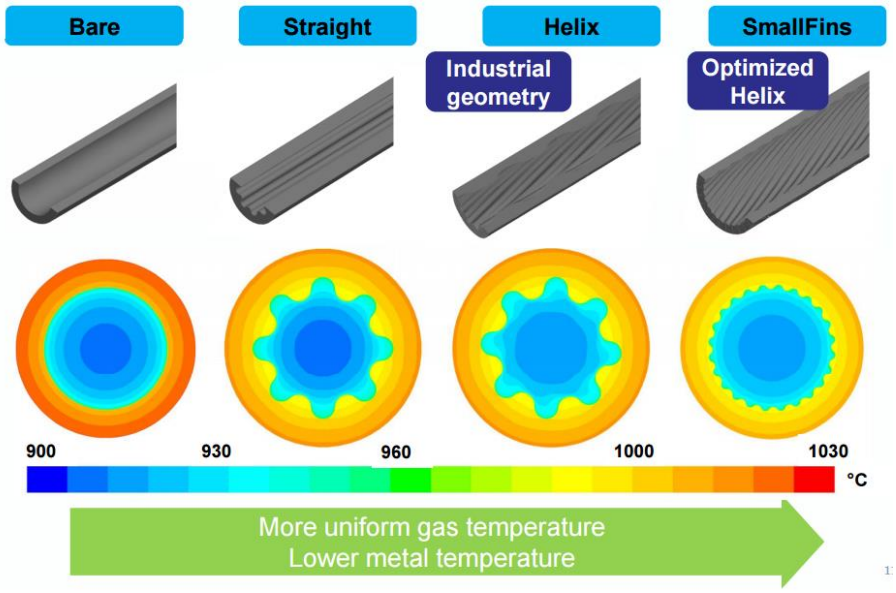

Figure 1-5: Effect of tube geometry on the radial temperature profile [°C]; bare reactor, straight finned reactor; helicoidally finned reactor, optimized helicoidally finned reactor (SmallFins) [36].

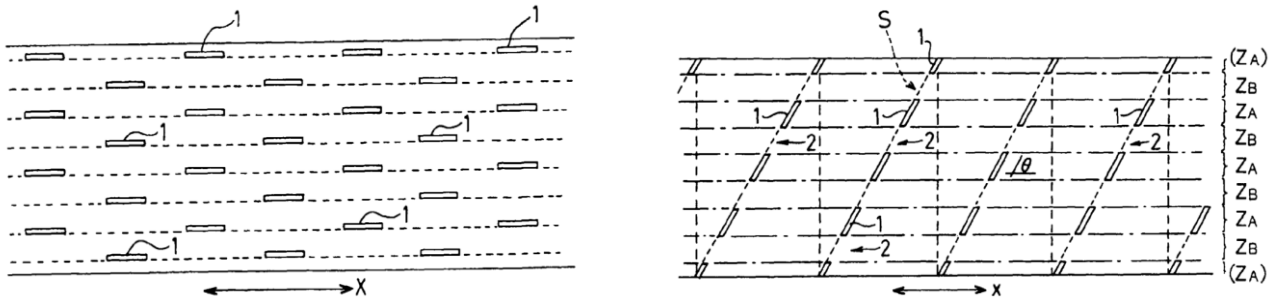

Figure 1-6: Schematic representation of the enhanced coil geometries T1 (left) and T4 (right) [34].

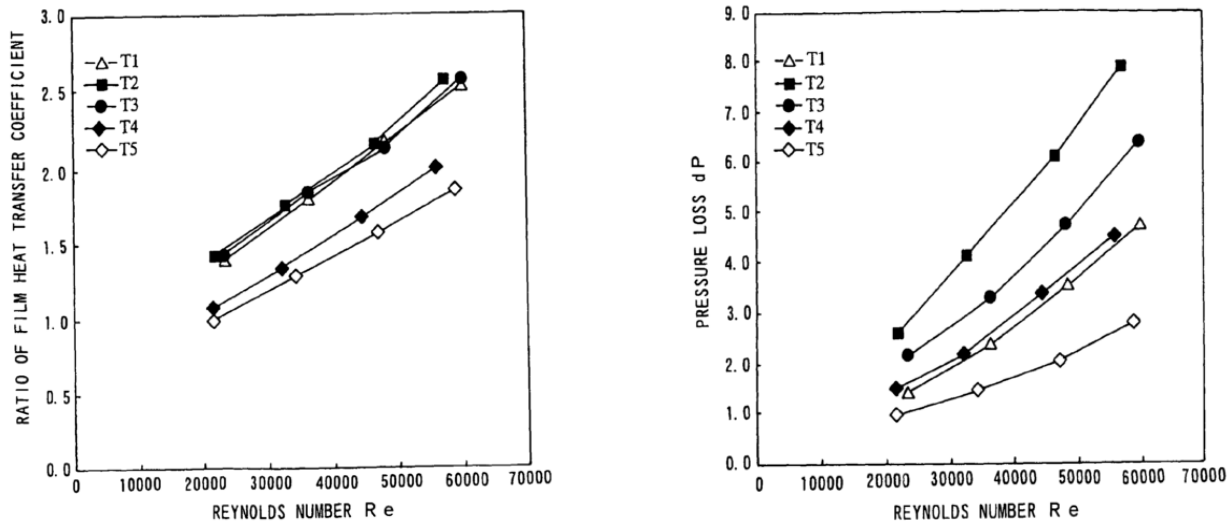

Figure 1-7: Heat transfer coefficient (left) and pressure drop (right) as function of the Reynolds number. T1-T4 are ribbed tubes, T5 is a bare tube [34].

An industrially used geometry is the so-called Mixing Element Radiant Tube (or MERT). MERT is an example of a coil geometry with an internal helical rib. The effectiveness of this geometry has been extensively studied by LES [38]. Experiments show that an increase in heat transfer of 50% is possible while only increasing the heat transfer area by 1% [32, 33]. While greatly improving the heat transfer, the pressure drop increases significantly as well [34]. Figure 1-7 shows that at high Reynolds numbers, the pressure drop can increase by a factor 4, depending on which type of rib is used. Based on the figure one can argue that the T1 tubes are the closest to optimal performance. The increase in heat transfer is similar to that for the T4, while the pressure drop increase is the lowest of all enhanced geometries.

Another type of enhanced geometry is the Swirl Flow Tube® (SFT) [31, 39-41]. Instead of using a straight tube with internal fins, a spirally shaped tube is used. The spiralling shape of the tube affects the flow pattern, introducing additional turbulence. Also, for an equal end-to-end distance, the spiralled tube has a greater external surface area, compared to the straight tube. The concept of using three dimensional tube geometries originated in the biomedical sciences, where a helical geometry is used in stents to reduce the chance of blockage of the stent as a result of depositions [42, 43]. Figure 1-8 shows the geometry of a Swirl Flow Tube®.

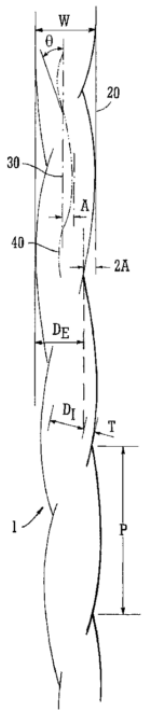

Figure 1-8: Swirl Flow Tube®, helicoidal tube technology owned by Technip [40, 41].

Both experimental and CFD data show that the increased pressure drop for this type of tubes is lower than for finned and ribbed tubes, while comparable gains in heat transfer can be achieved [31]. A same increase in heat transfer of 50 % is reported, while the pressure drop increases with a factor of only 1.8-2.5 for Reynolds numbers in the range of 35,000 to 110,000. Also, the dependency of the pressure drop increase on the Reynolds number is less strong than for the finned tubes, where the pressure drop increases by a factor 2-4 for Reynolds numbers in the range of 20,000-60,000.

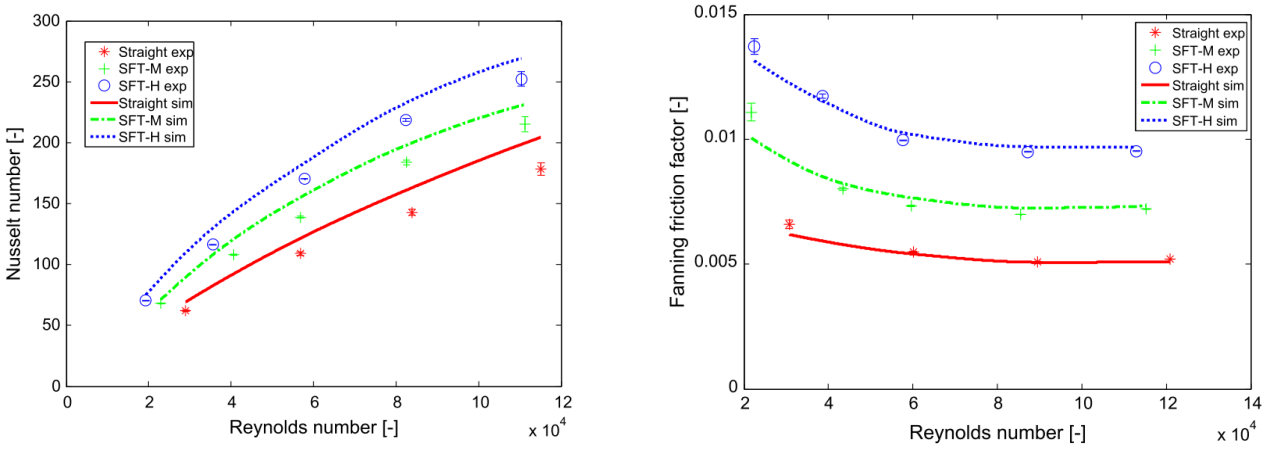

Figure 1-9: Nusselt number (left) and Fanning friction factor (right) as function of Reynolds number for different Swirl Flow Tubes [31].

1.4. Natural Gas Dehydration

Natural gas dehydration via supersonic swirling separation is a second field in which turbulence plays an important role. Natural gas is a complex hydrocarbon mixture of which the exact composition depends on the source [44]. Independently from the source, natural gas always contains a certain amount of water [45], and often the gas is found to be saturated with water. To prevent pipeline corrosion, hydrate formation or freezing, for water must be removed from the gas before being transported; the maximum water content is set at 110 mg_{water} Nm_{gas}^{-3} [46]. This corresponds to a dew point of approximately 230 K. Depending on location and company, the demands can vary somewhat. For example, due to the cold climate, in Canada the limit is 80 mg_{water} Nm_{gas}^{-3} [46, 47].To comply to these quite stringent conditions, dedicated natural gas dehydration facilities are required. Three main techniques have been commercialised to remove water from natural gas [45], both utilising additional liquid or solid chemicals to separate the water from the raw natural gas. Furthermore, the commercial technologies require voluminous equipment, such as absorption towers. The first technique is adsorption dehydration, where water adsorbed onto a so-called (solid) desiccant. These are often calcium or lithium chlorides and require frequent regeneration [48]. The second technology is based on the absorption of water into a solvent which has a high affinity towards water and a low affinity towards hydrocarbons. Typical dehydrating agents are ethylene glycols (mono-, di-, tri- or tetra-) [45]. Again, the drawback of this process is the high costs associated with the regeneration of the dehydrating agent. Figure 1-10 gives an overview of several conventional techniques and their respective water removal capacities. The figure clearly shows that the 230 K dew point is a challenging limit. A third commercialised technique is membrane technology, though its market share is limited to about 5 % [49]. While requiring significantly less equipment and chemicals, membranes are typically quite expensive.

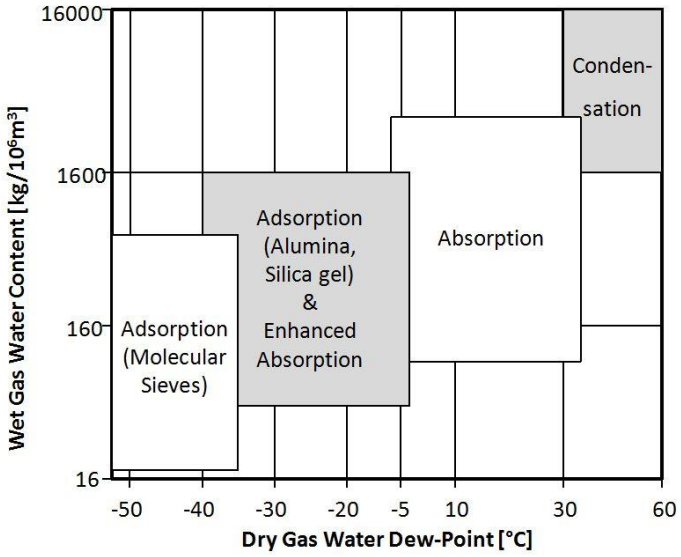

Figure 1-10: Overview of the conventional natural gas dehydration methods [50].

Besides the currently applied technologies, in recent years, some novel concepts for dehydration have been devised and patented [51-54]. These technologies are based on condensation of the water via the Joule-Thomson effect. The Joule-Thomson is an adiabatic phenomenon where the fluid temperature is decreased due to expansion. According to different applications, the temperature can decrease to below 200 K [51]. At such a low temperature, the water in the natural gas condensates. This effect can be observed around a jet accelerating to a Mach number greater than 1, as shown in Figure 1-11. To sufficiently accelerate the gas, all technologies based on the Joule-Thomson effect introduce a tangential component to the velocity. The resulting swirling flow creates a centrifugal field in which water droplets are forced outwards, where they can be easily removed. The advantage of the novel methods is their compactness and lack of moving parts.

Figure 1-11: Demonstration of the condensation of water through the Joule-Thomson effect as a jet accelerates to trans-sonic velocity.

1.4.1. Twister

The first of three important supersonic swirling dehydration technologies is the Twister technology [55-58]. Since its introduction in 1992 by Stork Product Engineering [53] and further development by Shell [54], the Twister technology has been further improved. In the earlier devices, the flow is initially swirl-free [59]. Figure 1-12 gives a schematic representation of the device. In the first section, the non-swirling flow passes through a Laval nozzle [60]. In the nozzle throat, a velocity corresponding to a Mach number of 1 is attained. In the diverging section, the flow accelerates further to above Mach 1 (supersonic flow). In this region, temperatures drop to values around 200 K. Just before the diverging section, an internal, swirl-inducing device is placed. The centrifugal field induced by this swirl drives all condensed water droplets to the periphery of the tube, where they are removed. The dry gas is then further expanded in the diffuser. In this final expansion, a transition takes place from supersonic to sub sonic flow. Such a transition is associated with a shockwave, which significantly contributes to the pressure drop in the device. There are three major drawbacks to this design. The first is the location of the swirl-inducing device. As it is located close to the diffuser, the droplets have only a limited time span in which they can travel to the tube outer perimeter. The droplet separation is potentially incomplete, resulting in an inefficient dehydration. The second drawback is also related to the swirl-inducing device. Water droplets that have formed upstream impact the device at very high velocity. This makes them highly abrasive, eventually destroying the swirl-inducing device. A final drawback is the high pressure drop (up to 30% of the inlet pressure), to which the shock in the diffuser significantly contributes.

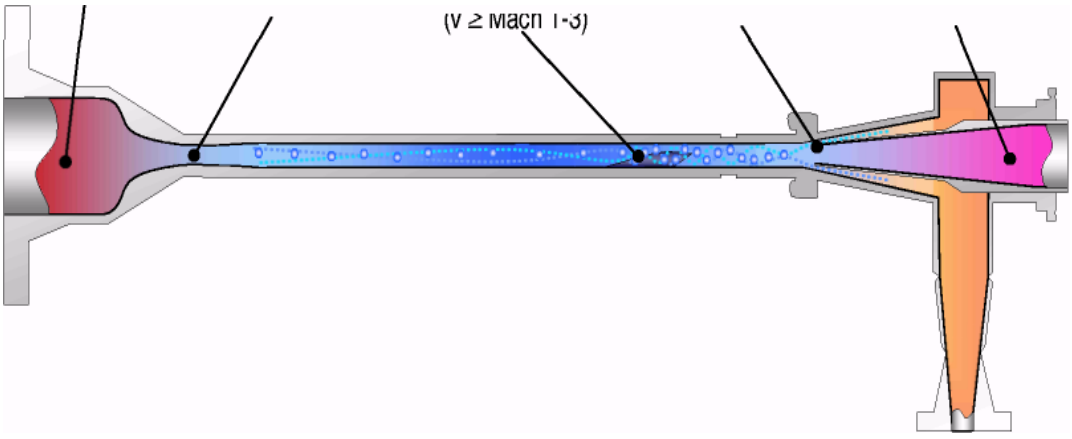

Figure 1-12: Schematic representation of the initial Twister device [51].

To overcome these problems, the device has been further developed [55, 56]. The current "advanced Twister" device is illustrated in Figure 1-13. It improves on all three points cited above. First of all, the swirl-inducing device now consists of a number of vanes, located upstream of the Laval nozzle, introducing swirl early on in the device. Secondly, the upstream position of the vanes prevents liquid droplets from impacting on them as upstream of the nozzle temperatures are still too high to allow condensation. Finally, the pressure drop as been tackled by introducing a tapered inner body in the diffuser. Nonetheless, pressure drop still remains quite high (15-25 % of the inlet pressure).

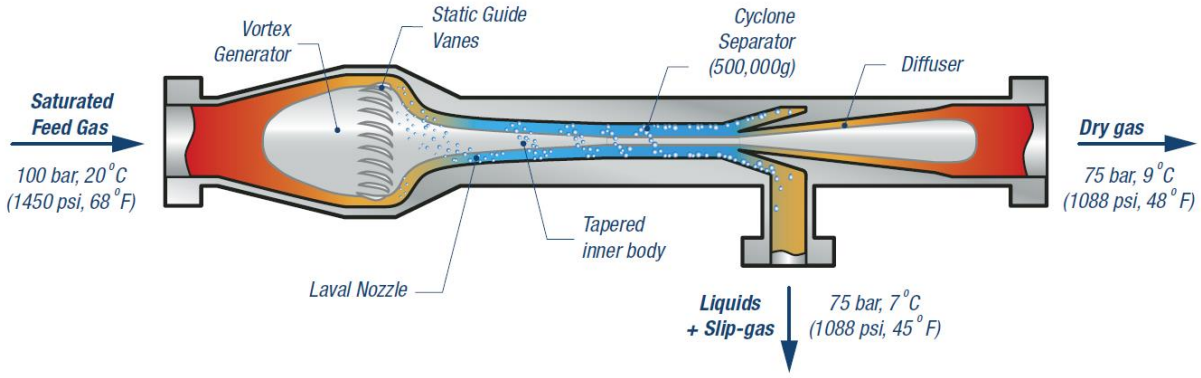

Figure 1-13: Schematic representation of the current Twister device for natural gas dehydration [57].

Of all swirl flow technologies, Twister is the most mature technology from a commercialisation point of view, reporting nearly 200,000 operating hours across the world [61]. Their largest facility is located in Malaysia (Petronas-Shell, with a capacity of 17,000,000 Nm^3 per day [58]. Other major facilities are located in Nigeria (Shell) and Colombia (Ecopetrol) [61]. Several sites in the Netherlands also use the Twister technology.

1.4.2. 3-S

A second technology, which is patented by TransLang Technologies Ltd. [52], is the 3-S separator. The general concept is the same as in the Twister design, though there are some distinct differences. The 3-S device is schematically illustrated in Figure 1-14. Similarly to Twister, the design implements a converging-diverging Laval nozzle (2), an extended working section (3) and a collector for the condensed liquid droplets (4). Contrarily to Twister, the inner body is not tapered. The swirl inducing vanes (1) are placed in front of the nozzle, but the central element does not extend throughout the length of the tube. Behind the diffusor (5), a second set of vanes is introduced. Their use is to recover some of the kinetic energy in the swirling component of the velocity and revert it back to static pressure, eying to reduce the total pressure drop over the device.

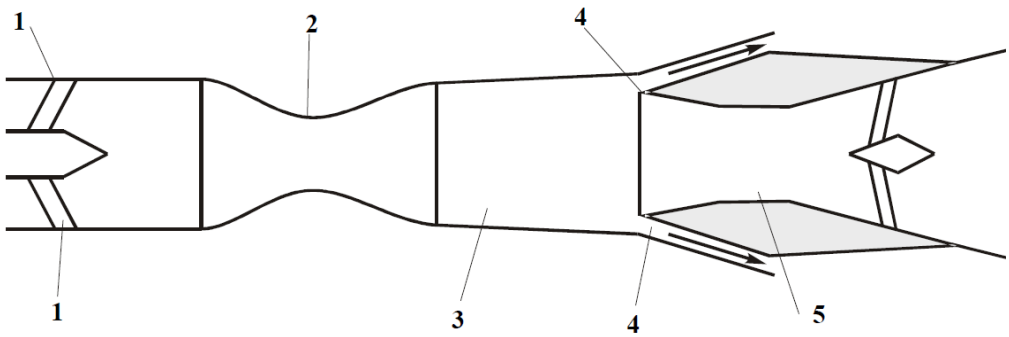

Figure 1-14: Schematic representation of the 3-S separator for natural gas dehydration [62].

At the moment, several testing/pilot facilities exist [62]. There is an experimental set-up in Moscow, larger scale testing complex in Calgary, Canada and a pilot plant in western Siberia. The focus of the 3-S separator is on separating C_3-C_5 hydrocarbons from water, rather than dehydration. While claiming a competitive pressure drop, no actual pressure drop data is reported [52].

1.4.3. SUSTOR

A final device and the focus of the simulations in Chapter 7, is the result of research done by SUSTOR (Supersonic Swirling Technology Original Research). Two different devices have been patented, SUSTOR1 [63] and SUSTOR2 [51]. Several geometries of the SUSTOR2 device have been tested, an example is illustrated in Figure 1-15. The concept is different from the two previously discussed devices. The flow enters the device tangentially, thus providing a strong tangential component to the velocity. At the centre of the inlet section, the flow accelerates through the nozzle. According to Borissov et al., the flow reaches a Mach number larger than 1, though the axial velocity is subsonic at all positions. It is claimed that due to this subsonic axial velocity, a transition from supersonic swirl flow to subsonic swirl flow is possible without a shockwave and accompanied high pressure drop. SUSTOR2 claims a minimum temperature of below 200 K, while having a pressure drop of only 5 % [51].

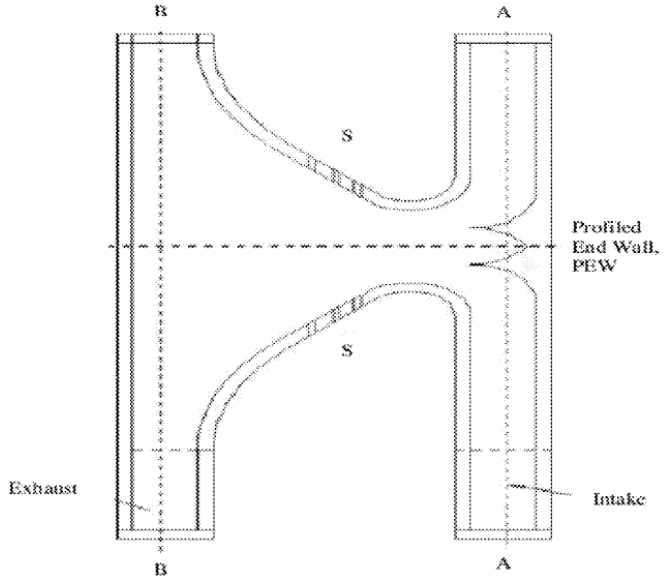

Figure 1-15: Schematic representation of the SUSTOR2 device [51].

In Figure 1-15, at the centre of the inlet section (right side), the wall exhibits a certain profile. The reason that a profiled end wall (PEW) is implemented is to attempt to reduce the amount of back flow through the nozzle. Figure 1-16 shows the velocity vectors in the SUSTOR2 geometry. The back flow is a result of recirculation of the flow at the end of the diverging section. This back flow exercises a significant amount of drag on the upward flow, increasing the pressure drop and is therefore undesired. It is however impossible to avoid recirculation completely, as it is naturally linked to vortex-like flows. It is similar to the downward winds in the eye of a tornado, as illustrated in Figure 1-17.

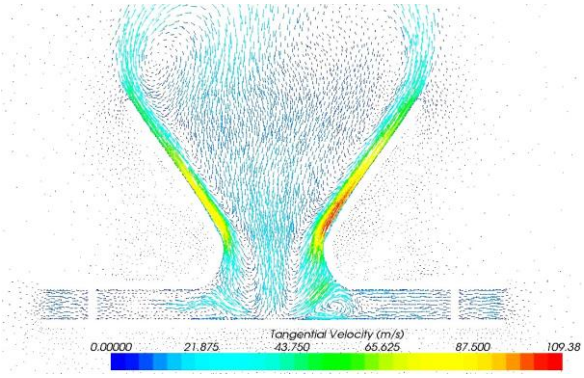

Figure 1-16: CFD-simulation of the SUSTOR2 by Shtern et al.: High velocity, swirling flow at the wall, low velocity backflow in the centre [64].

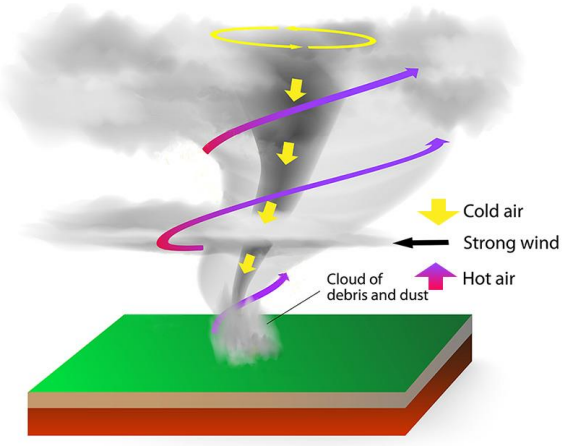

Figure 1-17: Air currents in a tornado: Upward swirling flow at outside and downwards, non-swirling flow at the centre [65].

1.5. Outline

Two main topics can be identified within this thesis. The primary subject is investigating the turbulent flow in relevant steam cracking coil geometries. This topic has already been introduced in the paragraphs 1.1 to 1.3. A second theme, which has been introduced in paragraph 1.4, is discussed in one separate chapter and focusses on the supersonic flow patterns in converging-diverging and swirling geometries.

Following this introduction is the literature study, which consists of two chapters. In the first chapter the theoretical aspects of turbulent flow modelling are investigated, ending with a study of several discretisation methods. These form the link with the second chapter, which discusses a number of available codes capable of performing direct numerical simulations. For each code, a specific aspect of turbulence is highlighted and the performance of the code in that area is discussed.

In chapter four, an overview is given of the equations of computational fluid dynamics and additional attention is given to the characteristics of the different meshes used in the different geometries. The reaction model and solution method are also shortly discussed here.

In the fifth chapter, the large eddy simulation results obtained from OpenFOAM of the different geometries are compared with each other as well as with one dimensional results obtained from CHEMKIN. The bare and ribbed tubes are based on work done by Zhu, using AVBP [38]. Comparison of the OpenFOAM results with the AVBP results is the subject of chapter six.

The seventh chapter covers the study of supersonic flow, focussing on the SUSTOR project. Based on 2D RANS simulations, the nozzle diameter, axial length and wall profile of the device are optimised. This geometry is subsequently used in a proof-of concept 3D simulation.

1.6. References

1. Ethene (Ethylene). http://www.essentialchemicalindustry.org/chemicals/ethene.html (22/09/2015),
2. Facts and Figures-Western European Market Review. http://www.petrochemistry.eu/about-petrochemistry/facts-and-figures.html (22/09/2015),
3. Propene (Propylene). http://www.essentialchemicalindustry.org/chemicals/propene.html (22/09/2015),
4. Koottungal, L., International Survey of Ethylene from Steam Crackers- 2015 *Oil & Gas Journal* **2015,** 113, (7), 85-91.
5. George, D. L.; Bowles, E. B., Shale Gas Measurement and Associated Issues. *Pipeline & Gas Journal* **2011,** 238, (7).
6. UOP Light Olefin Solutions for Propylene and Ethylene Production. http://www.uop.com/?document=uop-olefin-production-solutions-brochure&download=1 (22/09/2015),
7. Dijkmans, T.; Pyl, S. P.; Reyniers, M.-F.; Abhari, R.; Van Geem, K. M.; Marin, G. B., Production of bio-ethene and propene: alternatives for bulk chemicals and polymers. *Green Chemistry* **2013,** 15, (11), 3064-3076.
8. Picciotti, M., Ethylene Technologies-1: Novel ethylene technologies developing, but steam cracking remains king. *Oil and Gas Journal* **1997,** 95, (25).
9. DuBose, B., UOP sees methanol-to-olefins as solution to rising global propylene gap. In Hydrocarbon Processing, 2015.
10. Zimmermann, H.; Walzl, R., Propene. In *Ullmann's Encyclopedia of Industrial Chemistry*, Wiley-VCH Verlag GmbH & Co. KGaA: 2000.
11. Green, M. M.; Wittcoff, H. A., How Petroleum is Converted into Useful Materials: Cabocations and Free Radicals are the Keys. In *Organic Chemistry Principles and Industrial Practice*, Wiley-VCH Verlag GmbH & Co. KGaA: Weinheim, 2003; pp 4-5.
12. Burton, W. M. Manufacture of Gasolene. US1049667 (A), 1913.
13. Porter, F.; Duncan, J. M. Process for the manufacture of ethylene. US2185566 (A), 1940.
14. Porter, F. Process for the manufacture of ethylene. US2245819 (A), 1941.
15. The Linde Group Steamcracking Technology. http://www.linde-engineering.com/en/process_plants/chemical_and_petrochemical_plants/steam_cracking_technology/index.html (23/09/2015),
16. Van Geem, K. M.; Heynderickx, G. J.; Marin, G. B., Effect of radial temperature profiles on yields in steam cracking. *AIChE Journal* **2004,** 50, (1), 173-183.
17. Buffenoir, M. H.; Aubry, J.-M.; Hurstel, X., Large Ethylene Plants Present Unique Design, Construction Challenges. *Oil and Gas Journal* **2004,** 102, (3).
18. Ethylene Furnaces. In The Linde Group.
19. The Largest Productivity Ethylene Cracking Furnace in the World Started Operation. In Wison Engineering: 2011.
20. Petrochemical Processing. In The Linde Group.
21. Zimmermann, H.; Walzl, R., Ethylene. In *Ullmann's Encyclopedia of Industrial Chemistry*, Wiley-VCH Verlag GmbH & Co. KGaA: 2000.
22. Nowowiejski, G.; Reid, J. A., An Overview of Oxygenates in Olefins Units in Relation to Corrosion, Fouling, Product Specifications and Safety. In *American Institute of Chemical Engineers 2003 Spring National Meeting*, New Orleans, LA, 2003.
23. Geen, D. W.; Perry, R. H., Physical and Chemical Data. In *Perry's Chemical Engineers' Handbook*, 8 th ed.; McGraw-Hill Companies, Inc.: 2008; pp 2.1-2.517.
24. Towfighi, J.; Sadrameli, M.; Niaei, A., Coke Formation Mechanisms and Coke Inhibiting Methods in Pyrolysis Furnaces. *Journal of chemical engineering of Japan* **2002,** 35, (10), 923-937.
25. Zhou, J.; Wang, Z.; Luan, X.; Xu, H., Anti-coking property of the SiO2/S coating during light naphtha steam cracking in a pilot plant setup. *Journal of Analytical and Applied Pyrolysis* **2011,** 90, (1), 7-12.

26. Muñoz Gandarillas, A. E.; Van Geem, K. M.; Reyniers, M.-F.; Marin, G. B., Coking Resistance of Specialized Coil Materials during Steam Cracking of Sulfur-Free Naphtha. *Industrial & Engineering Chemistry Research* **2014,** 53, (35), 13644-13655.
27. Muñoz Gandarillas, A. E.; Van Geem, K. M.; Reyniers, M.-F.; Marin, G. B., Influence of the Reactor Material Composition on Coke Formation during Ethane Steam Cracking. *Industrial & Engineering Chemistry Research* **2014,** 53, (15), 6358-6371.
28. Wang, J.; Reyniers, M.-F.; Marin, G. B., Influence of Dimethyl Disulfide on Coke Formation during Steam Cracking of Hydrocarbons. *Industrial & Engineering Chemistry Research* **2007,** 46, (12), 4134-4148.
29. Dhuyvetter, I.; Reyniers, M.-F.; Froment, G. F.; Marin, G. B.; Viennet, D., The Influence of Dimethyl Disulfide on Naphtha Steam Cracking. *Industrial & Engineering Chemistry Research* **2001,** 40, (20), 4353-4362.
30. Wang, J.; Reyniers, M.-F.; Van Geem, K. M.; Marin, G. B., Influence of Silicon and Silicon/Sulfur-Containing Additives on Coke Formation during Steam Cracking of Hydrocarbons. *Industrial & Engineering Chemistry Research* **2008,** 47, (5), 1468-1482.
31. Schietekat, C. M.; Van Goethem, M. W.; Van Geem, K. M.; Marin, G. B., Swirl flow tube reactor technology: An experimental and computational fluid dynamics study. *Chemical Engineering Journal* **2014,** 238, 56-65.
32. Torigoe, T.; Hamada, K.; Inui, M.; Yoshitake, A., Mixing element of radiant tube (MERT) offers new concept for ethylene cracking. *Abstracts of Papers of the American Chemical Society* **1998,** 215, U609-U609.
33. Torigoe, T.; Hamada, K.; Furuta, M.; Sakashita, M.; Otsubo, K.; Tomita, M.; Aiche; Aiche, A., Mixing element radiant tube (MERT) improves cracking furnace performance. In *11th Ethylene Producers Conference, Proceedings*, 1999; Vol. 8, pp 126-141.
34. Inui, M.; Hamada, K.; Otsubo, K. Cracking tube having helical fins. US7799963 (B2), 2010.
35. Heynderickx, G., Simulation and comparison of the run length of an ethane cracking furnace with reactor tubes of circular and elliptical cross sections. **1998**.
36. Van Geem, K. M.; Schietekat, C. M.; Van Cauwenberge, D.; Marin, G. B., Steam Cracking Reactor Technology: The Good, the Bad and the Ugly. In *AIChE Spring Meeting*, San Antonio, Texas, 2013.
37. Schietekat, C. M.; Van Cauwenberge, D. J.; Geem, K. M.; Marin, G. B., Computational fluid dynamics-based design of finned steam cracking reactors. *AIChE Journal* **2014,** 60, (2), 794-808.
38. Zhu, M. Large eddy simulation of thermal cracking in petroleum industry. Université de Toulouse, 2015.
39. Van Cauwenberge, D. J.; Schietekat, C. M.; Floré, J.; Van Geem, K. M.; Marin, G. B., CFD-based design of 3D pyrolysis reactors: RANS vs. LES. *Chemical Engineering Journal* **2015**.
40. Caro, C. G.; Birch, P. L.; Tallis, W. Helical piping for an olefin production furnace. CA2580956 (C), 2013.
41. Caro, C. G.; Birch, P. L.; Tallis, W. Piping. USRE43650 (E1) 2012.
42. Caro, C. G.; Seneviratne, A.; Heraty, K. B.; Monaco, C.; Burke, M. G.; Krams, R.; Chang, C. C.; Coppola, G.; Gilson, P., Intimal hyperplasia following implantation of helical-centreline and straight-centreline stents in common carotid arteries in healthy pigs: influence of intraluminal flow†. *Journal of The Royal Society Interface* **2013,** 10, (89).
43. Doorly, D. J.; Caro, C. G.; Mclean, M. A. Stents for blood vessels. 1999.
44. González, T.; Netusil, M.; Ditl, P. *Raw Gas Dehydration on Supersonic Swirling Separator - Odwadnianie Gazu Naturalnego w Naddzwiekowym Oddzielaczu Mieszajacym*; Politechniki Krokowskiej: 2012.
45. Wang, X.; Economides, M., Natural Gas Processing. In *Advanced Natural Gas Engineering*, Gulf Publishing Company: Houston, Texas, 2009; pp 115-170.
46. Foss, M. M. *Interstate Natural Gas-Quality Specifiations and Interchangeability*; Bureau of Economic Geology - The University of Texas: Austin, TX, 2004; p 52.
47. TransCanada, Gas Quality Specifications. In 2016.
48. Fumo, N.; Goswami, D. Y., Study of an aqueous lithium chloride desiccant system: air dehumidification and desiccant regeneration. *Solar Energy* **2002,** 72, (4), 351-361.
49. Baker, R. W.; Lokhandwala, K., Natural Gas Processing with Membranes: An Overview. *Industrial & Engineering Chemistry Research* **2008,** 47, (7), 2109-2121.

50. Netusil, M.; Ditl, P., Natural Gas Dehydration. In *Natural Gas-Extration to End-Use*, Gupta, S. B., Ed. InTech: 2012; pp 3-22.
51. Borissov, A.; Mirzoev, G.; Shtern, V. Supersonic Swirling Separator 2 (Sustor2). US 20120180668 A1, 2012.
52. Alferov, V. I.; Baguirov, L. A.; Feygin, V. I.; Arbatov, A. A.; Imaev, S. Z.; Dmitriev, L. M.; Rezunenko, V. I. Vortex tube for liquefaction and separation of components in a gas mixture. WO2000/023757 (A1), 2000.
53. Van Holten, T. Method and device for separating a gas from a gas mixture. EP0496128 (A1), 1992.
54. Tjeenk, W. C. A. Method for removing condensables from a natural gas stream, at a wellhead, downstream of the wellhead choke. WO0040834 (A1), 2000.
55. Betting, M.; Epsom, H., Supersonic Separator Gains Market Acceptance. *World Oil* 2007, pp 197-200.
56. Betting, M.; Epsom, H., Separation Goes Supersonic. *Exploration & Production* 2007.
57. Twister B.V., Factsheet 1 How Does Twister Work? In.
58. Schinkelshoek, P.; Epsom, H., Supersonic Gas Conditioning-Commercialisation of Twister Technology. In *GPA*, Grapevine, Texas, USA, 2008.
59. Shtern, V.; Mirzoev, G.; Borissov, A. *SUSTOR-Business Plan*; 2013.
60. Laval, C. C. Separator for Use in Boreholes of Limited Diameter. US4148735 (A), 1979.
61. Twister B.V. Experience. http://twisterbv.com/products-services/twister-supersonic-separator/experience/ (28/04/2016),
62. Feygin, V. I.; Imayev, S.; Alfyorov, V., Supersonic Gas Technologies. In TransLang Technologie Ltd.: Calgary, Canada.
63. Borissov, A.; Mirzoev, G.; Shtern, V. SUSTOR1-Provisional. 60/595001, 2005.
64. Shtern, V.; Borissov, A. *Cold Flow in a Vortex Nozzle*; SUSTOR: 2015.
65. Tenenbaum, D. J. Tornadoes Strike Again. How Do They Work? http://whyfiles.org/2014/tornadoes-strike-again-how-do-they-work/ (25/04/2016),

2

CFD-Calculation of Turbulence

2.1. Introduction

Turbulence is a phenomenon which occurs both in nature and in many industrial practices. It is linked to chaotic variations in the flow parameters and can be both desirable or detrimental. Turbulence has the characteristic to increase uniformity in the flow. This increases heat, mass and momentum transfer. Increased heat and mass transfer is advantageous as they promote temperature uniformity and increase mixing and reaction rates. Contrarily, the increase in momentum transfer is paired with a significant increase in friction and therefore in pressure drop. In the laminar flow regime, the pressure drop in a cylindrical geometry depends linearly on the fluid velocity as expressed in the Hagen-Poiseuille equation [1].

$$\frac{\Delta P}{L} = \frac{128\mu}{\pi D^4} Q \quad Re \leq 2{,}100 \tag{2-1}$$

In the case of turbulent flow in a cylindrical geometry the pressure drop becomes quadratically dependent of the fluid velocity. This is expressed in the Darcy-Weissbach equation [1].

$$\frac{\Delta P}{L} = \frac{2\rho f}{D} v^2 \tag{2-2}$$

Note that the Hagen-Poiseuille equation is in fact no more than a simplification of the Darcy-Weissbach equation as in the given flow regime ($Re \leq 2{,}100$), the friction factor becomes equal to $f = 16/Re$.

The flow of fluids is fully described by the conservation equations of mass, momentum and energy, written here in their most general forms [2, 3].

$$\frac{\partial \rho}{\partial t} + \nabla \cdot (\rho \boldsymbol{v}) = 0 \tag{2-3}$$

$$\frac{D\rho \boldsymbol{v}}{Dt} = \rho \boldsymbol{g} + \nabla \cdot \boldsymbol{\tau} \tag{2-4}$$

$$\nabla \cdot (\lambda \nabla T) + \dot{q} + \Lambda = \nabla \cdot (P\boldsymbol{v}) + \frac{\rho}{2}\frac{Dv^2}{Dt} + \rho \frac{Du}{Dt} + \rho \frac{D(gy)}{Dt} \tag{2-5}$$

The stress tensor $\boldsymbol{\tau}$ can be written as function of pressure and velocity via Stokes's viscosity relation [4].

$$\tau_{ij} = \tau_{ji} = \mu \left(\frac{\partial v_i}{\partial x_j} + \frac{\partial v_j}{\partial x_i} \right) - \delta_{ij} \left(\mu \frac{2}{3} \nabla \cdot \boldsymbol{v} + P \right) \tag{2-6}$$

For incompressible flow, the conservation equations can be simplified to the following.

$$\nabla \cdot \boldsymbol{v} = 0 \tag{2-7}$$

$$\rho \frac{D\boldsymbol{v}}{Dt} = \rho \boldsymbol{g} - \nabla P + \nabla(\mu \nabla \cdot \boldsymbol{v}) \tag{2-8}$$

$$\nabla \cdot (\lambda \nabla T) + \dot{q} + \Psi = \rho c_v \frac{DT}{Dt} \quad \textbf{(2-9)}$$

The nature of these equations and the stochastic character of turbulence make analytical studies of turbulence impossible. The randomness of turbulence cannot be incorporated in an analytical (deterministic) solution. Therefore, turbulence must be studied either via an experimental route or via numerical simulations in computational fluid dynamics (CFD). Experimental studies are often tedious and will always contain some (experimental) error. Computational studies, while also containing (numerical) error, can be far more time and resource efficient. Furthermore, CFD results in highly detailed descriptions of the flow field. Such level of detail can never be achieved on an experimental basis.

There are several different methods to approach CFD [5]. As expected turbulence poses a major issue in all of them. A first approach is to use Reynolds-Averaged Navier-Stokes (RANS) equations. Here all aspects of turbulence are modelled, for example in the Reynolds Stress Model (RSM). While RANS is computationally the least costly of the three options, it is not adequate for investigating the nature of turbulence. It is used when the size of the case prohibits the use of more advanced turbulence models, for example in reactor design [6-9]. A second method is Large Eddy Simulation (LES). Here only the smallest turbulent scales are modelled while the other scales are explicitly resolved. This makes modelling easier as the smallest scales can be assumed to be isotropic. These isotropic turbulence scales are modelled in sub-grid stress models (SGS, see paragraph 2.3.3), which are the LES-equivalent of the RSM in RANS. The increasing availability of computational power is making it possible to study larger and more complex systems with LES [10-14]. The final route via which turbulence can be approached are Direct Numerical Simulations (DNS). Here all scales of turbulence are resolved down to the Kolmogorov scale. This means that the only errors present are introduced by the methods used to solve the numerical problem. While this approach yields the most in-depth information in turbulent properties, it requires a very high mesh resolution and hence the computational demands are very high. DNS can be used as validation for LES and RANS models either alone or in combination with experimental data [15-17].

Due to the increased availability and performance of High Performance Computing (HPC) clusters, the high computational demands of LES and DNS have become less and less of an obstacle. This makes them an excellent research tool for validating and improving SGS models and RANS turbulence models.

2.2. Turbulence

2.2.1. The Characteristics of Turbulence

As turbulence is a stochastic process, providing a definition for it is not straightforward. To circumvent this issue, Tennekes and Lumley [18] described turbulence by its most important properties.

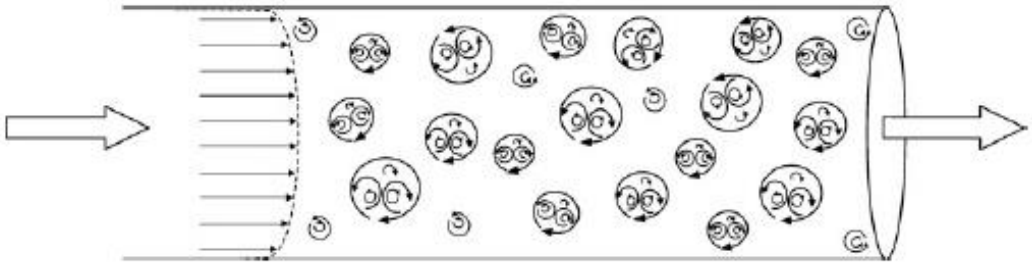

Figure 2-1: Turbulent eddies of different length scale in pipe flow [5].

First and foremost, turbulence is irregular. It comprises several different length, time and velocity scales. These different scales are perceived as turbulent eddies: random swirling motions in the fluid. Figure 2-1 provides a schematic view of eddies in a turbulent flow. It shows that the region occupied by a certain eddy is not necessarily exclusive to that eddy. Smaller eddies can coexist within larger eddies. When measuring a flow parameter (e.g. velocity) in a given point as function of time, fluctuations will occur. This is illustrated in Figure 2-2. One can say that the actual fluctuations are a superposition of two scales of fluctuations. The larger scale corresponds to the passing of large eddies and can be simulated via LES. The smaller scale fluctuations are attributed to the passing of small eddies, which can only be simulated via DNS.

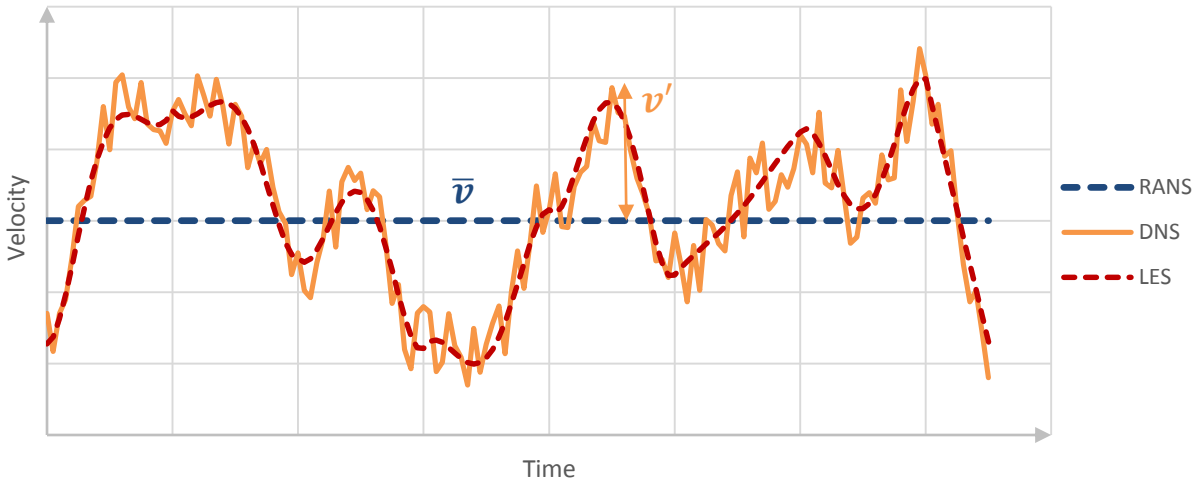

Figure 2-2: Different methods to calculate the velocity field: RANS, LES and DNS.

A second characteristic of turbulence is that it is diffusive. This means that the turbulent motions increase diffusive transport of mass, momentum and energy in all directions. This aspect of turbulence is further elaborated on in paragraph 2.2.2.

The third property describes the origin of turbulence. It arises as a result of instabilities in the flow at high Reynolds numbers. Two major factors affect flow stability. The first is the (stabilizing) viscous damping, expressed in the third term of the right hand side of equation (2-8). The second is the (destabilizing) convective transport, expressed in the spatial derivatives in the left hand side of eq.(2-8). Each of these two phenomena have their own time scale. Turbulence occurs when the time scale for viscous damping is much larger than the time scale for convective transport, that is when the destabilizing effect of convection is dominant over the stabilizing effect of viscous damping.

Before elaborating on these two time scales, Figure 2-2 will be revisited in more detail. On the figure it is indicated that the velocity at any given time can be decomposed into the Reynolds averaged velocity and an instantaneous velocity fluctuation. The Reynolds averaged velocity is defined as per equation (2-10) [5]. In steady state and for an appropriate length of the integration interval θ, the calculated average velocity will be independent of t.

$$\bar{v}(\boldsymbol{x}) = \frac{1}{\theta}\int_{t}^{t+\theta} v(\boldsymbol{x}, \tilde{t})d\tilde{t} \qquad \textbf{(2-10)}$$

The instantaneous velocity fluctuation can then be defined as below. This corresponds to the notation on Figure 2-2.

$$v'(\boldsymbol{x}, t) = v(\boldsymbol{x}, t) - \bar{v}(\boldsymbol{x}) \qquad \textbf{(2-11)}$$

This decomposition of the velocity field forms the starting point of RANS modelling of turbulence.

For a flow that is characterised by a linear dimension L, a mean velocity $\bar{v}$, an instantaneous velocity fluctuation v′ and a kinematic viscosity ν, the following approximation can be made. Assuming L is representative for the distance to the nearest damping surface and that v′ is the velocity of the turbulent eddy, this eddy will reach the wall in a time $t_{convective}$ given by equation (2-12).

$$t_{convective} = \frac{L}{v'} \qquad \textbf{(2-12)}$$

Viscosity is present in the Navier-Stokes equation, hence it will act over a distance l given by equation (2-13).

$$l = \sqrt{t_{convective} \cdot \nu} \qquad \textbf{(2-13)}$$

A necessary condition for the occurrence of turbulence is $l < L$ or

$$1 \ll \frac{L \cdot v'}{\nu} \ll \frac{L \cdot \bar{v}}{\nu} = Re \quad \textbf{(2-14)}$$

Here it is assumed that the fluctuations are much smaller than the mean velocity. The actual 'critical Reynolds number' beyond which the flow is fully turbulent depends on flow geometry [19]. Some values of the critical Reynolds number for the transition from laminar to turbulent flow are listed in Table 2-1 [5].

Table 2-1: Critical Reynolds numbers for the transition to turbulent flow [5].

Flow Type		*Critical Reynolds number*
Internal flow	Pipe flow	2,100
	Flow between parallel plates	800
External flow	Flow around a sphere	350
Boundary layer flow	Flow along a surface	500,000

The fourth characteristic of turbulence is that it is a three-dimensional phenomenon. Turbulent mechanisms such as vortex stretching cannot be described in two dimensions. However, from a statistical point of view it is possible to describe turbulence in a two-dimensional simulation.

Turbulence is dissipative, meaning that without a continuous input of energy, it will die out quickly. The mechanism of energy dissipation is described in the energy cascade. This principle was first devised by Richardson and further elaborated by Kolmogorov [20-22]. The energy cascade was summarised by Richardson as follows [20].

Big whorls have little whorls,
Which feed on their velocity;
And little whorls have lesser whorls,
And so on to viscosity.

In the energy cascade, kinetic energy is passed down from large eddies to continuously smaller eddies. Once the size of the eddies has become sufficiently small, viscous effects begin to dominate and energy is dissipated in the form of thermal energy. These scales at which the smallest eddies still exist are much larger than the molecular scale. This implies that turbulence is a continuum phenomenon. Therefore, all motions can be described by the conservation equations of mass, momentum and energy. The fact that turbulence is completely described by a set of deterministic equations might seem contradictory to its random character. The randomness of turbulence is the result of two observations. The first is that turbulent flows are sensitive to perturbations in the experimental conditions, environmental influences and fluid properties. The second one is that these perturbations cannot be avoided and will be present in any turbulent

flow [23]. This is similar to the observation that it is not possible to exactly reproduce the results of any experiment, resulting in a spread on the data.

Finally, turbulence is a characteristic of the flow, not of a fluid. Any fluid can be turbulent at sufficiently high Reynolds number.

2.2.2. The Energy Cascade

One property of turbulent flows that requires some further elaboration is the energy cascade. In the context of the energy cascade, Kolmogorov made three hypotheses [21]. His hypotheses are presented in terms of an n-point distribution F_n in a four-dimensional (**x**,t)-space. The first hypothesis is the hypothesis of local isotropy.

"… in an arbitrary turbulent flow with a sufficiently large Reynolds number the hypothesis of local isotropy is realized with good approximation in sufficiently small domains of the four-dimensional space (x_1, x_2, x_3, t) not lying near the boundary of the flow or its other singularities. By a 'small domain' we mean here a domain, whose liner dimensions are small in comparison with L and time dimensions – in comparison with $T = U/L$…"

The second hypothesis, also known as the first similarity hypothesis is based on the argument that the statistics of small-scale motions are similar in any turbulent flow.

"For the locally isotropic turbulence, the distributions F_n are uniquely determined by the quantities ν and ε."

The range where this hypothesis is valid is named the dissipative range. Here turbulent kinetic energy is no longer passed down from larger eddy to smaller eddy, but it is dissipated to thermal energy through viscous effects. The length, time and velocity scales that correspond to this range are known as the Kolmogorov scales.

$$\eta = \left(\frac{\nu^3}{\varepsilon}\right)^{\frac{1}{4}} \quad \textbf{(2-15)}$$

$$v_\eta = (\varepsilon\nu)^{\frac{1}{4}} \quad \textbf{(2-16)}$$

$$\tau_\eta = \left(\frac{\nu}{\varepsilon}\right)^{\frac{1}{2}} \quad \textbf{(2-17)}$$

These scales are of great importance in DNS. As no modelling of turbulence is done, all scales of the fluid motion must be resolved, including these Kolmogorov scales. For example, in a typical steam cracking coil has length of approximately 100 m and a coil diameter of 0.1 m. Typical flow rates are in the order of

1 m^3 s^{-1}, with the furnace providing 1 MW m^{-3}. This corresponds to an energy dissipation rate of 10^6 m^2s^{-3}. The viscosity of a gas is around 10^{-4} m^2 s^{-1} at typical cracking temperatures of around 1000 K. The Kolmogorov length scale is then of the order $\eta \approx 10$ µm and time scale $\tau_\eta = 10$ ns. To simulate these scales both a very fine mesh and very small time steps are required. Simulating the entire coil (1 m^3) would require 10 billion (10^{10}) cells with Kolmogorov dimensions. Also, it should be noted that theses scales are intrinsically laminar. The Reynolds number for these scales is by definition one, proving the dominance of viscous forces.

The third hypothesis, or the second similarity hypothesis concerns turbulence at intermediate scales.

"For any turbulent flow, at scales $\eta \ll l \ll l_0$, the distributions F_n are uniquely determined by the quantity ε and do not depend on ν."

In this range, also known as the inertial subrange, the characteristic velocity and time scales are thus formed by l and ε, resulting in the following definitions.

$$v_l = (\varepsilon l)^{\frac{1}{3}} \tag{2-18}$$

$$\tau_l = \left(\frac{l^2}{\varepsilon}\right)^{\frac{1}{3}} \tag{2-19}$$

These different ranges are summarised in Figure 2-3. L denotes the general scale of the system, while l_0 represents the scale of the largest turbulent eddies. The velocity and time scales in this range are defined by the dissipation of turbulent kinetic energy and by the kinetic energy itself, leading to the following time and velocity scales.

$$v_{l_0} = \left(\frac{2}{3}k\right)^{\frac{1}{2}} \tag{2-20}$$

$$\tau_{l_0} = \frac{k}{\varepsilon} \tag{2-21}$$

Once the eddies become sufficiently small, it can be assumed that they react very quickly to changes in external conditions. This allows the assumption of local equilibrium for small eddies, or mathematically, $T_{l_{EI}} = T_{l_{DI}} = \varepsilon$. The previous means that, in the inertial subrange, the only method of energy transport is by passing energy from larger scales to smaller ones. There is no dissipation in this range. l_{EI} can be regarded as the demarcation of the isotropic and anisotropic scales. Further, it is often assumed that $l_{DI} \approx 60\eta$, forming the limit of the dissipative range. This length scale determines the two regions in which the first and second similarity hypotheses are valid.

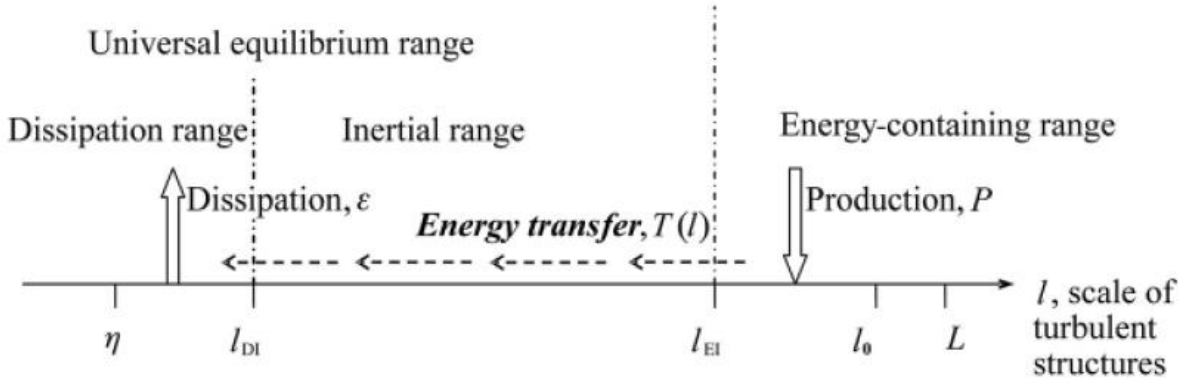

Figure 2-3: Graphical representation of the energy cascade introduced by Kolmogorov. [5]

Often, turbulence is analysed using the energy spectrum and wave numbers (κ) instead of length scale as the previous discussions gives no indication of the distribution of the turbulent energy over the different scales [24]. The spectrum of the kinetic energy is defined as follows.

$$k = \int_0^\infty E(\kappa) d\kappa \tag{2-22}$$

The turbulent energy spectrum of a homogeneous turbulent flow is shown in Figure 2-4. Homogeneous turbulence means that mean flow field is invariant under translation (while isotropy refers to invariance under reflections and rotations [23]). This corresponds to uniform, non-zero mean velocity gradients. In this case of homogeneous turbulence three different regions can be discerned in the spectrum [5].

A. The eddies in this region, centred around κ_e, contain most of the energy. They interact with the main flow, extracting energy from it and passing it on to smaller eddies, which eventually transition to region B. This region corresponds to the region with length scales $l > l_{EI}$. No dissipation of energy takes place here.
B. The region situated between κ_e and κ_d corresponds to the inertial subrange. Neither production nor dissipation of energy takes place, only a net flux of energy through the range.
C. The range containing eddies with wavenumbers situated around κ_d corresponds to the dissipative range. This is the Kolmogorov scale, where kinetic energy is dissipated as thermal energy.

Within the inertial range, Kolmogorov's spectrum law is valid for fully developed turbulent flows. This function for E was derived by Obhukov [25]. Equation (2-23) can be used to assess whether the turbulence in a flow is fully developed.

$$E(\kappa) = C_\kappa \epsilon^{\frac{2}{3}} \kappa^{-\frac{5}{3}} \qquad \frac{1}{l_0} \ll \kappa \ll \frac{1}{\eta} \tag{2-23}$$

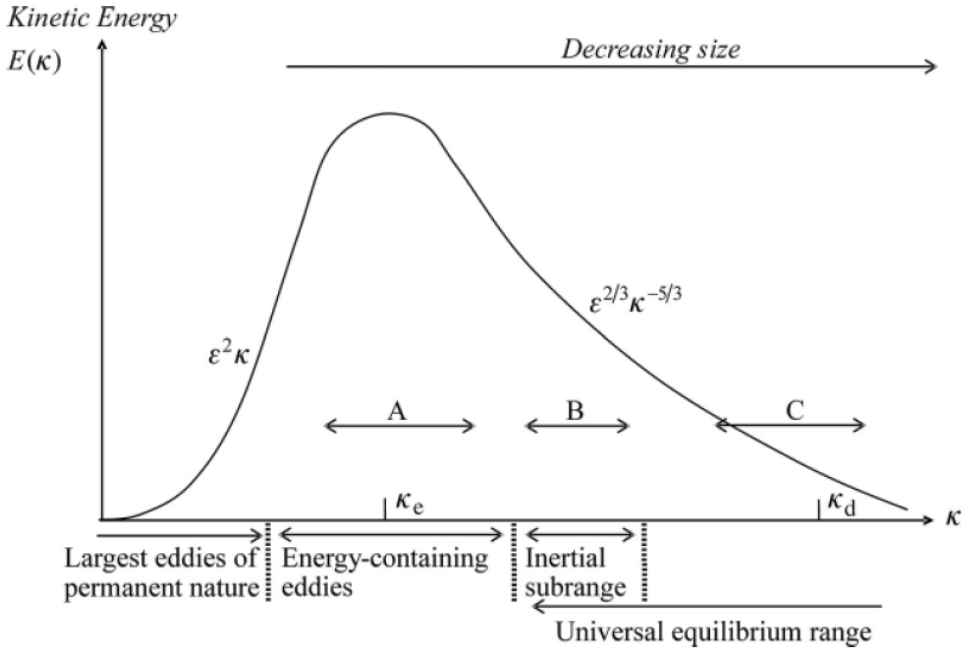

Figure 2-4: Energy cascade represented as the energy spectrum for a homogeneous turbulent flow [5].

2.2.3. Near-wall Effects on Turbulence

As stated by Kolmogorov's first hypothesis, the previous is only valid in the absence of or sufficiently far from surfaces affecting the fluid flow. Therefore, it is important to discuss the effect of the presence of a wall on turbulence. In free flows, the contribution of viscous stresses can be neglected compared to the Reynolds stresses $-\rho\langle v_i v_j\rangle$. Contrarily, in wall bounded flows, at the wall the fluid velocity tends to zero (known as the no-slip condition). This implies that the Reynolds stresses go to zero at the wall, as is shown in Figure 2-5. Flow at the wall is therefore dominated by viscous effects [26]. This also means that close to the wall the flow is always considered laminar. Nonetheless, turbulence is typically accompanied by an increase in drag and heat transfer even though both phenomena are the result of boundary layer effects [27]. Therefore, turbulent phenomena must persist in a part of the boundary layer. This is quantified in the streak instability theory in which the increase in drag and heat transfer are attributed to the presence of three dimensional coherent structures such as lifted near-wall streaks, longitudinal vortices and internal shear layers [28-31].

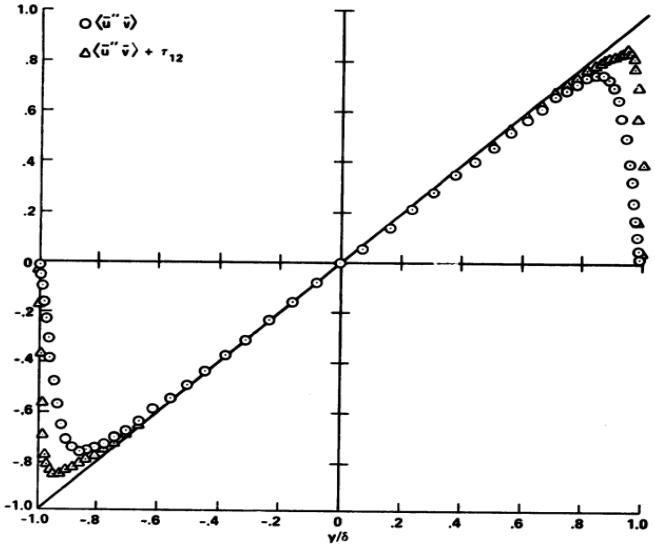

Figure 2-5: Reynolds stresses go to zero at the wall in open channel flow for Re=13,800 (solid line is total shear stress) [32, 33].

While these structures are only minutely influenced by the bulk turbulence, the bulk turbulence is significantly affected by the wall region turbulence [31]. In the bulk, dissipation of turbulence typically exceeds production of turbulence (cfr. the dissipative character of turbulent flows). The energy required to sustain turbulence in the bulk flow originates from the boundary layer. It is known that the larger eddies contain most of the energy (Figure 2-4) and that the size of the eddies is limited by the distance to the wall [31]. Therefore, an inverse cascade, known as the 1/k cascade) of eddies increasing in size from the wall to the bulk must exist. This has been experimentally confirmed [34]. It should be noted that in Figure 2-6 the eddies in the 1/k cascade are sketched connected to the wall. This is as illustration of the attached eddy hypothesis of Townsend [35]. This states that eddies that diffuse form the wall to the bulk, will not transfer significant amounts of energy to the larger eddies of the bulk flow.

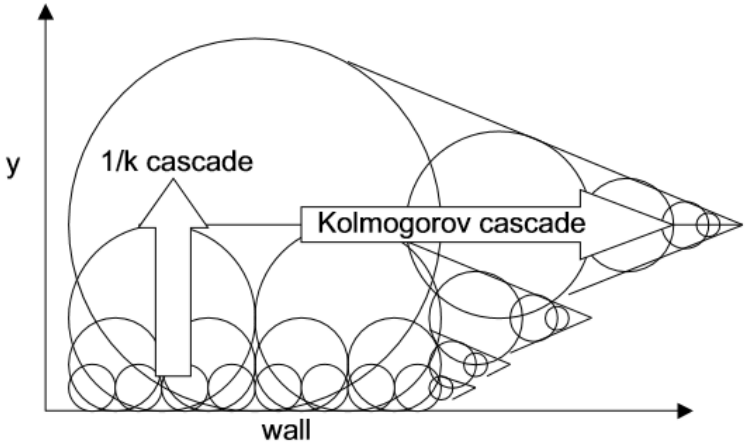

Figure 2-6: Inverse energy cascade from the wall to the bulk [31].

2.3. Large Eddy Simulations

2.3.1. Introduction

Large Eddy Simulations or LES take advantage of several of the aspects that have been discussed in the previous paragraph. The most important one is Kolmogorov's hypothesis of local isotropy. Isotropic phenomena are typically easier to model than non-isotropic ones. In the Reynolds averaging (RANS) approach, after decomposition of the velocity and averaging in time, the Reynolds stress term appears in the momentum equation. This term is modelled either via Reynolds stress modelling or via the Boussinesq approximation [36]. The latter results in the frequently used k-ε and k-ω models [5]. In the Boussinesq approximation it is however assumed that all turbulence is isotropic. According to Kolmogorov's hypothesis of local isotropy, this is not necessarily true. This is where LES provides a significant advantage. Since in LES the large, anisotropic scales are resolved, the assumption of isotropy at the sub-grid scales is acceptable.

2.3.2. Concept

The general concept of LES is using a spatial filter to separate the length scales that are to be resolved from those that will be modelled [37]. This filtering function is always accompanied by a cut-off width Δ. This cut-off width is a measure for the dimension of the smallest eddies that are to be resolved.

$$\tilde{\varphi}(\boldsymbol{x},t) = \iiint_{-\infty}^{+\infty} G(\boldsymbol{x},\boldsymbol{x}',\Delta)\,d\boldsymbol{x}' \tag{2-24}$$

Two commonly used examples of filters in LES are the box filter (2-25) and the Gaussian filter (2-26).

$$G(\boldsymbol{x},\boldsymbol{x}',\Delta) = \begin{cases} \frac{1}{\Delta^3} & |\boldsymbol{x}-\boldsymbol{x}'| \le \frac{\Delta}{2} \\ 0 & |\boldsymbol{x}-\boldsymbol{x}'| > \frac{\Delta}{2} \end{cases} \tag{2-25}$$

$$G(\boldsymbol{x},\boldsymbol{x}',\Delta) = \left(\frac{\gamma}{\pi\Delta^2}\right)^{3/2} \exp\left(-\gamma\frac{|\boldsymbol{x}-\boldsymbol{x}'|^2}{\Delta^2}\right) \tag{2-26}$$

Applying this filtering method to a transport equation results in an expression that is – in appearance – very similar to that for the Reynolds Averaged Navier Stokes method (equation (2-11)). In LES the $\tau_{ij,SGS}$ are mostly referred to as the Sub-Grid-Stresses, which can be further decomposed, in contrast to the Reynolds stresses [5, 37]. In time averaging the average is invariant to the transformation, this does not hold for filtering.

$$\bar{\bar{\varphi}} = \bar{\varphi} \quad but \quad \tilde{\tilde{\varphi}} \neq \tilde{\varphi} \tag{2-27}$$

$$\rho\frac{d\widetilde{v_i}}{dt}+\nabla(\tilde{\boldsymbol{v}}\rho\widetilde{v_i})=\rho\boldsymbol{g}-\frac{d}{dx_i}\tilde{P}+\nabla\cdot(\mu\nabla\widetilde{v_i})-\nabla(\rho\widetilde{v_i}\tilde{\boldsymbol{v}}-\rho\widetilde{v_i}\tilde{\boldsymbol{v}}) \quad \textbf{(2-28)}$$

$$\nabla(\rho\widetilde{v_i}\tilde{\boldsymbol{v}}-\rho\widetilde{v_i}\tilde{\boldsymbol{v}})=\frac{d}{dx_j}\tau_{ij,SGS} \quad \textbf{(2-29)}$$

$$\varphi=\tilde{\varphi}+\varphi' \quad \textbf{(2-30)}$$

$$\tau_{ij,SGS}=\underbrace{\left(\rho\widetilde{\widetilde{v_i}\widetilde{v_j}}-\rho\widetilde{v_i}\widetilde{v_j}\right)}_{\text{I}}+\underbrace{\left(\rho\widetilde{\widetilde{v_i}v_j'}+\rho\widetilde{\widetilde{v_j}v_i'}\right)}_{\text{II}}+\underbrace{\rho\widetilde{v_i'v_j'}}_{\text{III}} \quad \textbf{(2-31)}$$

$$\rho\overline{v_i'v_j'}=\tau_{ij,RS} \quad \textbf{(2-32)}$$

As a result, the decomposition of the sub-grid stresses according to equation (2-31) yields three terms. The first (eq. (2-31) I), known as the Leonard stresses after the scientist who first derived an approximation for this term [38], accounts for the fact that filtering of a filtered value does not necessarily return the initial filtered value. It hence expresses solely effects of the resolved flow. The second term (eq. (2-31) II) contains the resolved and non-resolved scales and thus takes the effect of the sub-grid field on the resolved field into account. The term is referred to as the cross stresses. An approximation for this expression has been derived by Ferziger [39]. The final term (eq. (2-31) III) is a purely sub-grid term and is most closely related to the Reynolds stress term in RANS (eq. (2-32)), hence it is denoted as the LES Reynolds stresses. The modelling of these terms requires some extra attention. In the next paragraph the most important aspects of modelling in LES are assessed.

2.3.3. Modelling in LES

There are two major regions in which modelling is required in LES. Obviously the sub-grid stresses must be modelled, but also the near-wall region requires attention.

As for the sub-grid stresses, very often the analogy between the sub-grid stresses and Reynolds stresses is continued. As mentioned previously, the Boussinesq approximation is frequently used in RANS. Due to Kolmogorov's hypothesis of local isotropy [21], it is assumed that the isotropy of the eddies increases with decreasing scale [40]. Therefore, introducing the concept of eddy viscosity, which is the LES equivalent of the turbulent viscosity in RANS, is justified. This approach is followed in the Smagorinsky and Smagorinsky-Lilly model [40, 41]. In the Smagorinsky model, the eddy viscosity concept is only applied to the LES Reynolds stress term (eq. (2-31) III). The two other terms are then described by approximate forms. More recently it has been noticed that in finite volume LES for industrially relevant simulations, it is common to extend this concept to the Leonard and cross stresses as well [37, 42]. Lumping all stresses results in only one SGS turbulence model (equation (2-33)). The term $\frac{1}{3}\tau_{ii}\delta_{ij}$ ensures that the sum of the modelled normal SGS stresses equals the total kinetic energy of the sub-grid eddies.

$$\tau_{ij,SGS} = -2\mu_{SGS}\widetilde{S_{ij}} + \frac{1}{3}\tau_{ii}\delta_{ij} = -2\mu_{SGS}\left(\frac{d\widetilde{v_i}}{dx_j} + \frac{d\widetilde{v_j}}{dx_i}\right) + \frac{1}{3}\tau_{ii}\delta_{ij} \quad \textbf{(2-33)}$$

In the Smagorinsky-Lilly model, the eddy viscosity is determined in analogy to Prandtl's mixing length model for the turbulent viscosity in RANS [37]. This means that the (kinematic) eddy viscosity is modelled as being proportional to the product of a length scale and a velocity scale. In LES the obvious choice for the length scale is the filter cut-off width Δ. The velocity scale can then be defined as the product of the length scale and the strain rate in the filtered flow $|\tilde{S}|$.

$$\mu_{SGS} = \rho {C_{SGS}}^2 v_{char} l_{char} \quad \textbf{(2-34)}$$

$$v_{char} = \Delta|\tilde{S}| \quad with \ |\tilde{S}| = \sqrt{2\widetilde{S_{ij}}\widetilde{S_{ij}}} \quad \textbf{(2-35)}$$

$$\mu_{SGS} = \rho(C_{SGS}\Delta)^2|\tilde{S}| \quad \textbf{(2-36)}$$

The Smagorinsky-Lilly model is a very simple and widely used model [43] in contrast to its RANS analogue, where k-ε and k-ω models are mostly used. The drawback of this method is that the value of the proportionality factor C_{SGS} is strongly case dependent. Several authors report different intervals in which C_{SGS} should be chosen [43-46]. Overall, the value of C_{SGS} is reported to be between 0.1 and 0.24. Another algebraic model that should be mentioned is the Wall Adaptive Local Eddy viscosity (WALE) model [47]. This model attempts to describe the near-wall behaviour of the eddy viscosity better. In the Smagorinsky-Lilly model, the eddy viscosity is different from zero in the presence of a velocity gradient. Near the wall, independently of Reynolds numbers, viscous damping becomes dominant and turbulence is damped. Hence the eddy viscosity should approach zero at the wall, following a y^3 decline [47]. In the Smagorinsky-Lilly model, the strain rate tensor $\tilde{S}$ is used as measure for the turbulent activity. The strain rate tensor is still used in the WALE model, however the traceless, symmetric part of the square of the velocity gradient tensor S_{ij}^d is also used.

$$S_{ij}^d = \frac{1}{2}\left(\widetilde{g_{ik}}\widetilde{g_{kj}} + \widetilde{g_{jk}}\widetilde{g_{ki}}\right) - \frac{1}{3}\delta_{ij}{\widetilde{g_{kk}}}^2 \quad \textbf{(2-37)}$$

It is found that $S_{ij}^d S_{ij}^d$ behaves according to y^2 near the wall, implying that $\left(S_{ij}^d S_{ij}^d\right)^{3/2}$ behaves correctly as y^3. Considering numerical stability and scaling (the final dependency should have units of frequency), the following relationship for the eddy viscosity is proposed [47]. C_w depends on $\widetilde{S_{ij}}$ and C_{SGS} and is typically between 0.55 and 0.6.

$$\mu_{SGS} = \rho(C_w\Delta)^2 \frac{\left(S_{ij}^d S_{ij}^d\right)^{3/2}}{\left(\widetilde{S_{ij}}\widetilde{S_{ij}}\right)^{5/2} + \left(S_{ij}^d S_{ij}^d\right)^{5/4}} \quad \textbf{(2-38)}$$

For a more sophisticated and robust modelling, additional transport equations for e.g. the kinetic energy can be constructed [48]. They have some resemblance to the RANS k-ε and k-ω models, but are not discussed here.

For the near-wall region, several approaches are possible [31]. It is possible to completely resolve the wall region at LES scale (Wall-Resolved LES or WRLES), however this incurs a high computational cost [49]. It has been found that the number of grid points, and thus the computational cost, required for WRLES scales with the Reynolds number to the power 13/7 [50]. The other extremum is using equilibrium treatments for the wall (Wall-Modelled LES or WMLES) [44, 48, 51, 52]. These methods presume a universal behaviour of the near-wall region, allowing the region to be described by a single wall function. The stresses in the first off-wall grid point can then be easily calculated as shown in Figure 2-7. The computational cost for WMLES is significantly lower than that for WRLES, as the grid point requirement scales with the Reynolds number to the power 1 [50].

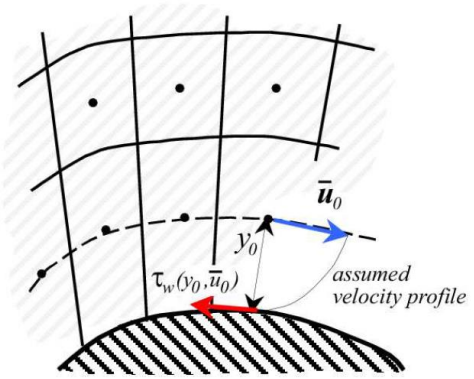

Figure 2-7: Implementation of wall functions [31].

The alternative to fully resolving and fully presuming the behaviour of the wall region is using zonal models. Here, in general two approaches are possible. In the first, known as the two layer models or TLM, the grid is decoupled into two regions. The grid describing the bulk can have a relatively coarse mesh, while the grid describing the near-wall region must have a fine grid. This is illustrated in Figure 2-8.

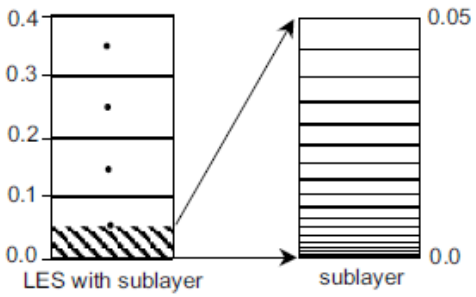

Figure 2-8: TLM, illustrating the decoupling of grid scales [31].

Different models exist to treat the sublayer [53, 54], though it is common to use simplified equations in the sublayer [31]. These equations are referred to as the thin boundary layer equations (TBLE), which are essentially time-dependent RANS equations.

The second type of zonal models are the LES/RANS hybrid models. These use only one grid spacing, but the employed turbulence model changes depending on the region. In the bulk, a LES turbulence model is implemented, while close to the wall a RANS turbulence model is used. The best-known hybrid model is the detached eddy simulation (DES) model [55, 56]. As RANS modelling requires the grid spacing to be larger than the largest eddies, the grid spacing near the wall can be the same as the spacing in the bulk [31].

Other, more complex wall models exist as well. Examples are the stochastic backscatter model [57] and the self-similarity model [58].

2.4. Direct Numerical Simulations

2.4.1. General

Direct Numerical Simulations or DNS solve the time-dependent Navier-Stokes equations, without modelling any turbulence. The computations return instantaneous values for the velocity components, and pressure [37]. Temperature can also be calculated if the energy balance is added to the set of equations [59]. The fact that no modelling must be done in DNS, makes that from a conceptual point of view, it is a very simple technique. Direct numerical simulations are acclaimed to have several beneficial characteristics [60, 61].

- It is possible to calculate turbulence parameters in very high time and spatial detail. This is relevant in the validation of new and improvement of existing turbulence models.
- The level of detail, both spatially and temporally, that can be achieved with DNS is unmatched by any experimental set-up.
- Advanced experimental set-ups can be calibrated using DNS results.
- DNS offers the possibility to fundamentally and independently study different aspects of turbulence. Depending on what the topic of the study is, certain aspects of the flow can be explicitly included or excluded, resulting in unphysical flows, but allowing detailed studies of specific phenomena.

The above also imply that the main goal of DNS is not to visualise flow fields, streamlines, etc. While this can be relevant for industrial applications, the main strength of DNS is the detailed study of the statistical properties of turbulence. This is illustrated in Figure 2-9 and Figure 2-10. Though some authors do report visualisations of among others temperature, vorticity and wall friction [62-65], it is much more common practice to report statistical properties (such as probability density functions and spectra), especially in the near-wall region [66-70].

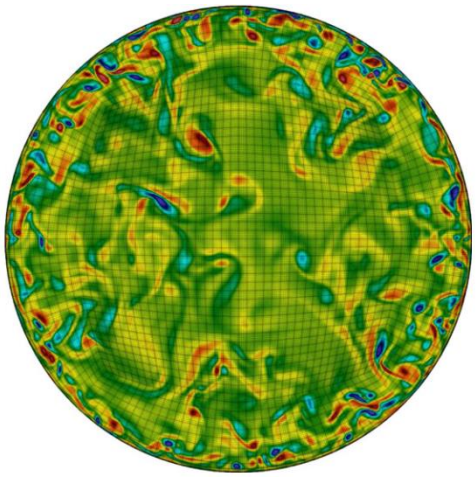

Figure 2-9: Instantaneous axial vorticity in pipe flow at a Reynolds number of 19,000 [64].

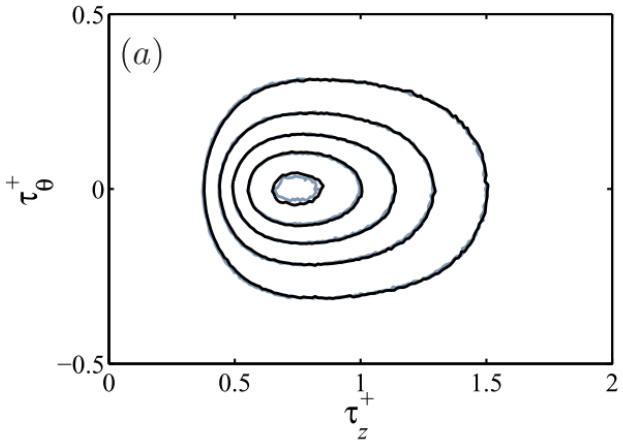

Figure 2-10: Joint PDF of the wall shear stresses in axial (τ_z^+) and azimuthal (τ_θ^+) directions for pipe (black) and channel (grey) flows at a Reynolds number of 1,000 [70].

DNS has steadily increased in complexity throughout the past decades. The first DNS was performed by Orszag and Patterson in 1972 and was based on a spectral code [71]. Due to the limited computational resources at the time, their simulation consisted of a 32x32x32-cell grid and simulated isotropic turbulence at a Reynolds number of 35. The CDC 7600 computer used at the time could deliver a peak of 36 Mflop/s [72]. As a comparison, the current average desktop/laptop computers can deliver 1-10 Gflop/s, while the average smartphone is capable of 200 Mflop/s [73]. The most powerful supercomputer at the moment (the Chinese Tianhe-2) has the capacity to deliver a peak of 54.9 Pflop/s [74]. The next hurdle that was taken in increasing the complexity, is the simulation of compressible flows, by Feiereisen in 1981 [75], though in-depth study of compressible turbulence was only done from the early 1990s [76, 77]. In the late 1990s, the first simulations of wall bounded turbulent flows using DNS were reported [78, 79]. The Reynolds numbers of these early DNS, are typically quite low, ranging from the order 10^1 - 10^3. It is only rather recently that flows with Reynolds numbers of the order 10^4 have been simulated [63, 64, 80, 81]. These high Reynolds number flows can only be calculated either on a very small system (order 100x100x100 grid cells) [63, 80], or using the best available supercomputing infrastructure available on grids of the order 1000x1000x1000 cells [81]. Finally, in recent years, simulations on non-isothermal and reactive flows have been performed using DNS [59, 82-84]. Again, these are limited in spatial and temporal extent, simulating volumes of the order of 10^{-9} – 10^{-7} m^3. This brief summary of the evolution of DNS shows that the main constraint on its possibilities is the availability of computational resources.

2.4.2. Difficulties

DNS is accompanied by several challenges. All challenges are directly or indirectly related to numerical aspects of the simulation [37, 60]. The only errors that are present in the results of a DNS are numerical ones and errors that arise due to incorrect implementation of boundary and initial conditions.

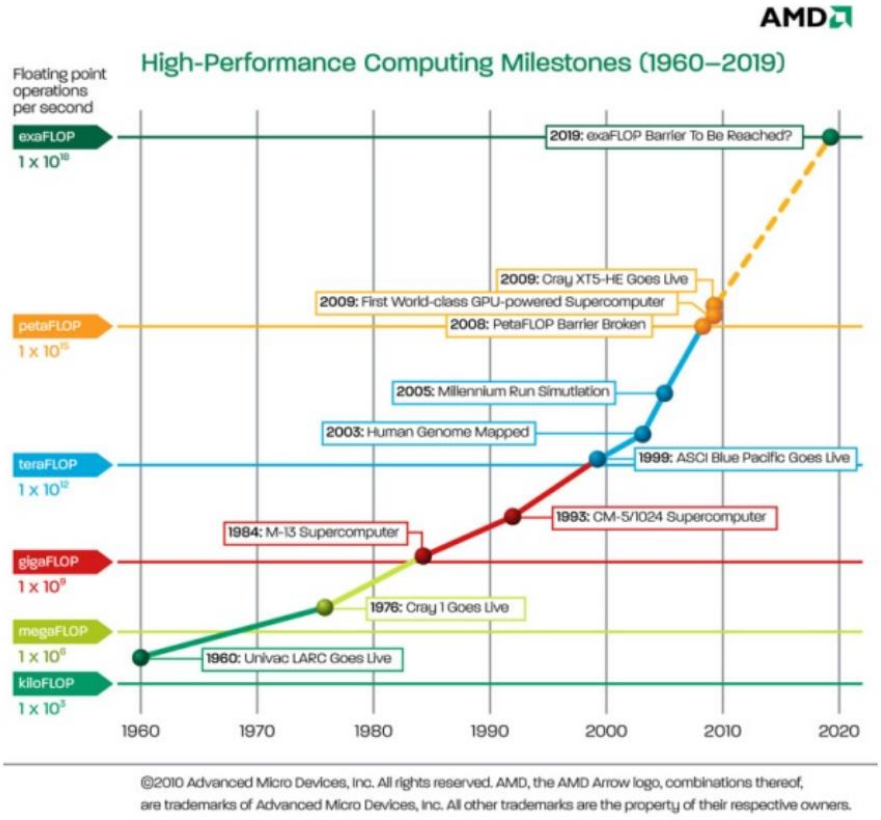

Figure 2-11: Evolution of the capacity of High-Performance Computers [85].

A first issue has already been mentioned implicitly in the previous paragraph, namely the computational cost of DNS. The reason for this high cost can be found in the large range of time and length scales that make up turbulence. The ratio between the highest length scales (the energy containing eddies) and the lowest scales (the Kolmogorov scale in the dissipative range) scales with the Reynolds number to the power 3/4. As a result, the minimum number of cells per dimension scales with the same power of the Reynolds number. In three dimensions, the number of grid points (and the related computational cost) thus scales with the Reynolds number to the power 9/4 [46]. A more extensive study of the scaling of the number of grid points shows a dependency on the Reynolds number to the power 37/14 [50]. Similarly, the ratio of the longest and shortest time scales, scales with $\sqrt{Re}$. The minimum amount of time steps required in a simulation would hence also scale with $\sqrt{Re}$. However, in reality, significantly more time steps are required. To obtain statistically meaningful averages of the longest time scales too, the simulation time must be much longer than the longest time scale. Speziale estimated that simulating turbulent pipe flow at a Reynolds number of 500,000 would require a super computer with a capacity of 10 Pflop/s or 10 million times faster than the state of the art supercomputing capacity at the time [86]. Today, the six most powerful, publicly listed supercomputers are capable of these speeds, but only just [74]. Figure 2-11 shows the trend of the increase in computing power over the past decades. If this trend persists in the following years [87], it cannot be deemed impossible that in the foreseeable future, it will become possible to simulate turbulent flows at Reynolds numbers of the order 10^5. On the other hand, it has been noted by Moin [60] that in some cases it is not

necessary, or even relevant, to simulate flows at such high Reynolds numbers using DNS. The finding that production and dissipation of turbulence balance near the wall, is quasi-independent of the Reynolds number, making it irrelevant to study this aspect of turbulence at Reynolds numbers of $>10^3$ - 10^4. On the other hand, rigorous studies of the local isotropy of turbulence would require simulations at high Reynolds numbers [60]. The sense or non-sense of using DNS at very high Reynolds numbers therefore depends on what the goal of the simulation is.

A second issue is related to the spatial discretisation and resolution. Using spectral methods, it has been found to be sufficient to resolve the majority of the turbulence dissipation [88-91]. This translates to the fact that the resolution in one (if not all) coordinate directions can be lower than the Kolmogorov length scale. This is due to the fact that the majority of dissipation takes place in the range of 15η [88]. The coarsest meshes can be used in isotropic turbulence and homogeneous shear [89], allowing a reduction of the required number of grid points by around a factor 10^2. When using central differencing schemes, which suffer from differentiation errors, the order of the scheme becomes very important. Schemes of order 2, 4 and 6 require a mesh spacing of 0.26η, 0.55η and 0.95η respectively, while a Fourier-based spectral method requires a spacing of 1.5η [60].

Another problem in DNS is the temporal resolution. The wide range of time scales that characterise turbulence result in a stiff system for time advancement. These systems are quite common in traditional (RANS) CFD calculations. They are solved using implicit time advancement algorithms and large integration steps. This approach is, unfortunately, not applicable to DNS, where large time steps would give erroneous results. Therefore, in DNS it is common practice to use implicit methods for the viscous terms and explicit methods for the convective ones. However, a general statement concerning which time advancement methods should be used cannot be made [60].

A final relevant difficulty in DNS, are the boundary conditions of the simulation. Strictly speaking, the only correct boundary conditions for a turbulent flow, is the solution [60]. The solution being unknown, several methods have been devised to apply boundary conditions on the turbulence in- and outflows, that at least after some transition region give the correct boundary conditions. This transition region hence contains results which are in se incorrect, increasing the size of the simulation domain and correspondingly the computational cost of the simulation. The earlier methods, the specification on the inflow of turbulence consisted of generating a three-dimensional, divergence-free field of random fluctuations that was homogeneous in the streamwise direction. These methods required quite some distance to evolve into 'real' turbulence [92]. Others used an instantaneous turbulent field from a separate simulation [93, 94], significantly reducing the distance required to attain true turbulence. Various other boundary conditions can be applied. In pipe and channel flow, periodicity is still a frequently used boundary condition [95, 96].

2.5. Discretisation Methods

2.5.1. Finite Differencing Method

The finite differencing method (FDM) is the most straightforward method of discretising sets of differential equations. In this approach, the derivatives are directly approximated by algebraic equations [97]. FDMs are typically only applied to problems in a Cartesian coordinate system (Figure 2-12) as cylindrical or spherical coordinate systems are very difficult to describe in a FDM. Hence, finite differencing is rarely used as such in either LES or DNS. However, a short description is given here because some parts of the more commonly used finite volume method (FVM) make use of the finite differencing principles, while the spectral methods can be regarded as an extension of the FDM.

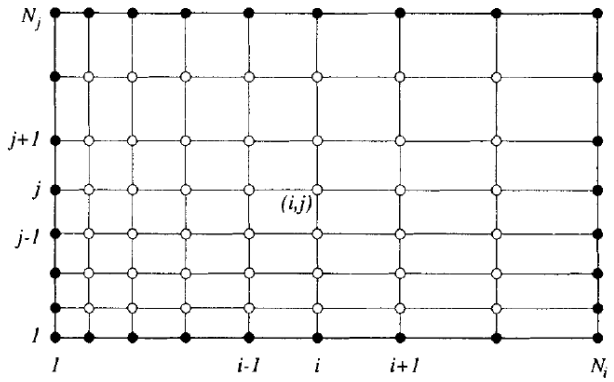

Figure 2-12: Cartesian grid for FDM [97].

The finite differencing method bases the approximation of the derivatives on the definition of the derivative [98].

$$\frac{d\varphi}{dx} = \lim_{\Delta x \to 0} \frac{\varphi(x+\Delta x) - \varphi(x)}{\Delta x} = \lim_{\Delta x \to 0} \frac{\varphi(x) - \varphi(x-\Delta x)}{\Delta x} = \lim_{\Delta x \to 0} \frac{\varphi(x+\Delta x) - \varphi(x-\Delta x)}{2\Delta x} \quad \textbf{(2-39)}$$

Based on which one of the definitions is used, one arrives at either the first order forward, backward or central differencing method (in the same order as in eq. (2-39)). While the three definitions are equivalent, the three obtained differencing schemes no longer give the same results.

$$\frac{d\varphi}{dx} \approx \frac{\varphi(x_{i+1}) - \varphi(x_i)}{x_{i+1} - x_i} \quad \textbf{(2-40)}$$

$$\frac{d\varphi}{dx} \approx \frac{\varphi(x_i) - \varphi(x_{i-1})}{x_i - x_{i-1}} \quad \textbf{(2-41)}$$

$$\frac{d\varphi}{dx} \approx \frac{\varphi(x_{i+1}) - \varphi(x_{i-1})}{x_{i+1} - x_{i-1}} \quad \textbf{(2-42)}$$

The truncation error of the FDM, which is the error between the exact derivative and the numerical derivative, can be estimated via Taylor expansion [98].

$$\varphi(x_{i+1}) = \varphi(x_i) + (x_{i+1} - x_i)\frac{d\varphi}{dx} + \frac{(x_{i+1} - x_i)^2}{2!}\frac{d^2\varphi}{dx^2} \quad \textbf{(2-43)}$$

The abovementioned forward and backward differencing schemes are of the same order (namely first order) and hence their truncation errors are found to be equal disregarding the sign. The central differencing mentioned above scheme is of the second order and hence will have a lower truncation error. The forward and backward schemes are (in this case) exact for linear functions, while this central differencing scheme is also exact for parabolic functions [98]. By using higher derivatives of the function and more points, higher order differencing schemes can be constructed.

$$err_{BD/FD} \approx \pm\frac{(x_{i+1} - x_i)}{2!}\frac{d^2\varphi}{dx^2} \quad \textbf{(2-44)}$$

$$err_{CD} \approx \frac{(x_{i+1} - x_i)^2}{12}\frac{d^3\varphi}{dx^3} \quad \textbf{(2-45)}$$

Higher order accuracy can be achieved by using polynomial interpolations. In this approach, n points are used to fit a polynomial of order $n-1$ [99]. The derivatives of this polynomial are then used as approximation for the derivative of the unknown function. In uniformly spaced grids, this results in the so-called compact differencing schemes [97]. The Padé schemes are an example of these compact schemes [100, 101]. It should be noted that high order differencing schemes require more function evaluations but improve the accuracy. This can result in a prolongation of the computation time. Besides accuracy, resolution of the solution is an important characteristic of the numerical method, especially in DNS. In this context, resolution can be conceived as accuracy in the wavenumber (Fourier) domain. While higher order compact schemes result in higher resolution, it is possible to construct low (e.g. fourth) order schemes which come very close to spectral resolution [99]. If the order of the interpolation polynomial goes to infinity, a spectral method is obtained. Hence the spectral methods, which will be discussed in paragraph 2.5.3, can be seen as a limit of the finite differencing method.

2.5.2. Finite Volume Method

The finite volume method discretises the spatial solution domain, starting from the integral form of the conservation equations [102]. The equations (2-3), (2-4) and (2-5) are written in differential form. In their integral forms, these equations become [103-105]

$$\int_{c.s.} \rho(\boldsymbol{v}\cdot\boldsymbol{n})dA + \frac{\partial}{\partial t}\int_{c.v.}\rho dV = 0 \quad \textbf{(2-46)}$$

$$\sum \boldsymbol{F} = \int_{c.s.} \boldsymbol{v}\rho(\boldsymbol{v}\cdot\boldsymbol{n})dA + \frac{\partial}{\partial t}\int_{c.v.} \boldsymbol{v}\rho dV \tag{2-47}$$

$$\frac{\delta Q}{dt} - \frac{\delta W}{dt} = \int_{c.s.} e\rho(\boldsymbol{v}\cdot\boldsymbol{n})dA + \frac{\partial}{\partial t}\int_{c.v.} e\rho dV \tag{2-48}$$

In equation (2-48), e denotes the total specific energy, comprising internal specific energy, potential energy, and kinetic energy.

$$e = u + gy + {v^2}/{2} \tag{2-49}$$

The finite volume method in its most general form for the conservation of a general transported scalar φ can be written as follows [102].

$$\frac{d}{dt}\int_{V(t)} \rho\varphi dV + \int_{\Omega(t)} \rho\varphi(\boldsymbol{v}\cdot\boldsymbol{n})dA = -\int_{\Omega(t)} (\boldsymbol{q_\varphi}\cdot\boldsymbol{n})dA + \int_{V(t)} s_\varphi dV \tag{2-50}$$

$$Accumulation \;+\; Convection \;=\; Other\ Transport + Source/Sink$$

It is explicitly stated here that the shape and size of the control volume can vary in time. For the remainder of the discussion however, it will be assumed that there is no time dependence of Ω or V.

Only one condition is to be fulfilled to use the finite volume method: there should be no overlap between adjacent discrete control volumes in the computational domain. The shape and size of the control volumes is of no consequence for the finite volume method. If the control volumes do not overlap, the finite volume method ensures conservation both locally and globally [106]. Three basic steps can be discerned in the finite volume method. The first step is the generation of the grid, defining the control volumes. Construction of the grid is possible in two different ways. One can either start by defining the control volumes and then assigning computational nodes to each volume (node centred), or one can construct a network of computational nodes around which the control volumes are constructed (c.v.-faces centred). In the latter method, the faces of the control volumes will be located equidistant to two nodes. This allows more accurate approximations of the fluxes at the faces in a central differencing scheme (CDS) [102]. In the former method, the nodes are defined as the centroid of each control volume, therefore nodal values will represent the volume averaged cell values with higher accuracy than in the c.v.-faces centred one. In this context, other ways to define cells are possible.

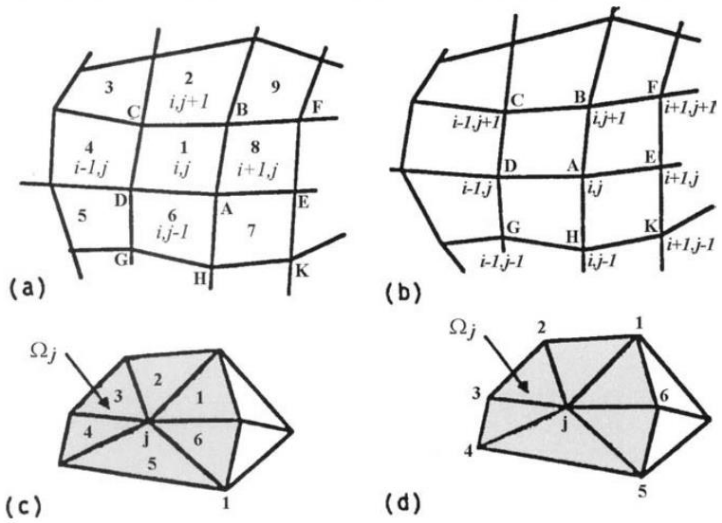

Figure 2-13: Different types of 2D finite volume meshes (a) Cell centred, structured FV mesh (b) Vertex centred, structured FV mesh (c) Cell centred, unstructured FV mesh (d) Vertex centred, unstructured FV mesh [107].

Instead of centring the nodes in the bulk of the control volume, it is possible to define them on the intersections of different cells [107]. This is called vertex centring. A two dimensional representation is given in (a) and (b) of Figure 2-13. A final distinction can be made between structured and unstructured meshes. Structured meshes consist of control volumes of which the edges lie on the intersection of 2 (in three dimensions 3) families of lines. This allows the cells to be attributed a certain coordinate (i,j or i,j,k). Unstructured meshes exist of control volumes of triangular (tetrahedral in 3D) cells. Consequently, it is not possible to assign coordinates to the cells. Each cell must be given a number, in a certain order. Obviously this requires additional memory, slowing down calculations [107]. Unstructured meshes are able to describe complex geometries with less cells than structured meshes. The cell size should be carefully chosen. In DNS, the dimensions of each cell must be smaller than the Kolmogorov scale. In LES, the cell size should be of the same order as the cut-off width [37]. If the dimension of the cell is chosen to be much larger than the cut-off width, the turbulence with length scales in the range between the cell dimension and the cut-off cannot be calculated. This results in an irretrievable loss of information. If the dimension of the cell is chosen to be much smaller than the cut-off width, the computational effort will increase needlessly. Due to the filtering, turbulence is modelled in the range between the cut-off width and the cell diameter. Hence, the decreased cell size does not contribute to improved accuracy.

The second step consists of discretizing the integral conservation equations on the cell volumes. The integral equation (2-50) is first rewritten. The following terms are defined,

$$\Phi = \int_V \rho\varphi dV \tag{2-51}$$

$$\int_\Omega (\boldsymbol{N}\cdot\boldsymbol{n})dA = \int_\Omega \rho\varphi(\boldsymbol{v}\cdot\boldsymbol{n})dA + \int_\Omega (\boldsymbol{q_\varphi}\cdot\boldsymbol{n})dA \tag{2-52}$$

$$S_\varphi = \int_V s_\varphi dV \tag{2-53}$$

resulting in the following simplified expression.

$$\frac{d\Phi}{dt} + \int_\Omega (\boldsymbol{N} \cdot \boldsymbol{n}) dA = S_\varphi \tag{2-54}$$

In the finite volume method, these three terms are to be calculated. In each cell, only one computational node is available, hence it is advisable to work with cell volume averaged values for Φ and S_φ.

$$\bar{\Phi} = \frac{1}{V_{c.v.}} \int_{V_{c.v.}} \rho\varphi dV \tag{2-55}$$

$$\overline{s_\varphi} = \frac{1}{V_{c.v.}} \int_{V_{c.v.}} s_\varphi dV \tag{2-56}$$

Higher order approximations of the cell volume averaged quantities are possible as well, but they require interpolation of Φ. Especially in three dimensions, this can be quite complex, though for a Cartesian equidistant mesh, a fourth order approximation is readily found. It is a direct extension of the two-dimensional case [102]. An approximation of the surface transport integral is required as well. The total surface integral can be split into separate integrals for each surface.

$$\int_\Omega \boldsymbol{N} d\boldsymbol{\Omega} = \sum_k \int_{\Omega_k} N dA \tag{2-57}$$

To evaluate these integrals, φ should be known on the entire surface of the cell. Due to the previously discussed approach, only the cell averages are known. Therefore the surface integrals should first be approximated as function of values at one location on each surface, then these values are to be expressed as function of the average cell values [108]. Linking the surface values to the average values of the surrounding cell nodes is done via interpolation. Several interpolation schemes exist. The simplest ones are linear interpolation and the upwind schemes [109]. More complex interpolation schemes include the power law interpolation and the QUICK scheme [108, 109]. The simplest way to approximate the surface integrals is via the midpoint rule, which is second order accurate and approximates the integral by product of the function value at the centre of the surface and the surface area.

$$\int_{\Omega_k} N dA = N_k \Omega_k + \mathcal{O}(\Delta y^2) \tag{2-58}$$

Higher order methods will have better accuracy, but require more function evaluations and consequently more interpolated values. Additionally, the interpolation methods should be of at least the same order as

the one for approximating the integrals [108]. In case of the Navier-Stokes equations, this does not yet fully solve the problem. The term $\sum \boldsymbol{F}$ in equation (2-47) comprises quite crudely all right-hand terms of equation (2-8). Of these terms, only the term $\rho \boldsymbol{g}$ is a body-force corresponding to a volume-integral. The other terms (pressure and shear stress) reduce to surface integrals due to the gradient operators. For pressure this corresponds to equation (2-58), for the shear stress a second approximation must be made [110]. Through equation (2-6), it is clear that τ_{ij} depends on the velocity field. As this field is not known initially, one must write (disregarding the pressure term for the normal stresses)

$$\int_{\Omega_k} \tau_{ij} dA = \int_{\Omega_k} \mu \left(\frac{\partial v_i}{\partial x_j} + \frac{\partial v_j}{\partial x_i} \right) dA \tag{2-59}$$

Or, once equation (2-58) is used

$$\int_{\Omega_k} \tau_{ij} dA = \mu \left(\frac{\partial v_i}{\partial x_j} + \frac{\partial v_j}{\partial x_i} \right) \Omega_k \tag{2-60}$$

The differentials that are still present here can be determined via a central differencing scheme which is second order accurate (see paragraph 2.5.1). Any other approximation of the differentials is possible as well though. However, using higher order methods (e.g. four-point central differencing or Padé schemes) requires more function evaluations in a higher number of points, increasing the computational cost of the operation [111].

The above approximations of the different integrals make it possible to write the conservation equations as a set of linear(ised) algebraic equations. These equations can be written in matrix form and hence be solved via efficient algorithms [109].

2.5.3. Spectral Methods

In the aforementioned methods, better accuracy and convergence is related to decreasing the grid spacing. A different approach has already been alluded to in paragraph 2.5.1, suggesting to increase the order of the interpolation polynomial to achieve better results. This is the basis of the spectral methods [98]. Spectral methods are only used for discretisation of the spatial domain. Time integration is done by classical time stepping methods such as Runge-Kutta and Adams-Bashforth methods [112].

It is generally known that any function can be expanded in a sequence of orthogonal functions $\{\phi_k\}$, with the Fourier, Chebyshev and Legendre polynomial expansions being the best known [112, 113].

$$f(x) = \sum_{k=-\infty}^{+\infty} \hat{f}_k \phi_k(x) \tag{2-61}$$

The discretisation principle is essentially replacing the unknown function values at the different grid points, by a given number of (time-dependent) expansion coefficients and known base functions over the entire domain. The derivatives of the original function at different grid points can then, quite easily, be transformed into functions of the expansion coefficients. As the base functions are time independent, the resulting equations are ordinary differential equations in time. As said above, these can be accurately integrated using typical integration schemes. Essentially, this approach is exact, resulting in no fundamental error. However, it is not possible to do calculations with an infinite set of base functions, so an implementable method requires the truncation of the expansion at a given number of base functions. The error between the true expansion and the truncated one is known as the truncation error. If f has favourable properties (and most naturally occurring phenomena do), the error goes to zero faster than $1/N^{\alpha}$, with α being a randomly large but finite number. This is known as spectral accuracy, a property which has already been mentioned in the context of high-order finite difference methods. Besides the truncation error, using a finite number of grid points (interpolation) also gives rise to a new type of error, known as aliasing [113]. By combining eqs. (2-61) and (2-62) and using the orthogonality of the base functions, eq. (2-63) is found, showing each mode k also depends on the modes $k + Nm$. This is because on the grid $\phi_k(x_j) = \phi_{k+Nm}(x_j)$. The modes $k + Nm$ are referred to as aliases of mode k as they cannot be distinguished from each other.

$$f(x_j) = \sum_{k=-N/2}^{N/2-1} \check{f}_k \phi_k(x_j) \tag{2-62}$$

$$\check{f}_k = \hat{f}_k + \sum_{\substack{m=-\infty \\ m\neq 0}}^{+\infty} \hat{f}_{k+Nm} \tag{2-63}$$

The phenomenon of aliasing is illustrated in Figure 2-14, which clearly shows that with 8 spatial points, it is impossible to determine which of the three sine functions is the correct function behind the points. However, methods have been devised to counter this effect. In the limit, the influence of aliasing on the accuracy of the method is the same as that of the truncation error [114].

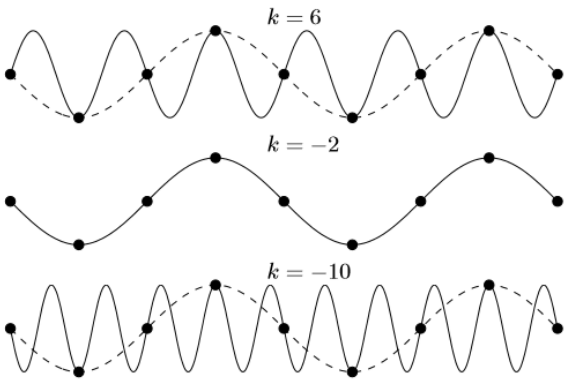

Figure 2-14: Aliasing of the mode k=-2, using an 8-point grid.

In what follows, the approximation of the derivatives using expansion of the function will be further elaborated, using the Fourier expansion as example [113, 115]. Analogous approaches are used for expansions with other base functions.

Substituting the Fourier base functions in eq. (2-61), the Fourier sequence is obtained. As a discretised expression for the derivative of f is desired, both sides of eq. (2-64) are derived, with respect to the spatial coordinate.

$$f(x) = \sum_{k=-\infty}^{+\infty} \hat{f}_k \exp(ikx) \tag{2-64}$$

$$\frac{df(x)}{dx} = \sum_{k=-\infty}^{+\infty} ik\hat{f}_k \exp(ikx) \tag{2-65}$$

An expression for the derivative of f is now available. However, it is still continuous and infinite, hence the sequence is truncated and interpolated on a discrete number of grid points N. The expression for $\check{f}_k$ is now explicitly written out.

$$\left.\frac{df(x)}{dx}\right|_{x=x_j} \approx \sum_{k=-N/2}^{N/2-1} \left(\exp(ikx_j) \frac{ik}{N} \sum_{l=0}^{N-1} f(x_l) \exp(-ikx_l) \right) \tag{2-66}$$

Eq. (2-66) shows the power of the spectral methods. While in finite difference and finite volume methods the derivatives are approached by local values of the function, the spectral method uses the values in the entire solution domain. The required Fourier transformations – one in each summation – can be done via the very efficient fast Fourier transform (FFT) algorithms. To come to an expression for the second derivative, the step (2-64) → (2-65) is repeated starting from eq. (2-65). In the end, for a partial differential equation in both space and time, one can write the following.

$$\left.\frac{df(x)}{dt}\right|_{x=x_j} = \mathcal{F}\big(f(x_i)\big) \quad i,j = 0..N-1 \tag{2-67}$$

It can be shown that in n dimensions, the Fourier transformation is independent in the different coordinates [116]. This allows an easy extension of the above discussion to a 2- and 3-dimensional case. The above corresponds to the so-called collocation method in which the strong (differential, e.g. eq. (2-68)) form of the to-be-solved equation is used as starting point [115]. As a result, the problem is solved in the actual space domain, or that the actual function values at the different grid points are determined. An alternative is starting from the weak (integrated differential, eq. (2-69)) form of the equation. Then the problem is solved in the transformed space, meaning that the expansion coefficients are determined.

$$\frac{df(x)}{dt} + \frac{df(x)}{dx} = 0 \tag{2-68}$$

$$\int \left(\frac{df(x,t)}{dt} + \frac{df(x,t)}{dx}\right) \phi_k(x)dx = 0 \tag{2-69}$$

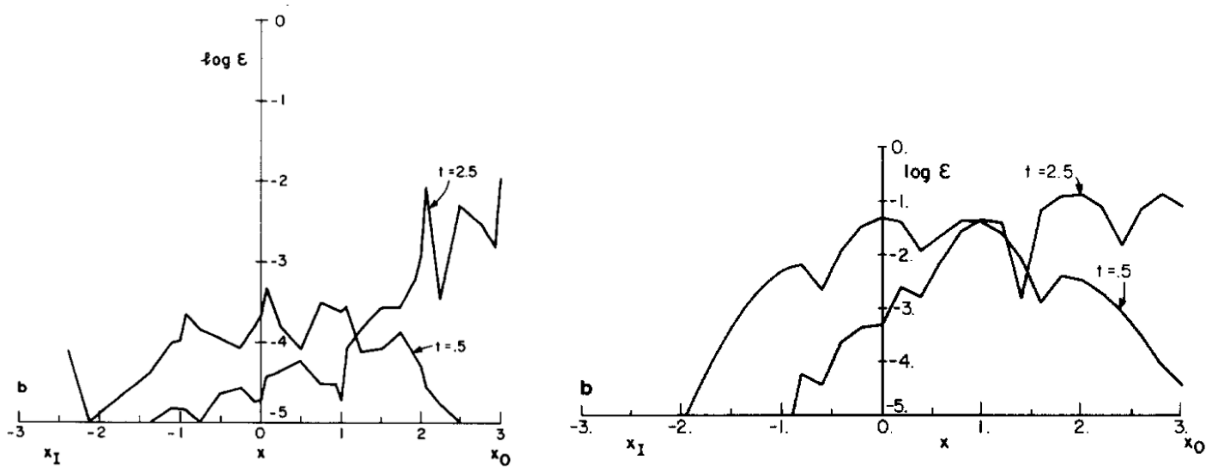

Figure 2-15: Error for spectral element method (left), using 5 elements and 7 collocation points per element (N_t=31) and finite element method (right) using the same number (N_t) of points. Simulation of an inflow-outflow, advective-diffusion equation [117].

The spectral elements method (SEM) is an extension of the spectral method, combining it with aspects of the finite element method (which has not been discussed here). The finite element method is *in se* quite similar to the spectral methods, only it uses non-spectral base functions and is applicable to much more complex geometries [118, 119]. In the traditional spectral methods, the weak form of the differential equation is typically imposed on the complete domain. This results in very high order polynomials [119]. In the finite element method, the weak formation is imposed on each element separately. This can be compared to solving the integral form of the equation for each cell volume compared to solving it for the entire system volume (see the Finite Volume Method). The spectral elements method uses this same approach, but with

the rapidly converging spectral base functions rather than linear ones, resulting in an error of one to three orders of magnitude lower (Figure 2-15) [117].

It is fitting to end this paragraph with some comparisons, advantages and disadvantages between the three discussed methods. The finite differencing method is very simple, both conceptually and implementation-wise [120]. However, it is restricted to structured grids and simple geometries. Even cylindrical coordinates can pose quite a challenge to implement. Additionally, the finite differencing formulation is non-conservative, making local and even global mass and energy imbalances possible. As mentioned in paragraph 2.5.1, this method is not used in DNS or LES. The simplicity of the FDM led to it being the method of choice for one of the first ever numerical flow simulations in 1933 [121]. The finite volume method is potentially the most applied discretisation method in CFD [109]. The FVM is based on local conservativeness, and has nearly no restrictions on the grid and cell shapes [120]. Due to its success, plenty and efficient algorithms exist to solve the equations. The main drawback of the FVM is that it can produce numerical or false diffusion [122]. To avoid this very fine meshes are required, even though methods have been devised to counter this. The spectral methods are the most used method in turbulence studies as they achieve excellent accuracy due to their high order character [119]. However, this (excessively) high order is also their greatest drawback. They deteriorate the conditioning of the system, requiring very small time steps and they introduce aliasing errors. Additionally, spectral methods are inapt at treating complex geometries. Nonetheless, the first DNS were performed using spectral codes [71]. The spectral element method can handle complex geometries, is conservative and very accurate, combining the best of the spectral methods and finite element methods.

2.5.4. Time Advancement

The aforementioned methods are only used for spatial discretisation. In simulations of turbulent flows, however, the time-dependent conservation equations must be solved. This means that discretisation in time is also required. This is typically done via numerical integration methods such as the Runge-Kutta and Adams-Bashforth methods [120, 123]. Compared to the methods used for spatial discretisation, these are quite simple methods. The fact that complex methods have only little added value when it comes to time integration is due to the nature of time [123]. Regarding flow, only characteristics of the flow in the past can influence those at the considered time. The ‘future’ solution does not influence the ‘present’ solution [123]. In space, this is not true. At a given point, the solution may be influenced by any other point in the grid, it is this interaction that requires the use of more complex discretisation methods. Hence it is convenient to apply so-called time stepping or time marching methods.

One important aspect of time discretisation is the choice of the time step. In DNS, a first restriction on the time step, which is desired to be as large as possible, is the Kolmogorov time scale (eq. (2-17)). In order to resolve the smallest turbulence scales, the time step should be smaller than the Kolmogorov time scale. As demonstrated in paragraph 2.2.2, this can be in of order of 10^{-6} s. The second restriction is the Courant flow

number (CFL) or Courant number, which should be smaller than unity at each moment during the simulation [123]. This condition is related to stability of the time stepping method. It can be interpreted as the statement that no fluid element may 'skip' a computational cell when advancing time.

$$\Delta t < \left(\frac{\nu}{\varepsilon}\right)^{\frac{1}{2}} \tag{2-70}$$

$$CFL = v\frac{\Delta t}{\Delta x} < 1 \tag{2-71}$$

To end this section, a brief overview of the two most used time stepping methods is given [124]. The fourth order Runge-Kutta method is a one-step, explicit method. It can only be used for first order, ordinary differential equations of the form

$$\frac{dv}{dt} = \mathcal{F}(v, t) \tag{2-72}$$

Once the velocity, pressure and temperature fields have been solved at a given time, the Navier-Stokes equations can be reduced to such a form (this is further elaborated in paragraph 2.5.5). The fourth-order Runge-Kutta method then reads

$$v(t_{i+1}) = v(t_i) + \frac{1}{6}(K_1 + 2K_2 + 2K_3 + K_4)\Delta t \tag{2-73}$$

$$K_1 = \mathcal{F}(v(t_i), t_i) \tag{2-74}$$

$$K_2 = \mathcal{F}\left(v(t_i) + \frac{1}{2}K_1\Delta t, t_i + \frac{1}{2}\Delta t\right) \tag{2-75}$$

$$K_3 = \mathcal{F}\left(v(t_i) + \frac{1}{2}K_2\Delta t, t_i + \frac{1}{2}\Delta t\right) \tag{2-76}$$

$$K_4 = \mathcal{F}(v(t_i) + K_3\Delta t, t_i + \Delta t)t \tag{2-77}$$

It can be shown that the global truncation error of the fourth order Runge-Kutta method is $\mathcal{O}(\Delta t^4)$ and the local error $\mathcal{O}(\Delta t^5)$ [124]. Considering the time step requirements (eq. (2-70) and (2-71)), this means that the absolute error on the time advancement is $\mathcal{O}(10^{-20}\ s)$. While providing excellent numerical accuracy, the Runge-Kutta methods require a number of function evaluations equal to their order (the fourth order method required four evaluations of $\mathcal{F}$). Increased accuracy is hence inherently coupled to more function evaluations and/or interpolation.

The second frequently used method is the Adams-Bashforth method. Where the Runge-Kutta methods rely on function evaluations solely at the considered time step, the Adams-Bashforth methods use function evaluations at past times as well [124], making it an explicit, multi-step method. The fourth-order Adams-Bashforth method is the following, for the same differential equation as given in eq. (2-72).

$$v(t_{i+1}) = v(t_i) + \frac{\Delta t}{24}\left(55v(t_i) - 59v(t_{i-1}) + 37v(t_{i-2}) - 9v(t_{i-3})\right) \quad \textbf{(2-78)}$$

The order of the global error is the same as for the Runge-Kutta method. However, as data from past time steps still have to be (quickly) accessible, the memory cost of the Adams-Bashforth methods is higher than that for the Runge-Kutta methods.

2.5.5. Navier-Stokes Equations

To conclude this chapter, attention is given to the Navier-Stokes equations specifically. As shown by eq. (2-3)-(2-5), the set of equations that has to be solved is strongly coupled. Even when considering isothermal and non-reactive flow, a set of coupled partial differential equations must be solved. In the classical notation, both equations are staged as equations in velocity. The pressure field must be solved as well, but the classical notation does not provide an independent equation to do so [110]. In cases where compressibility effects are important (Mach number higher than 0.3 [125]), the equation for the conservation of mass can be used as an independent equation for the density. The pressure for the momentum equation can then be calculated via an equation of state, the simplest of which being the ideal gas law [126]. The incompressible case or compressible cases at low Mach numbers provide a greater challenge. It is possible to write the momentum equation (2-8) in a more compact form [127]. This is in the form required for the Runge-Kutta methods (eq. (2-72)).

$$\rho \frac{dv_i}{dt} = \mathcal{H}_i - \frac{dP}{dx_i} \quad \textbf{(2-79)}$$

Here $\mathcal{H}_i$ combines the advective and viscous terms in the momentum equation. From this form, it is possible to derive the so-called Poisson equation for the pressure (in which Δ represents the Laplace operator).

$$\Delta(P) = \frac{d\mathcal{H}_i}{dx_i} \quad \textbf{(2-80)}$$

This gives an explicit equation for the pressure, which can be solved using any of the methods described above. However, the numerical properties of solving the pressure equation together with the momentum equation are not favourable [109]. Hence, during the 70's and 80's, several algorithms have been devised to decouple pressure and momentum and solve them in an iterative way. The two most important algorithms are the SIMPLE (semi-implicit method for pressure linked equations) [128] and variants and the PISO (pressure implicit with splitting of operators) [129] algorithms. Both algorithms rely on using an initial guess for the pressure field, solving the velocity field based on this guess using eq. (2-79) and the determining the pressure field with eq. (2-80). This procedure is repeated until convergence is achieved.

The SIMPLE algorithm uses a guess-correct iterative procedure. The method is explained below for Cartesian coordinate systems. First an initial guess of the pressure (P^*) is required. Typically, for each

discrete point, the upstream pressure is a fair guess. With this estimate, the discretised momentum equations can be solved. This results in the first estimates of the velocity field ($\boldsymbol{v}^*$). The difference between the estimated value and the true value is denoted by P'.

$$P = P^* + P' \tag{2-81}$$

$$\boldsymbol{v} = \boldsymbol{v}^* + \boldsymbol{v}' \tag{2-82}$$

Based on these expressions, the velocity fluctuations can be approximated by the below expression, in which C_i is a geometric parameter of the mesh and i the index along the x-coordinate.

$$v_{x,i}{}' = C_i(P_i' - P_{i-1}') \tag{2-83}$$

These relations are substituted in the continuity equation (note that the SIMPLE algorithm does not use the Poisson pressure equation). Enforcing continuity now leads to the pressure correction equation. The equation is given for a 2-dimensional grid (i,j being the indices in x,y directions respectively) $a_{i,j}$ are coefficients depending on the cell geometry, $b_{i,j}{}'$ arises from the mass imbalance caused by the estimated velocity field.

$$a_{i,j}p_{i,j}' = a_{i+1,j}p_{i+1,j}' + a_{i-1,j}p_{i-1,j}' + a_{i,j+1}p_{i,j+1}' + a_{i,j-1}p_{i,j-1}' + b_{i,j}{}' \tag{2-84}$$

Eq. (2-84) is constructed for each grid point, resulting set of algebraic equations which can easily be solved. Now the actual pressure and velocity field can be calculated. The pressure correction equation is sensitive to divergence. To avoid this, before performing the convergence check, under-relaxation is used.

$$p^{new} = p^* + \alpha_p p' \tag{2-85}$$

$$\boldsymbol{v}^{new} = \boldsymbol{v}^* + \alpha_v \boldsymbol{v}' \tag{2-86}$$

The under-relaxation coefficients should be chosen carefully. Too high coefficients will not effectively mitigate instability, too low coefficients will increase the amount of iterations required to reach convergence. Convergence is reached when the difference between p^{new} and p^{old} and $\boldsymbol{v}^{new}$ and $\boldsymbol{v}^{old}$ is smaller than a specified value. A schematic overview of the SIMPLE algorithm is shown in Figure 2-16.

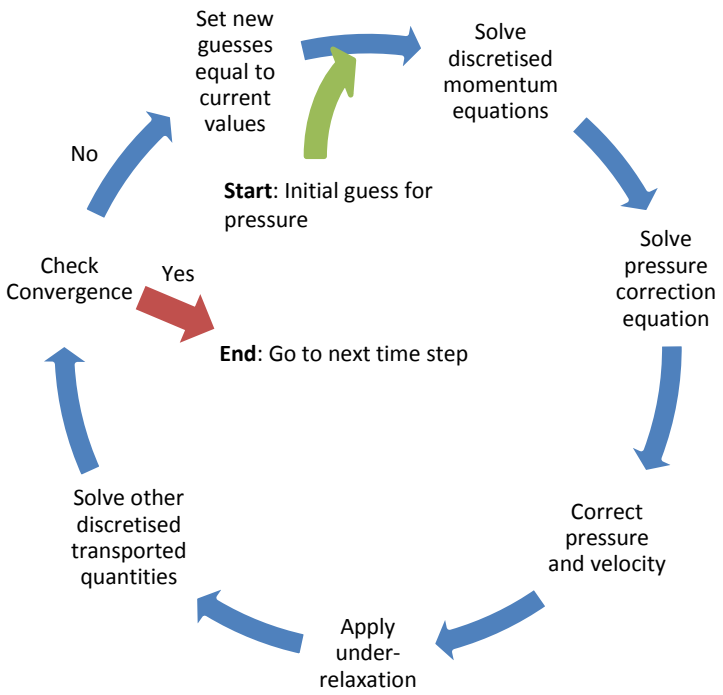

Figure 2-16: SIMPLE algorithm for pressure-velocity coupling, adapted from Versteeg [126].

The PISO algorithm uses a very similar reasoning as the SIMPLE algorithm, but extends it with a second correction step. The first correction to the pressure is calculated via the exact same steps as in the SIMPLE algorithm (eq. (2-84)). However, then it is stated that

$$P^{**} = P^{*} + P' \tag{2-87}$$

$$\boldsymbol{v}^{**} = \boldsymbol{v}^{*} + \boldsymbol{v}' \tag{2-88}$$

This newly calculated pressure P^{**} is now used in the discretised momentum equation to determine a new velocity field $\boldsymbol{v}^{***}$. This is considered to be the correct velocity field within the iteration.

$$P^{***} = P^{**} + P'' = P^{*} + P' + P'' \tag{2-89}$$

The second correction P'' is found by substituting the discrete expressions for $\boldsymbol{v}^{***}$ in the continuity equation. This results in an expression quite similar to eq. (2-84), the coefficients $b_{i,j}{}''$ are slightly different, though.

$$a_{i,j}p''_{i,j} = a_{i+1,j}p''_{i+1,j} + a_{i-1,j}p''_{i-1,j} + a_{i,j+1}p''_{i,j+1} + a_{i,j-1}p''_{i,j-1} + b_{i,j}{}'' \tag{2-90}$$

Once the corrections are determined, the true pressure field can be calculated. After again applying adequate under-relaxation, convergence of the solution can be checked. A simplified flow chart of the PISO algorithm is presented in Figure 2-17.

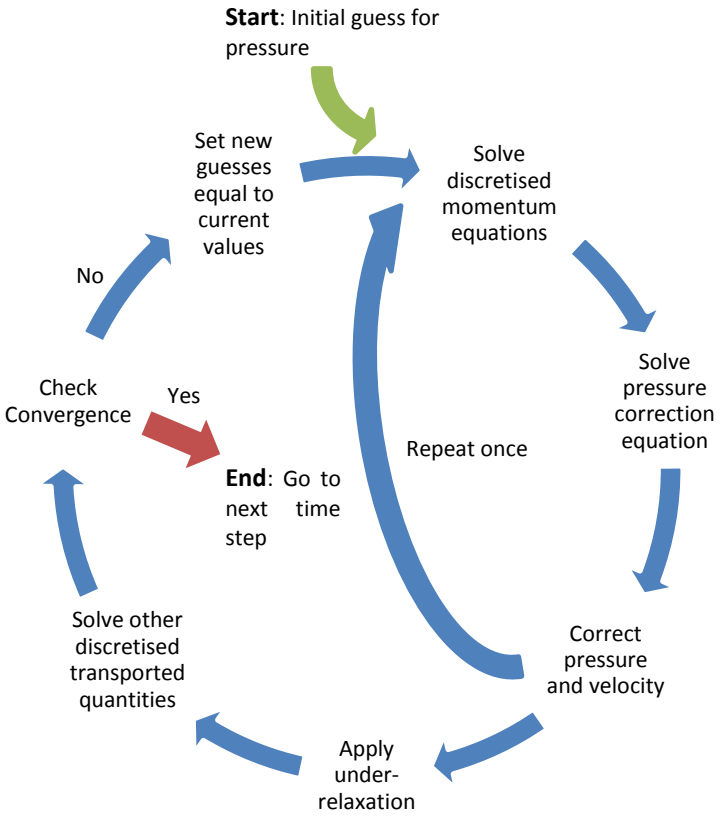

Figure 2-17: PISO algorithm for pressure-velocity coupling, adapted from Versteeg [126].

2.6. Conclusion

In this chapter, computational aspects of turbulence modelling have been discussed Three different approaches are possible. Reynolds averaging models all turbulence, while large eddy simulations only model the isotropic small scales of turbulence. Direct numerical simulations resolve all aspects of the flow and do not resort to any turbulence models. RANS is not elaborated on here, but some LES models, of which the Smagorinsky-Lilly [40, 41] model is an important one, are covered. In DNS, the main complexity is not constructing an accurate model, but devising computationally efficient algorithms to solve the equations. The final part of the chapter discusses several important discretisation methods, both spatially and temporally. Spectral (element) methods are found to have the potential to significantly outperform the finite differencing and finite volume methods, especially considering their limited numerical diffusivity of the solution and generally higher order of accuracy. The downside of spectral (elements) methods are their higher computational cost. In CFD, time advancement is typically done by time stepping, *i.e.* the solution is calculated at a given time, the time is advanced and a new solution is determined at the new time step. Another particularity in CFD is the fact that the momentum and mass balance equations are a coupled set for pressure and velocity. To solve for pressure and velocity explicitly, pressure-velocity coupling algorithms have been devised. Examples are the SIMPLE [128] and PISO [129] algorithms.

2.7. References

1. Geen, D. W.; Perry, R. H., Fluid and Particle Dynamics. In *Perry's Chemical Engineers' Handbook*, 8 th ed.; McGraw-Hill Companies, Inc.: 2008; pp 6.1-6.56.
2. Welty, J. R.; Wicks, C. E.; Wilson, R. E.; Rorrer, G. L., Differential Equations of Fluid Flow. In *Fundamentals of Momentum, Heat, and Mass Transfer*, John Wiley and Sons, Inc.: , 2008; pp 99-112.
3. Welty, J. R.; Wicks, C. E.; Wilson, R. E.; Rorrer, G. L., Differential Equations of Heat Transfer. In *Fundamentals of Momentum, Heat, and Mass Transfer*, John Wiley and Sons, Inc.: , 2008; pp 217-223.
4. Welty, J. R.; Wicks, C. E.; Wilson, R. E.; Rorrer, G. L., Shear Stress in Laminar Flow. In *Fundamentals of Momentum, Heat, and Mass Transfer*, John Wiley and Sons, Inc.: , 2008; pp 81-91.
5. Andersson, B.; Andersson, R.; Hakansson, L.; Mortensen, M.; Sudiyo, R.; Wachem, B. v., Turbulent-Flow Modelling. In *Computational Fluid Dynamics for Engineers*, Cambridge University Press: 2012; pp 62-112.
6. Schietekat, C. Computational Fluid Dynamics-based Design of Steam Cracking Reactors. Universiteit Gent, 2015.
7. Zhang, Y.; Qian, F.; Schietekat, C. M.; Van Geem, K. M.; Marin, G. B., Impact of flue gas radiative properties and burner geometry in furnace simulations. *AIChE Journal* **2015,** 61, (3), 936-954.
8. Hu, G.; Schietekat, C. M.; Zhang, Y.; Qian, F.; Heynderickx, G.; Van Geem, K. M.; Marin, G. B., Impact of radiation models in coupled simulations of steam cracking furnaces and reactors. *Industrial & Engineering Chemistry Research* **2015,** 54, (9), 2453-2465.
9. Hu, G.; Wang, H.; Qian, F.; Van Geem, K. M.; Schietekat, C. M.; Marin, G. B., Coupled simulation of an industrial naphtha cracking furnace equipped with long-flame and radiation burners. *Computers & Chemical Engineering* **2012,** 38, 24-34.
10. Ghasemian, M.; Nejat, A., Aero-acoustics prediction of a vertical axis wind turbine using Large Eddy Simulation and acoustic analogy. *Energy* **2015,** 88, 711-717.
11. Clements, A. G.; Black, S.; Szuhánszki, J.; Stęchły, K.; Pranzitelli, A.; Nimmo, W.; Pourkashanian, M., LES and RANS of air and oxy-coal combustion in a pilot-scale facility: Predictions of radiative heat transfer. *Fuel* **2015,** 151, 146-155.
12. Mahesh, K.; Constantinescu, G.; Apte, S.; Iaccarino, G.; Ham, F.; Moin, P., Large-eddy simulation of reacting turbulent flows in complex geometries. *Journal of Applied Mechanics* **2006,** 73, (3), 374-381.
13. Robert, A.; Richard, S.; Colin, O.; Poinsot, T., LES study of deflagration to detonation mechanisms in a downsized spark ignition engine. *Combustion and Flame* **2015,** 162, (7), 2788-2807.
14. Quillatre, P.; Vermorel, O.; Poinsot, T.; Ricoux, P., Large Eddy Simulation of Vented Deflagration. *Industrial & Engineering Chemistry Research* **2013,** 52, (33), 11414-11423.
15. Xu, X.; Lee, J. S.; Pletcher, R. H., A compressible finite volume formulation for large eddy simulation of turbulent pipe flows at low Mach number in Cartesian coordinates. *Journal of Computational Physics* **2005,** 203, (1), 22-48.
16. Lampitella, P.; Colombo, E.; Inzoli, F., A dynamic mixed subgrid-scale model for large eddy simulation on unstructured grids: application to turbulent pipe flows. *Journal of Physics: Conference Series* **2014,** 501, (1), 012020.
17. Ramaj, V.; Dhori, A.; Dhoska, K.; Koleci, A.; Konjusha, E., CFD Code Turbulence Models Validation for Turbulent Flows Over a Wavy Surface. *Annals of DAAAM for 2010 & Proceedings of the 21st International DAAAM Symposium* **2010,** 21.
18. Tennekes, H.; Lumley, J. L., *A first course in turbulence*. Cambridge (Mass.) : MIT press: 1972.
19. Welty, J. R.; Wicks, C. E.; Wilson, R. E.; Rorrer, G. L., Viscous Flow. In *Fundamentals of Momentum, Heat, and Mass Transfer*, John Wiley and Sons, Inc.: , 2008; pp 137-167.
20. Richardson, L. F., *Weather Prediction by Numerical Process*. Cambridge University Press: 1922; p 262.

21. Kolmogorov, A. N. In *The local structure of turbulence in incompressible viscous fluid for very large Reynolds numbers*, Dokl. Akad. Nauk SSSR, 1941; 1941; pp 299-303.
22. Kolmogorov, A. N. In *Dissipation of energy in locally isotropic turbulence*, Dokl. Akad. Nauk SSSR, 1941; 1941; pp 16-18.
23. Pope, S. B., The Statistical Description of Turbulent Flows. In *Turbulent Flows*, Cambridge University Press: 2000; pp 34-82.
24. Pope, S. B., The Scales of Turbulent Motion. In *Turbulent Flows*, Cambridge University Press: 2000; pp 34-82.
25. Obukhov, A. In *On the distribution of energy in the spectrum of turbulent flow*, Dokl. Akad. Nauk SSSR, 1941; 1941; pp 22-24.
26. Pope, S. B., Wall Flows. In *Turbulent Flows*, Cambridge University Press: 2000; pp 264-332.
27. Holman, J. P., Principles of Convection. In *Heat Transfer*, 10 ed.; The McGraw-Hill Companies, Inc.: 2010; pp 215-276.
28. Jeong, J.; Hussain, F.; Schoppa, W.; Kim, J., Coherent structures near the wall in a turbulent channel flow. *Journal of Fluid Mechanics* **1997,** 332, 185-214.
29. Le, A.-T.; Coleman, G. N.; Kim, J., Near-wall turbulence structures in three-dimensional boundary layers. *International Journal of Heat and Fluid Flow* **2000,** 21, (5), 480-488.
30. Schoppa, W.; Hussain, F., Coherent structure dynamics in near-wall turbulence. *Fluid Dynamics Research* **2000,** 26, (2), 119-139.
31. de Villiers, E. The Potential of Large Eddy Simulation for the Modeling of Wall Bounded Flows. Imperial College of Science, Technology and Medicine, 2006.
32. Moin, P.; Kim, J., Numerical investigation of turbulent channel flow. *NASA Ames Research Center* **1981**.
33. Moin, P.; Kim, J., Numerical investigation of turbulent channel flow. *Journal of Fluid Mechanics* **1982,** 118, 341-377.
34. Saddoughi, S. G.; Veeravalli, S. V., Local isotropy in turbulent boundary layers at high Reynolds number. *Journal of Fluid Mechanics* **1994,** 268, 333-372.
35. Townsend, A. A., *The structure of turbulent shear flow*. Cambridge university press: 1980.
36. Boussinesq, J., Essai sur la théorie des eaux courantes. In *Mémoires présentés par divers savants a l'académie des sciences de l'Institut National de France*, Imprimerie nationale: 1877; Vol. 23, 24, p 772.
37. Versteeg, H. K.; Malalasekera, W., Turbulence and its Modelling. In *An Introduction to Computational Fluid Dynamics*, Pearson Education Limited: Harlow, 2007; pp 40-114.
38. Leonard, A. In *Energy cascade in large-eddy simulations of turbulent fluid flows*, Turbulent Diffusion in Environmental Pollution, 1974; 1974; pp 237-248.
39. Ferziger, J. H., Large Eddy Numerical Simulations of Turbulent Flows. *AIAA Journal* **1977,** 15, (9), 1261-1267.
40. Smagorinsky, J., General Circulation Experiments with the Primitive Equations. *Monthly Weather Review* **1963,** 91, (3), 99-164.
41. Lilly, D. K., *On the application of the eddy viscosity concept in the inertial sub-range of turbulence*. National Center for Atmospheric Research: 1966.
42. Peyret, R., Introduction to high-order approximation methods for computational fluid dynamics. In *Advanced Turbulent Flow Computations*, Springer: 2000; pp 1-79.
43. Chen, Q. Y.; Zhai, Z. J., The use of Computational Fluid Dynamics tools for Indoor Environmental Design. In *Advanced Building Simulation*, Malkawi, A. M.; Augenbroe, G., Eds. Spon Press Taylor and Francis Group: 2003.
44. Deardorff, J. W., A numerical study of three-dimensional turbulent channel flow at large Reynolds numbers. *Journal of Fluid Mechanics* **1970,** 41, (02), 453-480.
45. Lilly, D. K. In *The representation of small scale turbulence in numerical simulation experiments*, IBM Scientific Computing Symposium on environmental sciences, 1967; 1967; pp 195-210.
46. Rogallo, R. S.; Moin, P., Numerical simulation of turbulent flows. *Annual Review of Fluid Mechanics* **1984,** 16, (1), 99-137.
47. Nicoud, F.; Ducros, F., Subgrid-scale stress modelling based on the square of the velocity gradient tensor. *Flow, Turbulence and Combustion* **1999,** 62, (3), 183-200.
48. Schumann, U., Subgrid scale model for finite difference simulations of turbulent flows in plane channels and annuli. *Journal of Computational Physics* **1975,** 18, (4), 376-404.

49. Chapman, D. K., Computational aerodynamics development and outlook. *AIAA Journal* **1979,** 17, (12), 1293-1313.
50. Choi, H.; Moin, P., Grid-point requirements for large eddy simulation: Chapman's estimates revisited. *Physics of Fluids (1994-present)* **2012,** 24, (1), 011702.
51. Piomelli, U.; Balaras, E., Wall-layer models for large-eddy simulations. *Annual Review of Fluid Mechanics* **2002,** 34, (1), 349-374.
52. Grötzbach, G., Direct numerical and large eddy simulation of turbulent channel flows. *Encyclopedia of Fluid Mechanics. West Orange NJ* **1987,** 13.
53. Cabot, W.; Moin, P., Approximate wall boundary conditions in the large-eddy simulation of high Reynolds number flow. *Flow, Turbulence and Combustion* **2000,** 63, (1-4), 269-291.
54. Johnson, D. A.; King, L., A mathematically simple turbulence closure model for attached and separated turbulent boundary layers. *AIAA Journal* **1985,** 23, (11), 1684-1692.
55. Spalart, P.; Jou, W.; Strelets, M.; Allmaras, S., Comments on the feasibility of LES for wings, and on a hybrid RANS/LES approach. *Advances in DNS/LES* **1997,** 1, 4-8.
56. Spalart, P. R.; Allmaras, S. R., A one-equation turbulence model for aerodynamic flows. **1992**.
57. Mason, P. J.; Thomson, D., Stochastic backscatter in large-eddy simulations of boundary layers. *Journal of Fluid Mechanics* **1992,** 242, 51-78.
58. Nicoud, F.; Winckelmans, G.; Carati, D.; Baggett, J.; Cabot, W., Boundary conditions for LES away from the wall. *CTR, ARTICLE of the Summer Program* **1998**, 413-422.
59. Redjem-Saad, L.; Ould-Rouiss, M.; Lauriat, G., Direct numerical simulation of turbulent heat transfer in pipe flows: Effect of Prandtl number. *International Journal of Heat and Fluid Flow* **2007,** 28, (5), 847-861.
60. Moin, P.; Mahesh, K., Direct numerical simulation: a tool in turbulence research. *Annual Review of Fluid Mechanics* **1998,** 30, (1), 539-578.
61. Lumley, J. L., Whither Turbulence? Turbulence at the Crossroads. In *Lecture Notes in Physics*, Araki, H.; Ehlers, J.; Hepp, K.; Kippenhahn, R.; Ruelle, D.; Weidenmuller, H. A.; Wess, J.; Zittartz, J., Eds. Springer-Verlag: 1989.
62. Asen, P. O.; Kreiss, G.; Rempfer, D., Direct numerical simulations of localized disturbances in pipe Poiseuille flow. *Computers & Fluids* **2010,** 39, (6), 926-935.
63. Boersma, B. J., Direct numerical simulation of turbulent pipe flow up to a Reynolds number of 61,000. *Journal of Physics: Conference Series* **2011,** 318, (4), 042045.
64. El Khoury, G. K.; Schlatter, P.; Noorani, A.; Fischer, P.; Brethouwer, G.; Johansson, A. V., Direct Numerical Simulation of Turbulent Pipe Flow at Moderately High Reynolds Numbers. *Flow, Turbulence and Combustion* **2013,** 91, (3), 475-495.
65. Jaszczur, M., DNS benchmark solution of the fully developed turbulent channel flow with heat transfer. *Journal of Physics: Conference Series* **2014,** 530, (1), 012022.
66. Ghosh, S.; Sesterhenn, J.; Friedrich, R., DNS and LES of compressible turbulent pipe flow with isothermal wall. In *Direct and Large-Eddy Simulation VI*, Springer: 2006; pp 721-728.
67. Chin, C.; Monty, J. P.; Ooi, A., Reynolds number effects in DNS of pipe flow and comparison with channels and boundary layers. *International Journal of Heat and Fluid Flow* **2014,** 45, 33-40.
68. Del Alamo, J. C.; Jimenez, J.; Zandonade, P.; Moser, R. D., Scaling of the energy spectra of turbulent channels. *Journal of Fluid Mechanics* **2004,** 500, 135-144.
69. Li, Q.; Schlatter, P.; Brandt, L.; Henningson, D. S., DNS of a spatially developing turbulent boundary layer with passive scalar transport. *International Journal of Heat and Fluid Flow* **2009,** 30, (5), 916-929.
70. El Khoury, G. K.; Schlatter, P.; Brethouwer, G.; Johansson, A. V., Turbulent pipe flow: Statistics, Re -dependence, structures and similarities with channel and boundary layer flows. *Journal of Physics: Conference Series* **2014,** 506, (1), 012010.
71. Orszag, S. A.; Patterson Jr, G., Numerical simulation of three-dimensional homogeneous isotropic turbulence. *Physical Review Letters* **1972,** 28, (2), 76.
72. Bell, G. In *A Seymour Cray Perspective*, Seymour Cray Lecture Series, University of Minnesota, 1997; University of Minnesota, 1997.
73. Fasui, A. A.; Olteanu, A.-C.; Tapus, N. In *On using Grid and distributed computing for mobile applications*, Systems and Computer Science (ICSCS), 2013 2nd International Conference on, 2013; IEEE: 2013; pp 92-97.

74. TOP500 The List - November 2015. http://www.top500.org/lists/2015/11/ (16/01/2016),
75. Feiereisen, W. J.; Reynolds, W. C.; Ferziger, J. H. Numerical simulation of a compressible homogeneous, turbulent shear flow. Stanford University, 1981.
76. Blaisdell, G.; Mansour, N.; Reynolds, W., Compressibility effects on the growth and structure of homogeneous turbulent shear flow. *Journal of Fluid Mechanics* **1993,** 256, 443-485.
77. Lee, S.; Lele, S. K.; Moin, P., Eddy shocklets in decaying compressible turbulence. *Physics of Fluids A: Fluid Dynamics (1989-1993)* **1991,** 3, (4), 657-664.
78. Coleman, G. N.; Kim, J.; Moser, R., A numerical study of turbulent supersonic isothermal-wall channel flow. *Journal of Fluid Mechanics* **1995,** 305, 159-183.
79. Rai, M. M.; Gatski, T. B.; Erlebacher, G., AIAA 9590583 Direct Simulation of Spatially Evolving Compressible Turbulent Boundary Layers. **1995**.
80. Brauckmann, H. J.; Eckhardt, B., Direct numerical simulations of local and global torque in Taylor–Couette flow up to Re= 30 000. *Journal of Fluid Mechanics* **2013,** 718, 398-427.
81. Hawkes, E. R.; Chatakonda, O.; Kolla, H.; Kerstein, A. R.; Chen, J. H., A petascale direct numerical simulation study of the modelling of flame wrinkling for large-eddy simulations in intense turbulence. *Combustion and Flame* **2012,** 159, (8), 2690-2703.
82. Chen, J. H.; Choudhary, A.; de Supinski, B.; DeVries, M.; Hawkes, E. R.; Klasky, S.; Liao, W. K.; Ma, K. L.; Mellor-Crummey, J.; Podhorszki, N.; Sankaran, R.; Shende, S.; Yoo, C. S., Terascale direct numerical simulations of turbulent combustion using S3D. *Computational Science & Discovery* **2009,** 2, (1), 015001.
83. Desoutter, G.; Habchi, C.; Cuenot, B.; Poinsot, T., DNS and modeling of the turbulent boundary layer over an evaporating liquid film. *International Journal of heat and Mass Transfer* **2009,** 52, 6028-6041.
84. Saha, S.; Ooi, A. S. H.; Blackburn, H. M., Validation Criteria for DNS of Turbulent Heat Transfer in Pipe Flow. *Procedia Engineering* **2014,** 90, 599-604.
85. Mims, C. Moore's Law Over, Supercomputing "In Triage," Says Expert. http://www.technologyreview.com/view/427891/moores-law-over-supercomputing-in-triage-says-expert/ (16/01/2016),
86. Speziale, C. G. *Analytical methods for the development of Reynolds stress closures in turbulence*; DTIC Document: 1990.
87. Moore, G. E., Cramming more components onto integrated circuits. *Proceedings of the IEEE* **1998,** 86, (1), 82-85.
88. Moser, R. D.; Moin, P., The effects of curvature in wall-bounded turbulent flows. *Journal of Fluid Mechanics* **1987,** 175, 479-510.
89. Rogers, M. M.; Moin, P.; Reynolds, W. C. The structure and modeling of the hydrodynamic and passive scalar fields in homogeneous turbulent shear flow. Stanford University, California, 1986.
90. Spalart, P. R., Direct simulation of a turbulent boundary layer up to R θ= 1410. *Journal of Fluid Mechanics* **1988,** 187, 61-98.
91. Kim, J.; Moin, P.; Moser, R., Turbulence statistics in fully developed channel flow at low Reynolds number. *Journal of Fluid Mechanics* **1987,** 177, 133-166.
92. Le, H.; Moin, P.; Kim, J., Direct numerical simulation of turbulent flow over a backward-facing step. *Journal of Fluid Mechanics* **1997,** 330, 349-374.
93. Akselvoll, K.; Moin, P., Large-eddy simulation of turbulent confined coannular jets. *Journal of Fluid Mechanics* **1996,** 315, 387-411.
94. Mahesh, K.; Lele, S. K.; Moin, P., The influence of entropy fluctuations on the interaction of turbulence with a shock wave. *Journal of Fluid Mechanics* **1997,** 334, 353-379.
95. Chin, C.; Ooi, A.; Marusic, I.; Blackburn, H., The influence of pipe length on turbulence statistics computed from direct numerical simulation data. *Physics of Fluids* **2010,** 22, (11), 115107.
96. Niu, Z.; Jiao, K.; Zhang, F.; Du, Q.; Yin, Y., Direct numerical simulation of two-phase turbulent flow in fuel cell flow channel. *International Journal of Hydrogen Energy* **2016**.
97. Ferziger, J. H.; Peric, M., Finite Difference Methods. In *Computational Methods for Fluid Dynamics*, 3rd ed.; Springer-Verlag: Berlin, 2002; pp 39-70.
98. Spencer, S.; Peiró, J., Finite Difference, Finite Element and Finite Volume Methods for Partial Differential Equations. In *Handbook of Materials Modeling. Volume I: Methods and Models*, Springer: 2005.

99. Lele, S. K., Compact finite difference schemes with spectral-like resolution. *Journal of Computational Physics* **1992,** 103, (1), 16-42.
100. Hirsh, R. S., Higher order accurate difference solutions of fluid mechanics problems by a compact differencing technique. *Journal of Computational Physics* **1975,** 19, (1), 90-109.
101. Liniger, W.; Willoughby, R. A., Efficient Integration Methods for Stiff Systems of Ordinary Differential Equations. *SIAM Journal on Numerical Analysis* **1970,** 7, (1), 47-66.
102. Lermusiaux, P., Lecture 18: Finite Volume Methods. In MIT open courseware: 2011.
103. Welty, J. R.; Wicks, C. E.; Wilson, R. E.; Rorrer, G. L., Conservation of Mass: Control-Volume Approach. In *Fundamentals of Momentum, Heat, and Mass Transfer*, John Wiley and Sons, Inc.: , 2008; pp 34-42.
104. Welty, J. R.; Wicks, C. E.; Wilson, R. E.; Rorrer, G. L., Newton's Secon Law of Motion: Control-Volume Approach. In *Fundamentals of Momentum, Heat, and Mass Transfer*, John Wiley and Sons, Inc.: , 2008; pp 43-62.
105. Welty, J. R.; Wicks, C. E.; Wilson, R. E.; Rorrer, G. L., Conservation of Energy: Control-Volume Approach. In *Fundamentals of Momentum, Heat, and Mass Transfer*, John Wiley and Sons, Inc.: , 2008; pp 63-80.
106. Chen, L., Finite Volume Methods. In University of California-Irvine.
107. Cebeci, T.; Shao, J. P.; Kafyeke, F.; Laurendeau, E., Numerical Methods for Model Hyperbolic Equations. In *Computational Fluid Dynamics For Engineers*, Horizons Publishing Inc.: Long Beach, California, 2005; pp 141-178.
108. Ferziger, J. H.; Peric, M., Finite Volume Methods. In *Computational Methods for Fluid Dynamics*, 3rd ed.; Springer-Verlag: Berlin, 2002; pp 71-90.
109. Andersson, B.; Andersson, R.; Hakansson, L.; Mortensen, M.; Sudiyo, R.; Wachem, B. v., Numerical Aspects of CFD. In *Computational Fluid Dynamics for Engineers*, Cambridge University Press: 2012; pp 24-61.
110. Ferziger, J. H.; Peric, M., Solution of the Navier-Stokes Equations. In *Computational Methods for Fluid Dynamics*, 3rd ed.; Springer-Verlag: Berlin, 2002; pp 157-216.
111. Gilat, A.; Subramaniam, V., Numerical Differentiation. In *Numerical Methods An introduction with Applications Using Matlab*, John Wiley & Sons, Inc.: 2011; pp 211-248.
112. Hussaini, M. Y.; Zang, T. A., Spectral Methods in Fluid Dynamics. *Annual Review of Fluid Mechanics* **1987,** 1, (19), 339-367.
113. Canuto, C.; Quarteroni, A.; Hussaini, M. Y.; Zang, T. A., Polynomial Approximation. In *Spectral methods : fundamentals in single domains*, Springer-Verlag: 2006; pp 39-116.
114. Kreiss, H.-O.; Oliger, J., Stability of the Fourier method. *SIAM Journal on Numerical Analysis* **1979,** 16, (3), 421-433.
115. Canuto, C.; Quarteroni, A.; Hussaini, M. Y.; Zang, T. A., Basic Approaches to Constructing Spectral Methods. In *Spectral methods : fundamentals in single domains*, Springer-Verlag: 2006; pp 117-165.
116. Osgood, B. G., n-Dimensional Fourier Transform. In *EE261 - The Fourier Transform and its Applications*, Stanford Engineering Everywhere: pp 365-402.
117. Patera, A. T., A spectral element method for fluid dynamics: Laminar flow in a channel expansion. *Journal of Computational Physics* **1984,** 54, (3), 468-488.
118. Babuška, I.; Banerjee, U.; Osborn, J. E., Generalized finite element methods—main ideas, results and perspective. *International Journal of Computational Methods* **2004,** 1, (01), 67-103.
119. Limiton An Introduction to Spectral Element Method. http://limiton.cn/upfile/SEM.pdf
120. Bakker, A. Lecture 5 -Solution Methods: Applied Computational Fluid Dynamics. http://www.bakker.org/dartmouth06/engs150/05-solv.pdf
121. Thom, A., The Flow Past Circular Cylinders at Low Speeds. *Proceedings of the Royal Society of London A: Mathematical, Physical and Engineering Sciences* **1933,** 141, (845), 651-669.
122. Torrance, K. E., Comparison of finite-difference computations of natural convection. *Journal of research of the National Bureau of Standards* **1968,** 72, (4), 281-301.
123. Ferziger, J. H.; Peric, M., Methods for Unsteady Problems. In *Computational Methods for Fluid Dynamics*, 3rd ed.; Springer-Verlag: Berlin, 2002; pp 135-156.
124. Gilat, A.; Subramaniam, V., Ordinary Differential Equations: Initial Value Problems. In *Numerical Methods An introduction with Applications Using Matlab*, John Wiley & Sons, Inc.: 2011; pp 293-376.

125. Ferziger, J. H.; Peric, M., Basic Concepts of Fluid Flow. In *Computational Methods for Fluid Dynamics*, 3rd ed.; Springer-Verlag: Berlin, 2002; pp 1-21.
126. Versteeg, H. K.; Malalasekera, W., Solution algorithms for pressure-velocity coupling in steady flows. In *An Introduction to Computational Fluid Dynamics*, Pearson Education Limited: Harlow, 2007; pp 179-211.
127. Iaccarino, G., Solution Methods for the Incompressible Navier Stokes Equations. In Stanford University: 2004.
128. Patankar, S. V.; Spalding, D. B., A calculation procedure for heat, mass and momentum transfer in three-dimensional parabolic flows. *International Journal of heat and Mass Transfer* **1972,** 15, (10), 1787-1806.
129. Issa, R. I., Solution of the implicitly discretised fluid flow equations by operator-splitting. *Journal of Computational Physics* **1986,** 62, (1), 40-65.

3

DNS Codes

3.1. Introduction

To perform DNS, several commercial and non-commercial codes are available. Many researchers also use in-house codes for specific purposes [1-6]. In this chapter, an overview will be given of some available codes. For each code, the numerical methods are discussed, along with some examples for which the code has been used. At the end of this chapter an evaluation is made on which code appears to be most promising to simulate reactive flow in enhanced reactor geometries.

3.2. OpenFOAM

OpenFOAM is an acronym of Open Field Operations And Manipulations [7]. OpenFOAM comprises a large number of solvers, each suitable for different problems. Amongst these is dnsFOAM, which is the solver designed to numerically solve the conservation equations of mass, energy and momentum. OpenFOAM is an open-source code, making it freely accessible/adaptable for any user.

3.2.1. Discretisation Methods

All calculations in OpenFOAM are based on the finite volume discretization method. This makes discretization easy for arbitrarily shaped cells.

The solution variables of the equations are defined at the centre of each cell. The solution is achieved in a segregated, iterative manner. After discretization (and linearization if necessary), a matrix equation is obtained for each equation. It is possible to combine these equations into a single matrix equation. However, in OpenFOAM, the separate matrix equations are solved in sequence, followed by iteration until convergence is attained.

The temporal discretization method used by OpenFOAM depends on the problem. For non-stiff problems, the fifth-order Cash-Karp Runge-Kutta method with error prediction and adaptive time step control is employed, while the stiff problems are solved using a similar, fourth order method. The advantage of Runge-Kutta methods is that they are one step methods and have a well-developed theory for adaptive time steps [8]. A disadvantage of the Runge-Kutta methods is that they require more function evaluations than linear multistep methods [8]. When complex functions are to be evaluated this can be decisive for choosing a different method (e.g. STEP [9]). The method used in OpenFOAM and described by Cash and Karp tries to minimize the amount of function evaluations, resulting in a more time efficient algorithm.

An important aspect of the DNS code is the possibility of parallel computing [10]. To be able to solve the problem on multiple processors, the spatial domain must be divided into subdomains. Time stepping can only be done sequentially. Besides the decomposition of the domain, communication between the different processors is very important. This communication requires additional software, known as message passing

interface software (MPI) [11]. OpenFOAM provides such software, though it is possible to use own MPI software as well.

OpenFOAM is not frequently used for direct numerical simulations. However, some research has been carried out using OpenFOAM. Some cases in which OpenFOAM has been used, are discussed in the following paragraphs.

3.2.2. Zhang et al.: Flame Propagation Velocity

Zhang et al. investigated the laminar burning velocities of one- and three-dimensional flames [12]. Simulating reactive flows requires the addition of a balance for all species. A challenge in simulating reactive flows is the time step requirements. In paragraph 2.5.4 it is mentioned that the time step should be smaller than the smallest turbulent time scales ($\mathcal{O}(10^{-5}\ s)$). When reaction is to be simulated directly as well, the time step must be smaller than the time scale of reaction. The time scale of reaction can be much smaller than the Kolmogorov time scales, by more than three orders of magnitude. To deal with this problem, the chemistry is calculated using the Cantera [13] software. A one-dimensional flame is simulated to validate the solution method, with good results. The three-dimensional case simulates a hydrogen/air flame with an inlet equivalence ratio of 0.33, an inlet temperature of 300 K and an inlet pressure of 1 bar. Weiβ designed an experimental set-up to determine the flame propagation velocity [14]. To compare the DNS results with experimental data, the mesh is constructed similar to this setup. It is assumed that there are two planes of symmetry in the problem, reducing the simulation domain to a quarter of a sphere (Figure 3-1). The diameter of the spherical domain is 8 cm. The central cells have a volume of 10^{-12} m^3. The cell volume is a function of the radial coordinate and increases towards the outside. In total there are approximately 144 million cells and the time step is 0.4 μs.

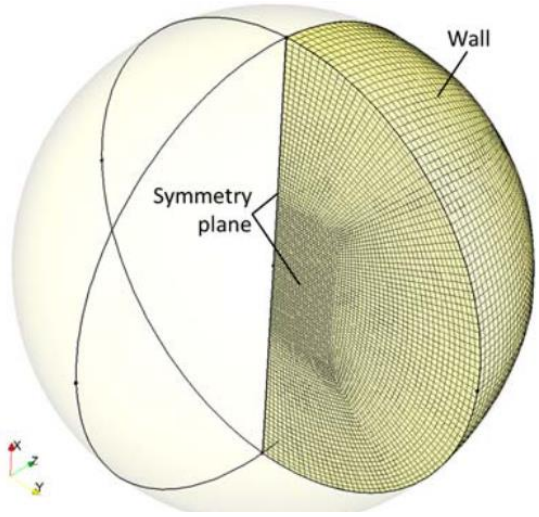

Figure 3-1: Mesh for the simulation of a spherical flame [12].

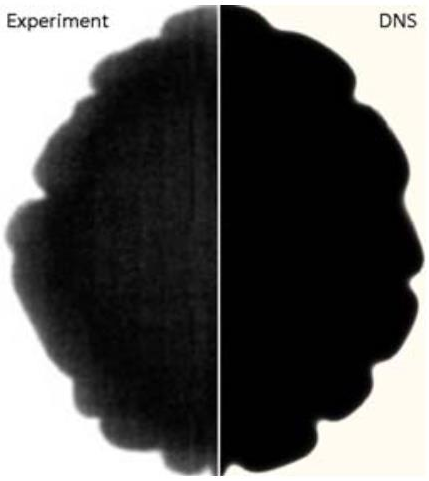

Figure 3-2: Comparison of the experimental and numerical flame fronts in a spherical vessel [12].

Figure 3-2 indicates a very good qualitative agreement between the simulated and measured flame front geometries. The laminar flame propagation velocities are also found to be quantitatively very similar. To truly judge the performance of the OpenFOAM-Cantera coupled solver, statistical properties of the solution should be compared to the experimental ones.

3.2.3. van Haren: DNS Capability of OpenFOAM

Van Haren investigated the capability of OpenFOAM to perform DNS [15]. He simulated both pipe and channel flow at Reynolds numbers (based on the friction velocity) in the range 150-180. An important aspect of the simulations is the assumption of periodicity in the streamwise direction. In non-isothermal and non-isobaric flows however, periodicity of temperature and pressure is not possible. Heat transfer through the wall will result in an increase or decrease of the fluid temperature, while a decrease in pressure is always present to compensate for the energy losses due to friction. The solution used by van Haren, is to split both temperature and pressure fields into a periodic part and a non-periodic part [15].

$$P = P_{per} + \frac{\Delta P}{L} x \tag{3-1}$$

$$T = T_{per} + \frac{\Delta T}{L} x \tag{3-2}$$

Based on a balance of forces, it is found that the pressure gradient is constant (as function of the streamwise coordinate) and hence the pressure can be written as in eq. (3-3). The temperature is somewhat more complex. A similar expression as for the pressure is found by assuming a constant heat flux trough the wall. The temperature change throughout the domain is, however, linked to the heat flux and thermal properties of the fluid, resulting in eq. (3-4). The respective expressions for pressure and temperature are then substituted into the momentum and energy balances.

$$P = P_{per} + \frac{dP}{dx} x \tag{3-3}$$

$$T = T_{per} + \frac{2\dot{q}_w}{H\rho c_p v_{bulk}} x \tag{3-4}$$

For pipe flow, the DNS results from OpenFOAM are compared to benchmark data from Saad [16], Eggels [17] and Fukagata-Kasagi [18]. These cases simulate pipe flow at low Reynolds numbers and on small domains, making them very feasible on current high performance computers.

Figure 3-3 and Figure 3-4 show velocity and shear stress results in the near wall region. Both velocity and shear stress show a good agreement with the benchmark simulations. This indicates that the dnsFOAM solver is adequate for DNS.

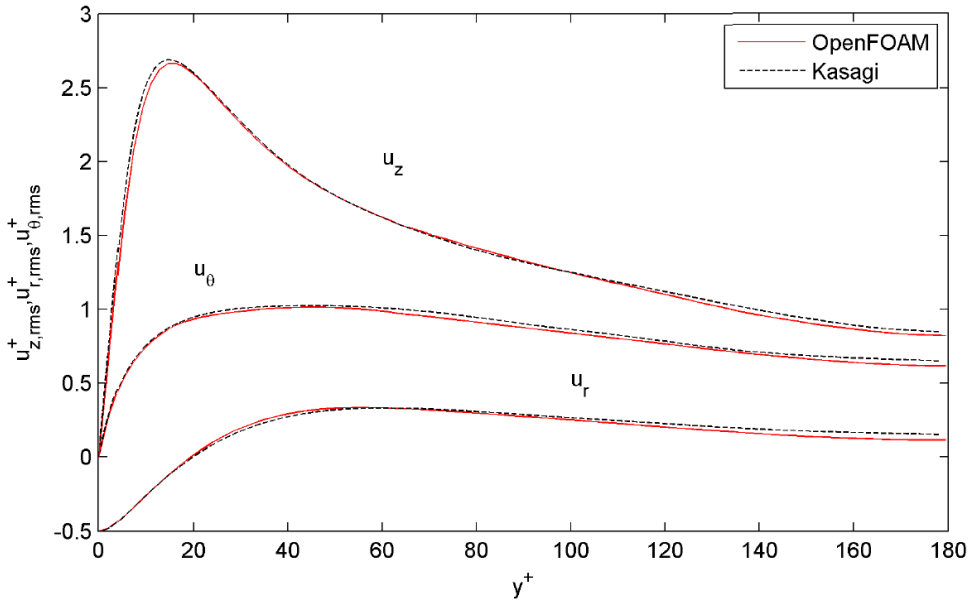

Figure 3-3: Root-mean-square values of the wall-normalized velocities, as function of the wall distance for pipe flow at $Re_\tau = 180$ [15, 18].

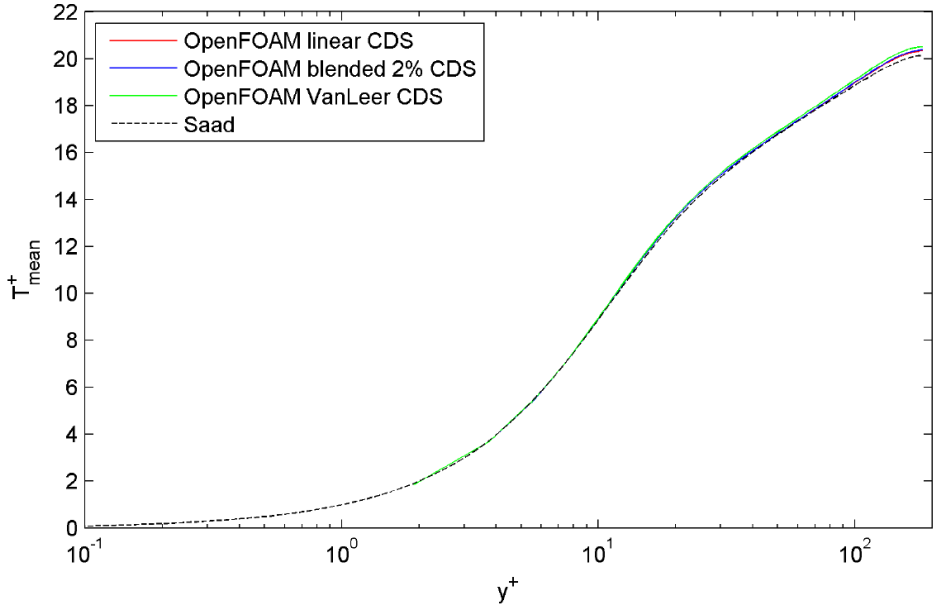

Figure 3-4: Mean value of the wall-normalized shear stress as function of the wall-distance, using different central differencing schemes (CDS) in OpenFOAM, for pipe flow at $Re_\tau = 180$ [15, 16].

Van Haren also simulated turbulent mixing in a T-junction. The bulk-Reynolds number at both inlets is 2188, the bulk-Reynolds number at the outlet is thus 4376. The simulation times are quite short to reduce the computational time, resulting is inaccurate average values [15]. A similar case has been studied by Fukushima [19]. Contrarily to van Haren, Fukushima used square pipes, with different diameters. There are however some qualitative similarities that strengthen the confidence in the OpenFOAM results. At the lowest simulation time in Figure 3-6, a small back-flow zone can be distinguished, as can be seen in Figure

3-5. The interface between the two mixing flows is very smooth in the van Haren case. The Fukushima case shows that the interface becomes increasingly turbulent at longer simulation times, indicating that such a smooth surface is not impossible at low simulation times and lower Reynolds numbers. Finally, both cases show that the interface becomes increasingly unstable farther downstream of the T-junction.

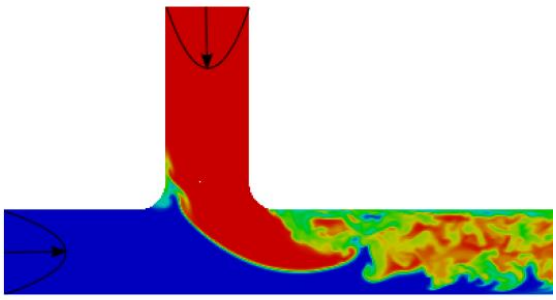

Figure 3-5: Normalized temperature profile (red=1, blue=0) in a T-junction, $Re_{b,inlet} = 2188$ [15].

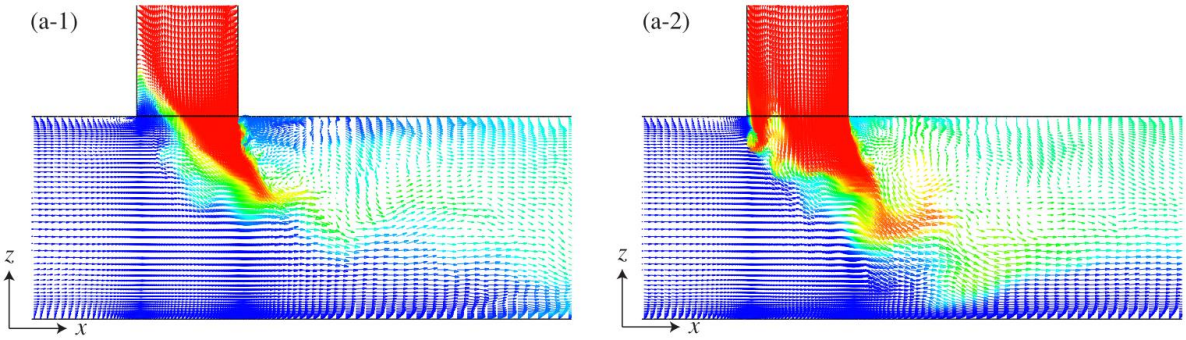

Figure 3-6: Normalized temperature profiles (red=1, blue=0) and velocity vectors in a T-junction, $Re_{b,inlet} = 4485$. Left: at t=16.1 s; Right: at t=19.0 s [19].

3.3. Nek5000

Nek5000 is a spectral element code, developed by Argonne National Laboratories since 1996 [20]. The code is open-source and can be used for a wide variety of flows, such as incompressible wall bounded flows, low Mach number, compressible flows and combustion. The code can efficiently run in parallel on over 200,000 separate processors.

3.3.1. Discretisation Methods

As mentioned above, Nek5000 uses the spectral element method based on the Legendre polynomials for spatial discretisation. The main concepts of the SEM have been discussed in paragraph 2.5.3, the main strength of the SEM is the absence of numerical diffusion, which is crucial in stability calculations, high Reynolds numbers or long simulation times [21]. For time advancement, a semi-implicit method is used [22]. The viscous terms of the Navier-Stokes equations are treated using an implicit third order backward differencing scheme, while the non-linear terms make use of an third order extrapolation scheme.

3.3.2. El Khoury: Turbulent Pipe Flows

El Khoury et al. investigated turbulence in pipe flow for several different Reynolds numbers and geometries [22, 23]. He studied the three so-called canonical flows, namely the pipe, the channel and the spatially evolving boundary layer. The pipe has a length of 25R. The length of the pipe is an important parameter of the simulation. The pipe should be sufficiently long to capture all relevant turbulent structures, but not too long as not to increase the computational time unnecessarily [24]. With increasing Reynolds number, the size of the domain must increase to capture all structures. The length of 25R is taken to be sufficient to capture all structures up to $Re_\tau = 1000$.

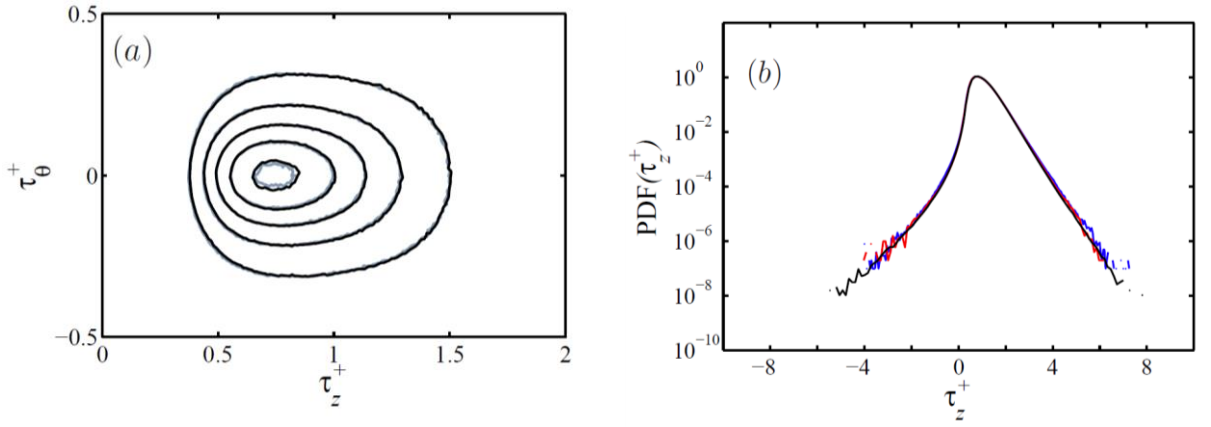

Figure 3-7: (a): Joint-PDF of the wall shear stress in axial/stream wise (τ_z^+) and azimuthal/span wise (τ_θ^+) directions for pipe (black) and channel (grey) flow at $Re_\tau = 1000$. (b): PDF of the wall shear stress in stream wise direction for pipe (black), channel (red) and boundary layer (blue) flow at $Re_\tau = 1000$. Pipe by El Khoury [23], channel by Lenaers [25], and boundary by Schlatter [26].

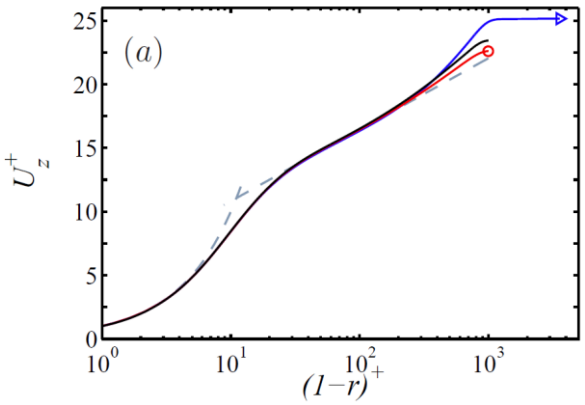

Figure 3-8: Stream wise mean velocity as function of the distance to the boundary surface for pipe (black), channel (red) and boundary layer (blue) flow at $Re_\tau = 1000$. Pipe by El Khoury [23], channel by Lenaers [25], and boundary by Schlatter [26]. The grey dotted lines correspond to the universal law of the wall.

Comparing the different geometries in the near-wall region shows that, in the viscous sub-layer, the behaviour of the flow is independent of the geometry. This is illustrated in Figure 3-7. For all three geometries, the PDFs of the wall shear stresses coincide nearly perfectly. It should be noted that the

Reynolds numbers are approximately one order of magnitude higher than those in the cases discussed in section 3.2. Obviously, farther away from the wall, differences start appearing between the different cases. An illustration of this observation is given in Figure 3-8, where the streamwise mean velocity is equal for all geometries up to a dimensionless wall distance of approximately 100. Up to the same distance, the universal law of the wall is also followed with excellent precision.

Another aspect of the flow that is investigated is the turbulent kinetic energy (TKE) budget. The TKE is defined as half of the sum of the diagonal terms of the Reynolds stress (eq. (3-5)). The budget of the TKE is given by eq. (3-6), and is no more than the balance for the TKE, with the terms on the right hand side expressing production, diffusion due to pressure, viscosity and turbulence and dissipation.

$$k = \frac{\sum_i \overline{u_i^2}}{2} \tag{3-5}$$

$$\frac{Dk}{Dt} = P^k + \Pi^k + D^k + T^k + \varepsilon \tag{3-6}$$

The TKE budget of the three geometries can be visualised as function of the distance to the wall. As was the case with the wall shear stress and average velocity, the TKE budget of all three cases is quasi identical both at low and high Reynolds numbers, as can be seen in Figure 3-9.

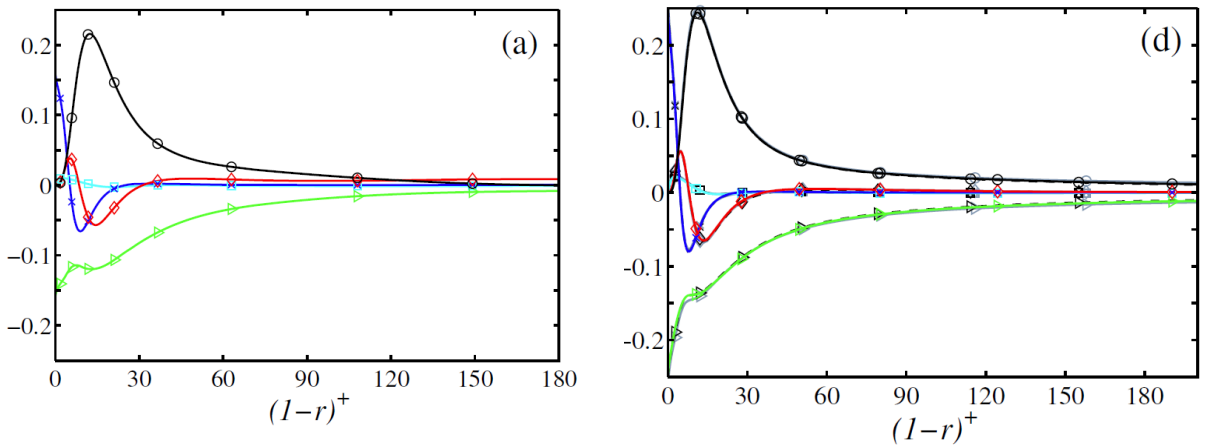

Figure 3-9: TKE budget at different Reynolds numbers (a): $Re_\tau = 180$, (d): $Re_\tau = 1000$. In (d) the data for channel (dotted) and boundary layer (grey) flows are also included. Black: P^k, green: ε, light blue: Π^k, dark blue: D^k, red: T^k [22]. Channel by Lenaers [25] and boundary by Schlatter [26].

It is observed that close to the wall viscous diffusion and viscous dissipation of TKE dominate, which is to be expected as close to the wall viscous effects are dominant. Within the buffer layer, which is the transitional zone between the laminar sublayer and the turbulent boundary layer, a peak in TKE production is observed. In this area, a net production of TKE is observed. Balance of TKE is maintained via the negative turbulent and viscous diffusion. Towards the bulk, most terms tend to zero, except for production and dissipation, which balance each other.

3.3.3. Sprague: Comparison to OpenFOAM

Sprague made a very informative comparison between OpenFOAM and Nek5000, based on the simulation of turbulent channel flow [27] and benchmarked against data from Kim, Moin and Moser (MKM) [28]. As mentioned in paragraph 3.2.1, OpenFOAM uses a FVM, which is typically second order accurate. Contrarily, Nek5000 uses a SEM, which is characterised by high order (spectral) accuracy. The main points on which the performance of the two codes is evaluated are the accuracy for a given spatial grid and the solution time required for a given accuracy.

The simulated channel comprises two parallel, infinite plates. The distance between the plates is 2δ (y-dimension), in the x-dimension the domain has a length of 4πδ and in the z-dimension of 2πδ. The Reynolds number is 2800 and three different mesh resolutions are used. Due to the difference between SEM and FVM, the exact number of grid points is not the same for both codes. For OpenFOAM, the low resolution mesh comprises 48 x 32 x 40 cells, the medium resolution mesh 96 x 64 x 80 and the high resolution one 192 x 130 x 160. In Nek5000, the meshes consist of 7 x 4 x 6, 14 x 9 x 11 and 27 x 18 x 23 cells respectively, with each cell using 7 base functions. This implies that in Nek5000 the actual number of 'grid points' is 50 x 29 x 43, 99 x 64 x 78, 190 x 127 x 162, respectively, or roughly the same amount as in OpenFOAM.

In Figure 3-10 the superior accuracy of Nek5000 is illustrated by the frictional velocity. To achieve the same level of accuracy as with Nek5000, around twice as many grid points are required in a single direction in OpenFOAM. This implies that in three dimensions, around eight times (or about one order of magnitude) more grid points are necessary in OpenFOAM.

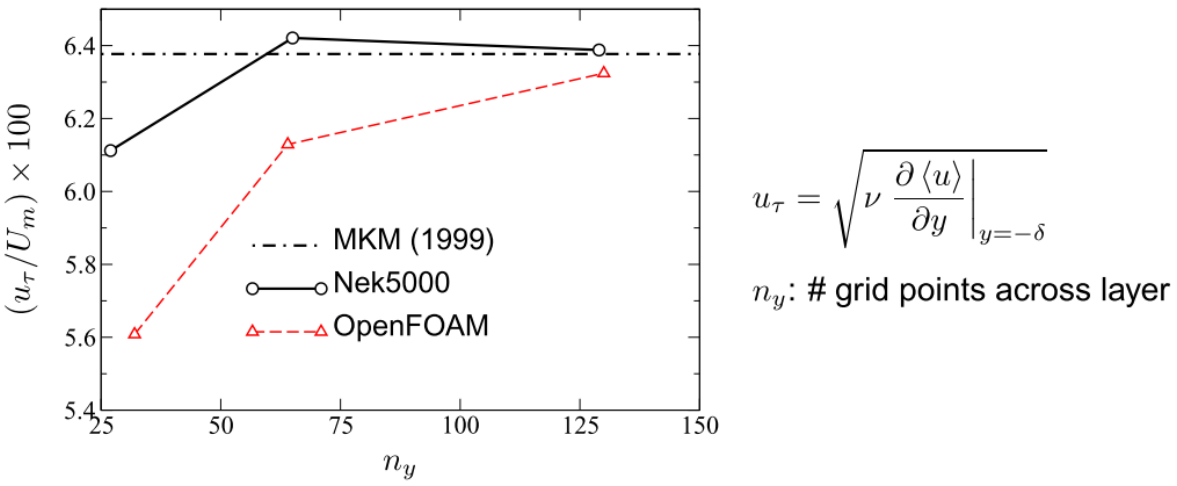

Figure 3-10: Comparison of the friction velocity in channel flow at $Re = 2800$ [27]. $\langle u \rangle$ is the time averaged velocity (denoted by $\bar{u}$ elsewhere).

The high accuracy of Nek5000 is further illustrated in Figure 3-11 for the RMS velocity fluctuations. With Nek5000, the benchmark data are simulated with good approximation even with the medium resolution mesh, while in OpenFOAM even the high resolution mesh still has noticeable deviations from the benchmark.

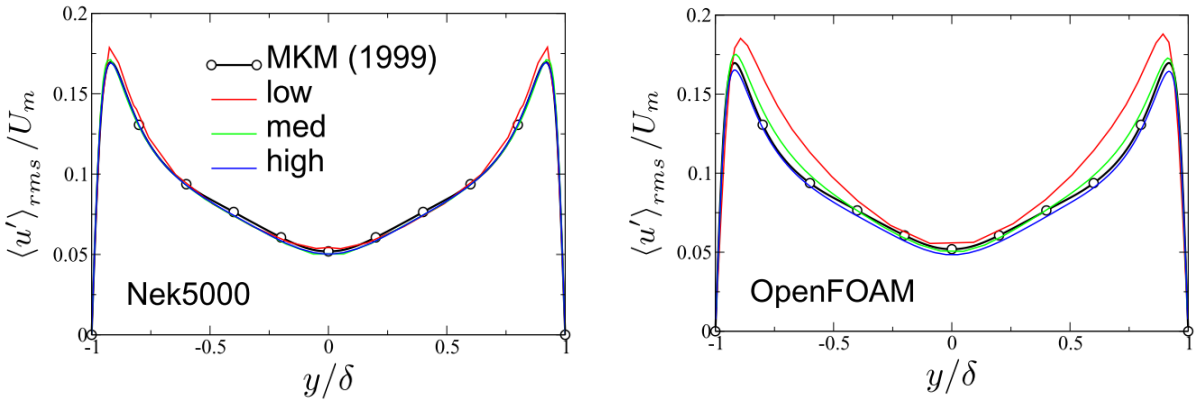

Figure 3-11: Comparison of the RMS velocity fluctuations over the height of the channel, using different mesh resolutions, $Re = 2800$ [27].

The second aspect on which the codes were compared is the time required to achieve a certain accuracy. Here a grid with approximately the same number of grid points is used in both codes $\approx 10^7$. Both codes are found to scale very well for more than 40,000 grid points per core. For the given resolution, there is only a slight difference in wall clock times for the two codes. However, considering the previous comparison, in Nek5000 the same accuracy as in OpenFOAM is with an order of magnitude less grid points, meaning that the computational time required to achieve a predetermined accuracy is significantly lower in Nek5000 than in OpenFOAM.

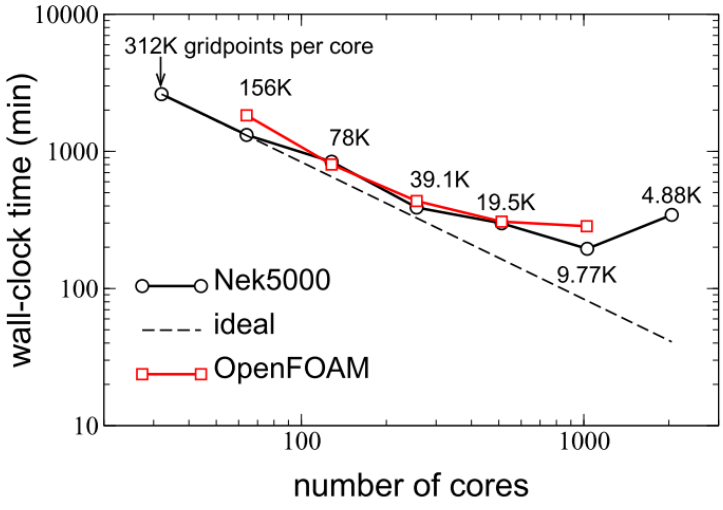

Figure 3-12: Scaling of the two codes and wall clock time [27].

3.4. S3D

S3D is a DNS code that has been purposefully developed by Sandia National Laboratories to simulate turbulent combustion of compressible flows on large numerical domains [29, 30]. Contrarily to the two previously discussed codes, S3D is not an open-source code and therefore not available to the general public.

3.4.1. Discretisation Methods

S3D uses an eighth order finite differencing method for discretisation of the first order spatial derivatives. The second order spatial derivatives are approximated as repetitive application of a first order derivative [30]. The use of finite differencing limits the use of S3D to structured meshes and therefore simple geometries [31]. Time integration is done via a fourth order, explicit Runge-Kutta method [29]. S3D is dedicated to reactive DNS and while this can provide a wide variety of useful information, introducing chemical reactions to the simulation results in an even greater separation of time and length scales. A major strength of the S3D code is its excellent scaling and parallelisation. The code has been adapted to allow GPU (graphics processing unit) accelerated computations [30]. The advantage of GPU accelerated computations over pure CPU computations is that a GPU is optimised for parallel (matrix) operations, while a CPU is optimised for sequential operations. Having computationally intensive matrix operations performed on GPU instead of CPU can significantly reduce the wall time of the simulation [32]. This is illustrated in Figure 3-13 for the scanning of a number of elements.

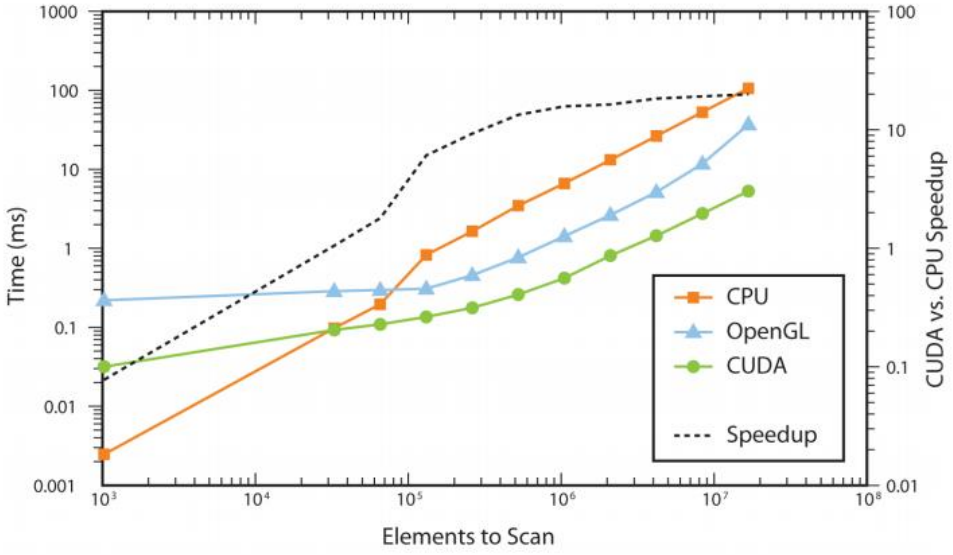

Figure 3-13: Scanning performance enhancement by using GPU computation [32].

3.4.2. Chen et al.: Terascale DNS of Turbulent Combustion

Chen et al. studied the turbulent combustion of hydrogen/air and methane/air flames, including detailed chemistry [33]. Two types of flames are investigated, namely a lifted flame (non-premixed) and a turbulent premixed flame.

The goal of the simulation of the lifted flame is to determine the main mechanism behind the stabilisation of the flame. This stabilisation is important in numerous practical applications such as spark ignition engines and diesel engines [34]. The domain is set up as follows. Fuel – a 65-35 vol% hydrogen-nitrogen mixture – enters via a central jet. This central jet is surrounded by co-flowing air at 1100 K. This temperature ensures that the upstream mixture is auto-ignitable. The size of the domain is 2.4 x 3.2 x 0.64 cm and comprises 1600 x 1372 x 430 ($\approx 10^9$) grid points. The Reynolds number of the jet is 11,000. The time step is set at 4 10^{-9} s and the solution is run for just under 10^{-3} s (approximately 250,000 time steps). The scale of this simulation immediately becomes apparent when comparing to previously discussed cases. This is also seen in the computational time required to obtain the solution, 3.5 million CPU-hours on a 50 Tflop supercomputer.

The simulations show that the temperature first increases in fuel-lean mixtures (*i.e.* low mixture fractions) before shifting towards richer mixtures (higher mixture fractions). An illustration hereof is given in Figure 3-14. This behaviour indicates that ignition occurs first where the ignition delay is the shortest, *i.e* where the temperature is high and the mixture is lean. It was consequently concluded that the main mechanism for flame stability is auto-ignition.

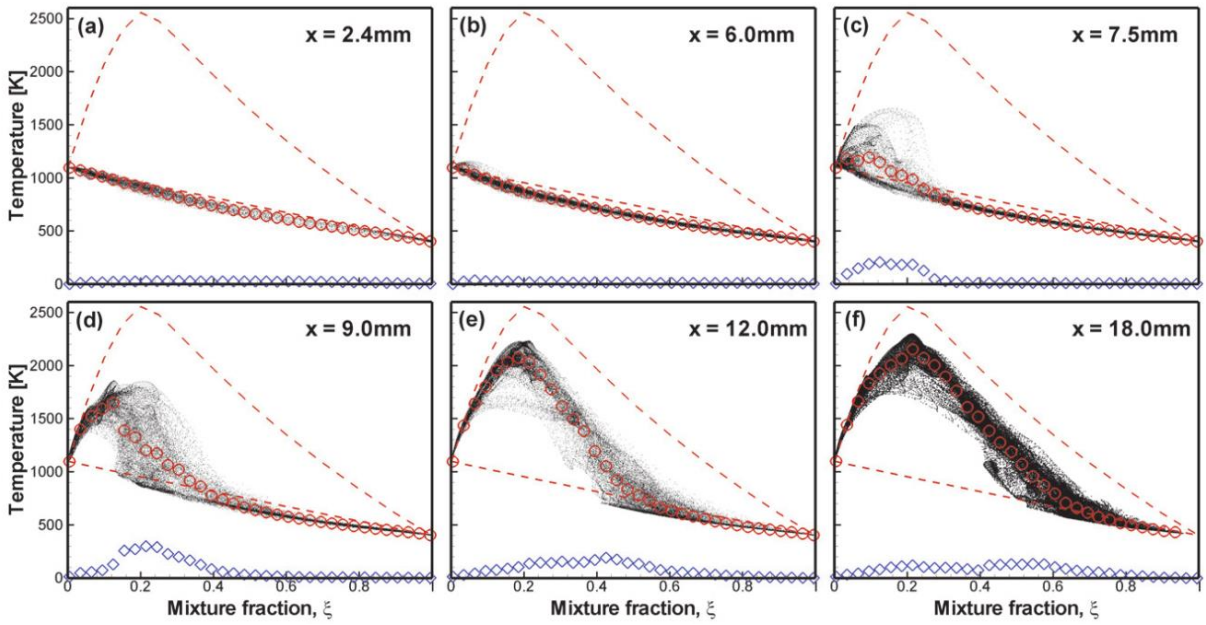

Figure 3-14: Scatter plots of temperature as function of mixture fraction at different axial positions. The open circles represent the mean temperature, the blue diamonds represent the standard deviation of the temperature [33].

Secondly, the premixed turbulent flame is simulated. The aim hereof is to determine how turbulence affects the flame structure as contradictory experimental results have been reported considering the thickening of the flame as a result of the combined effect of entrainment of small eddies and large-scale straining [35, 36]. In this case a Bunsen flame with detailed methane/air chemistry is simulated. Different cases are simulated with different domain sizes, but in all cases the domain comprise an order of magnitude less gird points. The premixed jet is at 800 K and a mixture equivalence ratio of 0.7. The effect of turbulence is investigated by altering the domain size and turbulence characteristics of the inflow. It was found that up until a critical inflow turbulence intensity, flame thickening occurs, while increasing the turbulence intensity beyond the critical value does not result in further thickening of the flame.

3.5. SIMSON

SIMSON is an acronym for pseudo-Spectral solver for IncoMpreSsible bOuNdary layer flows [37]. The name comprises the properties of the code. It is based on a spectral method and is suited for incompressible flows where a boundary layer is present, e.g. channel or pipe flow. SIMSON is again an open-source code.

3.5.1. Discretisation Methods

Spatial discretisation in SIMSON is based on a spectral method, quite similar to the Fourier-Chebyshev method used by Kim [28]. Temporal discretisation uses one of two possible semi-implicit schemes. The linear diffusion terms are discretised by a second order, implicit Crank-Nicholson scheme [38]. The Crank-Nicolson scheme can be seen as an average of the forward (explicit) and backward (implicit) Euler methods [39]. The non-linear terms of the Navier-Stokes equations are discretised in time via a third order Runge-Kutta scheme.

3.5.2. Schlatter et al.: Near-Wall and Boundary Layer Effects

Schlatter et al. investigated near-wall and boundary layer turbulence effects in various cases [26, 40]. A first case that is investigated is turbulence in a boundary layer [26]. The obtained data from this case have been used by El Khoury as a comparison to pipe flow turbulence [23]. The simulations are carried out on 3072 x 301 x 256 spectral collocation points. Only the terascale simulations using S3D use a higher number of points [33]. However, the Reynolds numbers here are much lower than in the case by Chen et al. The momentum thickness and free-stream velocity-based Reynolds number is at most around 2500. The momentum thickness is a measure for the boundary layer thickness and is defined as the distance that a surface must be moved parallel to itself in an inviscid fluid (*i.e;* a constant velocity profile), towards a reference plane, such that the momentum of this hypothetical situation is equal to the momentum in the true fluid [41]. This concept is illustrated in Figure 3-15. The momentum is proportional to the surface of the velocity profile. Hence the position of θ is always such that the blue shaded areas above and below θ are equal.

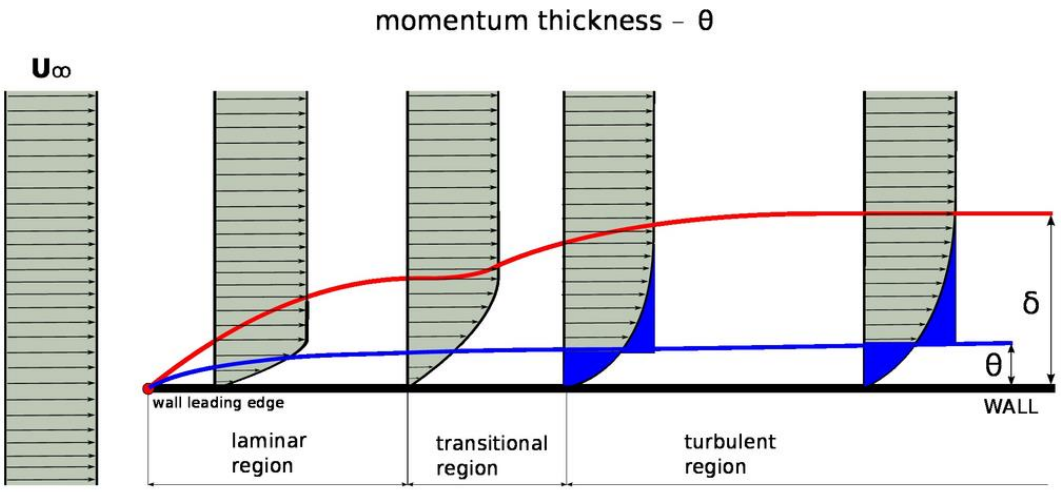

Figure 3-15: Illustration of the concept momentum thickness. The reference plane is typically at δ (the boundary layer thickness) which is the location at which the velocity is 99% of the bulk velocity [41].

A second case focusses on near-wall effects such as negative streamwise velocities, as their presence was debated [40]. Several different cases with different Reynolds numbers, grid spacings and domain sizes are simulated. The Reynolds number (based on the frictional velocity at the wall) ranges from 180 over 590 to 1000. For the highest Reynolds number, a single grid spacing is used, while for the other two, two cases are set up with different resolution. It is found that the different grid resolutions have only a minor impact on the accuracy of the results as the statistics of the streamwise velocities and the wall shear stress are found to be nearly identical. This can be seen in Figure 3-16, where the dotted and full lines are quasi indistinguishable. Only on investigating the occurrence of the negative velocities, some differences are observed between the different resolutions.

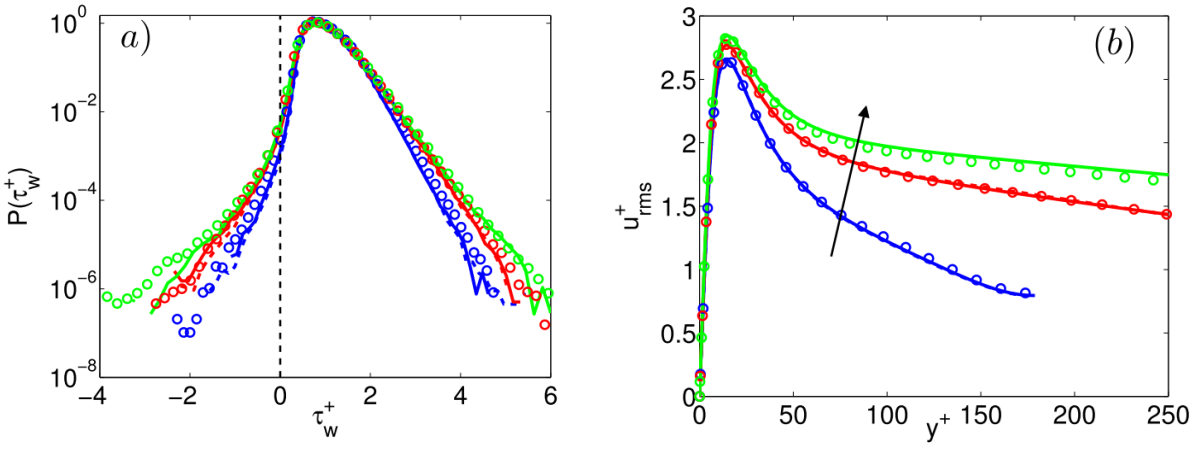

Figure 3-16: (a): PDF of the wall shear stress. (b): RMS of the velocity fluctuations. Full lines are the cases with the lowest resolution, dotted lines are the cases with the highest resolution [40]. Green: $Re_\tau = 1000$, red: $Re_\tau = 590$, blue: $Re_\tau = 180$. The circles are DNS data from Schlatter [42] and del Alamo [43].

An important parameter in analysing DNS data, that is explicitly mentioned in this study is the flatness factor [40]. Similarly to the mean, standard deviation and root mean square of a variable, the flatness factor is

a parameter that characterises a PDF. The flatness factor is defined as per eq. (3-7). This links the flatness factor to another statistical parameter, namely the kurtosis, which is $F-3$ [44], though the terminations are sometimes used interchangeably. The kurtosis is a measure for the contribution of extremes to the tailing behaviour of the distribution of a variable. Therefore, in the context of turbulence, a high kurtosis or a high flatness factor indicates that 'extreme' instantaneous velocities are present. In search of negative instantaneous streamwise velocities, a high flatness factor can be seen as an encouraging sign for their existence. Indeed, the simulations have shown that in the near wall region, for Reynolds numbers from 180-1000, a small percentage of flow reversal of between 0.01 % and 0.06 % is found. Depending on the Reynolds number, the region with flow reversal extends farther into the fluid [40].

$$F(v)=\frac{\overline{v'^4}}{v_{RMS}^4}=\frac{\overline{(v-\bar{v})^4}}{\overline{(v-\bar{v})^2}^2} \tag{3-7}$$

As the flatness factor is determined via time averaging, it is expected that its value will vary over time. This metric can be used to assess how long it takes for the simulated turbulence to reach statistical steady-state. This is illustrated in Figure 3-17, which indicate a transient zone for both velocity, velocity fluctuations and flatness factors. When using more than 2500 independent points (time steps), the statistical properties of the variables become more or less constant, indicating that the turbulent flow was averaged for a sufficiently long period of time to reach statistical steady-state.

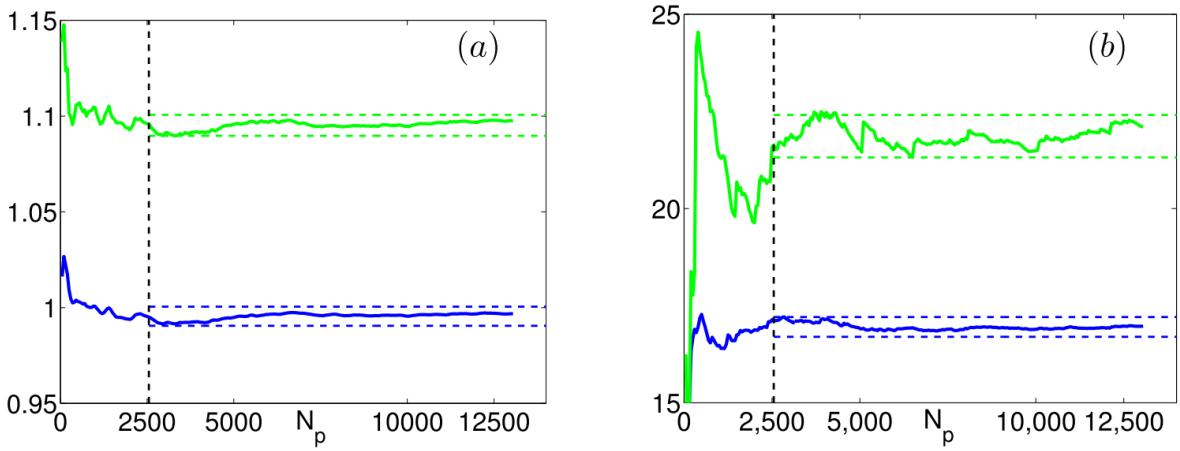

Figure 3-17: (a) Evolution of the RMS stream wise velocity fluctuation (green, scaled by a factor 3 for clarity) and average stream wise velocity (blue), the dotted horizontal lines indicate the 0.5 % confidence interval. (b) the flatness factor for the stream wise velocity (blue, scaled by a factor 4) and the velocity normal to the wall (green). The dotted lines represent the 1.5 % and 2.5 % confidence intervals respectively [40].

3.5.3. Ohlsson: Comparison between Nek5000 and SIMSON

Ohlsson et al. [45] compared Nek5000 to SIMSON based on criteria quite similar to those used by Sprague (see paragraph 3.3.3) and using the DNS data from Moser et al. [46] as benchmark [27]. The two criteria are wall-time per time step and number of grid points required to achieve a given accuracy. In this case channel

flow is also used as base for comparison and the Reynolds number based on the frictional velocity is 180. The simulations are performed for a wide range of resolutions. The resolution of the grid is expressed in degrees of freedom (DOF), the number of grid points is proportional to the third power of the DOF. Due to the slightly different characteristics of the two codes, it is not possible to exactly match the DOF in both cases. For SIMSON, the DOF ranges from 24 to 160, for Nek5000 from 29 to 155.

For the small scale case and on a single core, SIMSON is found to significantly outperform Nek5000 in terms of efficiency. A solution is obtained 4-6 times faster when considering wall-time per iteration and up to 20 times faster when the wall-time per unit of simulation time is examined. The latter is linked to the more strict time step restrictions in the SEM. Additionally, the difference increases as the size of the system increases, which is linked to the favourable properties of the fast Fourier transform (FFT) used by SIMSON.

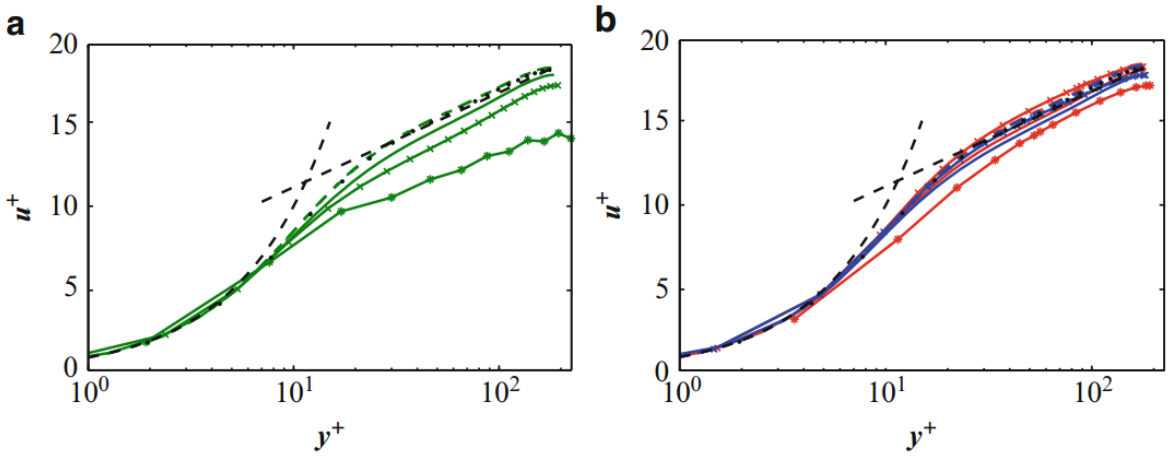

Figure 3-18: Average velocity profiles in channel flow at $Re_\tau = 180$ by SIMSON (a) and Nek5000 (b) red: 7th order, blue 11th order [45]. DOF increases from star-crossed-full-dashed-dotted dashed lines.

Figure 3-18 indicates that accurate simulation of the flow is achieved for a lower resolution in Nek5000 than for SIMSON, though the general trend is the same. The accuracy of the code depends on the parameter that is investigated though. The Reynolds stresses are consistently over-predicted by Nek5000, while SIMSON manages to give good approximations, even for the lower resolution cases. For the pressure fluctuations, quite similar accuracies are achieved, though SIMSON has higher accuracy near the wall, while Nek5000 has higher accuracy in the bulk.

It can be concluded that both codes achieve accurate results, each having slightly higher accuracy than the other for different parameters. The spectral code SIMSON is, however found to be significantly faster than the SEM code Nek5000. However, one should keep in mind that efficiency on a single core does not indicate efficiency on multiple parallel cores. In such a case, Nek5000 would be hugely advantaged as decomposition of the SEM domain is readily achieved as each element behaves spectrally, while for a spectral domain this is much more difficult. Also, the spectral method is only very efficient in the canonical flows. In more complex geometries it is much more advantageous to use the more flexible SEM code.

3.6. Gerris

As most of the codes discussed in this work, Gerris is an open-source code. It can be used to solve the time dependent, incompressible Navier-Stokes Equations with second order accuracy in time and space [47]. Gerris was developed at the National Institute of Water and Atmospheric Research in New Zealand. Therefore, it may not perform optimally for pipe- and other wall bounded flows. However, it uses some peculiar methods for discretisation which make it worth discussing here.

3.6.1. Discretisation Methods

The spatial discretisation in Gerris is based on the finite volume method, using square or cubic volumes and cell centred values. In classic FVM, on a structured mesh, the volumes are sequentially numbered via two or three indices in two or three dimensions respectively. This has been illustrated in Figure 2-13. In Gerris, the volumes (or cells) are structured via a hierarchical tree structure, known as a quadtree (in 2D) or octree (in 3D) [48]. Each cell, corresponding to a node in the tree structure can have a parent node and up to four and in 3D eight children. The root cell has no parent, while the leaf cells have no children. The level of a cell is defined as the amount of times a group of four children has been added, starting from zero at the root. This method must comply with some requirements to work efficiently [47]. While not of fundamental importance, these requirements allow further reduction of the amount of operations required during the simulation. A first requirement is that the level of directly neighbouring cells should not differ by more than one nor should the level of diagonally neighbouring cells. A second is that all cells neighbouring a so-called mixed cell should be of the same level. When irregular solid boundaries are present, it is inevitable that these will cut through certain cells. These cells are called mixed cells.

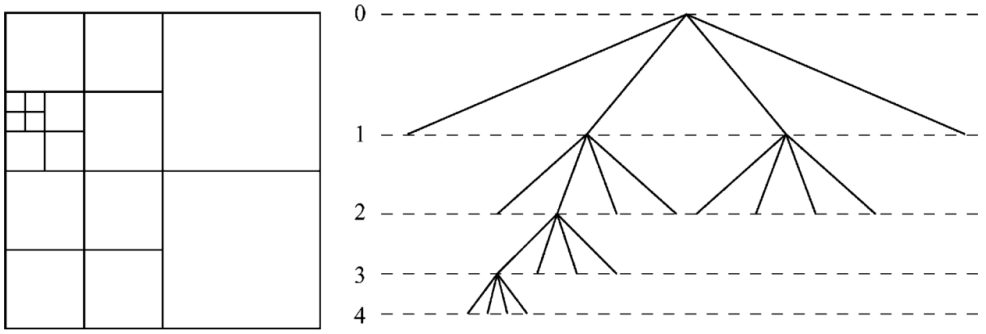

Figure 3-19: (left) Mesh structure and (right) corresponding hierarchical tree structure to organise the cells [47].

The tree-based cell hierarchy used in Gerris allows the number of operations required to access cell levels and coordinates to be reduced from $\mathcal{O}(N)$ to $\mathcal{O}(1)$, *i.e.* independent on the number of cells. The number of operations for the transversal of all cells becomes $\mathcal{O}(N \log N)$.

Time discretisation in Gerris in done via a second order, fractional-step projection method [47]. This method differs quite substantially from the typically used Runge-Kutta methods. They employ three concepts, being an approximation of the pressure gradient term, a formula to update the global pressure during time stepping and appropriate boundary conditions [49]. The method starts from a time-discrete semi-implicit form of the Navier-Stokes equations. However, instead of solving this equation as such, the velocity field at the advanced time step is replaced by an intermediate velocity field and the mass equation is replaced by a specific boundary condition on the intermediate velocity field, implying that this is not necessarily divergence-free. The next step, after solving the obtained equations for the intermediate velocity field, is projecting the field on the divergence-free space, resulting in the actual velocity field. The final step of the method is updating the pressure, which is not determined at time step n, but at time steps $n + 1/2$. These three steps illustrate the importance of the three concepts mentioned above. A detailed description of projection methods is given by Brown [49]. Full details of the different approximations and operations used in Gerris are given by Popinet [47].

3.6.2. Agbaglah: Multi-Phase Flows

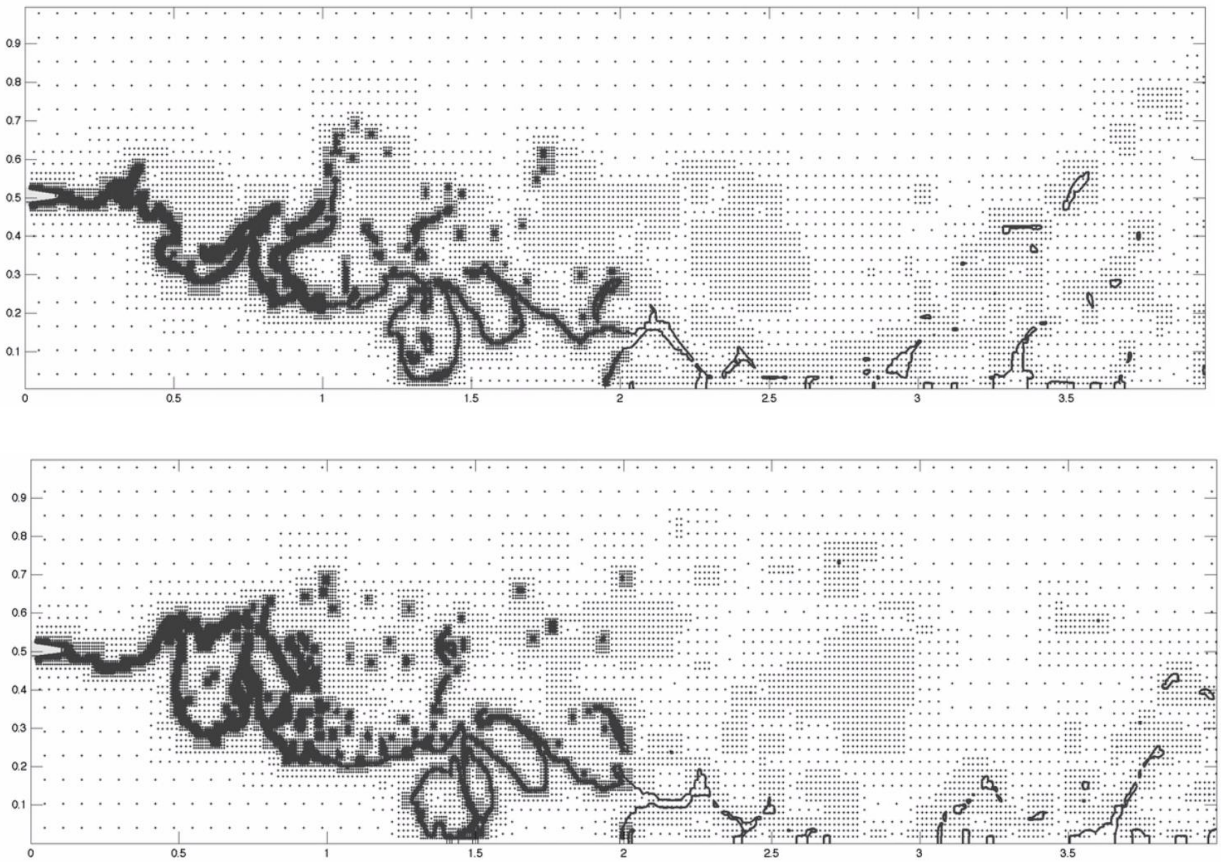

Figure 3-20: Illustration of the adaptive mesh. The top and bottom figures represent the water-air interface at different times. The density of the dots corresponds to the resolution of the grid [50, 51].

Gerris has been used on several occasions to simulate multi-phase flows, which is in line with its development for atmospheric research [52, 53]. The challenge in simulating multi-phase flow on DNS scale is correctly representing the phase interface. In Gerris, the interface is tracked using the volume of fluid method. To be able to correctly resolve the fluid interface with this method, the mesh should be very fine in proximity of the interface. Due to the transient character of the simulations, the interface will not be at the same location throughout the simulation. Therefore, the mesh should have the required resolution everywhere, incurring a significantly higher computational cost. This is avoided in Gerris by using an adaptive grid, which refines automatically in the region where the interface is situated, allowing a reduction in the number of grid points by two orders of magnitude, from around 500 million to 5 million [52].

Agbaglah simulated three types of multi-phase flow, namely droplet impact, atomisation of a jet and an oil-in-water plume. The results from the atomisation of a jet by air in co-flow in Figure 3-20 [50], illustrate the adaptive mesh refining of the code. Close to the interface, the resolution of the mesh is very high, while away from the interface, a much coarser grid is sufficient. For each time step, the mesh is refined anew, tracking the liquid-gas interface.

3.7. Conclusion

In sections 3.2 through 3.6, several codes for DNS have been discussed. The goal was to analyse which code seems most appropriate for DNS of reactive pipe flows. Research using the different codes has indicated that all codes are capable of providing results with acceptable accuracy, though differences in efficiency and wall times are definitely present.

Table 3-1 gives an overview of the treated codes. Paramount in this evaluation is the access to the source code. This implies that S3D cannot be considered. Due to the relatively limited computational resources available, it would not be possible to exploit the full potential of the code. Similarly and as has been mentioned in section 3.6, Gerris has been developed for very disparate domains. Additionally, the focus here is on single-phase flows, which do not require such extensive grid refinement methods as implemented in Gerris.

OpenFOAM has a great advantage compared to the other codes in the fact that in-house knowledge on working and adapting the code is available, albeit in RANS and LES. Its disadvantage is that the spatial discretisation method can give rise to troublesome numerical diffusion.

Based on application domains, SIMSON and Nek5000 are found to be optimal and frequently used for wall bounded flows. Pipe flow as such has not been frequently investigated using DNS, with most simulations being either on channel or boundary layer flow. There are cases in Nek5000 however that have investigated pipe flow. Nek5000 also solves the compressible Navier-Stokes equations, while SIMSON solves the incompressible equations. The thermal effects during chemical reactions make accounting for

compressibility effects important. Also, regarding ease of use and learning, Nek5000 is better documented and supported than SIMSON, providing a website and very large user base. Notwithstanding, it is possible that performance wise, SIMSON has the upper hand in certain geometries.

Table 3-1: Overview of the important properties of the different DNS codes discussed above.

Code	*Spatial Discretisation*	*Temporal Discretisation*	*Open Source*	*Main application*
OpenFOAM	FVM	Cash-Carp Runge-Kutta, 5th order	YES	Not dedicated to DNS, very broad applicability
Nek5000	SEM	BDS, 3rd order	YES	Wall-bounded flows
S3D	High-order FDM	Explicit Runge-Kutta, 4th order	NO	Reactive flows (combustion) in large numerical domains
SIMSON	Fourier-Chebyshev SM	Crank-Nicolson, 2nd order	YES	Wall-bounded flows
Gerris	FVM, octree structured, adaptive mesh	Fractional-step projection, 2nd order	YES	Atmospheric and aquatic research

Without any personal or in-house prior experience in DNS research, Nek5000 is thought to be the most promising code available. While the implemented SEM is quite complex, a large user base and extensive support and documentation is available. In not too complex geometries, Nek5000 can be outperformed by spectral code considering computational time efficiency. However, it is sought to perform (reactive) DNS on enhanced tube geometries, which can barely be considered non-complex. In such cases, spectral element codes such as Nek5000 are preferred.

3.8. References

1. Ahn, J.; Lee, J. H.; Lee, J.; Kang, J. H.; Sung, H. J., Direct numerical simulation of a 30R long turbulent pipe flow at Re-tau=3008. *Physics of Fluids* **2015,** 27, (6), 14.
2. Boersma, B. J., Direct numerical simulation of turbulent pipe flow up to a Reynolds number of 61,000. *Journal of Physics: Conference Series* **2011,** 318, (4), 042045.
3. Boersma, B., Large Scale Motions in the Direct Numerical Simulation of Turbulent Pipe Flow. In *Direct and Large-Eddy Simulation IX*, Springer: 2015; pp 243-249.
4. Chiva, J.; Lehmkuhl, O.; Ventosa, J.; Oliva, A., Direct Numerical Simulation of Low-Mach Turbulent Natural Convection Flow in an Open Cavity of Aspect Ratio 4. In *Direct and Large-Eddy Simulation IX*, Springer: 2015; pp 345-352.
5. Ghosh, S.; Foysi, H.; Friedrich, R., Compressible turbulent channel and pipe flow: similarities and differences. *Journal of Fluid Mechanics* **2010,** 648, 155-181.
6. Ghosh, S.; Sesterhenn, J.; Friedrich, R., DNS and LES of compressible turbulent pipe flow with isothermal wall. In *Direct and Large-Eddy Simulation VI*, Springer: 2006; pp 721-728.
7. OpenFOAM Features. http://www.openfoam.org/features/index.php (7/11/2015),
8. Cash, J. R.; Karp, A. H., A variable order Runge-Kutta method for initial value problems with rapidly varying right-hand sides. *ACM Transactions on Mathematical Software (TOMS)* **1990,** 16, (3), 201-222.
9. Shampine, L. F.; Gordon, M. K., *Computer solution of ordinary differential equations: the initial value problem*. WH Freeman San Francisco: 1975.
10. Ferziger, J. H.; Peric, M., Efficiency and Accuracy Improvement. In *Computational Methods for Fluid Dynamics*, 3rd ed.; Springer-Verlag: Berlin, 2002; pp 329-367S.
11. OpenFOAM-Parallel Computing. http://www.openfoam.org/features/parallel-computing.php (29/01/2016),
12. Zhang, F.; Bonart, H.; Zirwes, T.; Habisreuther, P.; Bockhorn, H.; Zarzalis, N., Direct Numerical Simulation of Chemically Reacting Flows with the Public Domain Code OpenFOAM. In *High Performance Computing in Science and Engineering '14*, Springer: 2015; pp 221-236.
13. Cantera. http://www.cantera.org/docs/sphinx/html/index.html# (29/01/2016),
14. Weiß, M.; Zarzalis, N.; Suntz, R., Experimental study of Markstein number effects on laminar flamelet velocity in turbulent premixed flames. *Combustion and Flame* **2008,** 154, (4), 671-691.
15. van Haren, S. W. Testing DNS Capability of OpenFOAM and STAR-CCM+. Delft University of Technology, 2011.
16. Redjem-Saad, L.; Ould-Rouiss, M.; Lauriat, G., Direct numerical simulation of turbulent heat transfer in pipe flows: Effect of Prandtl number. *International Journal of Heat and Fluid Flow* **2007,** 28, (5), 847-861.
17. Eggels, J. G. M.; Unger, F.; Weiss, M. H.; Westerweel, J.; Adrian, R. J.; Friedrich, R.; Nieuwstadt, F. T. M., Fully-Developed Turbulent Pipe-Flow - a Comparison between Direct Numerical-Simulation and Experiment. *Journal of Fluid Mechanics* **1994,** 268, 175-209.
18. Fukagata, K.; Kasagi, N., Highly Energy-Conservative Finite Difference Method for the Cylindrical Coordinate System. *Journal of Computational Physics* **2002,** 181, (2), 478-498.
19. Fukushima, N.; Fukagata, K.; Kasagi, N.; Noguchi, H.; Tanimoto, K. In *Numerical and experimental study on turbulent thermal mixing in a T-junction flow*, The 6th ASME-JSME Thermal Engineering Joint Conference, 2003; 2003; pp 16-20.
20. Nek5000. https://nek5000.mcs.anl.gov/about/ (08/02/2016),
21. Fischer, P. *NEK5000 Documentation*, 2015.
22. El Khoury, G. K.; Schlatter, P.; Noorani, A.; Fischer, P.; Brethouwer, G.; Johansson, A. V., Direct Numerical Simulation of Turbulent Pipe Flow at Moderately High Reynolds Numbers. *Flow, Turbulence and Combustion* **2013,** 91, (3), 475-495.
23. El Khoury, G. K.; Schlatter, P.; Brethouwer, G.; Johansson, A. V., Turbulent pipe flow: Statistics, Re -dependence, structures and similarities with channel and boundary layer flows. *Journal of Physics: Conference Series* **2014,** 506, (1), 012010.
24. Chin, C.; Ooi, A.; Marusic, I.; Blackburn, H., The influence of pipe length on turbulence statistics computed from direct numerical simulation data. *Physics of Fluids* **2010,** 22, (11), 115107.

25. Lenaers, P.; Li, Q.; Brethouwer, G.; Schlatter, P.; Örlü, R., Rare backflow and extreme wall-normal velocity fluctuations in near-wall turbulence. *Physics of Fluids (1994-present)* **2012,** 24, (3), 035110.
26. Schlatter, P.; Orlu, R.; Li, Q.; Brethouwer, G.; Fransson, J. H.; Johansson, A. V.; Alfredsson, P. H.; Henningson, D. S., Turbulent boundary layers up to retheta= 2500 studied through simulation and experiment. *Physics of Fluids* **2009,** 21, (5), 51702.
27. Sprague, M. A. In *A comparison of Nek5000 and OpenFOAM for DNS of turbulent channel flow*, Nek5000 Users Meeting, Argonne National Lab, 2010; Argonne National Lab, 2010.
28. Kim, J.; Moin, P.; Moser, R., Turbulence statistics in fully developed channel flow at low Reynolds number. *Journal of Fluid Mechanics* **1987,** 177, 133-166.
29. Hawkes, E. R.; Sankaran, R.; Sutherland, J. C.; Chen, J. H., Direct Numerical Simulations of Turbulent Nonpremixed Combustion: Fundamental Insights Towards Predictive Models. In Sandia National Laboratories: Livermore, California.
30. Grout, R. W.; Sankaran, R.; Levesque, J. M.; Woolley, C.; Posey, S.; Chen, J. H. In *S3D Direct Numerical Simulation: Preparation for the 10-100 PF era*, Scientific Computing GTC, San Jose, USA, 2012; San Jose, USA, 2012.
31. Levesque, J. M.; Sankaran, R.; Grout, R.; Ieee, Hybridizing S3D into an Exascale Application using OpenACC An approach for moving to Multi-Petaflops and Beyond. In *2012 International Conference for High Performance Computing, Networking, Storage and Analysis*, Ieee: New York, 2012.
32. Owens, J. D.; Houston, M.; Luebke, D.; Green, S.; Stone, J. E.; Phillips, J. C., GPU computing. *Proceedings of the IEEE* **2008,** 96, (5), 879-899.
33. Chen, J. H.; Choudhary, A.; de Supinski, B.; DeVries, M.; Hawkes, E. R.; Klasky, S.; Liao, W. K.; Ma, K. L.; Mellor-Crummey, J.; Podhorszki, N.; Sankaran, R.; Shende, S.; Yoo, C. S., Terascale direct numerical simulations of turbulent combustion using S3D. *Computational Science & Discovery* **2009,** 2, (1), 015001.
34. Lyons, K. M., Toward an understanding of the stabilization mechanisms of lifted turbulent jet flames: experiments. *Progress in Energy and Combustion Science* **2007,** 33, (2), 211-231.
35. Chen, Y.-C.; Mansour, M. S. In *Investigation of flame broadening in turbulent premixed flames in the thin-reaction-zones regime*, Symposium (International) on Combustion, 1998; Elsevier: 1998; pp 811-818.
36. Dinkelacker, F.; Soika, A.; Most, D.; Hofmann, D.; Leipertz, A.; Polifke, W.; Döbbeling, K. In *Structure of locally quenched highly turbulent lean premixed flames*, Symposium (International) on Combustion, 1998; Elsevier: 1998; pp 857-865.
37. Chevalier, M.; Schlatter, P.; Lundbladh, A.; Henningson, D. S. *SIMSON a Pseudo-Spectral Solver for Incompressible Boundary Layer Flows*; KTH Engineering Sciences: Stockholm, Sweden, 2007.
38. Crank, J.; Nicolson, P. In *A practical method for numerical evaluation of solutions of partial differential equations of the heat-conduction type*, Mathematical Proceedings of the Cambridge Philosophical Society, 1947; Cambridge Univ Press: 1947; pp 50-67.
39. Gilat, A.; Subramaniam, V., Ordinary Differential Equations: Initial Value Problems. In *Numerical Methods An introduction with Applications Using Matlab*, John Wiley & Sons, Inc.: 2011; pp 293-376.
40. Lenaers, P.; Li, Q.; Brethouwer, G.; Schlatter, P.; Örlü, R., Negative streamwise velocities and other rare events near the wall in turbulent flows. *Journal of Physics: Conference Series* **2011,** 318, (2), 022013.
41. Momentum Thickness. http://www.cfdsupport.com/OpenFOAM-Training-by-CFD-Support/node267.html (09/02/2016),
42. Schlatter, P.; Örlü, R., Assessment of direct numerical simulation data of turbulent boundary layers. *Journal of Fluid Mechanics* **2010,** 659, 116-126.
43. Del Alamo, J. C.; Jimenez, J.; Zandonade, P.; Moser, R. D., Scaling of the energy spectra of turbulent channels. *Journal of Fluid Mechanics* **2004,** 500, 135-144.
44. Westfall, P. H., Kurtosis as peakedness, 1905–2014. rip. *The American Statistician* **2014,** 68, (3), 191-195.
45. Ohlsson, J.; Schlatter, P.; Mavriplis, C.; Henningson, D. S., The Spectral-Element and Pseudo-Spectral Methods: A Comparative Study. In *Spectral and High Order Methods for Partial*

Differential Equations: Selected papers from the ICOSAHOM '09 conference, June 22-26, Trondheim, Norway, Hesthaven, S. J.; Rønquist, M. E., Eds. Springer Berlin Heidelberg: Berlin, Heidelberg, 2011; pp 459-467.

46. Moser, R. D.; Kim, J.; Mansour, N. N., Direct numerical simulation of turbulent channel flow up to Re= 590. *Phys. Fluids* **1999,** 11, (4), 943-945.
47. Popinet, S., Gerris: a tree-based adaptive solver for the incompressible Euler equations in complex geometries. *Journal of Computational Physics* **2003,** 190, (2), 572-600.
48. Samet, H., *Applications of Spatial Data Structures*. Addison-Wesley: Maryland, 1990.
49. Brown, D. L.; Cortez, R.; Minion, M. L., Accurate Projection Methods for the Incompressible Navier–Stokes Equations. *Journal of Computational Physics* **2001,** 168, (2), 464-499.
50. Fuster, D.; Agbaglah, G.; Josserand, C.; Popinet, S.; Zaleski, S., Numerical simulation of droplets, bubbles and waves: state of the art. *Fluid Dynamics Research* **2009,** 41, (6), 065001.
51. Agbaglah, G., Simulation of atomization processes in conditions close to experiments. In 2009.
52. Agbaglah, G.; Delaux, S.; Fuster, D.; Hoepffner, J.; Josserand, C.; Popinet, S.; Ray, P.; Scardovelli, R.; Zaleski, S., Parallel simulation of multiphase flows using octree adaptivity and the volume-of-fluid method. *Comptes Rendus Mecanique* **2011,** 339, (2), 194-207.
53. Comas, J. T. Numerical Simulations of Multiphase Flows-Atomization. Université Pierre et Marie Curie, Paris, 2014.

4

Computational Methods

4.1. Conservation Equations

At the base of all computational fluid dynamics simulations are the conservation equations for mass, momentum, energy and species [1]. These equations, in combination with the correct boundary and initial conditions fully describe the compressible fluid flow. The species equations can be seen as an extension of the mass conservation equation for the system to the mass conservation of the individual components. The first equation that co-describes the fluid flow is the conservation of mass, also referred to as the continuity equation.

$$\frac{\partial \rho}{\partial t} + \nabla \cdot (\rho \boldsymbol{v}) = 0 \tag{4-1}$$

A second set of equations are the momentum conservation equations, which are also referred to as the Navier-Stokes equations [2]. Sometimes, the combination of mass and momentum equations is referred to as the Navier-Stokes equations. The mass and momentum conservation equations fully describe single-phase, non-reacting and isothermal flow.

$$\frac{D\rho \boldsymbol{v}}{Dt} = \rho \boldsymbol{g} + \nabla \cdot \boldsymbol{\tau} \tag{4-2}$$

As mentioned in paragraph 2.5.5, these equations do not provide a practical method to solve for the velocity and pressure fields due to their strong correlation. Therefore, pressure-velocity coupling methods are typically applied. *In concreto*, in the present work the PIMPLE algorithm is used [3]. PIMPLE is a combination of the PISO and SIMPLE methods discussed in paragraph 2.5.5. The SIMPLE correction method is used as outer loop, while an inner correction loop employs the PISO algorithm. The result is that larger time steps can be used, compared to the individual methods [4].

The aim of this work is to perform simulations of reacting pipe flow, implying that the energy and species conservation equations are important [5, 6]. These equations are given by eq. (4-3) and eq. (4-4) respectively (in Newton notation).

$$\nabla \cdot (\lambda \nabla T) + \dot{q} + \Lambda = \nabla \cdot (P\boldsymbol{v}) + \frac{\rho}{2}\frac{Dv^2}{Dt} + \rho \frac{Du}{Dt} + \rho \frac{D(gy)}{Dt} \tag{4-3}$$

$$\frac{\partial C_i}{\partial t} + v_j \frac{\partial C_i}{\partial x_j} = D_{mol,i} \frac{\partial^2 C_i}{\partial x_j \partial x_j} + R_i(C_j) \tag{4-4}$$

The above equations are discretised based on the finite volume method. The order of discretisation can be chosen. In first approach, linear Gaussian discretisation is chosen. Though the order of approximation is low (and hence the accuracy as well), it provides the best convergence , which can be difficult to achieve in reactive LES. The trade-off is a higher influence of numerical diffusion.

4.2. Turbulence Model

In the momentum conservation equations, the term $\nabla \cdot \boldsymbol{\tau}$ must be modelled. In the concept of large eddy simulations, only those scales are modelled which cannot be resolved by the numerical grid, *i.e* those of which the dimensions are smaller than the grid resolution. This separation of scales is performed by applying a spatial filter. Examples of such filters have been given in paragraph 2.3.2. In the present work implicit filtering is applied, *i.e.* all length scales that are smaller than the cube root of the local cell volume are considered unresolved and are therefore modelled. Instead of solving for the true velocity and pressure, the equations are solved for the filtered velocity and pressure.

$$\rho \frac{d\widetilde{v_i}}{dt} + \nabla(\tilde{\boldsymbol{v}}\rho\widetilde{v_i}) = \rho \boldsymbol{g} - \frac{d}{dx_i}\tilde{P} + \nabla \cdot (\mu \nabla \widetilde{v_i}) - \frac{d}{dx_j}\left(\tau_{ij,SGS}\right) \quad \textbf{(4-5)}$$

The term $\tau_{ij,SGS}$, which represents the sub-grid scale stress tensor can no longer be determined solely based on the filtered velocity and thus must be modelled. In this work, the wall-adaptive local eddy viscosity (WALE [7]) model is used. This approach uses an eddy viscosity concept which is similar to the turbulent viscosity used in some RANS models. While in Reynolds averaging, the use of the turbulent viscosity is often not adequate, the use of the equivalent eddy viscosity in LES is acceptable. The underlying cause is that in RANS, the assumption that the modelled turbulence is isotropic, is generally invalid, while this assumption is valid for the small-scale turbulent effects that are modelled in LES. The main advantage of the WALE model is that it correctly represents the decay of the sub-grid scale turbulence in the near-wall region. This is of importance as the aim is to perform wall-resolved LES. The WALE model is based on the following equations.

$$\tau_{ij,SGS} = -2\mu_{SGS}\widetilde{S_{ij}} + \frac{1}{3}\tau_{ii}\delta_{ij} = -2\mu_{SGS}\left(\frac{d\widetilde{v_i}}{dx_j} + \frac{d\widetilde{v_j}}{dx_i}\right) + \frac{1}{3}\tau_{ii}\delta_{ij} \quad \textbf{(4-6)}$$

$$g_{ij} = \frac{dv_i}{dx_j} \quad \textbf{(4-7)}$$

$$S_{ij}^d = \frac{1}{2}\left(\widetilde{g_{ik}}\widetilde{g_{kj}} + \widetilde{g_{jk}}\widetilde{g_{ki}}\right) - \frac{1}{3}\delta_{ij}\widetilde{g_{kk}}^2 \quad \textbf{(4-8)}$$

$$\mu_{SGS} = \rho(C_w\Delta)^2 \frac{\left(S_{ij}^d S_{ij}^d\right)^{3/2}}{\left(\widetilde{S_{ij}}\widetilde{S_{ij}}\right)^{5/2} + \left(S_{ij}^d S_{ij}^d\right)^{5/4}} \quad \textbf{(4-9)}$$

The cut-off width Δ is determined per cell as the cubic root of the cell volume. C_w is set to the value 0.5, the other terms in the equations depend only on the filtered velocity and can thus be calculated. It should be noted that similar filtering of the energy and species conservation equations is required to carry out the simulations. Analogous to the eddy viscosity, these sub-grid effects are combined with the molecular thermal conductivity and molecular diffusion coefficient into an effective thermal conductivity and

effective diffusion coefficient, by correcting the eddy viscosity with the turbulent Prandtl and Schmidt number respectively. Based on recommendations in literature for these numbers, both are set at 0.5 (for comparison, they are both 0.6 in AVBP, used by Zhu) [8, 9].

$$\lambda_{eff} = \lambda_0 + \frac{\mu_{SGS}}{Pr_t} \quad \textbf{(4-10)}$$

$$D_{mol,eff} = D_{mol,0} + \frac{\mu_{SGS}}{Sc_t} \quad \textbf{(4-11)}$$

$$Pr = \frac{c_p \mu}{\lambda} \quad \textbf{(4-12)}$$

$$Sc = \frac{\mu}{\rho D_{mol}} \quad \textbf{(4-13)}$$

4.3. Reaction Model

Butane is used as hydrocarbon feedstock in all reacting flow simulations. A detailed reaction network is implemented, comprising 20 species and 149 reactions. The network was generated using RMG [10]. The following components are accounted for in the model.

Table 4-1: Components accounted for in the reaction model for butane steam cracking.

Transported species			
Hydrogen (H_2)	Methane (CH_4)	Ethane (C_2H_6)	Propane (C_3H_8)
n-Butane (C_4H_{10})	Ethene (C_2H_4)	Propene (C_3H_6)	Water (H_2O)
1-Butene (C_4H_8)	2-Butene (C_4H_8)	1,3-Butadiene (C_4H_6)	
Radical species			
Hydro ($H^\bullet$)	Methyl ($CH_3^\bullet$)	Ethyl ($C_2H_5^\bullet$)	n-Propyl ($C_3H_7^\bullet$)
iso-Propyl ($C_3H_7^\bullet$)	t-1-Methylallyl ($C_4H_7^\bullet$)	t-3-Butene-1-yl ($C_4H_7^\bullet$)	sec-Butyl ($C_4H_9^\bullet$)
n-Butyl ($C_4H_9^\bullet$)			

The average lifetime of the reactive radical species is typically much shorter than that of the non-radical species. The large spread on time scales of the different species makes the resulting set of differential equations highly stiff. To decrease the spread on the time scales and hence reduce the stiffness, the pseudo-steady-state assumption (PSSA) is applied to the reactive radical intermediates [11]. A detailed overview of the reaction rate equations and PSS species equations is given in Appendix A.

4.4. Numerical Grids

Three different geometries are investigated. The first is a bare tube, which serves as the reference case, *e.g.* for determining the enhancement factors for heat transfer and pressure drop. The second is an internally finned tube, which can be considered as the industrial reference case, as bare tubes are seldom applied in industry [12]. The final case is a helicoidally ribbed tube, also referred to as a mixing element radiant tube (MERT). In all three cases a structured, hexahedral mesh is used. To be able to perform wall-resolved LES, the cell centre of the first cell next to the wall must fulfil the criterion $y^+ < 1$. The actual dimension corresponding to $y^+ = 1$ depends on the Reynolds number, which is a result of the simulation and hence not known *a priori*. The results reported by Zhu [13] are to serve as reference data. Therefore, the targeted Reynolds number is approximately 72,000. To fulfil the criterion $y^+ < 1$, the cell centre of the first cell next to the wall should be located within a distance from the wall of 1.075 10^{-5} m in the radial direction. More details on the meshes are provided in the following sections. It should be noted that no conjugate heat transfer is taken into account, *i.e.* the tube metal is not simulated. The inlet conditions are the same as those in the work of Zhu and are listed in Table 4-2. The feed is butane, diluted with steam to achieve an initial butane mass ratio of 0.69 wt%.

Table 4-2: Inlet conditions for the reactive simulations of a bare tube reactor, an internally finned reactor and a helicoidally ribbed reactor [13].

Parameter	*Mass flow rate*	*Pressure*	*Temperature*	*Reactor Length*	*Butane mass fraction*
Value	0.0655 kg s^{-1}	235680 Pa	909.15 K	10 m	0.69 wt%

4.4.1. Bare Tube

The computational domain for the bare tube has a diameter of 38.1 mm and a length of 152 mm which corresponds to an L/D ratio of 4. This corresponds to the advised length range in domains with streamwise periodic boundary conditions [14, 15]. The numerical grid is characterised by the cell spacing in each of the three dimensions. The spacing in the 'y' direction (radial) is not constant in a cross-section. For this geometry, the cross-sectional mesh is constructed based on a butterfly-type mesh and a boundary layer. The butterfly mesh consists of a square-like inner region and an annular outer region. The radial spacing in the inner region is directly linked to the tangential spacing of the mesh. The tangential spacing is set to $y_\theta^+ = 25$, resulting in 111 cells to cover a quarter of the circumference. The value $y_\theta^+ = 25$ is consistent with the advised range for LES of $15 < y_\theta^+ < 30$ [16, 17]. The radial spacing in the outer region can be defined separately, though it is good practice to choose the number of radial cells in the outer region such that the spacing in the inner and outer region are equal. To this initial mesh, a boundary layer (comprising a certain number of extrusion layers) is added. In this boundary layer, the radial cell spacing gradually increases from the wall inwards, starting at $y^+ = 1$. This is characterised by the growth factor, which in case of the

bare tube is 1.1. The number of extrusion layers and the diameter of the butterfly mesh region should be chosen such that a smooth transition in cell spacing is obtained between the boundary layer and butterfly meshes. The characteristics of the cross-sectional mesh are given in Table 4-3 and are further illustrated in Figure 4-1. The spacing of the cells in the axial 'z' direction is based on the guidelines for LES that the spacing should correspond to a y_z^+ in the range $50 < y_z^+ < 130$ [16, 17]. A value of 120 is chosen, resulting in 118 cells in the axial direction. The final mesh consists of 3,968,694 hexahedral cells. This amount is similar to the number of tetrahedral cells used in the mesh of M. Zhu [13], even though wall resolved LES is performed ($y^+ = 1$, opposed to $y^+ \sim 20$ for M. Zhu).

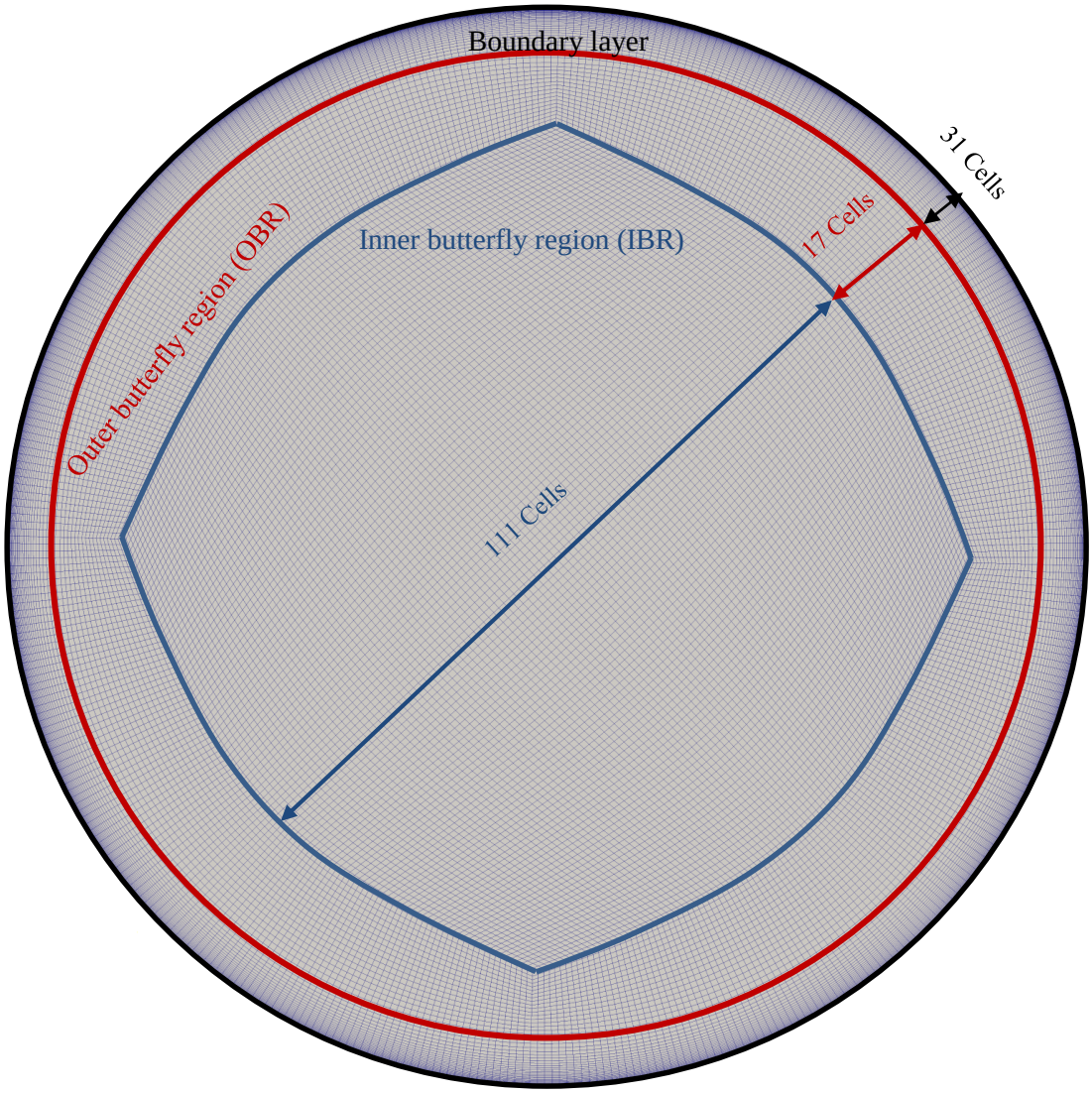

Figure 4-1: Illustration of the mesh regions for the bare tube.

Table 4-3: Properties of the cross-sectional mesh for the bare tube.

y at $y^+ = 1$	Radial growth factor	# extrusion layers	# tangential cells (1/4)	# radial cells OBR	Butterfly diameter
1.075 10^{-5} m	1.1	31	111	17	0.01719 m

4.4.2. Finned Tube

The finned tube has a constant cross-sectional surface area, as does the bare tube. The dimensions are chosen such that the cross-sectional flow area of the finned tube is the same as for the bare tube. Using eight identical fins with a height of 5.11 mm, the resulting inner tube diameter at the top of the fins becomes 42.97 mm. The length of the computational domain for the finned tube is identical to the computational domain length of the bare tube, namely 0.152 m. The cell spacing in the axial direction is also identical to the one in the bare tube ($y_z^+ = 120$, corresponding to 118 cells). The radial and tangential spacing of the cells, however, differs substantially. The tangential resolution should be sufficiently high to resolve the shape of the fins. To have sufficient radial resolution and limit the difference in cell spacing between the inner and outer regions, the tangential spacing is decreased to the lower limit of the advised range, *i.e.* $y_\theta^+ = 15$. This corresponds to 200 cells to cover a quarter of the circumference, and 100 cells to span the inner region in the radial direction. The outer layer is constructed by 41 cells in the radial direction. Initially, the same cell spacing at the wall was used as for the bare tube (*i.e.* 1.075 10^{-5} m and a growth ratio of 1.1). However, this results in a couple of cell layers at the boundary between the inner and outer region with radial dimensions that differ significantly from the surrounding cell layers. To solve this issue the radial cell dimensions are made more uniform in the boundary zone between the two regions via a smoothing function. Consequently, the wall spacing and growth factor is no longer constant in the azimuthal direction. The maximal wall spacing is now 2.219 10^{-5} m, corresponding to a $y^+ = 2.07$ for the same Reynolds number or a $y^+ = 1$ at a reduced Reynolds number of approximately 33,000. The growth factor ranges from 1.05 to 1.11. The important characteristics of the mesh are given in Table 4-4 and are further illustrated in Figure 4-2. While the maximal dimensionless radial wall spacing is significantly higher than 1, the cell centre of the first cell, at half the distance is still at approximately $y^+ = 1$. Mainly due to the decrease in tangential spacing, the total number of hexahedral cells in the finned tube mesh increases to 6,230,400.

Table 4-4: Properties of the cross-sectional mesh for a finned tube.

Average radial wall spacing	Max. radial wall spacing	Average radial growth factor	# tangential cells (1/4)	# radial cells outer region
1.424 10^{-5} m $y^+ = 1.33$	2.219 10^{-5} m $y^+ = 2.07$	1.07	200	41

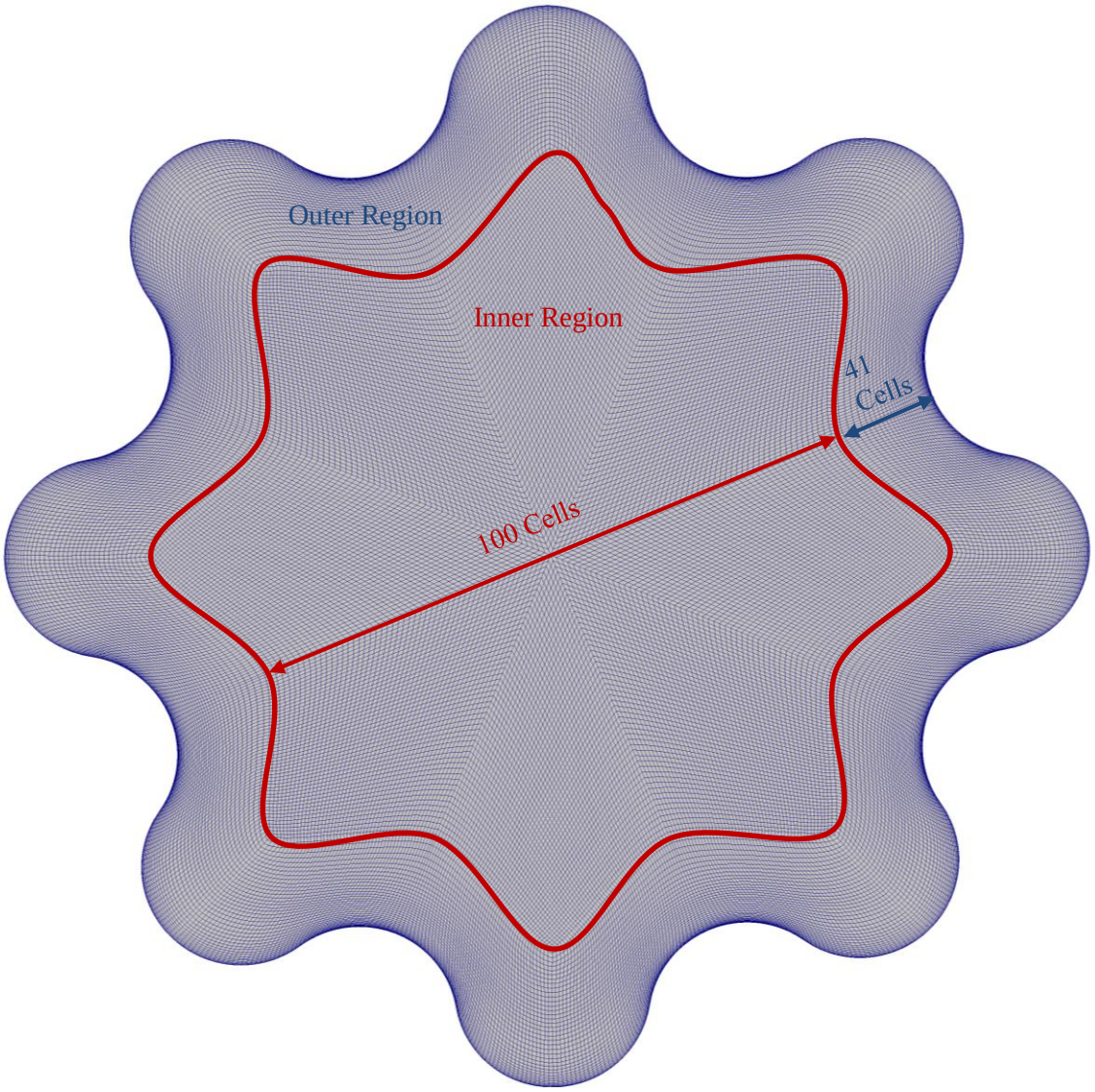

Figure 4-2: Illustration of the mesh regions for the finned tube.

4.4.3. Ribbed Tube

As the total volume of the transversal rib is low compared to the tube volume, no correction on the tube diameter is taken into account to maintain an equal cross-sectional flow area. The pitch of the transversal rib is 69.11 mm, while the height equals 1.875 mm. As periodic boundary conditions are imposed on the inlet and outlet, the length of the simulated domain should be an exact multiple of the pitch, resulting in a computational domain length of 138.22 mm, *i.e.* two pitch lengths. Where the fins still presented a constant cross-sectional surface area, the rib as a three-dimensional character. The same approach is used as in the bare tube, namely using a butterfly mesh as starting point and then adding the boundary layer. However, the mixing element disrupts the smooth circumference of the tube. To maintain a smooth transition in cell spacing between the different zoned, both the outer diameter of the butterfly mesh and the growth factor are significantly reduced compared to the bare tube. While the tangential spacing remains unchanged ($y_\theta^+ =$

25, 111 cells), reducing the diameter of the butterfly mesh reduces the radial spacing of the cells. The outer region of the butterfly mesh comprises 26 layers of cells in the radial direction. The cells at the wall again have a radial dimension such that $y^+ = 1$. The boundary region is made up of 96 layers. The previous two cases did not require high resolutions in the axial direction. However, here the curvature of the mixing element must be resolved adequately. Taking into account the lower limit for $y_z^+ = 50$, a value $y_z^+ = 60$ is chosen and found to acceptably represent the curved surface of the mixing element. This nearly doubles the number of axial cells to 214. As a result of the increased radial and axial resolution, the total number of cells in the mesh further increases to 14,228,646. This is a significant increase in cells compared to the case of Zhu [13]. This is linked to the use of a structured grid, in which it is much more difficult to resolve the three dimensional rib than with an unstructured grid and the wall resolving nature of the mesh. A summary of the properties can be found in Table 4-5, while Figure 4-3 illustrates the cross-section.

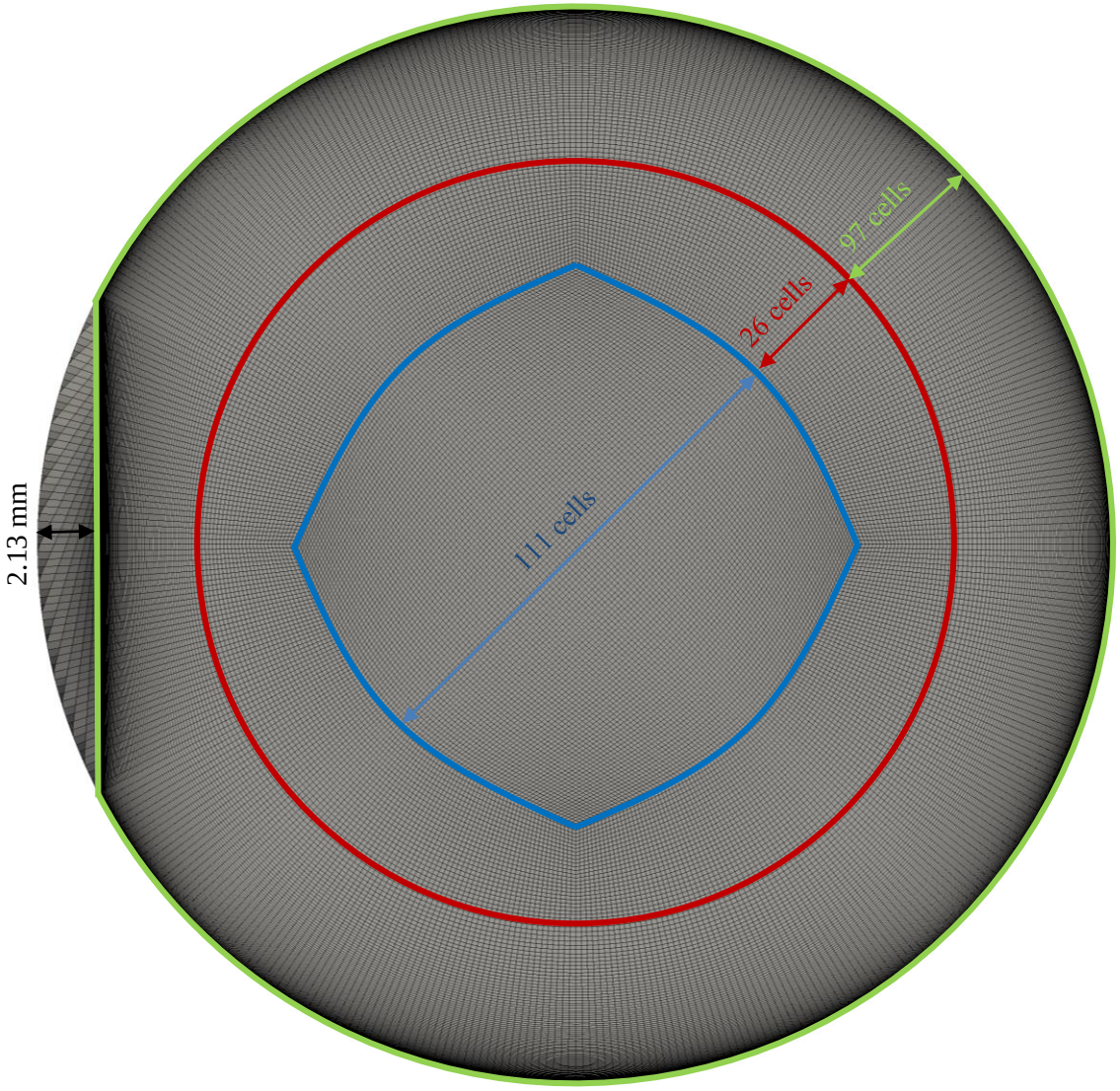

Figure 4-3: Illustration of the cross-sectional mesh for the ribbed tube.

Table 4-5: Properties of the mesh for the ribbed tube.

y at $y^+ = 1$	Growth factor	# extrusion layers	# tangential cells	# axial cells	# radial cells OBR	Butterfly diameter
$1.075\ 10^{-5}$ m	1.03	96	111	214	26	0.01338 m

4.5. Numerical Schemes

OpenFOAM makes use of the finite volume method for discretisation. A detailed overview of the method can be found in paragraph 2.5.2. The terms of each equation can be grouped into different categories, depending on their mathematical nature. OpenFOAM discerns four such classes and allows the user to specify specific discretisation schemes for each class in the file `fvSchemes`. Due to the discretisation of the different terms, there is a need for function values on the faces of the cells, requiring interpolation schemes as well. Again the user can specify which interpolation schemes are used in the file `fvSchemes`. On overview of the file structure of an OpenFOAM case is given in Appendix B. Table 4-6 lists the different classes, along with the default schemes, used in the present work. The maximal Courant number in the simulations is specified to be 0.5, but 0.8 is used in the ribbed tube as the fine mesh already reduces the time step.

Table 4-6: Default numerical schemes used in the simulations.

Keyword	*Mathematical Class*	*Default Scheme*	*Remarks*
`ddtSchemes`	Time derivative	`Backward`	
`gradSchemes`	Gradient	`cellLimited Gauss linear 1`	
`divSchemes`	Divergence	`Gauss limitedLinear 1`	`filteredLinear` for $\boldsymbol{v}$ and h
`LaplacianSchemes`	Laplacian	`Gauss linear corrected`	`uncorrected` for $\boldsymbol{v}$ and h
`interpolationSchemes`	Interpolation between cell values	`linear skewCorrected`	

The linear schemes are central differencing schemes, which are second order accurate. While the low order does not yield optimal accuracy, it does ensure good convergence. The limited schemes are used to avoid extreme gradients that may be the result of single non-converged cells. Initial simulations using the standard

`Gauss linear` schemes and a higher Courant number resulted in checkerboard-like temperature values. This effect is shown in Figure 4-4. The corrected schemes for the Laplacian are second-order accurate and conservative, but unbounded, while the uncorrected schemes are bounded, but only first order accurate and non-conservative. An interpolation scheme that corrects for the skewness of the cells is used. Only the in the finned case, cells with high skewness are present. The same scheme is used in all cases as other standard interpolation schemes such as the basic `linear` scheme were found to be incompatible with the `QSSAPipeFoam` solver. The incompatibility resulted in a periodic accumulation of numerical errors. This resulted in wave-like, alternating pressure fields, as illustrated by Figure 4-5. In Figure 4-6, near the tube axis, some regions with higher pressure can be observed, while lower pressures are systematically present near the wall. These pressure differences result in an annular-like flow pattern (Figure 4-7), with high velocities in close proximity of the walls. Consequentially, the pressure drop is significantly overestimated. The same type of pattern, though less pronounced, can be observed in Figure 4-8 for the ribbed geometry.

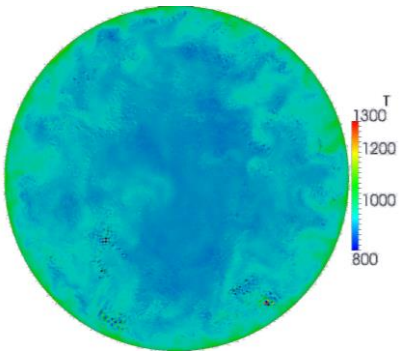

Figure 4-4: Checkerboard temperature field [K], using standard `Gauss linear` schemes.

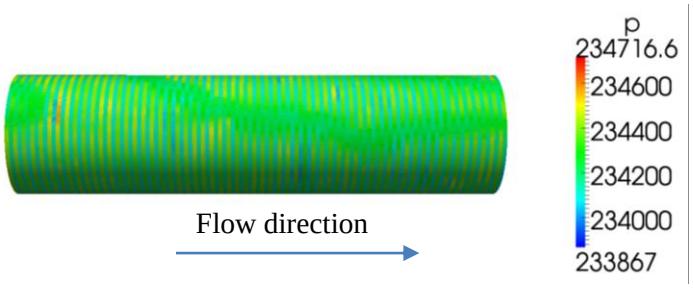

Figure 4-5: Alternating absolute pressure [Pa] in the bare tube case, axial view of the outer layer of cells.

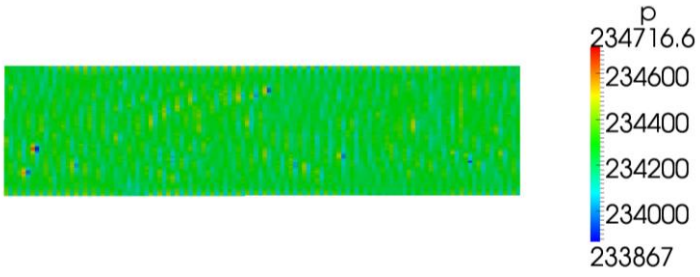

Figure 4-6: Erratic pressure field [Pa] in the bare tube case, axial cross-section.

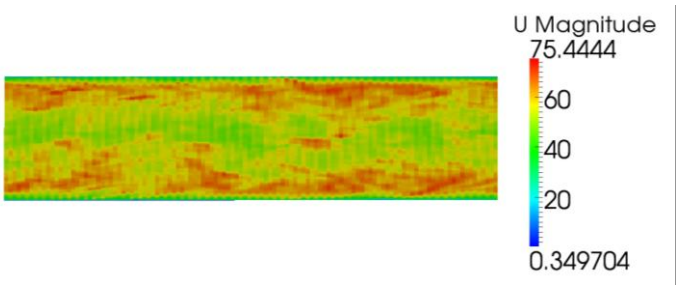

Figure 4-7: Annular velocity [m s^{-1}] in the bare tube case as a result of the pressure error, axial cross-section.

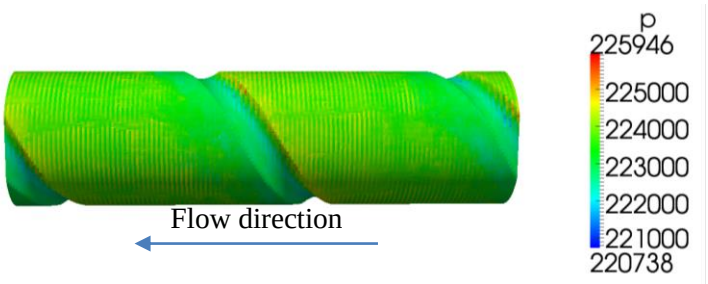

Figure 4-8: Alternating absolute pressure [Pa] in the ribbed tube case, axial view of the outer layer of cells.

4.6. `QSSAPipeFoam` Solver

The `QSSAPipeFoam` solver has been developed and validated at the LCT, specifically for reactive RANS and LES in tubular reactors [8]. The most obvious way to simulate a reactor is by defining a mesh with a length equal to that of the reactor. However, this results in an excessively large simulation domain (250-1000 million cells), considering the length of the reactor (10 m). The `QSSAPipeFoam` solver allows to reduce the computational domain to a fraction of the total domain, using streamwise periodic boundary conditions. The simulation domain is then advanced in time, corresponding to travelling through the physical reactor. At each time step, the average properties of the domain are the average properties at the corresponding axial position in the reactor. Figure 4-9 illustrates this concept. The transformation of the time of the transient simulation to the reactor axial position in a (statistically) steady simulation requires two major corrections to the conservation equations [8].

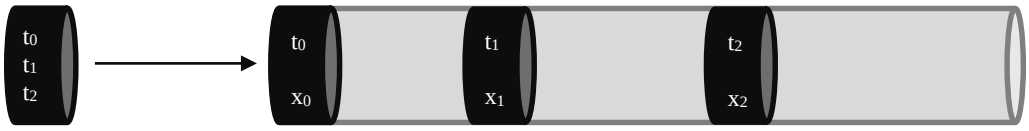

Figure 4-9: Illustration of the link between the periodic simulation and the position in the reactor [8].

The first is a source term to compensate for changes in the total mass contained in the periodic domain. These changes are a result of changes in density in the physical reactor. A second correction takes into account deviations from ideal plug flow, which is initially assumed when performing the transformation. This correction requires the solution of one additional conservation equation for the local fluid age. Details on the solver, which is schematically represented in Figure 4-10, will be published by Van Cauwenberge et al. [8].

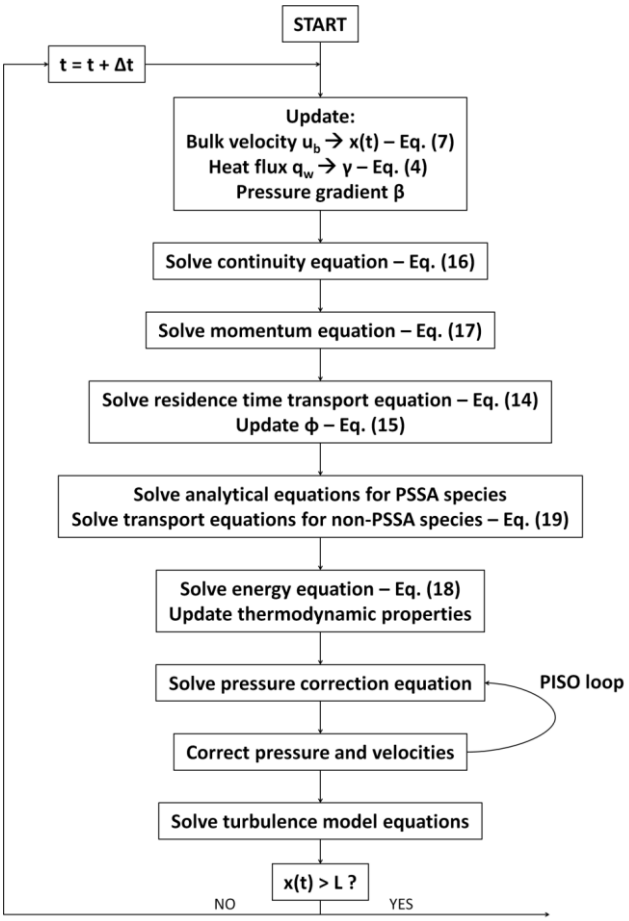

Figure 4-10: Schematic flow chart of the `QSSAPipeFoam` solver [8].

4.7. Heat Flux Profiles

Steam cracking is an endothermic process, therefore without external heat input into the system, no reaction takes place. There are two possible approaches to include this heat input in the simulation. The first method consists of not only simulating the reactor tubes, but also the furnace in so-called coupled reactor-furnace simulations [18, 19]. However, typically coupled simulations only use reactor model equations and focus on the flow patterns in the furnace, not in the reactor itself. Due to the scale of the simulation domain, using coupled simulations is not feasible at the level of large eddy simulation. The second, most commonly used method in case of CFD-reactor simulations, is imposing a heat flux profile as boundary condition on the tube wall [15, 20]. For obvious reasons, the second method will be used here. For the bare tube and ribbed, heat

flux profiles are available from the work of Zhu [13]. For the finned tube, the same heat flux profile as for the bare tube is used, corrected for the external wall surface area, such that the total, cumulative heat input to the finned tube is equal to that to the bare tube. The three profiles are shown in Figure 4-11. Equations (4-14) to (4-16) give the polynomial expressions that describe these curves. The finned tube has a much lower heat flux per unit surface area than the other two because the circumference, and hence the surface area for heat transfer, of the finned tube is much larger than the other two.

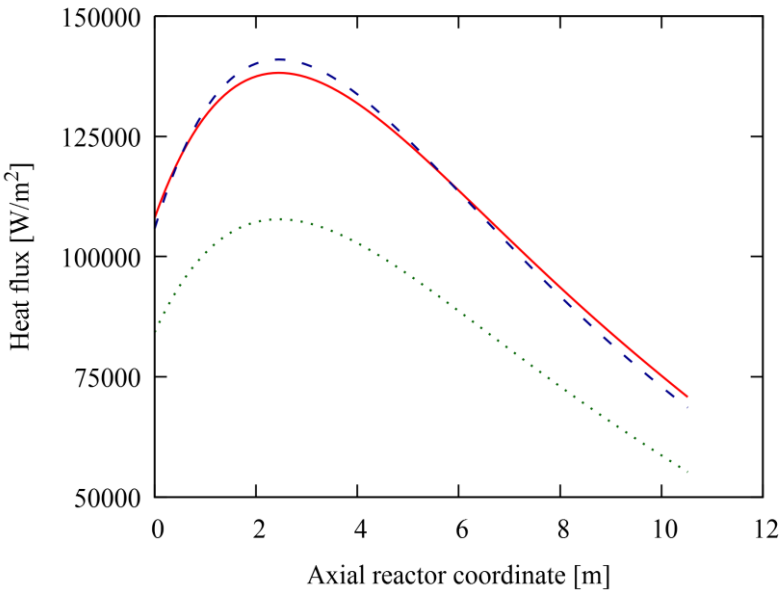

Figure 4-11: Heat flux profiles for the different geometries. Bare tube (—), Finned tube (· · ·), Ribbed tube (– –).

$$\dot{q}_{bare}(x) = -0.057x^6 + 3.07x^5 - 77.8x^4 + 1.137 \cdot 10^3 x^3 - 9{,}362 \cdot 10^3 x^2 + 29.466 \cdot 10^3 x + 108.047 \cdot 10^3 \quad \textbf{(4-14)}$$

$$\dot{q}_{ribbed}(x) = -0.072x^6 + 3.89x^5 - 96.9x^4 + 1.386 \cdot 10^3 x^3 - 11.125 \cdot 10^3 x^2 + 34.586 \cdot 10^3 x + 105.819 \cdot 10^3 \quad \textbf{(4-15)}$$

$$\dot{q}_{finned}(x) = \dot{q}_{bare}(x) \frac{p_{bare}}{p_{finned}} \quad \textbf{(4-16)}$$

4.8. Parallel Scaling

OpenFOAM is equipped with message passing interface (MPI) implementations, allowing cases to be run in parallel on several processors. The work of Sprague (see paragraph 3.3.3) shows that OpenFOAM should parallelise efficiently to around 40,000 cells per processor [21]. In the present case this implies that the bare tube case which comprises around 4 million cells should scale well on 100 processors. The finned and ribbed geometries which consist of 6 and 14 million cells respectively can be expected to scale on even more processors. The used HPC infrastructure relies on the Intel® MPI Library to communicate between nodes over the InfiniBand network. To check the scaling of the simulations using this tool, the bare and ribbed cases are run on different numbers of processors. The test is performed for non-reactive flow and in both cases is simulated for around 400 time steps. Due to the dependence of the time step on the mesh

spacing via the Courant number, this corresponds to 0.002 s in the bare tube (476 time steps) and 0.0002 s in the ribbed case (375 time steps). This results in an average time step of 4.2 10^{-6} and 5.33 10^{-7} s for respectively the bare and ribbed tubes.

The scaling results are summarised in Figure 4-12. Surprisingly, the ribbed tube appears to scale less efficiently than the bare tube despite having significantly more cells per processor. The method used for decomposition can be a cause of this counter-intuitive behaviour. The "scotch" method of OpenFOAM is used for decomposing the domain. However, several other methods exist, of which METIS [22] is frequently used. The decomposition method heavily influences the number of processor interfaces, which is an important parameter in the scaling efficiency. The lower the number of processor interfaces, the less communication is required between cores. Load balancing also depends heavily on the decomposition mechanism: a processor with a large number of easy-to-solve solid cells will be idling while others processors with fluid cells are still calculating. Dividing the computational load rather than the amount of cells uniformly over the available processors is the task of the decomposition scheme.

The ribbed tube poses additional difficulties for decomposition, due to its more irregular geometry. Differences in the efficiency with which the cases are decomposed can explain the unexpected scaling trend in Figure 4-12. For the bare tube the deviation from the theoretical speed-up sets in at a lower number of processors than reported by Sprague [21]. Based on these observations it is initially opted to decompose the meshes on 4 nodes (64 processors) for the bare and finned cases. Despite the lower efficiency, it is opted to decompose the ribbed geometry on 8 nodes (128 processors). The required simulation time on 4 nodes would simply be too long, as the time step of the ribbed simulations is an order of magnitude smaller than for the other two cases due to the smaller cell sizes and the CLF number limitation.

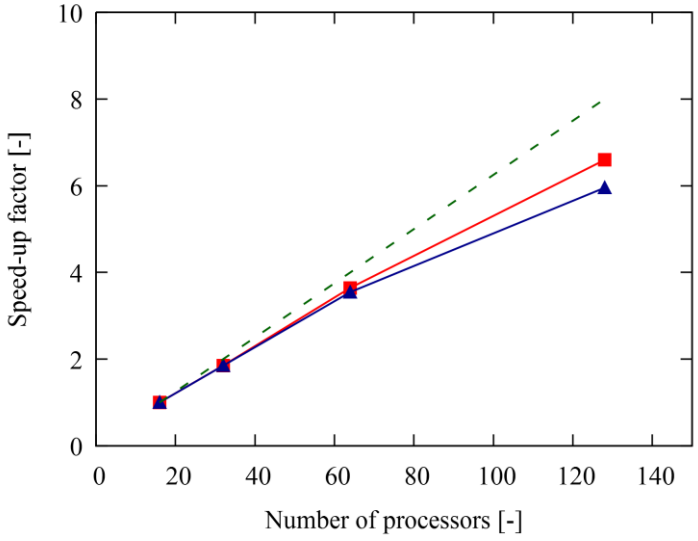

Figure 4-12: Speed-up factors on different numbers of processors. Theoretical speed-up factor (– –), actual speed-up factor for bare (■) and ribbed (▲) tubes.

4.9. References

1. Welty, J. R.; Wicks, C. E.; Wilson, R. E.; Rorrer, G. L., Differential Equations of Fluid Flow. In *Fundamentals of Momentum, Heat, and Mass Transfer*, John Wiley and Sons, Inc.: , 2008; pp 99-112.
2. Ferziger, J. H.; Peric, M., Solution of the Navier-Stokes Equations. In *Computational Methods for Fluid Dynamics*, 3rd ed.; Springer-Verlag: Berlin, 2002; pp 157-216.
3. Greenshields, C. J., *OpenFOAM: The Open Source CFD Toolbox User Guide*. OpenFOAM Foundation Ltd.: 2015; p 230.
4. Rodrigues, M. A.; Padrela, L.; Geraldes, V.; Santos, J.; Matos, H. A.; Azevedo, E. G., Theophylline polymorphs by atomization of supercritical antisolvent induced suspensions. *The Journal of Supercritical Fluids* **2011,** 58, (2), 303-312.
5. Fox, R. O., Turbulent Reacting Flows. In *Computational Models for Turbulent Reacting Flows*, Cambridge University Press: 2003; pp 1-26.
6. Welty, J. R.; Wicks, C. E.; Wilson, R. E.; Rorrer, G. L., Differential Equations of Heat Transfer. In *Fundamentals of Momentum, Heat, and Mass Transfer*, John Wiley and Sons, Inc.: , 2008; pp 217-223.
7. Ducros, F.; Nicoud, F.; Poinsot, T. In *Wall-adapting local eddy-viscosity models for simulations in complex geometries*, International Conference on Computational Conference, 1998; 1998; pp 293-300.
8. Van Cauwenberge, D. J.; Vandewalle, L. A.; Reyniers, P. A.; Van Geem , K. M.; Marin, G. B., Periodic Reactive Flow Simulation: Proof of Concept for Steam Cracking Coils. *AIChE Journal* **2016,** In preparation.
9. Moin, P.; Squires, K.; Cabot, W.; Lee, S., A dynamic subgrid-scale model for compressible turbulence and scalar transport. *Physics of Fluids A* **1991,** 3, (11), 2746-2757.
10. Gao, C. W.; Allen, J. W.; Green, W. H.; West, R. H., Reaction Mechanism Generator: Automatic construction of chemical kinetic mechanisms. *Computer Physics Communications* **2016,** 203, 212-225.
11. Reyniers, P. A.; Schietekat, C. M.; Van Cauwenberge, D. J.; Vandewalle, L. A.; Van Geem, K. M.; Marin, G. B., Necessity and Feasibility of 3D Simulations of Steam Cracking Reactors. *Industrial & Engineering Chemistry Research* **2015,** 54, (49), 12270-12282.
12. Zimmermann, H.; Walzl, R., Ethylene. In *Ullmann's Encyclopedia of Industrial Chemistry*, Wiley-VCH Verlag GmbH & Co. KGaA: 2000.
13. Zhu, M. Large eddy simulation of thermal cracking in petroleum industry. Université de Toulouse, 2015.
14. Chin, C.; Ooi, A.; Marusic, I.; Blackburn, H., The influence of pipe length on turbulence statistics computed from direct numerical simulation data. *Physics of Fluids* **2010,** 22, (11), 115107.
15. Van Cauwenberge, D. J.; Schietekat, C. M.; Floré, J.; Van Geem, K. M.; Marin, G. B., CFD-based design of 3D pyrolysis reactors: RANS vs. LES. *Chemical Engineering Journal* **2015**.
16. Chapman, D. K., Computational aerodynamics development and outlook. *AIAA Journal* **1979,** 17, (12), 1293-1313.
17. Kravchenko, A. G.; Moin, P., On the Effect of Numerical Errors in Large Eddy Simulations of Turbulent Flows. *Journal of Computational Physics* **1997,** 131, (2), 310-322.
18. Heynderickx, G. J.; Oprins, A. J.; Marin, G. B.; Dick, E., Three-dimensional flow patterns in cracking furnaces with long-flame burners. *AIChE Journal* **2001,** 47, (2), 388-400.
19. Hu, G.; Wang, H.; Qian, F.; Van Geem, K. M.; Schietekat, C. M.; Marin, G. B., Coupled simulation of an industrial naphtha cracking furnace equipped with long-flame and radiation burners. *Computers & Chemical Engineering* **2012,** 38, 24-34.
20. Schietekat, C. Computational Fluid Dynamics-based Design of Steam Cracking Reactors. Universiteit Gent, 2015.
21. Sprague, M. A. In *A comparison of Nek5000 and OpenFOAM for DNS of turbulent channel flow*, Nek5000 Users Meeting, Argonne National Lab, 2010; Argonne National Lab, 2010.
22. Karypis, G.; Kumar, V., A fast and high quality multilevel scheme for partitioning irregular graphs. *SIAM Journal on scientific Computing* **1998,** 20, (1), 359-392.

5

LES of Butane Cracking

5.1. Non-Reacting Flow Statistics: Two-Point Correlation

In paragraph 2.4.2 it has been mentioned that the only correct boundary condition for turbulent flow is the solution itself. Therefore it is impossible to immediately start with the reactive simulation. First, the turbulent flow field should be developed. The initial flow field for the cold simulation is a quasi-uniform velocity field, with perturbed regions near the wall. This perturbed field is generated by the `perturbUcyl` utility. The goal of the perturbations is to introduce some randomness in the computational domain from which turbulent structures can develop. Without these initial perturbations, turbulence could only develop from numerical inaccuracies during the simulation, which would take a considerable amount of time. In this pre-simulation stage, not only the turbulent velocity and pressure fields (mass and momentum equations) are developed, the wall- and bulk temperature fields (energy equation) are also developed, without increasing the mixing cup average temperature of the computational domain. To ensure that the turbulence is fully developed, the case is simulated for more than five times the flow-through time of the computational domain.

An important aspect of the numerical domain is its axial length. Due to the streamwise periodic boundary conditions imposed on the numerical domain, it is crucial that the axial domain length is sufficient to avoid feedback or resonance effects. Chin et al. [1] report different minimal lengths ranging from πR to $8\pi R$, depending on the property that is important. For flow characteristics such as turbulent intensity and velocity field, a minimum of $2\pi R$ is advised [2], decreasing with increasing Reynolds number [1]. Considering the high Reynolds number of the flow that is investigated in this work and the fact that the flow statistics are not the parameters of interest, the domain length of $8R$ should be sufficient to avoid feedback due to the streamwise periodic boundary conditions. Even in the ribbed tube geometry, in which the pitch of the rib resulted in a length of approximately $7R$, the recommended $2\pi R$ length is fulfilled. To confirm the absence of feedback, the streamwise two-point correlation, given by eq. (5-1), of the velocity is calculated. Ideally, the correlation at the centre of the domain should go to zero.

$$R_{ij}(z) = \frac{\frac{1}{N_z}\sum_{i=1}^{N_z} I(r,\theta,z)J(r,\theta,z+i\Delta z)}{\sigma_i \sigma_j} \qquad \textbf{(5-1)}$$

Figure 5-1 shows the two-point correlation in the bare tube. The correlation is calculated after averaging the velocity in different numbers of points. When only one point is used (no averaging), the correlation oscillates quite strongly. However, the oscillations are centred more or less around the x-axis. When the average data from four different points at a certain radial position is used, the oscillations are much less and the two-point correlation approaches zero quite well. The picture is somewhat different in Figure 5-2, which shows the two-point correlation for the finned tube case. Using only one point, the correlation appears to converge towards zero acceptably, however, when using two- or four-point averages, the correlation does not appear to converge. This could point out some feedback effects, as the outer radius of the finned tube

is substantially larger than the hydraulic diameter. The geometry is assumed to be adequate though, as the deviation of the two-point correlation is not too high. Finally, for the ribbed geometry, the two-point correlation is calculated at different radial positions and with different numbers of axial points. The results are shown in Figure 5-3. The radial position used for the calculation does not influence the general trend of the two-point correlation. On the other hand, using a larger number of axial points has a major impact. While for 100 axial points, the shape resembles that for the finned case in Figure 5-2, when using 200 axial points, the correlation converges to zero very well. In general, for all three of the meshes, it can be concluded that the axial domain is sufficiently long to prevent resonance effects from the streamwise periodic boundary conditions.

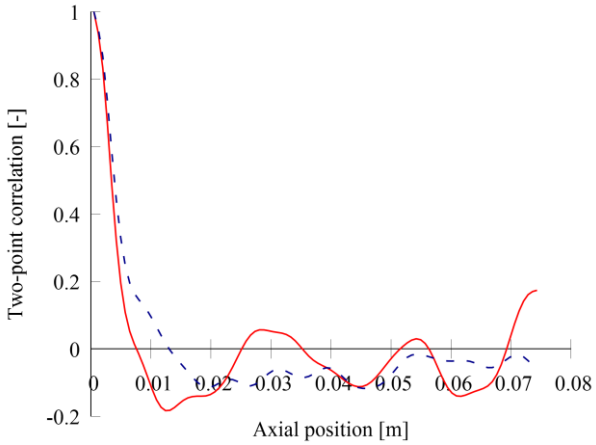

Figure 5-1: Two-point correlation in the bare tube. Correlation at a radial position of 0.005 m using 100 axial points and 1 (——) or 4 (- - -) tangential points.

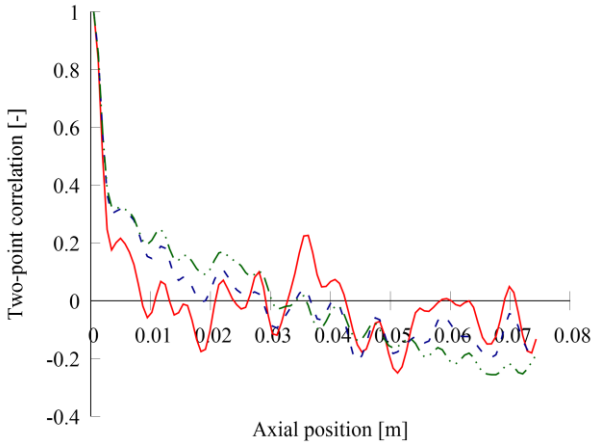

Figure 5-2: Two-point correlation in the finned tube. Correlation at a radial position of 0.004 m using 200 axial points and 1 (——), 2 (- - -) or 4 (· · —) tangential points.

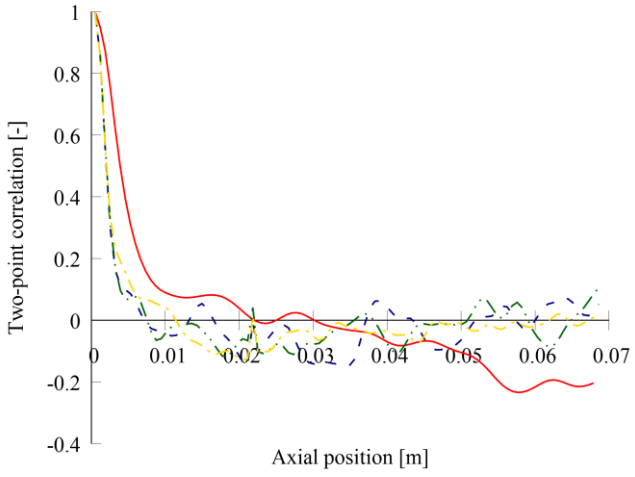

Figure 5-3: Two-point correlation in the ribbed tube. Correlation calculated with four different numerical conditions: Radial position of 0.0025 m, 100 axial and 8 tangential points (——); radial position of 0.001 m, 200 axial and 8 tangential points (- - -); radial position of 0.002 m, 200 axial and 8 tangential points (· · —); radial position of 0.004, 200 axial and 8 tangential points (—· —).

5.2. Comparison to 1D CHEMKIN

The `QSSAPipeFoam` solver has been validated by Van Cauwenberge [3]. A first validation of the simulation results is carried out by comparing them with the results of one dimensional simulations using CHEMKIN. In CHEMKIN the assumption of pseudo-steady state for the reactive, radical species is not applied. Furthermore, one-dimensional plug flow is assumed. Considering the process conditions in a steam cracking tube, this can be an acceptable assumption in the bare tube case [2]. Nonetheless, even in the bare geometry and especially in the ribbed geometry, the assumption of one dimensional flow will introduce significant error in the results. In the finned tube case, the geometry can be to some extent accounted for by using the hydraulic diameter and actual tube surface area. The three dimensional character of the rib makes this approach far less accurate in the ribbed tube. Consequently, it is expected that some deviations will be observed between the 1D simulations and the average profiles from the large eddy simulations. In her work, Zhu [4] simulated the reactors with an imposed pressure profile provided by TOTAL. Those same profiles are imposed on the 1D CHEMKIN simulations for the bare and ribbed cases. The same is true for the heat flux profiles. These have been given in section 4.7. For the finned case, no profiles are available. To have adequate heat flux and pressure profiles for the finned tube, those used in the bare tube case are scaled by the external surface. CHEMKIN assumes a bare tube, making it impossible to translate the finned geometry adequately. Therefore, the following assumptions are made for the one dimensional finned tube. The corresponding diameter is 0.0381 m and the heat flux profile is the same as in the bare tube. This ensures that the total heat input in both cases is equal, while the corrected pressure profile and correct cross-sectional area should estimate the velocity acceptably. As for the pressure drop, being an extrinsic quantity, the increased surface area will result in a proportional increase in the pressure drop. For all cases, an equal inlet pressure is assumed, to correspond to the inlet conditions in the LES. The pressure profiles are given in Figure 5-4. Equations (5-2) to (5-4) give the polynomial expressions for the pressure profiles.

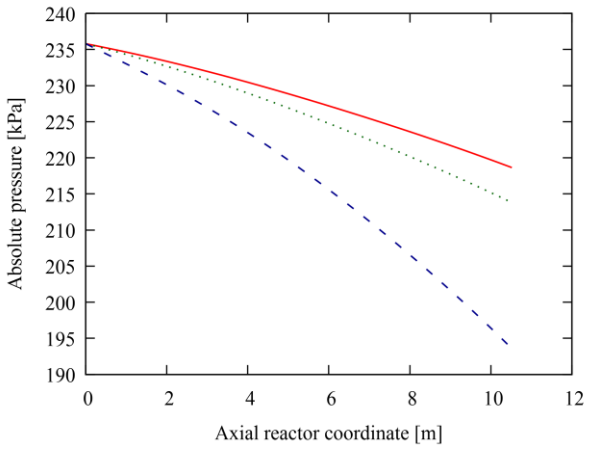

Figure 5-4: Pressure profiles for the different geometries. Bare tube (—), Finned tube (· · ·), Ribbed tube (– –).

$$P_{bare}(x) = 1 \cdot 10^{-6}x^6 - 5 \cdot 10^{-5}x^5 + 7 \cdot 10^{-4}x^4 - 0.002x^3 + 0.0595x^2 - 1.096x + 235.8 \quad \textbf{(5-2)}$$

$$P_{ribbed}(x) = 8 \cdot 10^{-6}x^6 - 4 \cdot 10^{-4}x^5 + 0.0066x^4 - 0.054x^3 + 0.0621x^2 - 2.798x + 235.8 \quad \textbf{(5-3)}$$

$$dP_{finned}(x) = dP_{bare}(x)\frac{p_{finned}}{p_{bare}} \quad \textbf{(5-4)}$$

The most important results from the simulation are the profiles of temperature, pressure and conversion, supplemented by those of velocity and mass fractions of ethene and propene. They are presented in Figure 5-5 to Figure 5-10. Based on the one dimensional simulations, the observed differences in the results between the different geometries are insignificant. As mentioned above, one dimensional simulations can only marginally account for the different geometries, which are inherently at least two dimensional (axial and radial variations). The only parameter in which a remarkable difference is observed is the velocity. However, as the flow is gaseous, pressure, temperature and velocity are strictly coupled via the equation of state. As the pressure profiles are imposed on the simulation, it is no surprise that the velocity follows. As expected, the CFD results do not agree with the CHEMKIN results quantitatively, though the qualitative agreement is very good. For example, the 1D simulations predict a change in slope of the temperature (Figure 5-5), which is quite abrupt. This change in slope is also predicted in the 3D turbulence simulations but much more gradual. As a result the temperature disagreement between the one and three dimensional simulations reaches up to 30 K. This is also reflected in the conversion (Figure 5-7) and olefin concentrations (Figure 5-9 and Figure 5-10). However, one would intuitively expect the conversion in the LES cases to be lower due to the lower temperature. The reason for the higher conversion at lower average temperatures, is that in these graphs the average temperature is considered. A detailed explanation for this counter-intuitive observation is given in paragraph 5.3.4. By the end of the reactor, the conversion profiles practically coincide. Throughout the entire reactor, the 1D simulations underestimate the ethene concentrations, while overestimating the propene concentrations. This too is the result of using only the average temperature for the calculation of the rates. This makes it impossible to account for important local differences in reaction rates. Regarding the pressure profiles (Figure 5-6), the quantitative agreement is much better, though the pressure drop is somewhat higher in the 3D simulations than the profiles imposed on the 1D simulations. This is encouraging as the imposed pressure profiles are industrial profiles given by TOTAL. Consequently, the velocity profile (Figure 5-8) from the one dimensional simulation can match that of the three dimensional simulation excellently.

From the above, it can be concluded that the results of the LES can be considered reliable, as one dimensional simulations are in good qualitative and reasonable quantitative agreement.

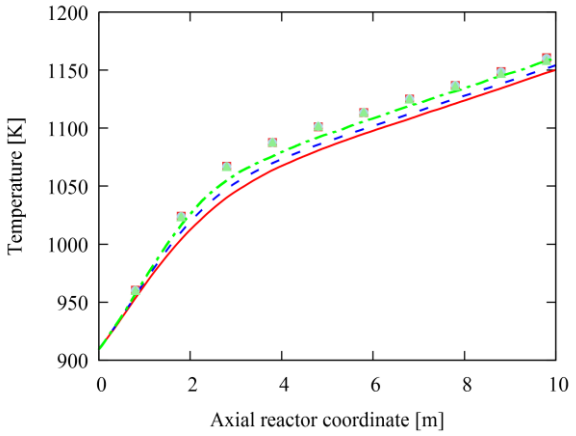

Figure 5-5: Temperature profiles as simulated in CHEMKIN: bare tube (■), finned tube (●) and ribbed tube (▲); and LES: bare tube (———), finned tube (– –) and ribbed tube (— -).

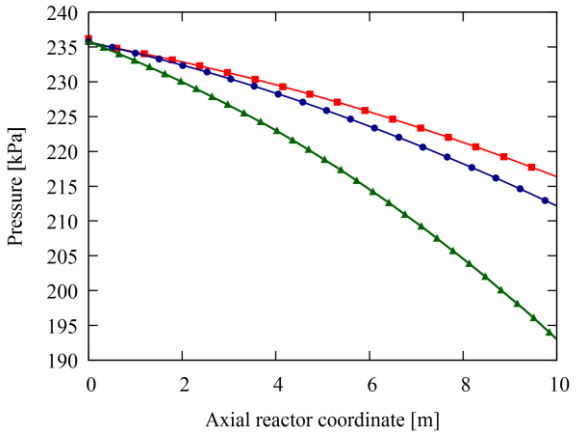

Figure 5-6: Pressure profiles as simulated in CHEMKIN: bare tube (■), finned tube (●) and ribbed tube (▲); and by LES: bare tube (———), finned tube (– –) and ribbed tube (— -).

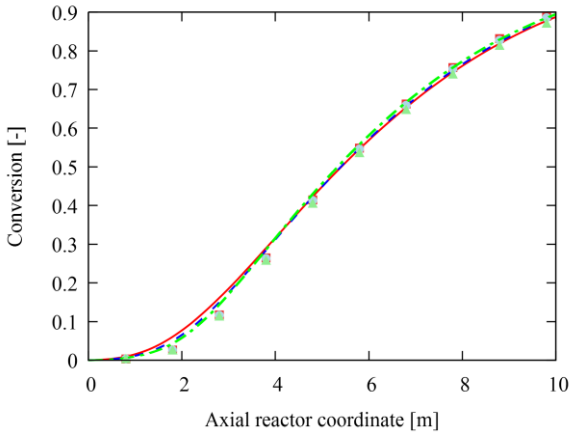

Figure 5-7: Conversion profiles as simulated in CHEMKIN: bare tube (■), finned tube (●) and ribbed tube (▲); and LES: bare bare tube (———), finned tube (– –) and ribbed tube (— -).

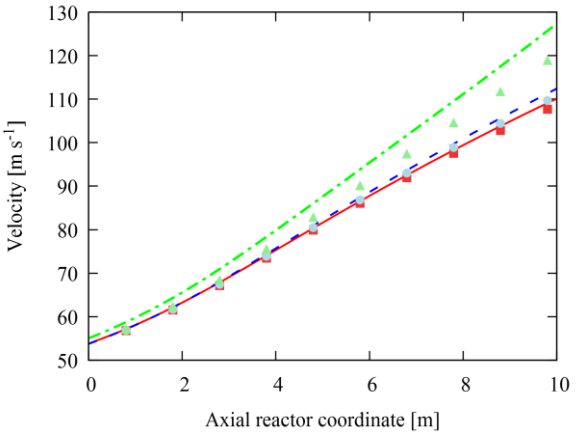

Figure 5-8: Velocity profiles as simulated in CHEMKIN: bare tube (■), finned tube (●) and ribbed tube (▲); and by LES: bare tube (———), finned tube (– –) and ribbed tube (— -).

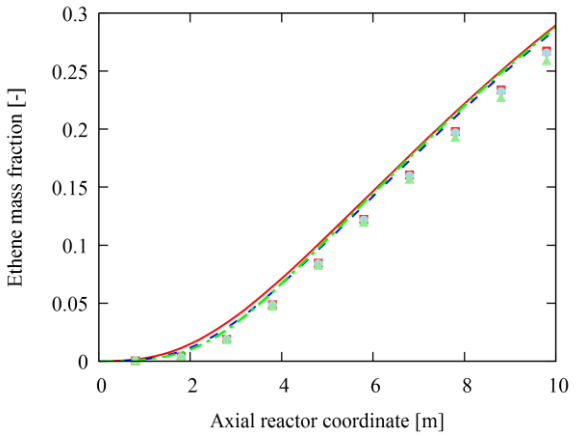

Figure 5-9: Ethene mass fraction as simulated in CHEMKIN: bare tube (■), finned tube (●) and ribbed tube (▲); and LES: bare tube (———), finned tube (– –) and ribbed tube (— -).

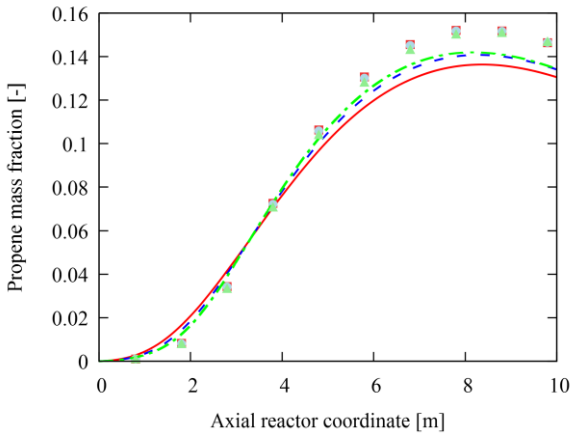

Figure 5-10: Propene mass fraction as simulated in CHEMKIN: bare tube (■), finned tube (●) and ribbed tube (▲); and LES: bare tube (———), finned tube (– –) and ribbed tube (— -).

5.3. Discussion of Results

5.3.1. Flow Patterns

The aim was to simulate flows with a Reynolds number corresponding to that in the work of Zhu [4], namely approximately 72,000. Due to the increasing velocity and decreasing density, the Reynolds number drops along the length of the reactor. The simulated inlet Reynolds numbers are 78,544; 61,582 and 79,518 for the bare, finned and ribbed tubes respectively. The reason for the low Reynolds number in the finned geometry, is the large difference in hydraulic diameter with the other cases. The hydraulic diameter of the finned geometry is 0.0297 m, while it is 0.0381 and 0.0374 for respectively the bare and ribbed cases. The finned geometry was designed based on an equal cross-sectional flow area as in the bare tube, to have an approximately equal bulk velocity. In all geometries, the Reynolds number drops by approximately 6 % throughout the first meter of the reactor and by 21.6, 21.9 % and 22.2 % by the end of respectively the bare, finned and ribbed reactors. Consequentially, the average Reynolds number is substantially lower than the inlet value. For the bare tube, the average Reynolds number is 66,641, for the internally finned tube it is 52,206 and for the ribbed tube the average Reynolds number is 67,158.

The instantaneous streamlines in the different geometries are displayed in Figure 5-11 to Figure 5-13 for plugs at an axial position around 0.8 m. Even though the plugs are not at identical positions, comparison of the general flow characteristics is still possible. Comparison of absolute values of instantaneous results does not make sense, even at identical axial positions, as turbulent fluctuations will distort the conclusions. Neither the bare nor the finned tube display any particular axial flow pattern, the stream lines are on average parallel to the tube axis (Figure 5-11and Figure 5-12) and the highest velocity zone is found in the centre of the tube. In the lobes of the finned tube, the flow does have a higher vorticity than in the centre, however the flow remains more or less unidirectional. In the ribbed tube, the flow has a swirling character, indicated by the non-coaxial lines with high vorticity in Figure 5-13. The swirling is a result of the rib making an angle with the tube axis. The flow that impinges on the rib is pushed towards the tube axis, but at an angle. This introduces a radial and tangential component to the velocity. The tangential component gives rise to the discussed swirling character, while the radial component gives rise to a sine-like flow axis. Figure 5-14 is an axial cross-section of the velocity field. The red line indicates the axis of the flow. In front of the rib, the flow is pushed away from the rib, while behind the rib, the flow is pulled back towards the rib as a result of the low pressure zone that is formed here. The square selection in Figure 5-15 shows such a low pressure zone. Two different low-velocity zones are observed, though their nature is very different. The first zone located on the trailing edge of the rib (rectangular selections in Figure 5-14), is the result of the detachment of the boundary layer at the top of the rib. The boundary layer reattaches near the extrema of the red flow axis, and remains attached until the next rib is reached. Consequentially, the region just behind the rib is bypassed by the flow. The same mechanism cannot be the cause of the second low-velocity zone (oval selections in Figure 5-14). The pressure is found to be low behind the rib and high in front of the rib (Figure

5-15). Via the simple Bernoulli equation, the high pressure in front of the rib implies that the velocity here will be low. Both low velocity zones impact the local heat transfer, influencing the local tube wall temperature.

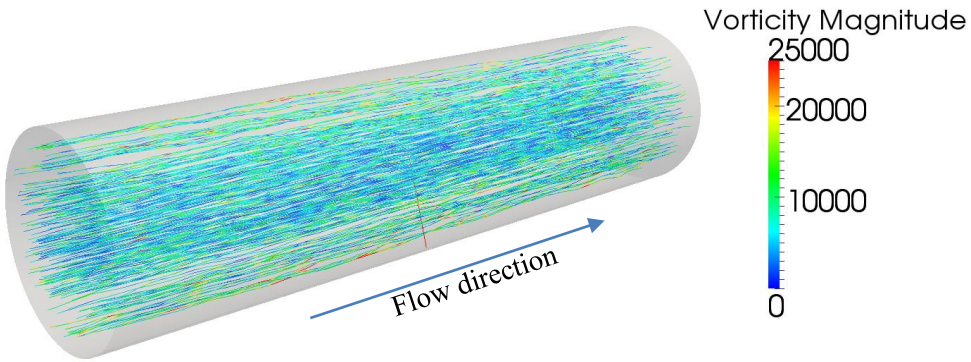

Figure 5-11: Streamlines coloured by vorticity [s^{-1}] in the bare tube, for a plug at an axial position of 0.718 m.

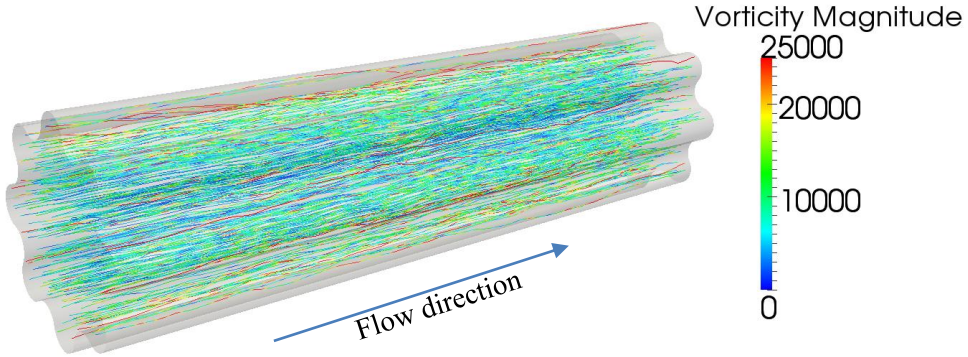

Figure 5-12: Streamlines coloured by vorticity [s^{-1}] in the finned tube, for a plug at an axial position of 0.86 m.

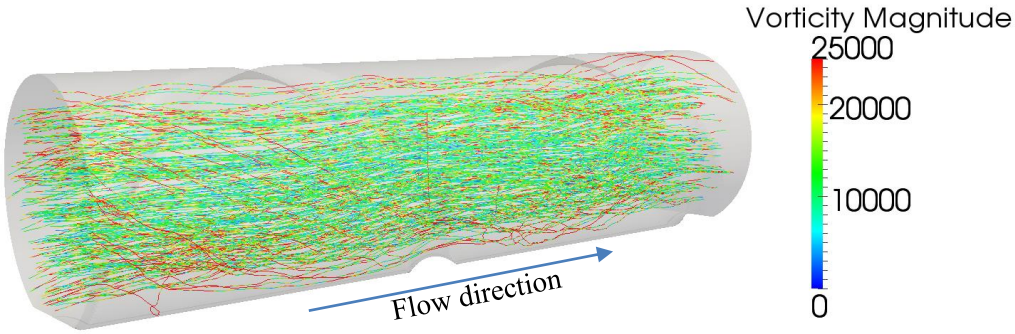

Figure 5-13: Streamlines coloured by vorticity [s^{-1}] in the ribbed tube, for a plug at an axial position of 0.825 m.

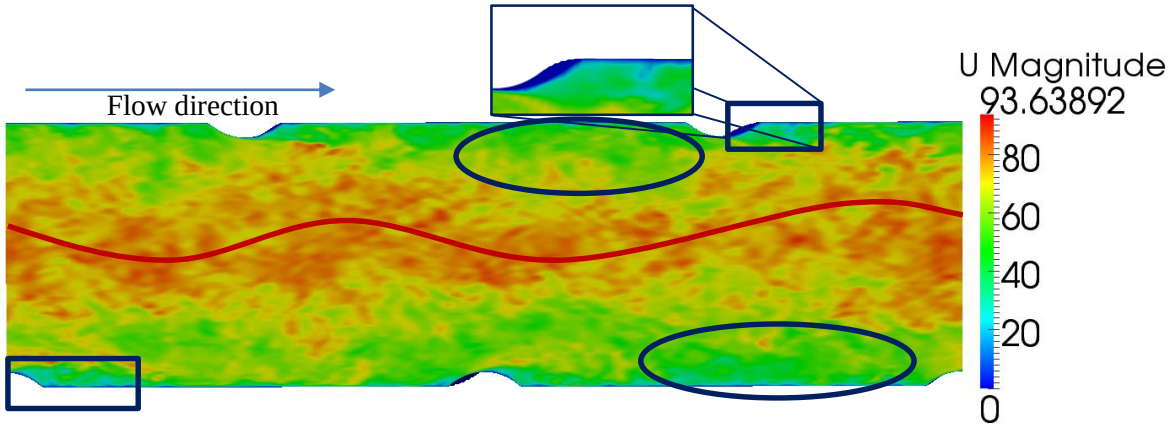

Figure 5-14: Velocity profile [m s^{-1}] in the ribbed tube, for a plug at an axial position of 0.825 m.

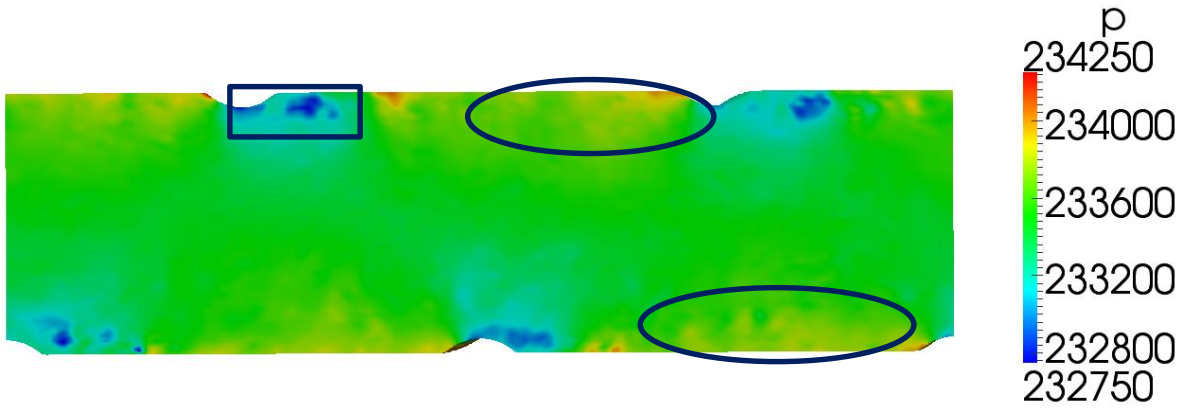

Figure 5-15: Absolute pressure field [Pa] in the ribbed tube, for a plug at an axial position of 0.825 m.

5.3.2. Heat Transfer

One of the most direct effects of enhanced coil geometries on the flow, is their influence on the heat transfer. Better heat transfer is expressed by a higher heat transfer coefficient. This implies that a lower difference between wall and bulk temperatures is possible at an equal heat flux. For equal bulk temperatures this results in a reduction of the average tube wall temperature. The heat transfer coefficient is expressed by the Nusselt number.

Figure 5-16 plots the profiles of the average wall- and bulk temperature for the different geometries. The differences in bulk temperature are only small, with the highest temperatures attained in the ribbed geometry, followed by the finned tube. There are however significant differences in the instantaneous temperature profiles between the different geometries. When comparing the right sides of Figure 5-18, Figure 5-19 and Figure 5-20, the temperature profile in the ribbed geometry is found to be the most uniform of the three, which is indicative of the highest turbulent heat transfer. This is in agreement with RANS simulations by Schietekat [5, 6], which have been discussed in section 1.3. One aspect of heat transfer that has not been accounted for in the present work, is the conductive heat transfer through the wall.

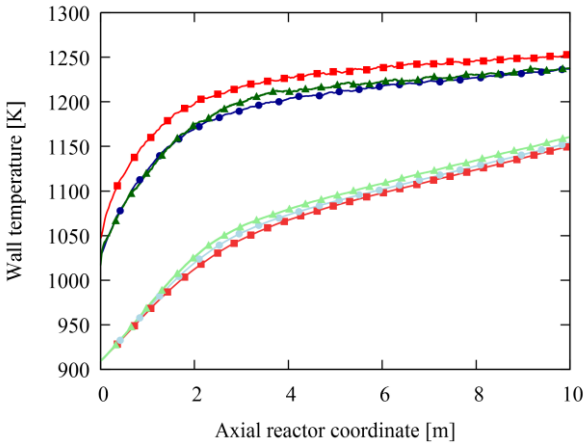

Figure 5-16: Wall temperature as function of the axial reactor coordinate in the bare (—■—), finned (—●—) and ribbed (—▲—) geometries and bulk temperature in the same order (—■—) (—●—) (—▲—).

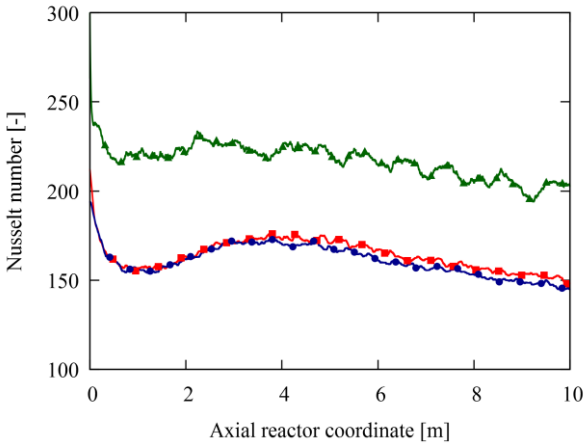

Figure 5-17: Nusselt number as function of the axial reactor coordinate in the bare (—■—), finned (—●—) and ribbed (—▲—) geometries.

For the bare and ribbed geometries this will have only minor influence on the results as the tube wall has an approximately constant thickness. For the finned tube, the tube wall thickness varies tangentially with the height of the fins. As can be seen in Figure 1-5, the fin tips (farthest away from tube centre) have a higher temperature than the fin valleys. The left image of Figure 5-19 shows that in the current simulation, this behaviour is not predicted. Though these local variations are not accounted for, the average tube wall temperature will not be affected much. The higher local temperature at the tips will be offset by a lower local temperature in the valleys. The average wall temperature for the finned and ribbed tubes are initially practically equal, while the bare tube wall is at a significantly higher temperature (by approximately 20 K). Due to the slightly higher maximal heat flux in the ribbed tube (Figure 4-11), at an axial position of about 1.8 m, the ribbed wall temperature surpasses the finned wall temperature. The heat flux decreases more rapidly towards the end of the ribbed reactor. Consequentially, at the end of the reactor, the temperature in the ribbed tube becomes equal to the temperature in the finned tube again. The lower wall temperature in the ribbed and finned coils indicates a high heat transfer coefficient. Indeed, Figure 5-17 shows that the ribbed tube has the highest Nusselt number. For the ribbed tube, comparison of the Nusselt number to that of the bare tube provides a fair comparison as the hydraulic diameters of these two geometries does not differ much (0.0381 in the bare vs. 0.0374 in the ribbed). The finned tube does not specifically promote turbulence, hence it is expected that the heat transfer coefficient and Nusselt number are of the same order as in the bare tube. Due to the lower Reynolds number, the values are even slightly lower than in the bare reactor. Nonetheless, the increased internal surface area allows an increase in heat transfer (in units W m^{-1} K^{-1}) of 25 %.

Table 5-1 provides an overview of the heat transfer characteristics in the three geometries. The improvement factor ($\frac{P_{geometry\,x} h_{geometry\,x}}{P_{bare} h_{bare}}$) is highest in the ribbed reactor. When comparing the relative improvement, an excellent agreement is found with results in similar ribbed geometries (Figure 1-7).

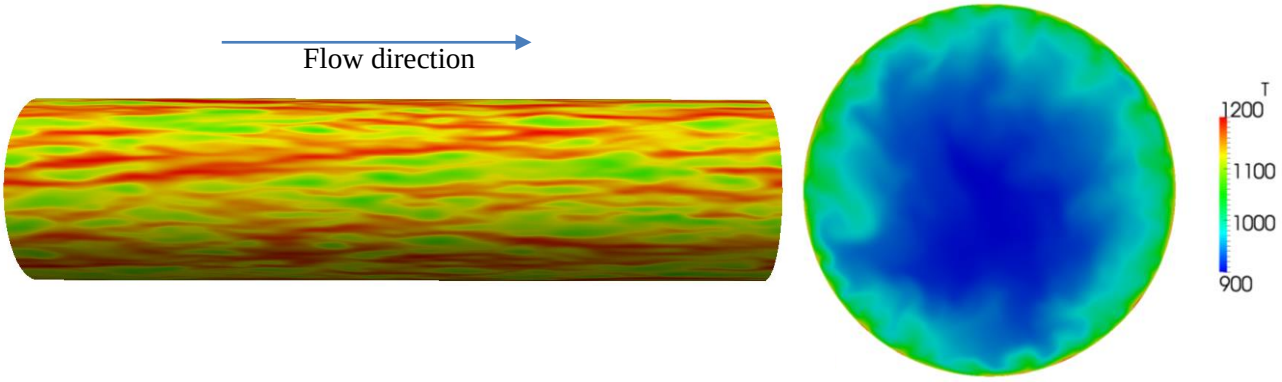

Figure 5-18: Temperature fields [K] in the bare tube, for a plug at an axial position of 0.718 m. Left: wall temperature, right: cross-sectional temperature profile.

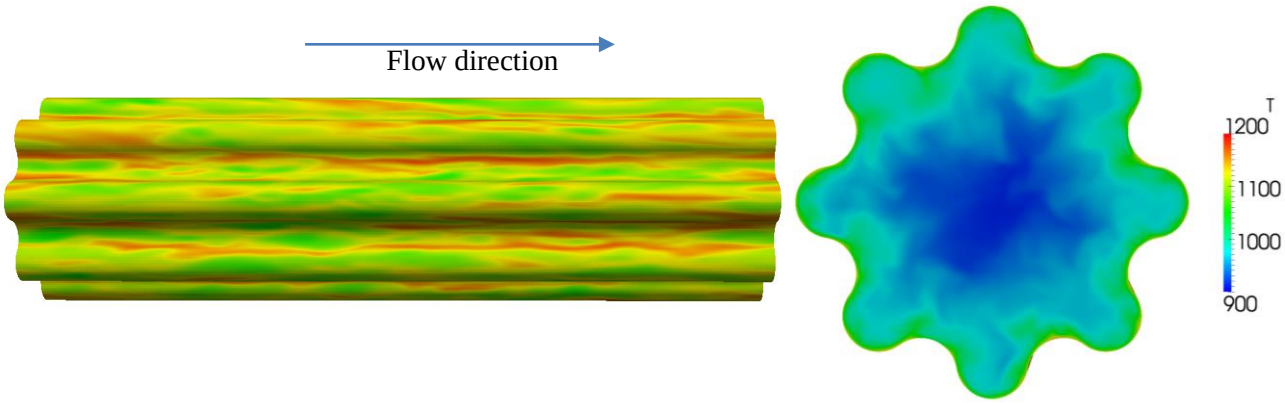

Figure 5-19: Temperature fields [K] in the finned tube, for a plug at an axial position of 0.86 m. Left: wall temperature, right: cross-sectional temperature profile.

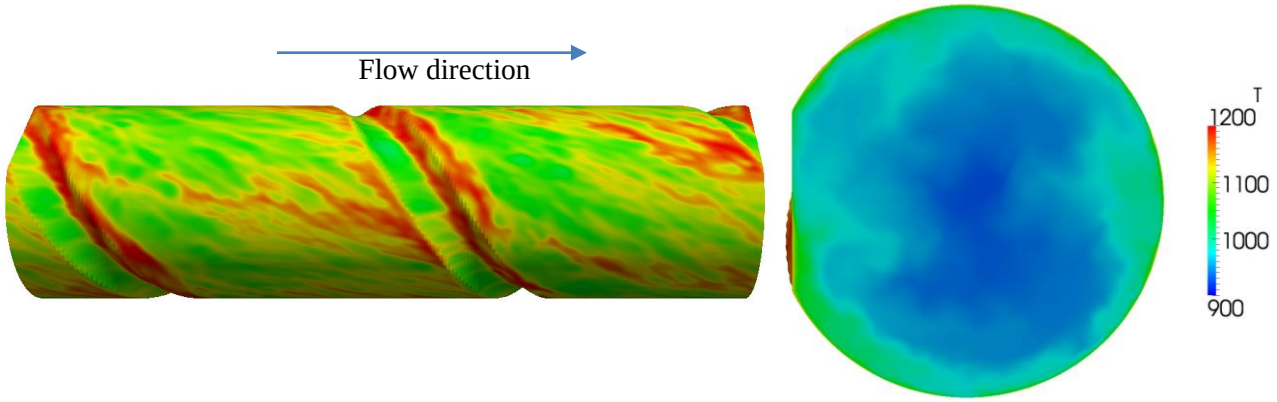

Figure 5-20: Temperature fields [K] in the finned tube, for a plug at an axial position of 0.825 m. Left: wall temperature, right: cross-sectional temperature profile.

Table 5-1: Summary of the heat transfer characteristics of the different geometries.

Geometry	*Average Nusselt number*	*Average heat transfer coefficient [W m^{-2} K^{-1}]*	*Improvement factor*
Bare	163.5	691.8	1.0
Finned	160.7	672.7	1.25
Ribbed	217.0	917.8	1.33

This paragraph is concluded by a comment on the used discretisation schemes. All flow parameters have been discretised using the variants of the `Gauss linear` schemes in OpenFOAM. Due to convergence issues of the solver, upwind schemes had to be used for the temperature and species equations. These upwind schemes are known to be very diffusive. This is illustrated in Figure 5-21. The simulations in which the turbulent velocity, pressure and temperature profiles are developed, are simulated using the `Gauss linear` schemes for the temperature as well. The result gives very detailed temperature fluctuations, similar to the velocity fluctuations in *e.g.* Figure 5-14. Once reaction is included, the upwind schemes are used and the temperature gradients and fluctuations are smeared out over the cross-section. While the large scale fluctuations are still visible, the small scale fluctuations have disappeared.

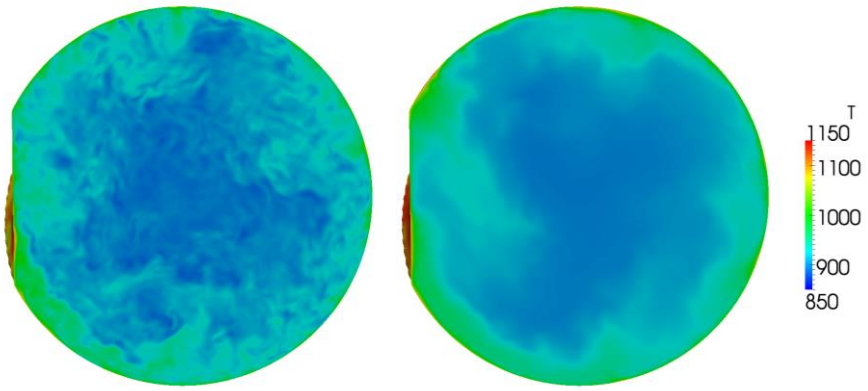

Figure 5-21: Cross-sectional temperature profiles in the ribbed geometry at the inlet of the reactor with Gauss linear discretisation (left) and at an axial position of 0.1 m with first order upwind discretisation (right).

5.3.3. Pressure Drop

In enhanced tube geometries, the increased heat transfer is always a trade-off with an increased pressure drop. For the bare and ribbed geometry, it has been shown that the pressure profiles match industrial profiles very well. In Figure 5-22, the simulated pressure profiles are displayed. The pressure drop in the ribbed geometry is much higher than in the other two geometries. One of the causes hereof is the swirling character of the flow. Due to the swirl, the path of a fluid element is longer and therefore it experiences more drag, increasing the pressure drop. Also the rib acts as an obstacle for the flow, hence momentum is transferred

when the fluid impacts on the rib. The higher Reynolds number in the ribbed tube naturally contributes to a higher pressure drop as well. Based on eq. (5-5), the friction factor can be determined along the axial length of the tubes.

$$f = \frac{D_H \left(\frac{dP}{dx}\right)}{2\rho v^2} \tag{5-5}$$

The Fanning friction factor is nearly constant throughout the entire reactor. Only close to the inlet, the values vary strongly. In the bare tube, the initial friction factor is very high, but converges rapidly to its stable value. In the finned tube, the friction factor at the inlet is only fractionally higher than the average and again, the stable value is attained early in the tube. The friction factor in the ribbed tube displays a strongly oscillating profile. It only slowly converges to a stable value. These oscillations, which even result in negative friction factors, are the result of difficult pressure convergence in the initial stages of the calculations. Due to the axis scale on Figure 5-22, it is not visible that the pressure oscillates at a high frequency in the first 0.5 m of the reactor. The amplitude of the oscillation is in the order of 10 Pa, however, the oscillation frequency is around 14,400 Hz. As the friction factor depends on the first spatial derivative of pressure, *i.e.* the pressure gradients, the amplitude of the friction factor is large. After approximately two meters, the oscillations even out and a stable value is also attained.

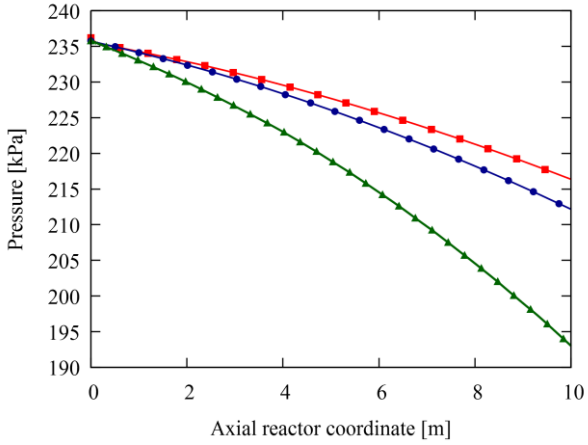

Figure 5-22: Pressure profiles in the bare (—■—), finned (—●—) and ribbed (—▲—) geometries.

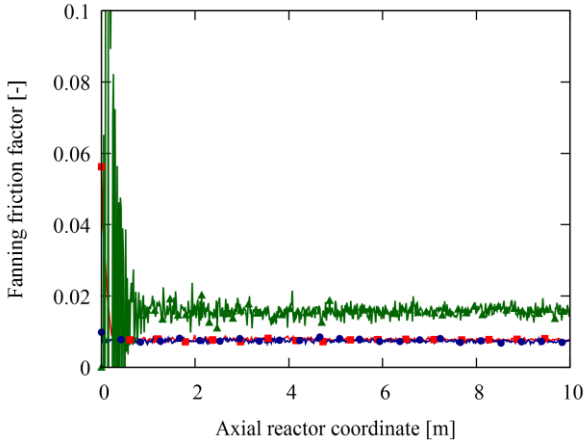

Figure 5-23: Fanning friction factor in the bare (—■—), finned (—●—) and ribbed (—▲—) geometries.

In the bare tube, the total pressure drop is 19.8 kPa, which is somewhat higher than the pressure drop of 16.1 kPa in the TOTAL data. The corresponding averaged friction factor is 0.0082. Comparing this friction factor to values from correlations such as the one proposed by Chen [7], is irrelevant. The correlations are developed for cold flow conditions. The prevailing reactive conditions are outside the boundaries of the applicability of the correlations. As expected, the pressure drop is higher in the finned reactor, namely 23.6 kPa. The fact that the average friction factor is nearly equal to that of the bare, indicates that the increase in pressure drop is simply the result of an increased internal surface area. The pressure drop in the ribbed reactor amounts to 42.7 kPa, which is 2.15 times the pressure drop of the bare reactor. In the ribbed

geometry, the friction factor is significantly higher than in both other geometries. This indicates that the increase in pressure drop is mainly related to the increased turbulence that is induced in the flow.

Table 5-2: Summary of the pressure drop characteristics in the different geometries.

Geometry	*Total pressure drop [kPa]*	*Average (Fanning) friction factor*	*Pressure drop ratio*
Bare	19.8	0.0082	1.0
Finned	23.6	0.0074	1.19
Ribbed	42.7	0.0157	2.15

5.3.4. Species Concentrations

In butane cracking, the most desired products are ethene and propene. Some butadienes will be formed as well, albeit only in small quantities. The most important by-products of butane cracking are methane, ethane, propane, butane isomers and hydrogen. Hydrogen and methane are separated and then used as fuel gas in the furnaces. The hydrogen mass fraction in the reactor outlet is very low – 0.45 wt % in the bare reactor, 0.43 wt % in the finned reactor and 0.44 wt % in the ribbed reactor – making it uneconomic to further separate this from the methane. The small quantities do not pose a real threat from a safety point of view either. Hydrogen is therefore not separately discussed as a product stream. Eqs. (5-6) to (5-8) show how respectively the conversion of butane and the yields and selectivities of the different components are determined.

$$X_{butane} = \frac{m_{butane} - m_{butane,0}}{m_{butane,0}} \quad \textbf{(5-6)}$$

$$Y_i = \frac{\left(m_i - m_{i,0}\right)}{m_{butane,0}} \quad \textbf{(5-7)}$$

$$S_i = \frac{\left(m_i - m_{i,0}\right)}{\left(m_{butane} - m_{butane,0}\right)} \quad \textbf{(5-8)}$$

Figure 5-24 and Figure 5-26 plot the selectivities towards respectively ethene and propene in the different geometries. A significant difference in selectivity is observed between the bare tube and the two enhanced coils. The difference is maximal at axial positions between 2 and 2.5 m, amounting to 2 percentage point. A similar, but inverse trend is observed in Figure 5-26 for the selectivity towards propene. The bare tube is remarkably less selective towards propene than the other two. It has been found that higher coil outlet temperatures (COT) result in higher ethene yields [8, 9]. Due to the monotonous character of the temperature (Figure 5-16), it is safe to assume that a higher COT corresponds to a higher average temperature. The bare tube is seen to have a significantly lower average bulk temperature than the other two geometries. The wall

temperature on the other hand, is the highest in the bare reactor. In Figure 5-34, it is shown that the majority of the reaction takes place close to the wall and thus at temperatures closer to the wall temperature than to the average bulk temperature. This explains why the yield of ethene (Figure 5-25) is highest in the bare tube. The effect of the temperature on the overall conversion is weaker than on the selectivities. The increased uniformity of the radial temperature implies that the elevated temperature extends farther towards the tube centre. Consequentially, the reactor volume is used more efficiently, compensating for the lower volumetric reaction rates. As yield, selectivity and conversion are related via $Y_i = X_{butane} S_i$, for similar conversions (Figure 5-7), the selectivity towards ethene will be higher as well. The same one-on-one theory does not hold for propene (Figure 5-27), which initially has a lower yield in the finned and ribbed tubes, before surpassing the bare propene yield at an axial position of 3.6 m. Table 5-3 summarises the important outlet characteristics in the three geometries. The bare reactor results in a final propene to ethene ratio of 0.451. The finned reactor is more selective towards propene, resulting in an propene to ethene ratio of 0.469. The total yield of light olefins is identical (61.0 %) in both the bare and finned reactors and is 61.3 % in the ribbed reactor. In the ribbed reactor, the propene to ethene ratio is 0.467. The higher propene to ethene ratios in the enhanced geometries are the result of the higher cracking severity near the wall, while the higher conversion is the result of the higher average bulk temperature.

Table 5-3: Overview of conversion, light olefin yields and selectivities.

Geometry	*Conversion*	*Ethene Selectivity*	*Ethene Yield*	*Propene Selectivity*	*Propene Yield*
Bare	0.887	0.477	0.420	0.215	0.190
Finned	0.891	0.469	0.415	0.220	0.195
Ribbed	0.894	0.471	0.418	0.220	0.195

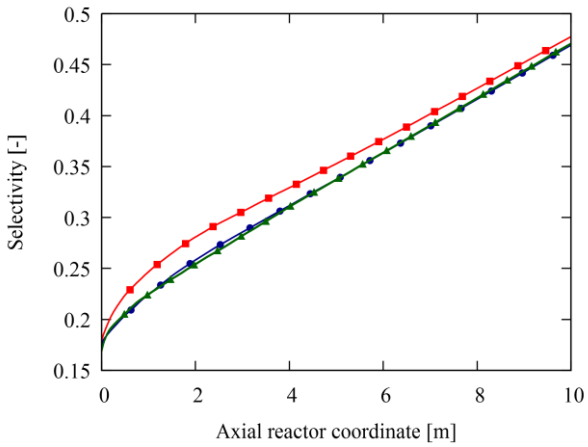

Figure 5-24: Ethene selectivity in the bare (—■—), finned (—●—) and ribbed (—▲—) geometries.

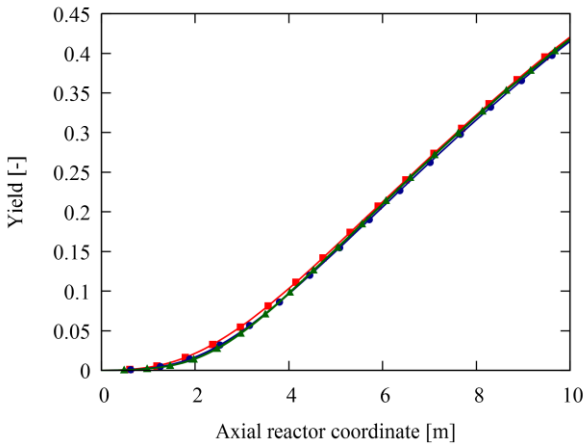

Figure 5-25: Ethene yields in the bare (—■—), finned (—●—) and ribbed (—▲—) geometries.

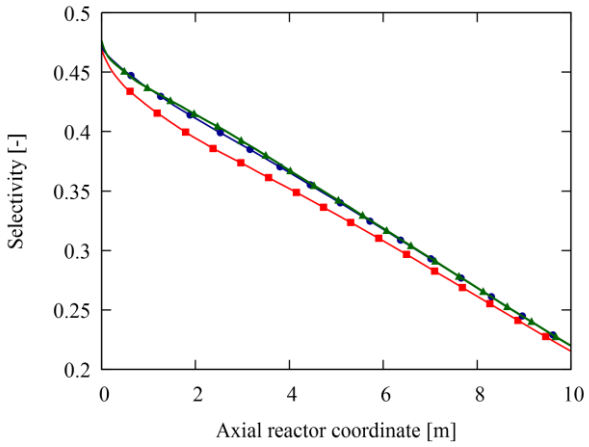

Figure 5-26: Selectivity towards propene in the bare (—■—), finned (—●—) and ribbed (—▲—) geometries.

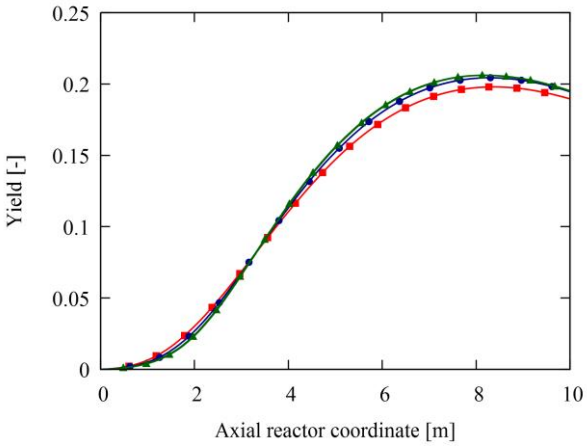

Figure 5-27: Propene yields in the bare (—■—), finned (—●—) and ribbed (—▲—) geometries.

Figure 5-28 and Figure 5-29 illustrate the evolution of the selectivities and mass fractions of the major reaction products along the axial coordinate in the bare tube. The other two geometries display some distinct differences in absolute values of the mass fractions, but the profiles follow the same qualitative trend. The initial reaction proceeds with a very high selectivity towards propene. Initially, the only reaction that takes place is the homolytic fission of butane, forming two radicals. In first approximation this creates hydro, methyl, ethyl, propyl and butyl radicals. Butane remains by far the most abundant species, therefore it is highly unlikely that a radical encounters any other molecule than butane. The above-mentioned radicals are all less stable than the butyl radical, therefore via a rapid hydrogen abstraction a butyl radical will be formed. Of the linear butyl radicals, the sec-butyl radical is the most stable. Beta-scission in the sec-butyl radical leads to the formation of propene and a methyl radical. Hence, in the initial stages of the reaction, due to the preferential formation of sec-butyl radicals and the subsequent beta-scission reaction, propene is formed with a high selectivity. As the reaction proceeds, the concentration of lighter hydrocarbons increases, increasing the selectivity towards ethene, while decreasing that towards propene. The selectivities towards methane, ethane and propane are not affected as much by the changing composition in the reactor. They are formed as secondary product in all occurring reactions, making them less sensitive to the concentrations of other components. Regarding the component mass fractions, the ethene fraction starts increasing slowly, but after approximately 3 m, continues increasing at a nearly constant rate. The propene fraction goes through a maximum at 8.06 m. The farther downstream in the reactor, the more severe the cracking conditions (*i.e.* higher bulk and wall temperature). In combination with a decreasing amount of butane and the stability of the propenyl radical (delocalisation of the radical), propene becomes the preferential component for hydrogen abstraction and subsequent reactions. Similar behaviour, but less pronounced, is observed for ethane. Propane is never formed in large quantities.

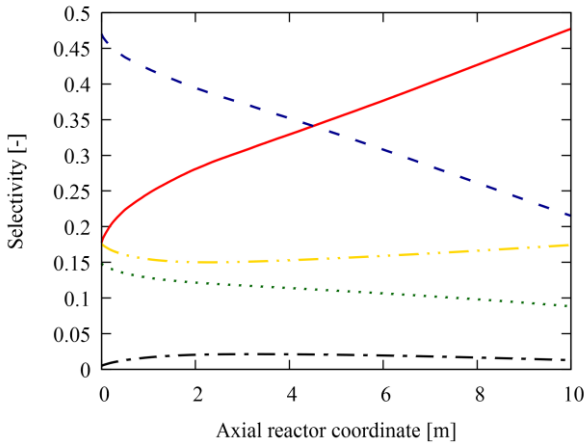

Figure 5-28: Selectivities towards the different components in the bare tube: ethene (——), propene (– –), ethane (· · · · ·), propane (— · —) and methane (— · · —).

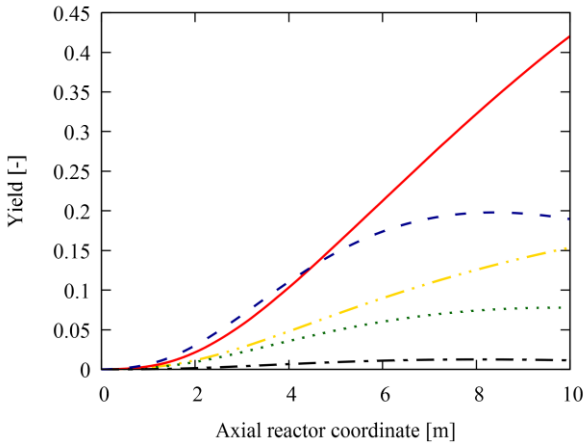

Figure 5-29: Mass fractions of the different components in the bare tube : ethene (——), propene (– –), ethane (· · · · ·), propane (— · —) and methane (— · · —).

The above discussion only considered mass fractions, selectivities and yields averaged over a plug at a given axial position. Within such a plug however, there are significant fluctuations in the concentrations and reaction rates of the species. Figure 5-30 to Figure 5-32 illustrate the ethene mass fraction fields in the different geometries, again for a plug around the position 0.8 m. Analogous conclusions can be drawn for the other species. In all cases, the highest ethene concentrations are found near the wall, where temperatures have been shown to be the highest. Near the centreline of the tubes, at this location in the reactor, there is no to little ethene present yet. However, similarly to the temperature, a gradation of mass fraction uniformity is observed. In the bare tube, the majority of the ethene is located in a narrow layer close to the wall. In the finned tube, this layer is noticeably thicker (note that in the image the tube diameter is the maximum diameter, *i.e.* from fin tip to fin tip) and the mass fraction near the wall is significantly lower, while in the ribbed tube, appreciable amounts of ethene are ascertained near the tube centreline. In both the bare and finned tubes, the ethene concentration is, on average, more or less uniform, while in the ribbed tube there are locations at which ethene is preferentially formed. These locations coincide with the locations of high temperatures, *i.e.* on the trailing edge of the rib and just in front of the leading edge. Compared to the two other geometries, the concentrations of ethene on other locations near the wall are quite low.

Figure 5-33 shows a sequence of cross-sectional ethene mass fraction fields in the bare tube. The total ethene mass fraction increases and so does the uniformity of the ethene fraction. A very similar trend is observed in the other two geometries as well. The increased uniformity could be attributed to either increased reaction taking place in the bulk or turbulent mixing. Figure 5-34 shows the butane reaction rates throughout a plug at two different locations in the reactor. The reaction rate is higher in the plug farthest in the reactor, however, even in the farthest plug, the reaction rate at the tube centreline is low, too low to explain the increase of ethene in the centre of the tube. Therefore, the main contribution to the increased homogeneity of the ethene mass fraction is turbulent mixing.

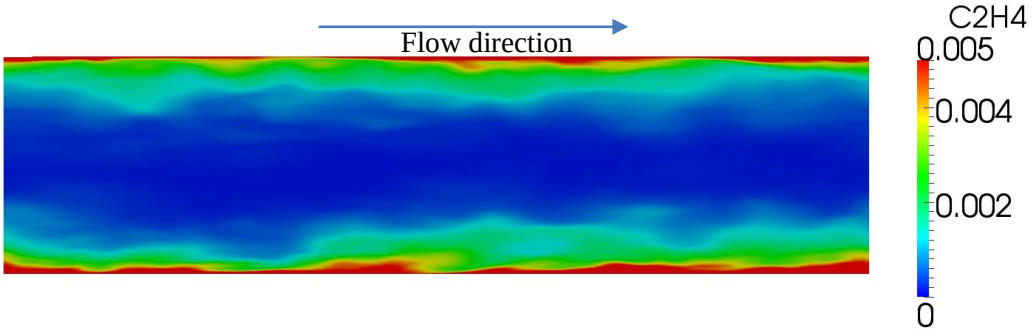

Figure 5-30: Ethene mass fraction in the bare tube for a plug at an axial position of 0.718 m.

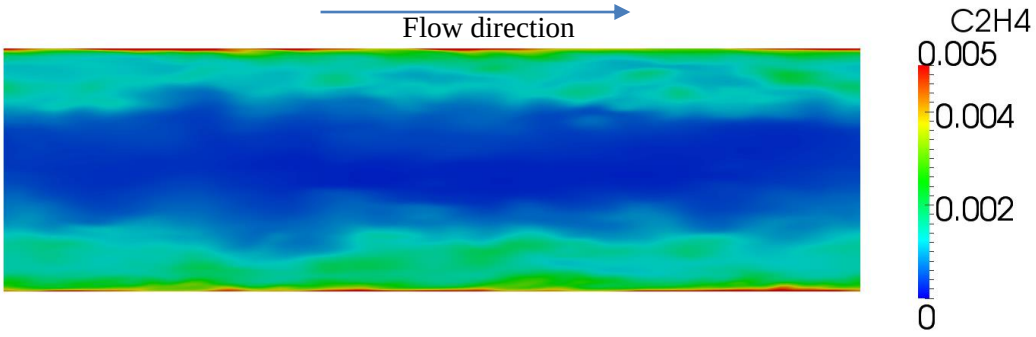

Figure 5-31: Ethene mass fraction in the finned tube for a plug at an axial position of 0.86 m.

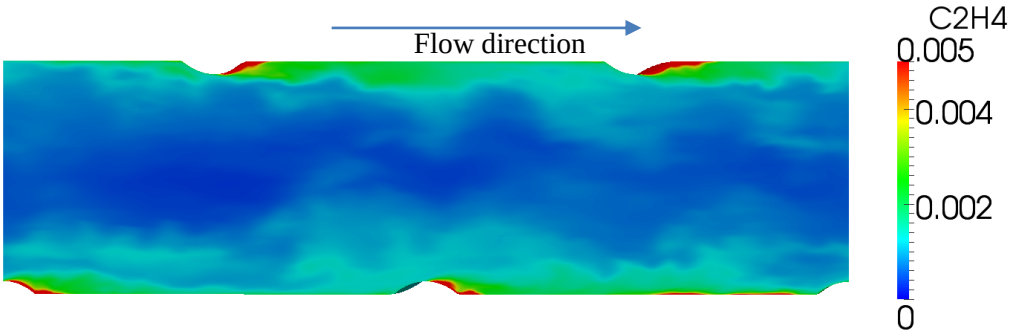

Figure 5-32: Ethene mass fraction in the ribbed tube for a plug at an axial position of 0.825 m.

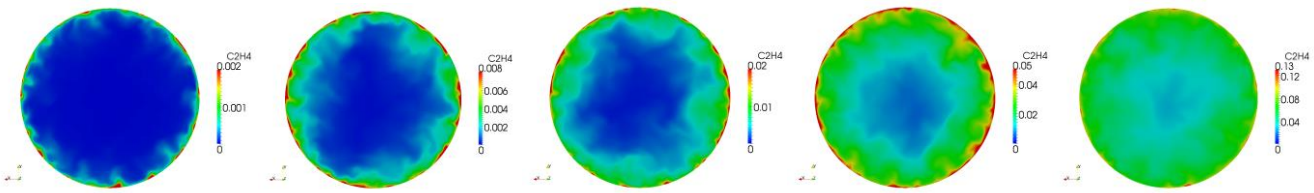

Figure 5-33: Evolution of the ethene mass fraction along the axial coordinate of the bare tube. The axial positions are, from left to right: 0.19 m, 0.718 m, 1.18 m, 2.15 m and 3.22 m. The maxima on the axis are, from left to right: 0.002, 0.008, 0.02, 0.05 and 0.13.

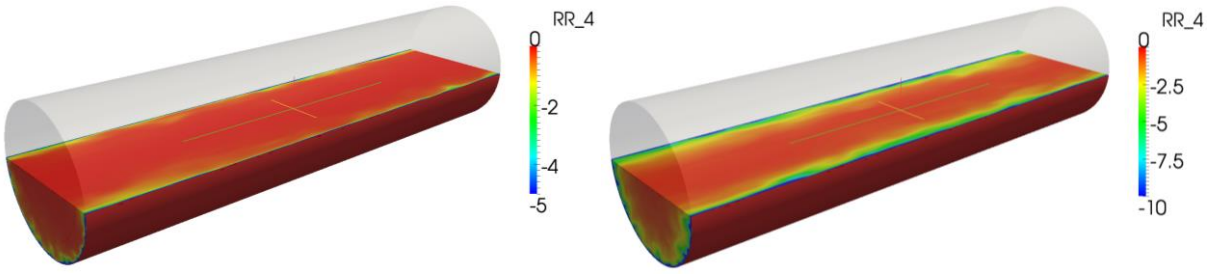

Figure 5-34: Butane rate of formation [kg m^{-3} s^{-1}], in the bare tube for a plug at an axial position of 0.718 m (left) and 2.15 m (right).

A final remark involving the species concentrations, concerns the comment made in section 5.2 on the conversion being higher in the three dimensional simulations while a lower bulk temperature is predicted than in the one dimensional CHEMKIN simulations. Considering the above discussion and Figure 5-18 to Figure 5-20, it is observed that the majority of the reaction takes place close to the wall, at temperatures that are up to 150 K higher than the average bulk temperature. Though not the entire reactor volume is effectively used for reaction, the tremendous acceleration of the reaction at the wall overcompensates for this inefficiency, resulting in a conversion which is initially nearly twice as high as predicted by the 1D simulations. At farther axial positions in the reactor, the effect of the high reaction rate at the walls is countered by an increasingly uniform concentration profile. The effect is still visible, though, as the average bulk temperature remains well below the 1D-predicted temperature, while the conversion is as high as the 1D-predicted conversion.

5.4. Coking Rates

Eventually, the main goal of employing enhanced coil geometries is to reduce the coke formation. Several kinetic models are available to determine the rate of coke formation, both for catalytic as well as for non-catalytic heterogeneous coking [10-12]. In the current work, only a basic study of the coking phenomena is made, *i.e.* the growth of the coke layer is not taken into account, neither is the influence of the tube wall material. Coking rates will be determined using the model of Plehiers [10], which is suited for light feedstocks such as butane in the present work. This model determines the coking rate using only ethene and propene as coke precursors. The rate equation is given in Eq. (5-9). The empirical constant f_c accounts for industrial effects that could not be incorporated in the model. Examples are the high difference between bulk and wall temperature, which could lead to incorrect fitting of the activation energies and the fact that the dilution steam gasifies a fraction of the deposited coke. Its value is 0.137.

$$R_{coke} = f_c \left(k_{coke,1} \frac{C_{ethene}^{\ 2}}{C_{propene}} + k_{coke,2} C_{ethene} + k_{coke,3} C_{propene} \right) \quad \textbf{(5-9)}$$

Three characteristics of coking are determined at several positions in the reactor. The first is the average coking rate. The average coking rate is determined as the average of all coking rates in the computational domain ("plug") for a given axial position in the reactor. As fluctuations in coking rates occur throughout the computational domain, it is also relevant to determine the maximal and minimal values of the coking rate, which give information on the uniformity of the coke formation.

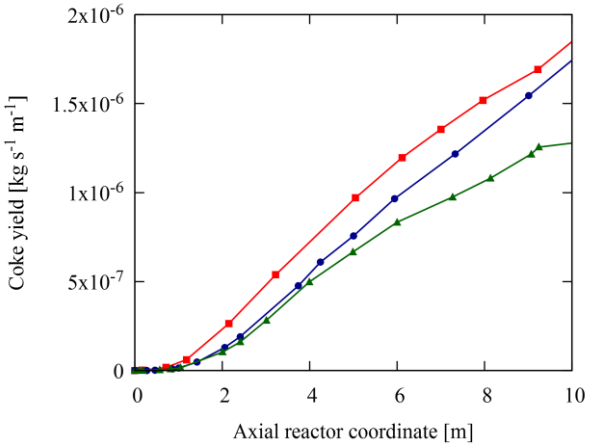

Figure 5-35: Average coke yields as function of the axial reactor coordinate in the bare (—■—), finned (—●—) and ribbed (—▲—) geometries.

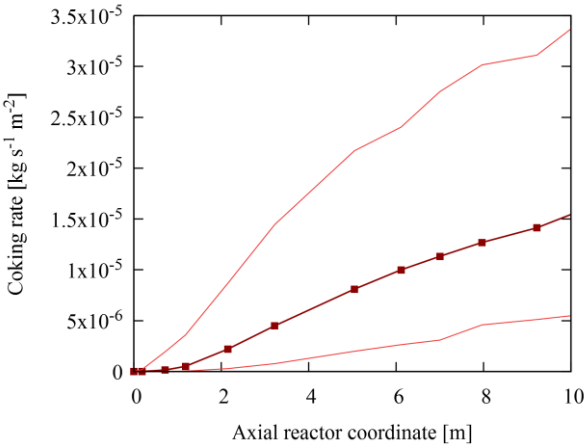

Figure 5-36: Coking rates in the bare tube: average (—■—) and minimum-maximum (——).

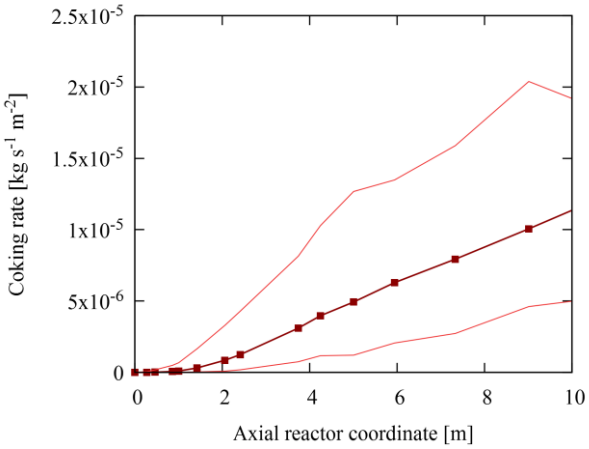

Figure 5-37: Coking rates in the finned tube: average (—■—) and minimum-maximum (——).

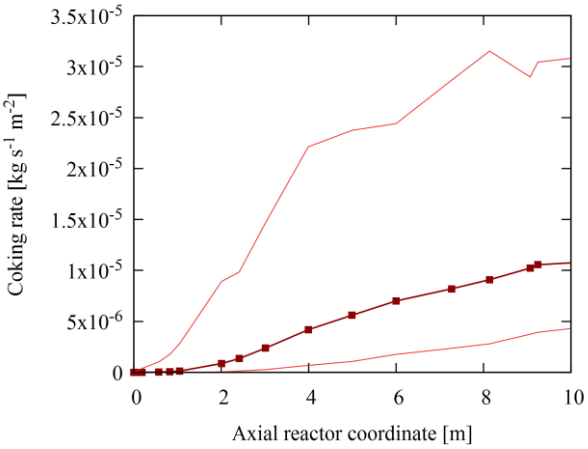

Figure 5-38: Coking rates in the ribbed tube: average (—■—) and minimum-maximum (——).

Figure 5-35 describes the average coke yield per meter of reactor. The total coke yield is obtained by integrating the profiles along the axial reactor coordinate. As expected the fastest coking is predicted in the bare tube. This is a result of the higher light olefin concentrations in the bare tube (Figure 5-9 and Figure 5-10) and the higher tube wall temperature (Figure 5-16). While the total coke yield in the ribbed coil is lower than in the finned coil, the intrinsic coking rate is higher. The finned tube has a greater internal surface area, and hence the lower intrinsic coking rate still results in a higher yield. The higher coking rate in the ribbed reactor is the result of the higher tube wall temperature beyond an axial position of 1.8 m. In Figure

5-36 and Figure 5-37, the average coking rate is compared to the maximal and minimal coking rate for the bare and finned tube respectively. In both cases similar profiles are obtained. The minimum coking rate is approximately 10 – 30 % of the average, while the maximum rate is 2 – 4 times higher than the average. When investigating the coking rates on the wall in Figure 5-39 and Figure 5-40, a wide range of coking rates is indeed observed. However, when comparing the profiles in Figure 5-39 and Figure 5-40 to those at other positions in the reactor, no trend in the location of the maximal and minimal coking rates can be found. This implies that coking in the bare and finned tubed takes place quite uniformly on an averaged base and that the fluctuations of the coking rate are purely the result of the randomness of the turbulent flow. Due to the nature of the coking model, the maximal coking rates are found at the same locations as the maximal temperature and ethene concentrations. As mentioned in paragraph 5.3.2, including the conductive heat transfer through the tube wall, will result in a higher temperature at the fin tips, thus resulting in higher coking rates in the lobes of the fins. A different picture is shown by Figure 5-38. In the ribbed tube, the minimal coking rate is less than 10 % of the average, while the maximal rates reach up to as much as 70 times the average rate. The highly asymmetrical spread in rates indicates that there are zones in which coking takes place preferentially. This is indeed confirmed by the coking rates in the computational domain, illustrated in Figure 5-41. Along the entire trailing edge of the rib, the coking rate is consistently higher than elsewhere. Similarly high coking rates are also at other axial positions in the reactor. Due to the low-velocity zone behind the rib (Figure 5-14), the wall temperature in this region is much higher than in the rest of the tube. This high temperature, combined with high light olefin concentrations (Figure 5-32) results in a high local rate of coke formation. A second location where high coking rates are observed is located in front of the rib. This zone does not cover the entire perimeter of the tube, but at any given position in the reactor, the same type of "plumes" are observed. Unlike the high-coking rate zone on the trailing edge of the rib, the position of these plumes is not fixed, implying some randomness. However, the velocity profiles (Figure 5-14) do show that the velocity is also lower just in front of the ribs leading edge (*cfr*. paragraph 5.3.1). In these regions the temperature is also expected (and observed) to be higher, resulting in higher coking rates. Outside of these zones, the coking rate in the ribbed tube is very low.

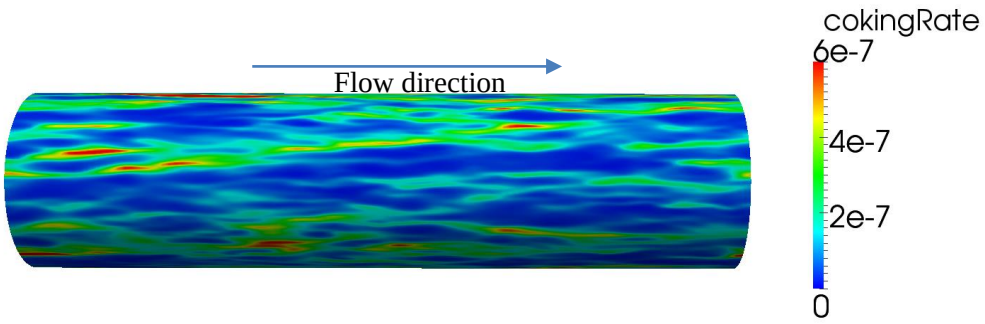

Figure 5-39: Instantaneous coking rate [kg s^{-1} m^{-2}] in the bare tube, for a plug at an axial position of 0.718 m.

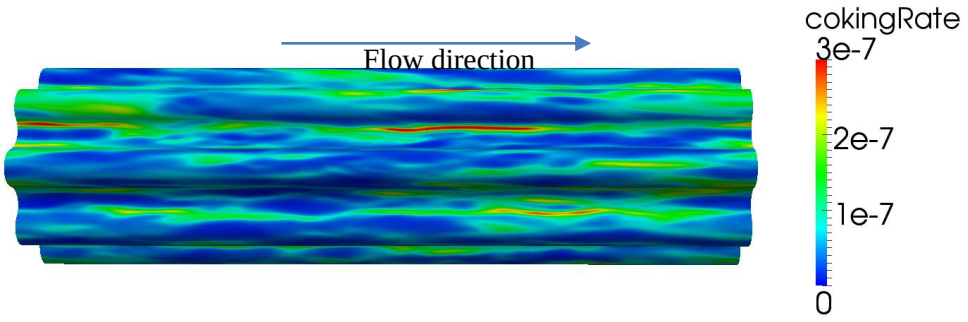

Figure 5-40: Instantaneous coking rate [kg s^{-1} m^{-2}] in the finned tube, for a plug at an axial position of 0.86 m.

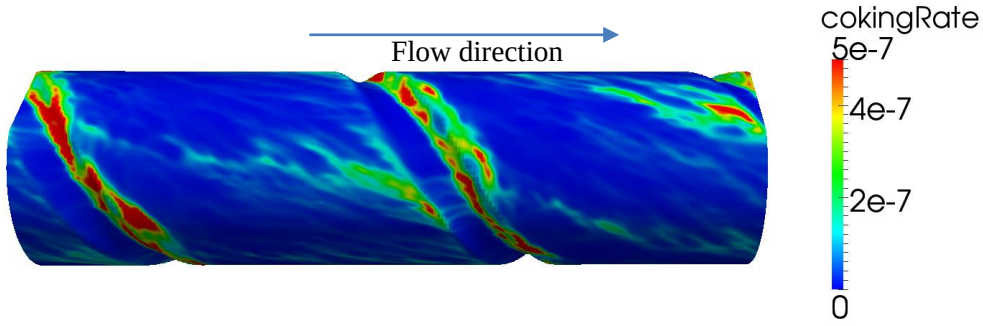

Figure 5-41: Instantaneous coking rate [kg s^{-1} m^{-2}] in the ribbed tube, for a plug at an axial position of 0.825 m.

No simulations have been performed taking into account the growth of the coke layer [13]. Without such data, it is difficult to predict the influence of the preferential coking just behind and – to less extent – in front of the rib. One consequence is that the transition to the wall from the top of the rib will be smoother, reducing the interruption of the boundary layer. The more the boundary layer remains attached to the wall, the less outspoken the low-velocity zones will be. This will again improve local heat transfer, lowering the local wall temperature and consequentially the coking rate. Despite improving the local heat transfer, overall heat transfer will deteriorate due to this local coke formation. The improved overall heat transfer in the ribbed geometry is the result of the large eddies being formed in the region behind the rib, improving radial mixing. The size of these eddies decreases when the transition from the top of the rib to the tube wall is more gradual. On the other hand, the formation of the coke layer will introduce an additional insulating layer, increasing the local wall temperature and hence the coking rate as well.

5.5. Conclusions

The large eddy simulations of butane cracking in different coil geometries provide data at a level of detail that is very hard or even impossible to achieve experimentally or with any other type of computational fluid dynamics simulations apart from the truly fundamental direct numerical simulations. The LES allows to investigate the different aspects of the turbulent flow and the influence of the tube geometry on these parameters. Using the bare tube as reference, some important conclusions can be drawn. From the simulations, it is found that the finned tube does not significantly change the flow pattern in the tube, while in the ribbed tube, the flow is given a swirling character. Different low- and high-velocity zones are created by the spiralling rib on the tube wall. This highly turbulent flow directly results in a severe increase in pressure drop in the ribbed tube. The pressure drop is 115 % higher than in the bare reactor The increased internal surface area of the finned tube also results in an increase in pressure drop. For the finned reactor, the pressure drop is increased by 19 % compared to the bare reactor. The heat transfer is more efficient in both enhanced geometries. In the finned tube, the main cause is the increased surface available for heat transfer. On the other hand, in the ribbed tube the main cause is the increased turbulence. Compared to the bare and finned tube, which have approximately the same Nusselt numbers, the ribbed tube Nusselt number is 33 % higher. This translates to heat transfer enhancement factors of 1.25 and 1.33 for the finned and ribbed coils respectively. Detailed profiles of species concentrations and reaction rates show the locations where reaction takes place at elevated rates. In both finned and ribbed tubes, these locations are spread along the tube wall statistically, corresponding to the randomness of turbulent flows. In the ribbed tube, the reaction rates are found to be consistently higher than elsewhere on the trailing edge of the rib and on the wall just in front of the leading edge, due to the high local temperatures. Consequentially, the olefin concentrations there are higher as well. All the previous combined, result in high local coking rates. Coking rates up to 70 times as high as the average coking rate are observed at these locations. On average however, the yields in both enhanced geometries are lower. In the bare reactor, the coke yield is $1.02\ 10^{-5}$ kg s^{-1}. The finned reactor achieves a reduction of 15.0 %. The total coke yield in the ribbed reactor is 33.1 % lower in than in the bare reactor. The intrinsic coking rate, however, is lower in the finned coil than in the ribbed coil. This is related to a higher average wall temperature as a result of differences in the imposed heat flux profiles. To truly assess the performance of the enhanced geometries, run-length simulations accounting for the growth of the coke layer are necessary.

5.6. References

1. Chin, C.; Ooi, A.; Marusic, I.; Blackburn, H., The influence of pipe length on turbulence statistics computed from direct numerical simulation data. *Physics of Fluids* **2010,** 22, (11), 115107.
2. Van Cauwenberge, D. J.; Schietekat, C. M.; Floré, J.; Van Geem, K. M.; Marin, G. B., CFD-based design of 3D pyrolysis reactors: RANS vs. LES. *Chemical Engineering Journal* **2015**.
3. Van Cauwenberge, D. J.; Vandewalle, L. A.; Reyniers, P. A.; Van Geem , K. M.; Marin, G. B., Periodic Reactive Flow Simulation: Proof of Concept for Steam Cracking Coils. *AIChE Journal* **2016,** In preparation.
4. Zhu, M. Large eddy simulation of thermal cracking in petroleum industry. Université de Toulouse, 2015.
5. Schietekat, C. M.; Van Cauwenberge, D. J.; Geem, K. M.; Marin, G. B., Computational fluid dynamics-based design of finned steam cracking reactors. *AIChE Journal* **2014,** 60, (2), 794-808.
6. Van Geem, K. M.; Schietekat, C. M.; Van Cauwenberge, D.; Marin, G. B., Steam Cracking Reactor Technology: The Good, the Bad and the Ugly. In *AIChE Spring Meeting*, San Antonio, Texas, 2013.
7. Chen, N. H., An explicit equation for friction factor in pipe. *Industrial & Engineering Chemistry Fundamentals* **1979,** 18, (3), 296-297.
8. Masoumi, M. E.; Sadrameli, S. M.; Towfighi, J.; Niaei, A., Simulation, optimization and control of a thermal cracking furnace. *Energy* **2006,** 31, (4), 516-527.
9. Van Geem, K. M.; Reyniers, M.-F.; Marin, G. B., Two Severity Indices for Scale-Up of Steam Cracking Coils. *Industrial & Engineering Chemistry Research* **2005,** 44, (10), 3402-3411.
10. Plehiers, P. M. Rigoreuze Modellen voor de Simulatie van Fornuizen voor de Thermische Kraking van Lichte Koolwaterstoffen. Rijksuniversiteit Gent, 1989.
11. Sundaram, K.; Froment, G., Kinetics of coke deposition in the thermal cracking of propane. *Chemical Engineering Science* **1979,** 34, (5), 635-644.
12. Albright, L. F.; Marek, J. C., Coke formation during pyrolysis: roles of residence time, reactor geometry, and time of operation. *Industrial & Engineering Chemistry Research* **1988,** 27, (5), 743-751.
13. Vandewalle, L. A.; Dedeyne, J. N.; Van Cauwenberge, D. J.; Van Geem, K. M.; Marin, G. B., Computational Fluid Dynamic Design of Steam Cracking Reactors: Extrusion Method for Simulation of Dynamic Coke Layer Growth. In *AIChE Spring Meeting*, Houston, TX, 2016.

6

Comparison OpenFOAM-AVBP

6.1. Introduction

Similarly to the different codes available for DNS as discussed in Chapter 3, LES too can be performed in a variety of different codes. In this work a comparison is made between the present results from OpenFOAM and the results obtained by M. Zhu in AVBP [1]. AVBP is from a numerical point of view similar to OpenFOAM [2]. It is based on the finite volume discretisation method (FVM), though it is possible to use finite element discretisation on specific parts of the equations in a way that is similar to the specification of the discretisation schemes in OpenFOAM. The accuracy of AVBP is second order, which is the same as in OpenFOAM. A third order explicit Runge-Kutta (RK) time advancement scheme is used in AVBP, while OpenFOAM uses a fifth order RK scheme. In contrast to OpenFOAM, which can handle structured, unstructured and hybrid meshes, AVBP is only suited for unstructured or hybrid meshes. The differences between the results obtained with the different codes, can therefore be attributed to specific differences in the numerical schemes of the code, the method used to determine pressure (pressure-velocity coupling in OpenFOAM versus an imposed pressure profile in AVBP) and different types of grids. The inlet conditions, heat flux profiles, kinetics and sub-grid scale model are the same in both cases. The geometry in OpenFOAM is based on the one used in AVBP.

6.2. Bare Tube

6.2.1. Mesh

A first difference between the simulations performed in OpenFOAM and AVBP is the mesh. As mentioned above, the mesh used in the work of Zhu is unstructured and consists of tetrahedral cells. A more important difference however, is the difference in axial length of the periodic computational domain. In the present work a length corresponding to four times the tube diameter is used (152 mm). In the AVBP case the periodic domain length is chosen to equal the pitch of the ribbed tube (69.11 mm). Therefore the domain is less than half the length of that in the present work. In section 5.1, it is noted that a minimal axial domain length of $2\pi R$ is advised to avoid feedback and resonance effects from the periodic boundary conditions. An axial length of 69.11 mm corresponds to a length to radius ratio of only 3.63, which is significantly lower than the advised ratio 2π. While Chin does report that a ratio of $L/R = \pi$, is sufficient to avoid feedback effects on the mean velocity field, all other properties require a higher length to radius ratio [3]. The total number of cells in both meshes does not differ much, namely 3.97 million for the OpenFOAM case and 3.14 million for the AVBP case. In the AVBP grid there are very large differences in the size of the cells. At the wall, the cell spacing corresponds to $y^+ \sim 20$, but the region inside D/2 is described by only 10 or so cells as seen in Figure 6-1. In the structured grid used in OpenFOAM (Figure 6-2), the spacing is nearly the same throughout the geometry, decreasing towards the wall where the spacing corresponds to $y^+ = 1$. This implies that the major difference between the meshes is that in OpenFOAM wall-resolved

LES is performed, while in AVBP wall-modelled LES is performed. This can have significant impact on the simulated wall temperatures.

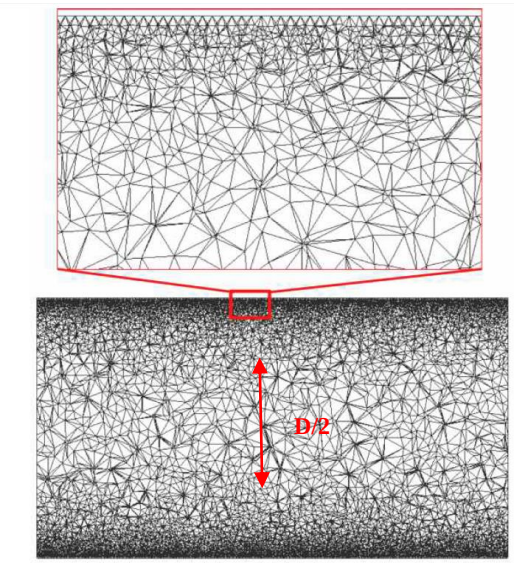

Figure 6-1: Axial view of the mesh for the bare case in AVBP [1].

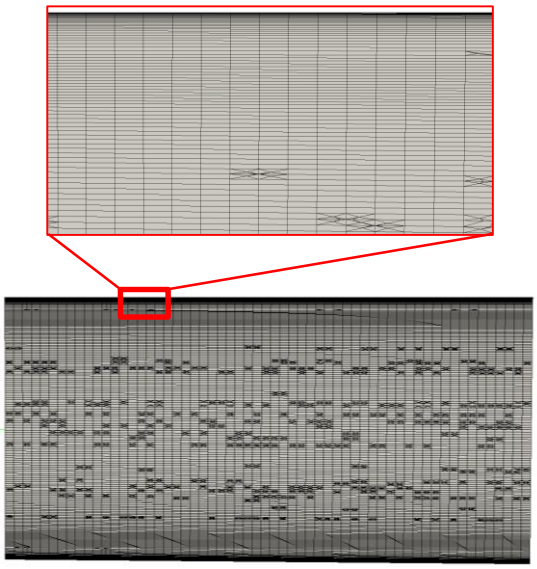

Figure 6-2: Axial view of the mesh for the bare case in OpenFOAM.

6.2.2. Results

The results from the present simulations are compared to the available data in the PhD thesis of Zhu [1]. Only the results up to a time of 42 ms are reported and available for comparison. Figure 6-3 shows that there is a severe mismatch between the temperature profiles simulated in the different codes. The most important cause for the apparent disagreement between the simulation results is the different averaging procedures that are used. In the OpenFOAM case, the average temperature is determined as mass-weighted average over all cells. Contrarily, in the AVBP case, the average is determined as a cell-volume-weighted average. This gives significantly more weight to the cells near the wall where temperatures are highest. As there are considerably more cells near the wall (Figure 6-1), the average temperature is overestimated. By performing mass-weighted averaging, the lower density in cells with a high temperature give comparably less weight to the cells near the wall. There are other potential causes for occurring differences between the simulated temperatures. It is reported that the same heat flux profile (corresponding to the ribbed profile in Figure 4-11) is used for the bare and ribbed cases in AVBP. The difference between the bare and ribbed heat flux profiles in Figure 4-11 can also be a source of discrepancy. In the OpenFOAM simulations, an upwind discretisation scheme is used for the temperature gradients. This results in a more smeared out temperature field, reducing the temperature gradients and potentially affecting the calculated heat transfer. Using wall-modelled LES in AVBP also contributes to the temperature mismatch, though one would expect this to result in lower average temperatures, rather than higher ones.

While the different averaging methods make comparing the temperature impossible, the yield profiles hint that the simulated temperature in the AVBP case is indeed higher than in the OpenFOAM simulations. Figure 6-4 compares the butane mole fractions. AVBP predicts a slightly faster consumption of butane than OpenFOAM, though after about 0.02 s, the difference appears to remain approximately constant. A second observation that corroborates the higher mass-weighted average temperature in AVBP is the higher ethene mole fraction in Figure 6-5. While the higher conversion naturally results in a higher ethene yield, the difference in conversion between the two cases in only around 1 %, while the difference in ethene yield is more than 10 %. This is only possible if the selectivity towards ethene is higher as well. In paragraph 5.3.4, it has been indicated that higher temperatures correspond to higher ethene selectivities. The difference in propene concentration (Figure 6-6) between the two simulations is only small as a result of the higher conversion being compensated for by a lower selectivity.

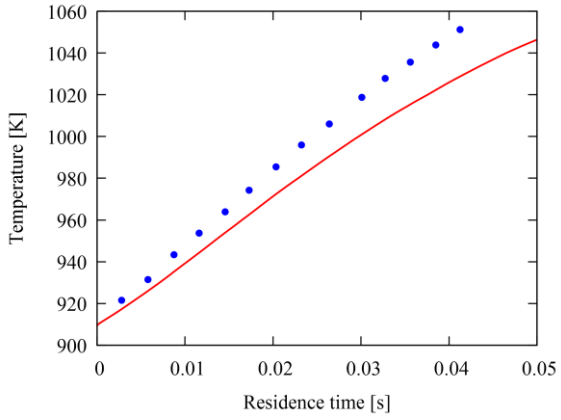

Figure 6-3: Temperature profile in the bare case, from OpenFOAM (——) and AVBP (●).

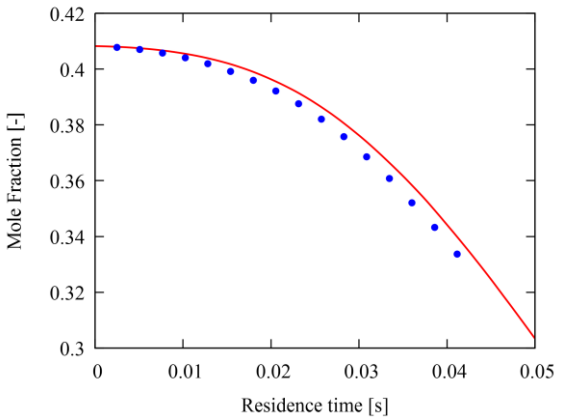

Figure 6-4: Butane mole fraction profile in the bare case, from OpenFOAM (——) and AVBP (●).

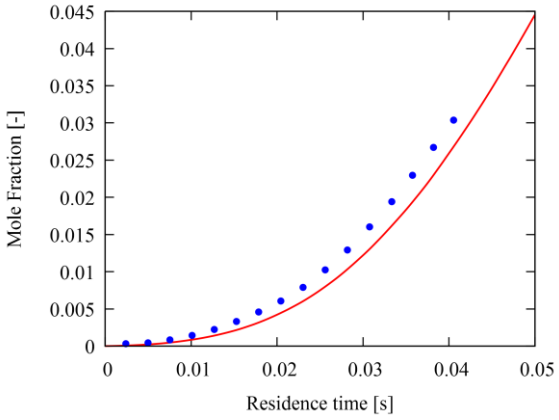

Figure 6-5: Ethene mole fraction in the bare case, from OpenFOAM (——) and AVBP (●).

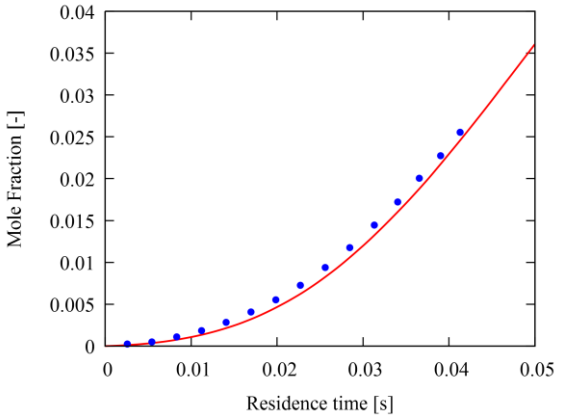

Figure 6-6: Propene mole fraction in the bare case, from OpenFOAM (——) and AVBP (●).

In chapter 5, apart from the two point correlations, no attention was devoted to the statistical results of the simulations. Those results are important though, as they give a mathematical foundation to the visual observation that the ribbed reactor has more uniform temperature and concentration profiles than the bare

reactor. The temperature distribution is the most important as the temperature directly affects reaction rates and species concentrations, thus affecting their distributions as well. Zhu reports the temperature distributions at residence times of 10 ms and 40 ms. From the OpenFOAM simulations, no full statistical data are available at these exact times, but a comparison to the distributions at respectively 13 ms and 37 ms is still relevant. Several differences are observed between the distributions in Figure 6-7.

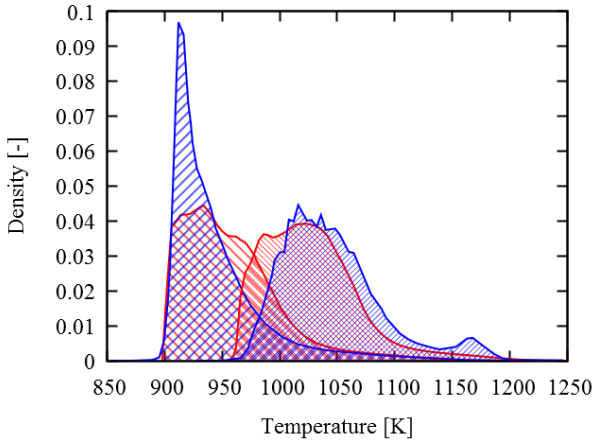

Figure 6-7: Temperature distribution in the bare case. OpenFOAM: 0.013 s ( ) and 0.03675 s ( ) – AVBP: 0.010 s ( ) and 0.040 s ( ) [1].

At the highest time, the distributions from the different codes agree well. The quantitative difference in the mean of the distribution is related to the difference in residence times. As the distribution from OpenFOAM is taken at an earlier residence time, the average temperature will be lower. The only significant difference is that in the AVBP distribution, a second peak is present. The location of the peak is close to the average wall temperature at the same residence time in OpenFOAM, implying that the wall temperature values might have been included in this distribution. Another possible cause could again be the volume-weighted averaging procedure. While the same averaging procedure is used in OpenFOAM, the distribution of cells is much more uniform in the OpenFOAM case than it is in the AVBP case (*cfr*. paragraph 6.2.1), explaining the occurrence of the second peak only in the AVBP-based distribution. At the low residence time, a large qualitative and quantitative difference is observed. The distribution of the temperature calculated by AVBP has a much smaller variance, resulting in a sharper and higher peak. This is indicative of a highly uniform temperature field, while the OpenFOAM temperature field shows a less uniform field, which is in agreement with Figure 5-15. In the reported figures of the axial temperature fields, little to no temperature gradients are observed at a residence time of 1 ms, nor is there any noticeable thermal boundary layer. This is in contrast to the results from OpenFOAM, where a thermal boundary layer has already been developed during the pre-simulation. The previous indicates that for the AVBP case, the development of the turbulent flow field was only performed for the velocity and pressure fields, but not for the temperature. The fact that the temperature field is not fully developed yet at the reactor inlet is another cause for the large difference in simulated temperatures. A uniform temperature field results in much higher heat transfer rates and hence the temperature gradient along the axial reactor coordinate is significantly overestimated.

6.3. Ribbed Tube

6.3.1. Mesh

For the mesh of the ribbed tube, the differences are even larger than for the bare tube. Due to the higher complexity, the structured grid requires much more cells to describe the curved rib in the axial direction. Combined with a wall-resolving character, the mesh for the ribbed case in OpenFOAM has 14.2 million cells, while the unstructured mesh for the AVBP case only has 3.68 million cells. Otherwise, the same remarks made in paragraph 6.2.1, still hold for the ribbed case.

6.3.2. Results

Overall, the average results in the ribbed case agree well, despite the different averaging procedures. Considering the temperature, displayed in Figure 6-8, this indicates that the results differ in two areas and that both cancel each other. The first is the volume-weighted averaging method which has been shown to result in higher temperatures than the mass-weighted method. The second is the wall-modelled character of the simulations. For bare tubes, the typical wall functions are expected to represent the boundary layer well. However, in the more complex ribbed geometry, the wall plays a very important role. Due to the unconventional shape of the wall, it is conceivable that the wall functions lack accuracy. Incorrect representation of the boundary layer, where temperatures are generally highest, will result in a lower calculated average temperature than in the wall-resolved simulations. In the ribbed case, identical heat flux profiles are used, which eliminates the overestimation of the temperature in the initial part of the reactor as well. As mentioned previously, the temperature is the most important parameter in determining the reaction rates and consequentially the concentrations of the species. As the temperature is approximately equal in both cases, the butane conversion simulated in OpenFOAM does not differ much from that simulated in AVBP. Beyond a residence time of 0.03 s, some deviation in the temperature is observed. Counter-intuitively, the butane conversion is higher in OpenFOAM at lower temperatures, as illustrated in Figure 6-9. A similar explanation as given in paragraph 5.3.4 is valid here. The difference between CHEMKIN and OpenFOAM was related to the absence of radial gradients in CHEMKIN and hence not taking into account the high temperatures near the wall where the majority of the reaction occurs. The difference between the OpenFOAM and AVBP cases is linked to not taking into account the boundary layer near the wall. This also neglects certain temperature gradients in the region where the reaction rates are highest, hence also underestimating the reaction rates. The fact that the temperature profile is not yet fully developed contributes to the underestimation of the reaction rates as well. The lack of thermal boundary layer (modelled or resolved) results in the underestimation of the radical concentrations. The difference in conversion is conveyed directly to the difference in ethene and propene concentrations in respectively Figure 6-10 and Figure 6-11, which are consequentially both higher in the OpenFOAM simulations than in the AVBP simulations.

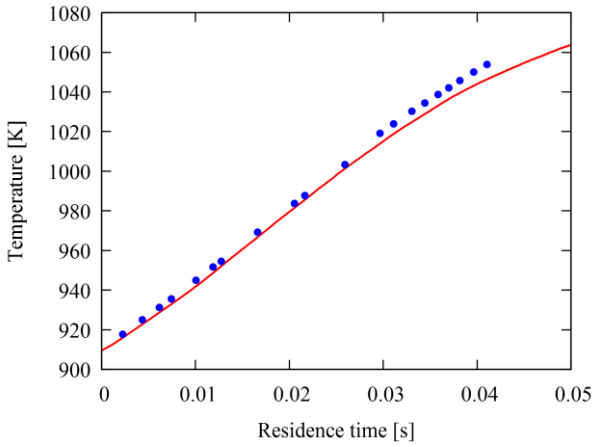

Figure 6-8: Temperature profile in the ribbed case, from OpenFOAM (——) and AVBP (●).

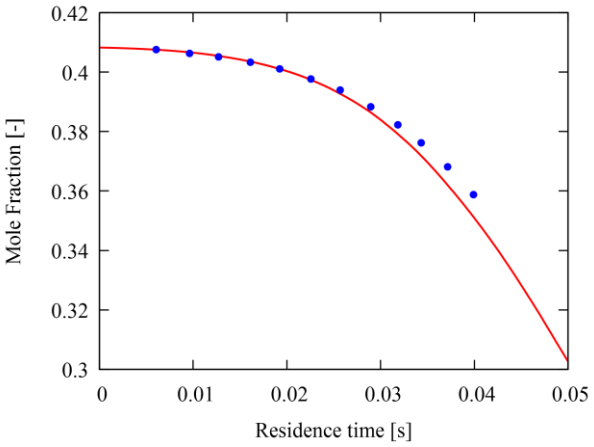

Figure 6-9: Butane mole fraction profile in the ribbed case, from OpenFOAM (——) and AVBP (●).

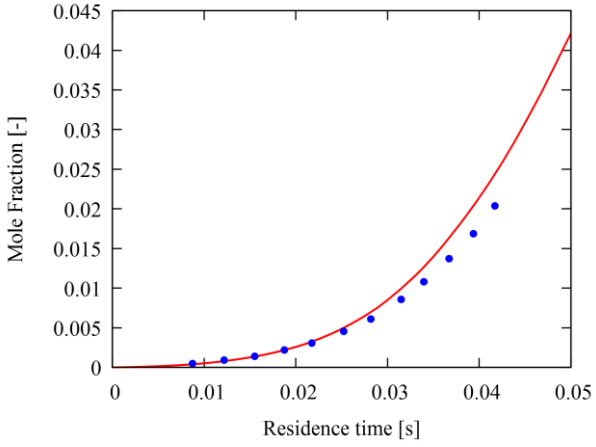

Figure 6-10: Ethene mole fraction in the bare case, from OpenFOAM (——) and AVBP (●).

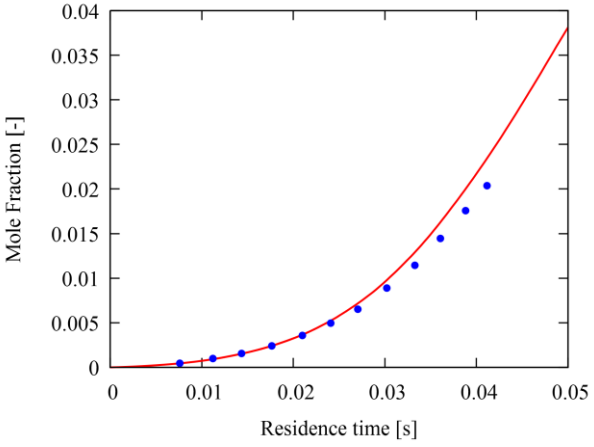

Figure 6-11: Propene mole fraction in the bare case, from OpenFOAM (——) and AVBP (●).

Figure 6-12 shows that the agreement between the temperature distributions is better than in the bare case, though there are still some important differences. In the AVBP simulations, the uniformity of the temperature profiles decreases (the variance increases), while in the OpenFOAM simulations the temperature profiles become more uniform. The latter corresponds to the intuition that during heating, initial temperature gradients are reduced until a uniform profile is attained. The low variance at the low residence time again corresponds to the non-developed temperature profile at the inlet of the reactor. Due to the better heat transfer and more turbulent flow, the temperature profile develops faster and remains more uniform throughout the reactor, explaining why the difference between the 10 ms and 40 ms distributions is not as outspoken as in the bare reactor. Finally, at 40 ms, a similar secondary peak as in the bare tube is observed. Here the peak is at lower temperatures, corresponding to the lower wall temperature simulated in the ribbed case, supporting the theory that the boundary layer has a greater weight in the volume averaging approach.

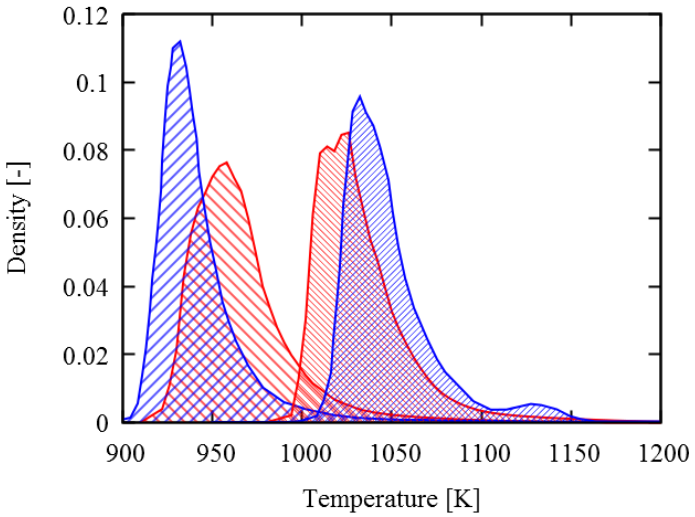

Figure 6-12: Temperature distribution in the ribbed case. OpenFOAM: 0.0145 s ( ) and 0.0336 s ( ) – AVBP: 0.010 s ( ) and 0.040 s ( ) [1].

6.4. Conclusions

The comparison of the different codes using different geometries indicates that there are important differences in the results calculated by OpenFOAM and AVBP. These differences are linked to intrinsic characteristics of the computational codes, but also to (even minor) differences in settings between the cases in the present work and that of M. Zhu. A first important difference is the mesh used in the different codes. Not only does AVBP use unstructured meshes, the considered case performed wall-modelled LES. For OpenFOAM on the other hand, fully structured meshes are used. This rapidly increases the required number of cells in more complex geometries. Additionally, wall-resolved LES has been performed in the current work with OpenFOAM. The second major difference concerns the statistics of the flow. The geometry used in AVBP is shorter than the recommended length in periodic simulations, possibly introducing feedback and resonance effects in the simulations. Furthermore, the turbulent temperature profile was not fully developed in a pre-simulation. This results in an underestimation of the radical concentrations near the wall, underestimating the reaction rates and hence the conversion. The existence of such differences indicates the necessity to conduct simulations in the different codes by a single user, using consistent settings and methods.

6.5. References

1. Zhu, M. Large eddy simulation of thermal cracking in petroleum industry. Université de Toulouse, 2015.
2. Poinsot, T.; Rudgyard, M.; Schönfeld, T., *The AVBP HandBook*. CERFACS: 2011.
3. Chin, C.; Ooi, A.; Marusic, I.; Blackburn, H., The influence of pipe length on turbulence statistics computed from direct numerical simulation data. *Physics of Fluids* **2010,** 22, (11), 115107.

7

Supersonic Swirling Flows

7.1. Theoretical Aspects of Nozzle Flow

SUSTOR2 makes use of a converging-diverging nozzle to accelerate the flow to supersonic velocities. While the general equations for fluid flow, as given in chapter 4, are still valid, it is worth discussing some aspects concerning trans- and supersonic flows.

When discussing sub-, trans- and supersonic flows, the Mach number is an important flow characteristic. It is defined as the ratio of the fluid velocity and the speed of sound. A flow is denoted subsonic when $M < 1$, supersonic when $M > 1$ and transonic when $M \approx 1$. For an ideal gas, the speed of sound is given by eq. (7-2) [1].

$$M = \frac{|\boldsymbol{v}|}{c} \tag{7-1}$$

$$c = \sqrt{\gamma(T)\frac{R}{MM}T} \tag{7-2}$$

The behaviour of a fluid along a nozzle can be derived from a basic energy equation (eq. (7-4), Bernoulli [2]) and the continuity equation (eq. (7-3)), resulting in eq. (7-5).

$$\dot{m} = \rho|\boldsymbol{v}|A \tag{7-3}$$

$$d\left(\frac{v^2}{2}\right) = vdv = -VdP \tag{7-4}$$

$$\frac{dA}{A} = \frac{1-M}{v^2}VdP \tag{7-5}$$

The latter equation shows that with decreasing cross-sectional area, the behaviour of the fluid (*i.e.* acceleration or deceleration) depends on the Mach number. For a Mach number greater than unity, an increase in surface area corresponds to a positive velocity gradient and hence to an acceleration of the fluid. For a Mach number smaller than unity, a decrease in cross-sectional area results in accelerated flow. For a Mach number equalling unity, the change in area is found to equal zero. This corresponds to the throat of the nozzle. Consequently it is physically impossible to accelerate a fluid to supersonic velocities using solely a converging pipe. When the flow reaches a Mach number of 1 in the throat of the nozzle, the flow is termed "choked". A property of choked flow is that the mass flow rate is determined by the upstream pressure of the nozzle. Under non-choked conditions, the mass flow rate will be determined by the downstream pressure as well. The backpressure does, however, have some significance. Three regions can be identified, they are illustrated in Figure 7-1. If the backpressure is higher than P_1, the flow will not become supersonic and a classical flow pattern is obtained. If the backpressure is equal to P_1, the flow will just reach the speed of sound in the nozzle, but will not accelerate in the diverging section. If the back

pressure is situated between P_1 and P_2, the flow will accelerate to $M > 1$. The exact velocity depends on the pressure difference between inlet and outlet. At a certain distance in the diverging section (also dependent on the pressure difference), a shockwave is formed. The formation of the shockwave is a result of the fluid no longer being able to fulfil all conservation equations, resulting in a discontinuity [1]. As the fluid is accelerated in the diverging section, the pressure continues to drop. At a certain point, the difference between the outlet pressure and the local pressure can no longer be recovered by simply decelerating the fluid. Part of the required pressure increase is achieved via the shockwave. Behind this wave, the flow is subsonic, and pressure increase is achieved by deceleration of the fluid. This discontinuity is observed in all properties. When the outlet pressure is close to P_2, the shockwave is not vertical and flow separation at the wall occurs. Finally, when the outlet pressure is lower than or equal to P_2, there is no need for pressure recovery in the tube and the fluid continuously accelerates. It should be noted that both P_1/P_0 and P_2/P_0 are fluid- and case specific properties, while P^*/P_0 is solely fluid-dependent (eq. (7-6)). P^*/P_0 is also known as the Laval pressure ratio and represents the ratio of the nozzle throat pressure under choked conditions and the inlet pressure. The Laval pressure ratio is 0.528 for air (at 17 °C and 1 atm) and 0.544 for methane (at 15°C and 1 atm) [3]. The Laval pressure ratio is temperature dependent through the temperature dependence of the ratio of specific heats.

$$\frac{P^*}{P_0} = \left(\frac{2}{1+\gamma}\right)^{\frac{\gamma}{\gamma-1}} \tag{7-6}$$

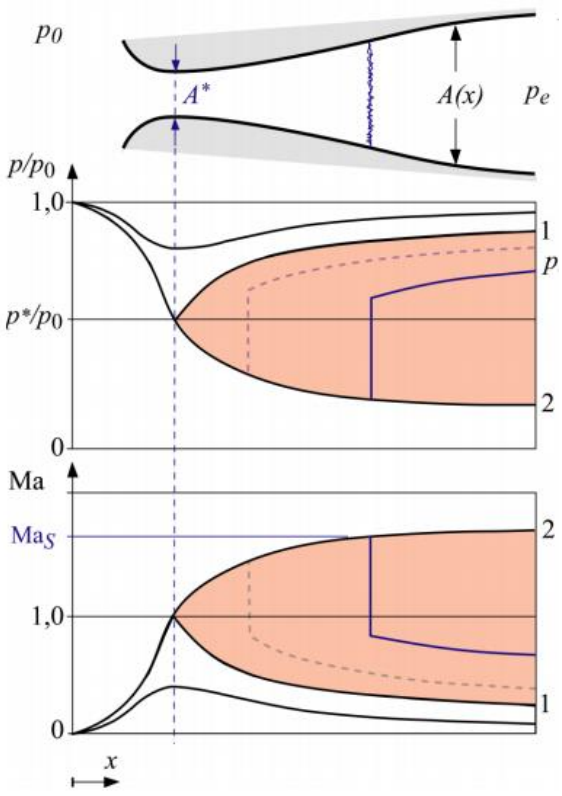

Figure 7-1: Profiles of pressure and Mach number along the centreline of a converging-diverging nozzle [1].

7.2. Joule-Thompson and Condensation

The principle of the SUSTOR technology is based on the temperature decrease that results from the expansion of the gas (the Joule-Thomson or Joule-Kelvin effect). While temperature decreases to below 200 K have been simulated [4], the condensation of water will release thermal energy, increasing the temperature of the gas. If this heat release is significant, it will become difficult to obtain a dew point of 230 K for the product. To investigate this effect, the temperature increase in saturated natural gas related to the condensation of water is estimated. Table 7-1 lists the used thermodynamic properties.

Table 7-1: Properties for the estimation of the temperature increase.

Pressure	Temperature	Methane density (@ 1 bar, 300 K) [3]	Latent heat water (@ 100 bar, 300 K) [3]	Heat capacity methane (@ 100 bar, 300 K) [3]
100 bar	300 K	0.644 kg m^{-3}	1318.5 kJ kg^{-1}	3002.8 J kg^{-1} K^{-1}

The amount of water that condensates depends on the amount of water initially present in the natural gas, which is assumed to have the same properties of methane for this estimate. It is assumed that the natural gas at the inlet is saturated with water. Several methods exist to determine the amount of water corresponding to saturation values. Lin et al. [5] provides an overview of different formulae and an experimental value at 100 bar and 298 K. Again, for simplicity and due to the limited effect of the 2 K temperature difference, this value (318.47 mg_{water} Nm_{gas}^{-3}) is taken. Taking 110 mg_{water} Nm_{gas}^{-3} as outlet condition, 0.44 mg_{water} kg_{gas}^{-1} must be condensed. This results in a heat release of 585.1 J kg_{gas}^{-1}, which can heat the gas by 0.19 K. This temperature rise does not significantly affect the amount of water that can be removed from the natural gas. Hence for optimisation purposes, single phase simulations will be able to accurately predict temperatures, making it unnecessary to implement complex multiphase models at this stage.

7.3. Flow in a Nozzle

Several authors have investigated fluid flow through a nozzle [6-8]. As a proof of concept and to find out which numerical settings are required to simulate shockwaves, the results of both Arina [6] and Karimi and Abdi [7] are reproduced.

7.3.1. Arina

The case studied numerically by Arina [6], was also verified in Fluent by Jassim et al. [9]. However, they report very little information on the exact settings of the simulations. The set-up of the present case is as follows. The nozzle itself has a total length of 0.1 m. At each end a straight section of 0.025 m is added to guarantee fully developed flow at the inlet and outlet. The nozzle is tubular (allowing an axisymmetric approach) and

the cross-sectional area follows the profile given by eq. (7-7). This results in a nozzle of which the converging and diverging sections are equal in length. The axisymmetric mesh is shown in Figure 7-2. The mesh is structured and has 24 cells in radial direction and 447 cells in axial direction, totalling 10,728 quadrilateral cells.

$$A(x) = \begin{cases} 2.5 \cdot 10^{-4} + 3 \cdot 10^{-4}\left(\frac{x}{x_{th}} - 1.5\right)\left(\frac{x}{x_{th}}\right)^2 & x \leq x_{th} \\ 3.5 \cdot 10^{-4} - 10^{-4}\left(\frac{x}{x_{th}}\right)\left(6 - 4.5\left(\frac{x}{x_{th}}\right) + \left(\frac{x}{x_{th}}\right)^2\right) & x \geq x_{th} \end{cases} \quad \textbf{(7-7)}$$

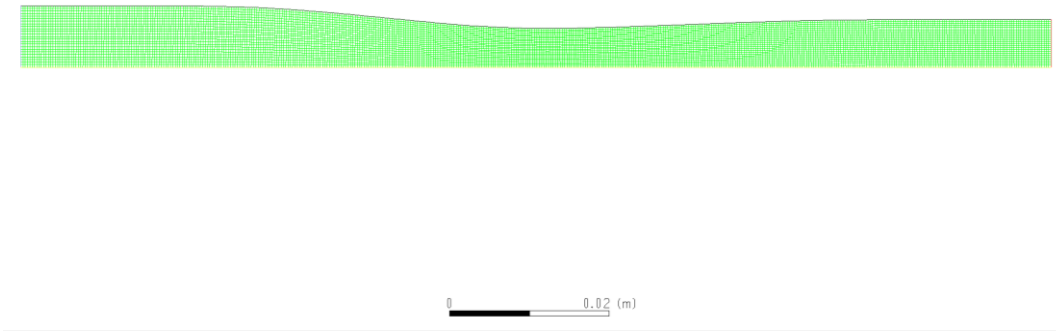

Figure 7-2: Mesh used for the simulations based on the work of Arina.

The fluid is CO_2, which is assumed to behave as an ideal gas. The specific heat is taken to be constant. The pressure is specified at both the inlet and outlet, the inlet pressure is adjusted to approximate an inlet velocity corresponding to M = 0.2395 in the simulation, as specified by Arina [6]. The inlet gauge pressure is set at 0 barg, and the total gauge pressure at 0.03790 barg. The outlet pressure is set at 83 % of the inlet absolute pressure, corresponding to -0.16951 barg. The inlet temperature is set at 288 K. The implicit, density based solver is used on an axisymmetric problem. Similar to the simulations by Arina and Jassim et al., the flow is considered inviscid. In separate simulations, the role of turbulence and the turbulence model will be investigated using the realizable k-epsilon model and the Reynolds stress model. First order upwind discretisation schemes are used, mainly due to stability and convergence of the simulation. Roughly 1000 CPU-s are required to obtain a converged solution.

The pressure profile along the nozzle centreline is given in Figure 7-3, where it is compared to the profile calculated by Arina. From Figure 7-3 it can be concluded that a good agreement with the results of Arina is achieved. The location of the pressure wave is almost exactly at 0.07 m from the start of the converging section. The pressure is slightly overestimated, the deviation is maximal at the nozzle throat (14 %). The deviations are most likely linked to the low discretisation order, more accurate results could be achieved using higher order discretisation schemes. However, even the second order scheme proved at best marginally stable and did not seem to improve the fitting of the results much. There was also some mismatch in the inlet conditions as the simulated Mach number differed slightly from the specified value (0.2426 as

opposed to 0.2395), which means that the fluid must be accelerated less to reach Mach=1 in the throat, in turn requiring a smaller pressure gradient. Furthermore, due to the Joule-Thomson effect, the temperature changes significantly along the nozzle centreline, as shown in Figure 7-4. A minimum temperature of 218 K and a maximal Mach number of 1.49 are simulated. Due to the temperature difference of nearly 100 K, the assumption of a constant heat capacity could result in deviations. Using piecewise polynomials for the heat capacity did not result in any significant improvement of the results.

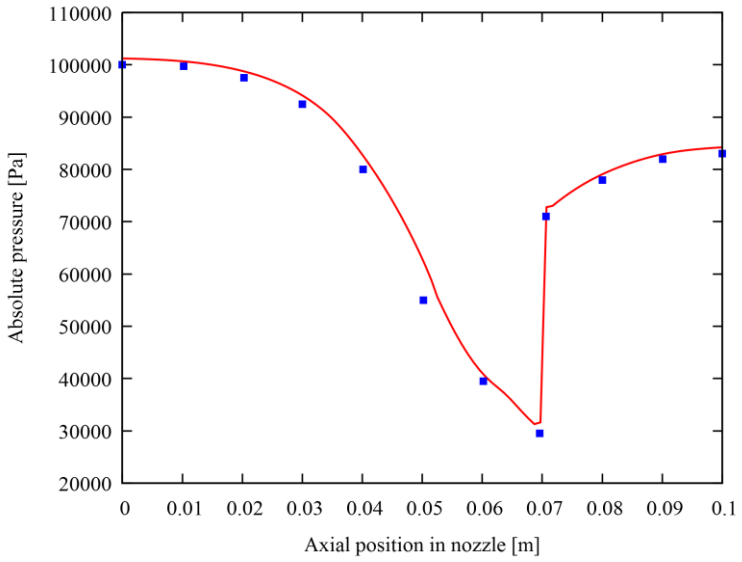

Figure 7-3: Simulated pressure profile along the nozzle centreline (—) and results from Arina (■)[6].

A second aspect that is investigated based on the Arina case is the influence of turbulence in a first approach, and secondly of the turbulence model that is used. For computational reasons, the turbulence models are limited to RANS. Two turbulence models are tested, the realizable k-epsilon model (RKE) and the Reynolds stress model (RSM). Both turbulence models allow to account for compressibility effects, which are of importance in trans- and supersonic flows. Also enhanced wall treatments are available allowing to account for pressure gradient effects. These can be important, especially in the region surrounding the shockwave. A first remark is that the use of turbulence models does not notably increase the time required to attain a converged solution. Figure 7-5 shows the pressure profiles for the different cases. The employed turbulence model has no impact on the pressure profile upstream of the nozzle. This is not surprising as in paragraph 7.1 it has been shown that the pressure upstream of the nozzle in choked flow does not depend on the downstream flow pattern. It is also observed that from a distance of 0.08 m on in the nozzle the profiles coincide again. The only remarkable difference is situated in the location of the pressure wave. Across the shockwave the total pressure (a measure for the energy) of the flow decreases. The dissipative effect of turbulence reduces the amount of energy that must be lost in the shockwave, decreasing the required pressure jump and hence shifting the location of the shockwave closer to the nozzle throat.

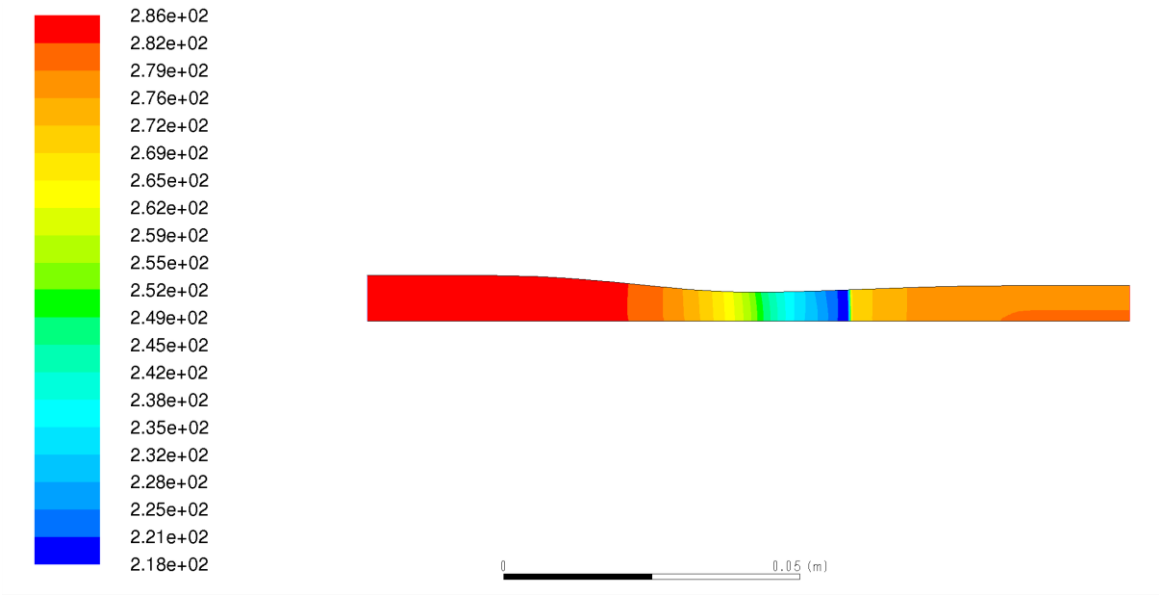

Figure 7-4: Temperature [K] for the inviscid simulation of the Arina case.

The mutual difference between the RKE and RSM models is only very small. Figure 7-6 and Figure 7-7 show the temperature profiles for the RKE model and RSM respectively. The simulated minimum temperature is similar in both cases, namely 233 K and 229 K for RKE and RSM respectively. The profiles of the Mach number are very similar to the temperature profiles, with low temperatures corresponding to high Mach numbers and *vice versa*. Using the RKE model, the Mach number is found to be within the range 0.18-1.29, while with the RSM, the range is 0.203-1.33. The lowest Mach numbers are found in a region close to the wall where flow separation occurs. This flow separation was not observed in the inviscid case and is related to the fact that the pressure wave is located closer to the nozzle throat than in the inviscid case.

Similarly to the inviscid case however, the second order discretisation methods diverged for the RKE model. With RSM it was possible to obtain a stable solution with second order discretisation. Figure 7-8 illustrates the differences between the solution with first order and second order discretisation schemes. There is only a minor difference in the location of the shockwave. Similar observations can be made considering the minimum temperature and maximum Mach number (230 K and 1.32), indicating that in this specific case, an accurate solution is obtained, even with first order discretisation.

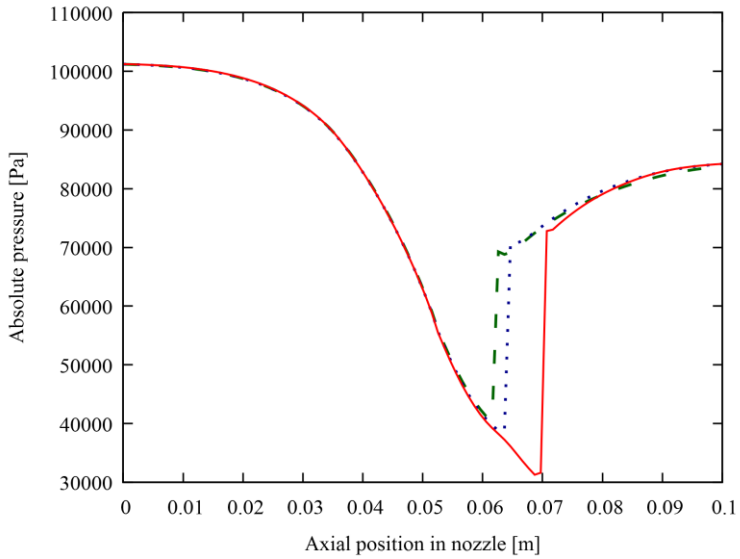

Figure 7-5: Pressure profiles using different turbulence models, based on the Arina case: Inviscid (——), RKE (– –) and RSM (· · · ·).

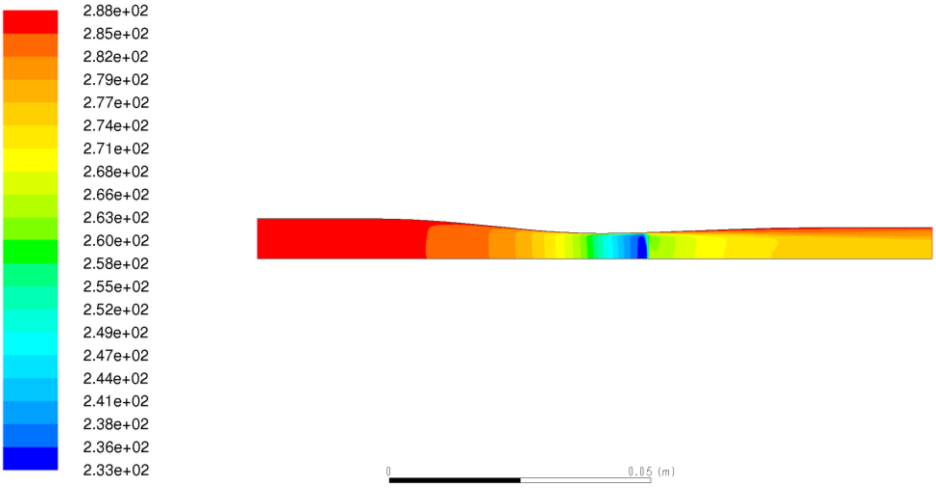

Figure 7-6: Temperature [K], using the RKE turbulence model and first order discretisation.

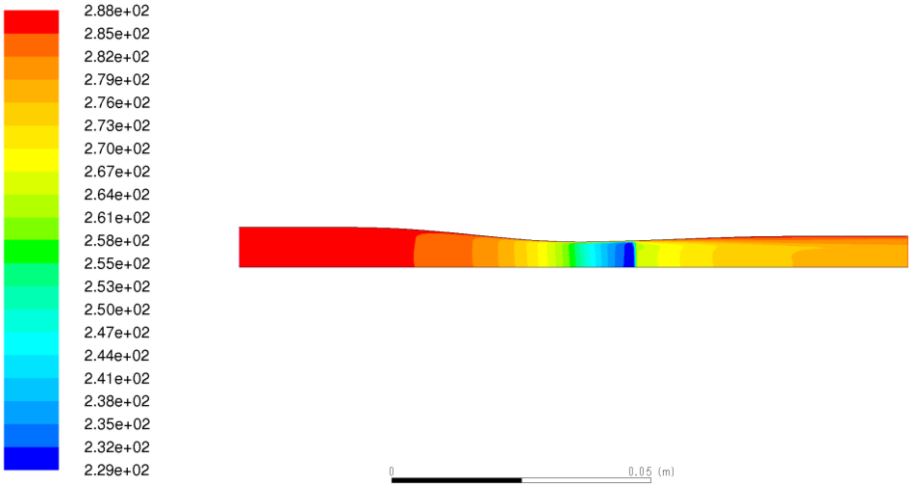

Figure 7-7: Temperature [K], using RSM and first order discretisation.

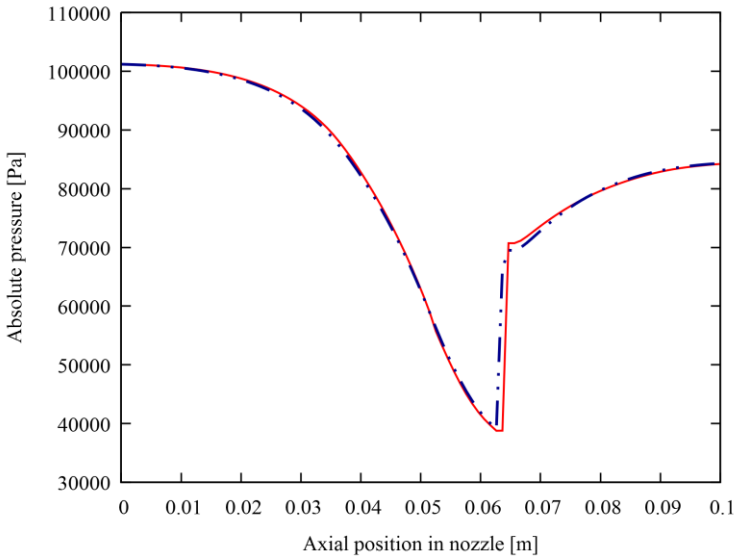

Figure 7-8: Pressure profile, using RSM: difference between first (——) and second (· · ——) order discretisation.

7.3.2. Karimi and Abdi

A second case that is investigated is that of a rectangular nozzle, following the work by Karimi and Abdi [7]. Contrarily to the previous case, the geometry is not axisymmetric, hence both "sides" of the nozzle must be simulated. Within the work of Karimi, two cases can be identified, each with a slightly different geometry.

7.3.2.1 Validation Case (Case A)

The first case (case A) is used by Karimi and Abdi as validation of the used model, with Fluent simulations as reference. The geometry for case A has the following description. The cross-sectional surface of the inlet is 0.04 m^2, with a height of 0.04 m and a depth of 1 m. The depth of the nozzle is constant throughout the domain. The nozzle throat has a height of 0.0163 m and the outlet has one of 0.03 m. The nozzle has a total length of 0.2 m, of which the diverging section takes 0.1473 m and the converging section 0.0527 m. As in the Arina case, straight lengths are added at the inlet and outlet (0.1 m and 0.05 m). The surface area of the nozzle decreases linearly towards the throat and increases linearly away from the throat. Again, a structured mesh, shown in Figure 7-9, is used. The mesh has 99 cells in the y (height) direction and 746 cells in the x (length) direction, totalling 73,854 quadrilateral cells. Approximately the same cell spacing is used as in the Arina case. A mass-flow inlet is used, specifying a mass flow of 300 kg s^{-1} of methane and a pressure of 90 bar. The inlet pressure is only necessary for initialisation of the problem, as in choked flow the actual inlet pressure and mass flow rate are related. The outlet pressure is specified at 70 bar. The inlet temperature is 291.65 K. Methane is assumed to behave as an ideal gas and the heat capacity as modelled by a piecewise polynomial. In a first approach, the fluid flow is taken to be inviscid and a density based solver with first order discretisation is used.

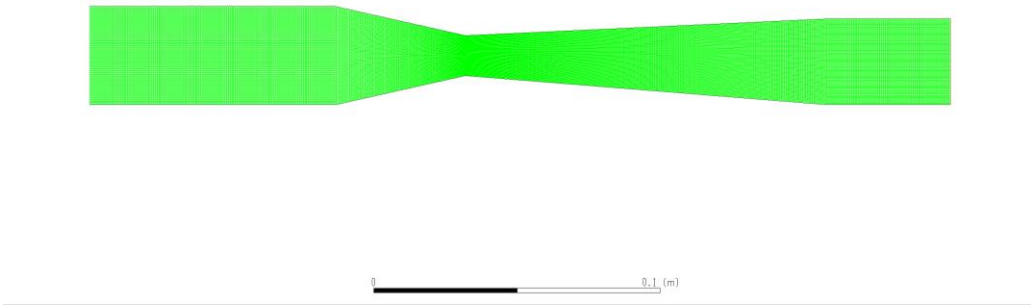

Figure 7-9: Mesh used for case A based on the work by Karimi and Abdi.

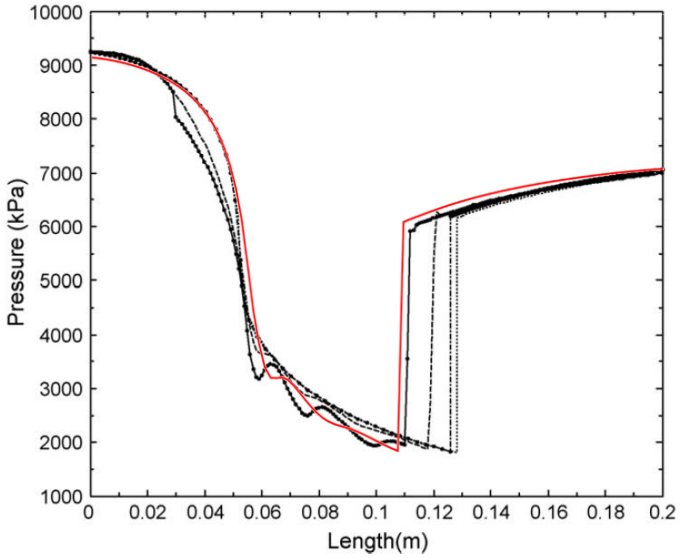

Figure 7-10: Comparison of pressure profiles in the current fluent simulation (—) to the simulations by Karimi [7]: Fluent isentropic (—), Fluent non-isentropic (- - -), 1D isentropic (-·-·-), 1D non-isentropic (·····).

Upon comparing the simulation results to the results reported by Karimi and Abdi in Figure 7-10, a decent agreement is found with the isentropic results. Isentropic flow is both adiabatic and non-dissipative, *i.e.* no viscous damping is assumed. As the studied case is that of adiabatic flow, inviscid and isentropic have the same meaning. A similar observation as in Figure 7-3 can be made, being that the current simulation lacks accuracy in the throat. While the pressure curves all display distinct paths, they all seem to have approximately the same value in the nozzle throat. This is to be expected, as the throat pressure in choked flow is a thermodynamic property of the fluid. Apart from this lack of accuracy in the throat, the results fit the reported pressure data quite well. It is remarkable that according to the results of Karimi and Abdi, the shockwave for non-isentropic flow is located farther away from the nozzle compared to the shockwave for isentropic flow. As shown in Figure 7-5, the introduction of viscous damping moves the shockwave closer to the nozzle. Additionally, there is some inconsistency in the reported results of Karimi and Abdi. Figure 7-11 and Figure 7-12 show the corresponding temperature and Mach number profiles. Here the shockwave in the inviscid simulation is located farther downstream compared to the shockwave in the viscous simulation. The occurrence of a shockwave and its location should be identical for all fluid properties. This

is clearly not the case in the reported simulations. Based on the simulations related to the Arina case, the profiles reported for temperature and Mach number are assumed to be closest to reality and hence are used as reference. This implies that the location of the shockwave predicted by the current Fluent simulations, does not agree with the results previously found by Karimi and Abdi. The extrema of temperature and Mach number are, however predicted with good accuracy. The occurring differences could be related to the used equation of state as Karimi and Abdi do not report which equation was used.

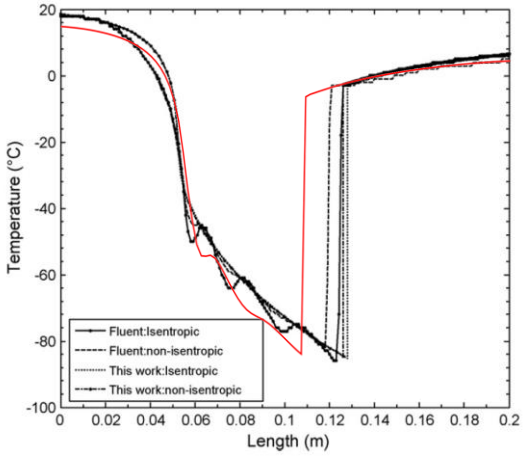

Figure 7-11: Temperature profiles for the current work (—) and the different models used by Karimi [7].

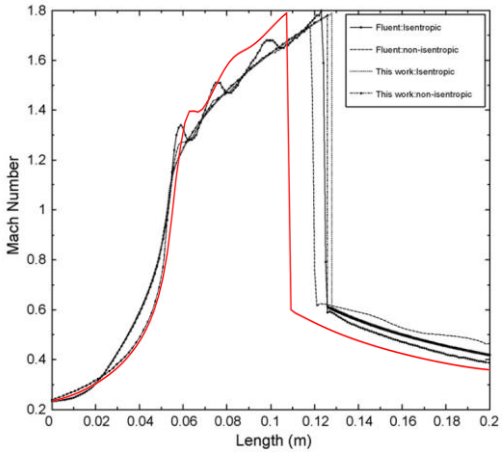

Figure 7-12: Mach number profiles for the current work (—) and the different models used by Karimi [7].

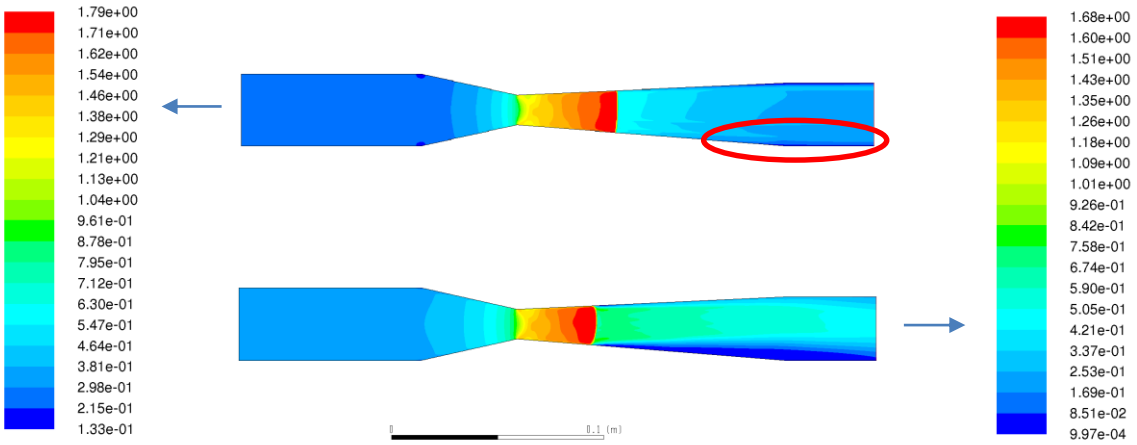

Figure 7-13: Mach number for the current simulation: Inviscid (top) and RKE (bottom).

To improve the accuracy of the results, an attempt is made using second order discretisation, however, no stable solution is obtained. The instability is caused by separation of the flow from the wall. The red encircled area in Figure 7-13 shows that flow separation is already visible in the inviscid solution. The flow separation becomes even more apparent when viscosity is introduced. Moreover, the flow separation is observed to be asymmetrical. Different authors have performed numerical simulations and experiments confirming the existence of a asymmetric flow separation behind the shockwave in planar geometries [10, 11]. While the accompanying secondary reflection phenomena are not visible in Figure 7-13, they are seen in

Figure 7-14 as a drop in pressure just behind the shockwave. This corresponds to a reacceleration of the flow as a result of reflection effects. A similar drop is reported by Karimi and Abdi as well, though the pressure profiles from other cases make it difficult to discern this in Figure 7-10. Performing the simulation with turbulence models only deteriorated the agreement with Karimi and Abdi's results as the location of the shockwave is predicted even further upstream.

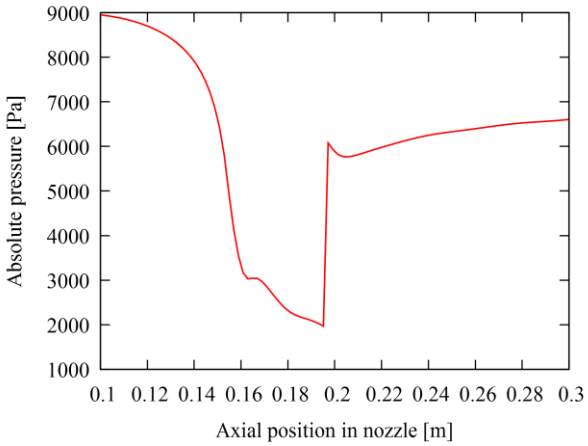

Figure 7-14: Pressure profile in the current simulation, using the RKE turbulence model and first order discretization.

7.3.2.2 Test Case (Case B)

In the second case several influences of the flow parameters are tested by Karimi and Abdi. However, only one set of flow parameters is simulated in this work. Though not specified, the nozzle used in case B is assumed to be rectangular with a depth of 1 m as well. The inlet, throat and outlet heights are 0.04 m, 0.021 m and 0.024 m respectively. An inlet section of 0.1 m is followed by a linearly converging section of 0.082 m, a linearly diverging section of 0.038 m and an outlet section of 0.08 m. The mesh for this case is very alike to the mesh for case A. The same number of quadrilateral cells is used for the height (99) and the length (746). The inlet conditions are 300 bar, 293.15 K and 22.278 kg s^{-1}. The outlet pressure is set at 210 bar. The same properties are used for methane as in case A. The simulation is performed using the RKE turbulence model, with enhanced wall treatment and compressibility effects. Considering the inlet conditions and the ideal gas law, it is deemed impossible that trans- and supersonic flow can be reached in the nozzle. The mass flow rate corresponds to a molar flow rate of 1.39 kmol s^{-1}. Via the ideal gas law this results in an inlet velocity of approximately 2.8 m s^{-1} and a nozzle velocity of approximately 30 m s^{-1}. This is more than an factor 10 below the speed of sound in methane, which is around 440 m s^{-1} depending on the exact conditions [3]. These findings are confirmed by the simulation results. The contours of the Mach number are shown in Figure 7-15, clearly indicating that the flow is far below transonic conditions. Due to these minimal velocity changes, the pressure is nearly constant. The Joule-Thomson effect does not occur at these low Mach numbers due to the limited amount of gas expansion and hence the temperature too is practically constant.

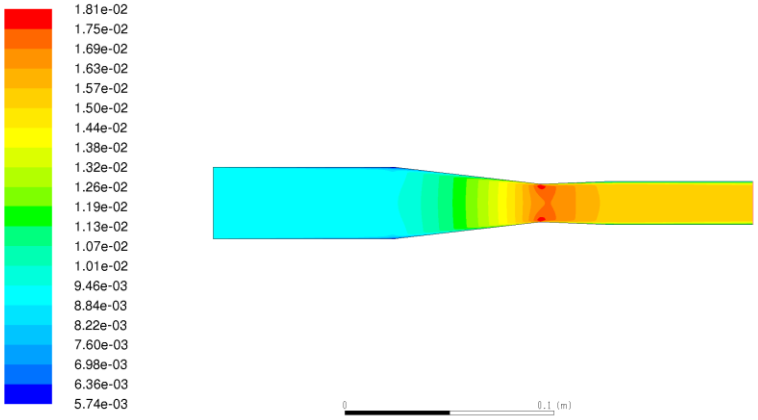

Figure 7-15: Mach number, for a rectangular duct. Inviscid flow, first order discretisation.

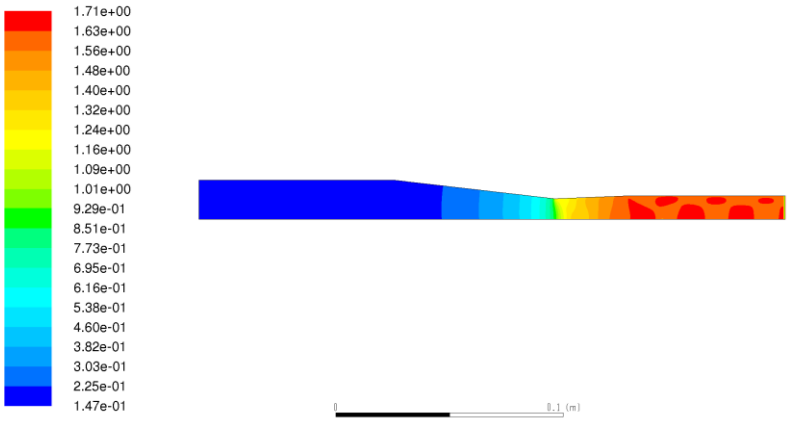

Figure 7-16: Mach number for a circular duct, inviscid flow, first order discretisation.

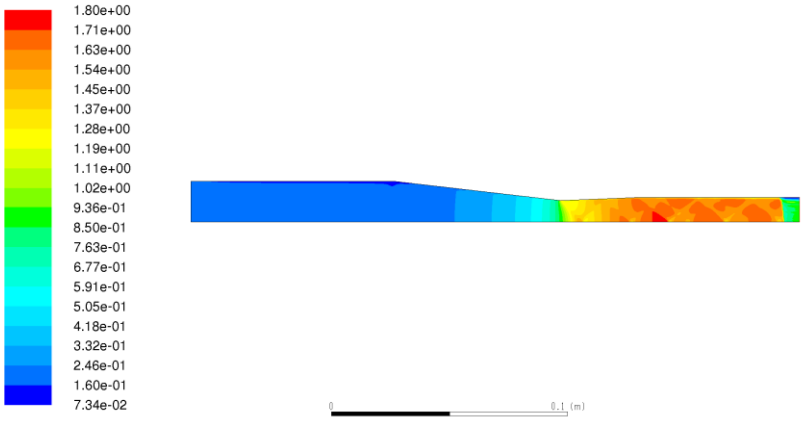

Figure 7-17: Mach number for a circular duct, RSM, second order discretisation.

The above findings point out the presence of inconsistencies in the work of Karimi and Abdi. As (nearly) identical inlet and outlet conditions are used, the assumption of a rectangular nozzle could be the source of the severe discrepancy between the simulated results and the results reported by Karimi and Abdi. The simulations are repeated, but using an axisymmetric, tubular geometry. Using a tubular geometry of which

the diameter equals the height of the rectangular geometry will increase the velocity by approximately a factor 30. In this geometry, choked flow is attained in the nozzle. However, due to the very limited length of the diverging section, the flow remains supersonic throughout the entire domain downstream of the nozzle, as illustrated in Figure 7-16. In Figure 7-17 it can be seen that simulations using the Reynolds stress model for turbulence and second order discretisation place the shockwave just inside the domain. This is clearly still in disagreement with the results of Karimi and Abdi, who reports the location of the shockwave to be 0.02 m behind the throat of the nozzle. Due to these major inconsistencies in the results, no further attention is given to this case.

7.3.3. Conclusion

The simulations discussed in the previous two paragraphs show that Fluent is capable of modelling shockwaves. However, this is a numerically difficult problem as the occurrence of a shockwave is the non-fulfilment of the flow equations on which the solver is based. Good agreement with the work of Arina [6] is achieved. It is also observed that in this simple geometry the discretisation method has only little influence on the result. Considering the work by Karimi and Abdi [7], case A could be reproduced with some accuracy, mainly in predicting the extrema of the flow parameters. For case B, too many inconsistencies in the reported results by Karimi and Abdi were found to provide a decent conclusion on the results. As for the specific settings, it is observed that acceptable results are obtained using a density based solver and first order discretisation. Some specific cases converged using second order discretisation, which remains the preferable discretisation method to limit numerical diffusion. The use of pressure or mass flow rate inlets depends on the case, but both provide a similar rate of convergence. Table 7-2 gives a short overview of the Fluent settings.

Table 7-2: Summary of the general Fluent settings used in the different simulations.

Parameter	*Type*	*Remarks*
Solver	Density-based	Pressure-base: diverges
Discretisation	Least-squares based First-order	Convergence of second order very case dependent
Turbulence	Inviscid-RKE-RSM	Viscous effects predict earlier shock
Outlet	Pressure	
Inlet	Pressure or Mass-flow	Inlet pressure and mass flow rate are thermodynamically linked in choked flow

7.4. 2D Simulations of SUSTOR2

7.4.1. Base Case

The starting point for the 2D simulations of the SUSTOR2 geometry is the work done by A. Malik during a summer internship in 2015 at the Laboratory for Chemical Technology in Ghent [12]. Initial mesh files and boundary conditions are available from the same work. Some settings are changed however, as summarised in Table 7-3. A density based solver is used for the axisymmetric swirl flow problem. First of all, as the context of the problem is the dehydration of natural gas, methane is used as fluid instead of nitrogen. The nozzle flow simulations discussed in section 7.3 showed that the assumption of inviscid flow gives decent results. However, due to the more complex geometry considered here, the solution becomes unstable when no viscous damping is present, making it impossible to perform inviscid simulations. The inlet mass flow rate is 0.14 kg s^{-1} and the vector of the inlet velocity is set at (0, -1, 5), corresponding to the (axial, radial, tangential/swirl) components. While the realisable k-epsilon turbulence model that has been used for all previous simulations should be able to describe swirling flows well [13], the RNG-k-epsilon (RNG) model incorporates a correction for swirl dominated flows. Due to the high swirl velocities in the SUSTOR2 geometry, the RNG model is preferred over the previously used realisable k-epsilon model for the SUSTOR2 simulations. The simulations are performed with first order spatial discretisation.

Table 7-3: Comparison of some important simulation settings between the work by Malik [12] and the current work.

Simulation Setting	*Internship-Malik*	*Current Work*
Fluid	Nitrogen	Methane
Turbulence model	Laminar with artificially increased viscosity	RNG-k-epsilon
Density	Real gas – SRK	Ideal gas
Mass flow rate	0.14 kg s^{-1}	0.14 kg s^{-1}
Outlet pressure	101325 Pa	202650 Pa
Inlet temperature	293 K	293 K
Spatial discretisation	Second order	First order

The geometry and dimensions of the base case are shown in Figure 7-18. For the bulk of the mesh an unstructured grid with triangular cells is used, while for the boundary layer a tetrahedral, semi- structured grid is used. The mesh is generated using the commercial software tool Pointwise. The left boundary is

identified as a symmetry plane. The bottom boundary is the axis of symmetry. The mesh consists of 26,487 cells.

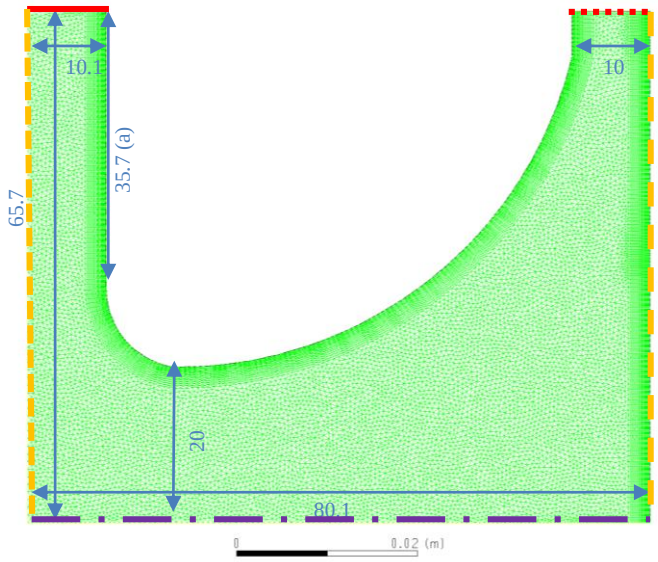

Figure 7-18: Starting geometry for the SUSTOR simulations. All dimensions are given in mm. "Inlet" ( ); "Outlet" ( ); "Left wall" ( ): symmetry plane; "Right wall" ( ): adiabatic wall; "Centreline" ( ): symmetry axis .

The results of the simulation are given in Figure 7-19 to Figure 7-24. A narrow high-velocity zone is present near the outer wall behind the nozzle throat. The flow remains subsonic at all times, *i.e.* the Mach number remains below unity, so with this geometry, it is not possible to exclude the occurrence of shockwaves in the SUSTOR2 device. A second consequence of the relatively low velocities is the limited expansion of the gas. Consequently, the Joule-Thomson effect is not strongly present, explaining why the minimal temperature reached in the device is only 263 K. Therefore, a device with these dimensions and operated at these conditions is not suited for natural gas dehydration. Nonetheless, there are several parallels with the claims made by the inventors of SUSTOR2. For one thing, a significant increase in swirl velocity is observed as the flow converges to the device's axis of symmetry. The same swirl velocity dies out quite rapidly after the flow passes through the narrowest section of the device. This is a result of severe friction losses caused by the high-velocity flow close to the wall. The axial velocity is seen to increase significantly in the region downstream of the nozzle. Additionally, a recirculation zone similar to the one described in reports of Shtern et al. [14, 15] is observed. The main part of the recirculation zone is located near the outlet of the device, but a significant backflow along the axis of symmetry is also observed. The proximity of a high (positive axial) velocity zone to a zone with significant negative axial velocity results in an interface experiencing significant friction losses, contributing to the pressure drop in the device. The inventors of SUSTOR2 claim that the kinetic energy of the tangential velocity component can be recovered as pressure by un-swirling the flow. This decreases the overall pressure drop in the device. While the recovery in the outlet is limited, the pressure increases from approximately 80 kPa to 100 kPa. Some changes in the geometry could result in a stronger recovery of pressure in the outlet section of the SUSTOR2 device.

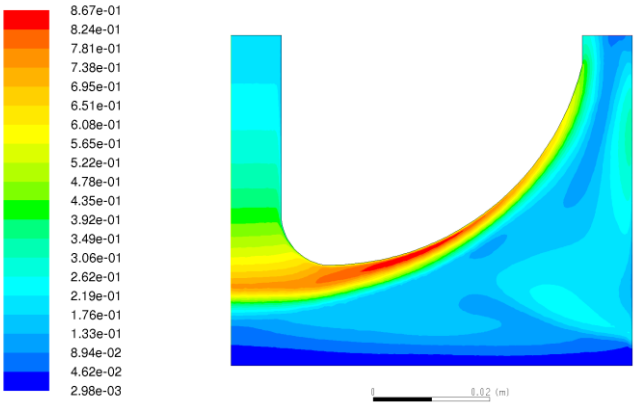

Figure 7-19: Mach number in the SUSTOR2 base case.

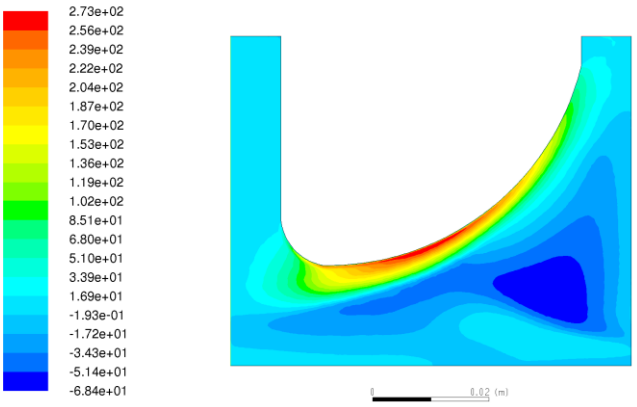

Figure 7-20: Axial velocity [m s^{-1}] in the SUSTOR2 base case.

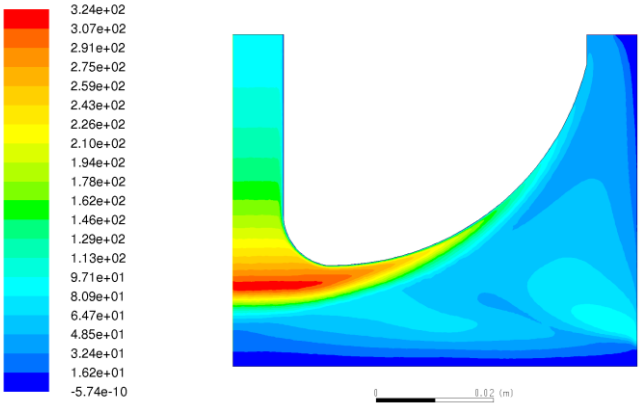

Figure 7-21: Swirl velocity [m s^{-1}] in the SUSTOR2 base case.

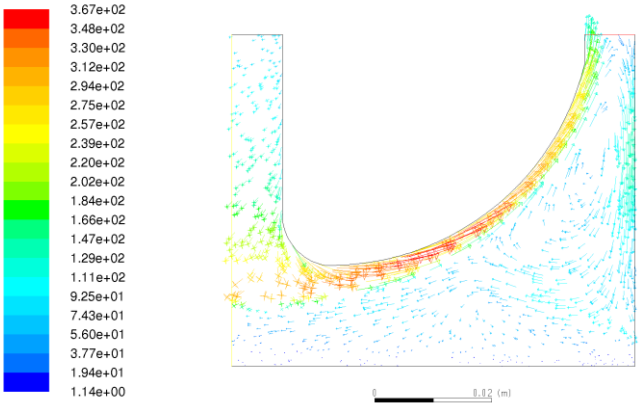

Figure 7-22: Vector of velocity [m s^{-1}] in the SUSTOR2 base case.

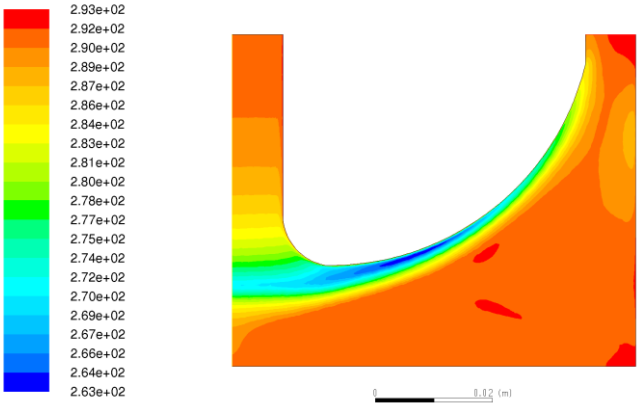

Figure 7-23: Temperature [K] in the SUSTOR2 base case.

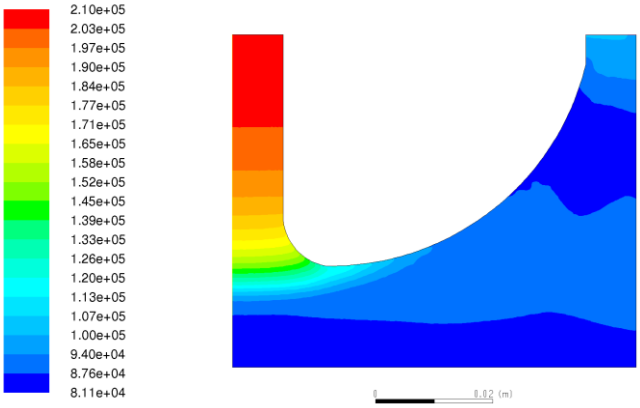

Figure 7-24: Pressure [Pa] in the SUSTOR2 base case.

7.4.2. Geometry Optimisation

The simulation of the base case showed that the initial geometry is far from optimal. Most importantly, the nozzle diameter is too large to accelerate the flow to supersonic velocities. The first step in the optimisation of the geometry will therefore be performing simulations with different throat diameters. A second observation in the base case was the presence of the recirculation zone in the throat of the device. The influence of a profiled end wall (PEW), both at the left and right sides of the device, on the location of the recirculation zone will be tested. A final optimisation parameter is the axial length of the separator. In the base case, the flow followed the profiled outer wall very well. The axial length of the SUSTOR device is shortened to see whether flow separation at the wall occurs for steeper wall profiles.

7.4.2.1 Nozzle Diameter

Three different nozzle throat diameters are simulated. All settings remain identical to those used in the base case. The mesh is adapted by altering the dimension (a) in Figure 7-18, maintaining an identical shape for the side wall profile. The tested diameters are 20 mm (base case), 10 mm and 5 mm. These are the diameters of the nozzle in the mesh. In the real geometry, this corresponds to the radius of the nozzle.

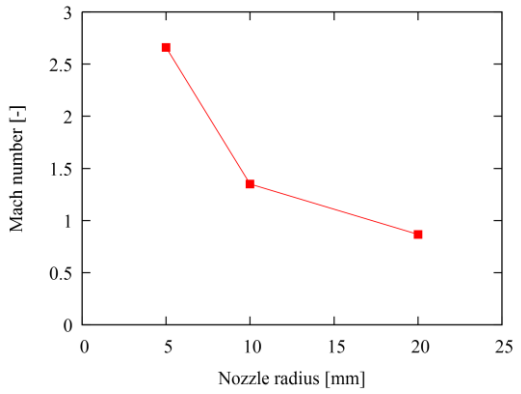

Figure 7-25: Maximal Mach number as function of the nozzle radius.

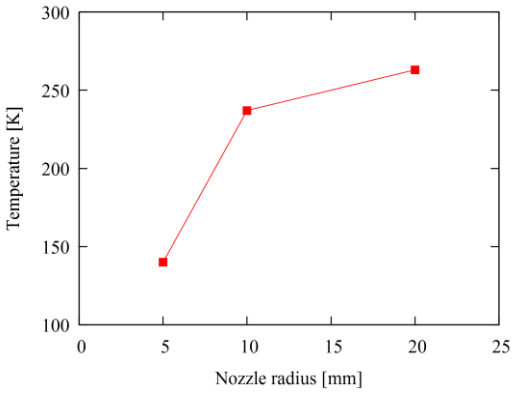

Figure 7-26: Minimal temperature as function of the nozzle radius.

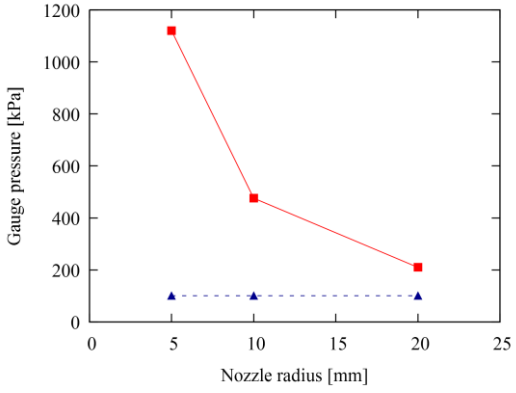

Figure 7-27: Inlet (-■-) and outlet (-▲-) pressures as function of the nozzle radius.

Figure 7-25 shows how the Mach number changes as function of the throat dimension. As expected, decreasing the nozzle diameter increases the maximum Mach number. Consequentially, the minimum temperature decreases as the throat diameter decreases (Figure 7-26). While from a temperature point of view, the narrowest nozzle seems the most promising for natural gas dehydration, pressure drop over the device must also be taken into account. The inlet and outlet pressures are given in Figure 7-27. For the case with a 20 mm nozzle, the pressure drop is approximately 33 % of the inlet absolute pressure, but this percentage increases to about 65 % for the 10 mm nozzle and reaches around 85 % for the narrowest nozzle. The greater part of the pressure drop takes place in the inlet section upstream of the nozzle throat (see Figure 7-24). The high swirl velocity results in high frictional pressure losses, while the acceleration of the gas converts the pressure to kinetic energy. The latter could potentially be recovered to pressure energy in the outlet section. While some pressure recovery is observed, in neither geometry does this amount to a significant decrease in pressure drop.

Besides affecting temperature, Mach number and pressure drop, the change in nozzle diameter also significantly affects the flow pattern in the device. When comparing the 20 mm case with the 10 mm case, it is seen that the backflow region no longer extends through the throat in the 10 mm case. The accelerating flow pushes the cone of the recirculation zone towards the outlet, which is illustrated by means of the axial velocity in Figure 7-28. The high-velocity flow is still located near the outer wall and no flow separation is observed, as proven in Figure 7-30. In the 5 mm nozzle case, no backflow in the throat region is observed in Figure 7-29. Moreover, a profile similar to the non-swirling shockwave cases discussed in paragraph 7.3 is found, rather than a profile as in the base case. The presence of this shockwave contributes to the high pressure drop predicted in this case. Also, at the wall severe flow separation is noticed. In this area some recirculation is predicted (the dark blue zone in Figure 7-31). In the cases with a nozzle diameter of 20 and 10 mm, the axial acceleration of the flow towards the nozzle throat is limited, while for the narrowest diameter, the axial acceleration is much stronger. A Mach number equalling unity is attained over the entire width of the throat, resulting in phenomena similar to those found in converging-diverging type nozzles.

To improve the accuracy of the results, simulations are attempted with second order discretisation. These did not converge to a stable solution and are therefore not suited for comparison with the first order simulations.

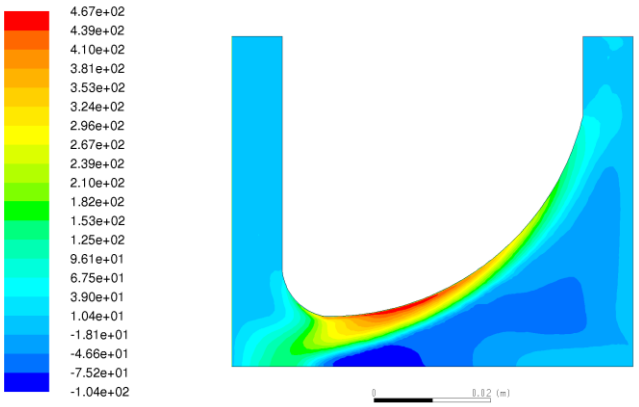

Figure 7-28: Axial velocity [m s^{-1}] in the 10 mm nozzle case.

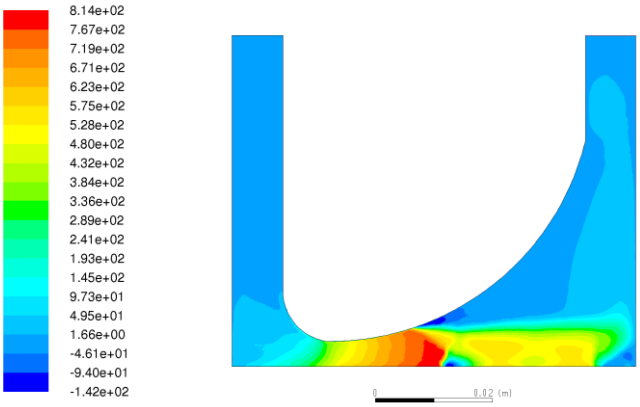

Figure 7-29: Axial velocity [m s^{-1}] in the 5 mm nozzle case.

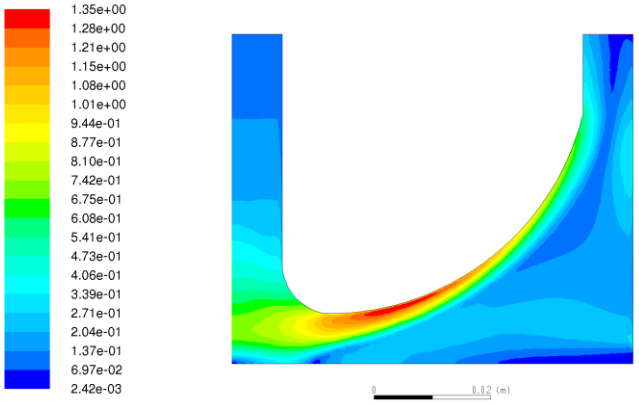

Figure 7-30: Mach number in the 10 mm nozzle case.

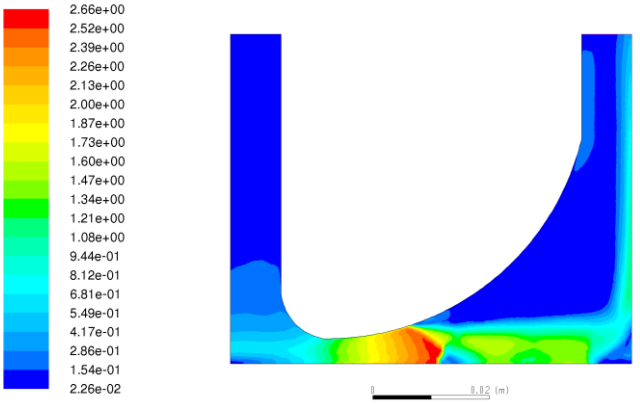

Figure 7-31: Mach number in the 5 mm nozzle case.

7.4.2.2 Profiled End Wall

Independently of the nozzle diameter, in the lower left corner of the domain, a low velocity zone is observed (Figure 7-19, Figure 7-30 and Figure 7-31). Again, this low velocity zone is in close proximity of a high velocity zone, introducing large amounts of drag and thus increasing the pressure drop. The introduction of a profiled end wall at the inlet centreline ("bottom PEW" case) is thought to reduce or eliminate this stagnant zone, decreasing the pressure drop. Additionally, the PEW is expected to move the cone of the backflow zone towards the outlet. As the simulations discussed in section 7.4.2.1 show that the design with a nozzle diameter of 10 mm exhibits the best trade-off between pressure drop and minimum temperature, this will be the starting case for the geometries with PEW. A similar stagnant zone can also be noticed in the bottom right of the domain. Introduction a PEW here ("top PEW") could shift the recirculation zone, altering the depth of the backflow region. Both PEWs have a profile following a Gaussian function. The bottom PEW is described by eq. (7-8), the top PEW by eq. (7-9), with y and x the coordinates in mm. The height of both PEWs is chosen to approximately cover the areas with the lowest velocity in Figure 7-30. The introduction of these PEWs implies a change in boundary conditions. While the case is still axisymmetric, it is practically impossible to construct a device which is symmetrical across the left wall

and use a PEW. Therefore, the left wall boundary condition is changed from symmetry plane to wall. Two cases will now be investigated, namely a case with only the bottom PEW and a case with both top and bottom PEW. The previous cases used a mesh with a structured wall boundary layer. Due to the increased complexity of the geometry, this is no longer possible and a completely unstructured, triangular cell mesh is used.

$$\begin{cases} x = 10\exp\left(-\frac{y^2}{40}\right) & 0 \le y < 20 \\ x = 0 \quad y = 20 \end{cases} \tag{7-8}$$

$$\begin{cases} x = 80 - 15\exp\left(-\frac{y^2}{500}\right) & 0 \le y < 50 \\ x = 80 \quad y = 50 \end{cases} \tag{7-9}$$

The results for the single PEW are compared to those without a PEW in Figure 7-32 to Figure 7-37, using the same colouring schemes. A first observation is that cone of the back flow region has penetrated through the nozzle throat after adding the PEW. Without the PEW, a central zone with intermediate velocity kept the backflow from penetrating through the nozzle. The addition of the PEW prevents the formation of this zone as the flow is already bent towards the wall by the profiled end wall. This is not the case in the original geometry, where the backflow region pushes the flow towards the wall. The high velocity region also appears to be located farther from the wall than without the PEW. This is most probably related to the unstructured boundary layer, which has a lower resolution than the structured boundary layer. Regarding the swirl velocity, it is found to be more concentrated along the wall and to die out at nearly the same rate as in the case without PEW. Even though the attained Mach number is lower with a bottom profiled end wall (1.28 compared to 1.35), the minimum temperature that is achieved is 3 K less, at 234 K. Moreover, the low temperature region is larger when a profiled end wall is used, making it possible to condense a larger quantity of water. A second advantage of the PEW is that the predicted pressure drop is lower. The required inlet pressure drops by 0.2 bar. The above shows the potential of a bottom PEW and optimising its geometry could lead to further improvement of the separation capacity.

A case with both top and bottom end walls is also investigated. However, the top end wall did not result in any significant changes in the flow pattern, pressure drop or minimal temperature. Therefore no further elaboration is made on these results, figures of contours of temperature, pressure and velocity components can be found on the enclosed DVD.

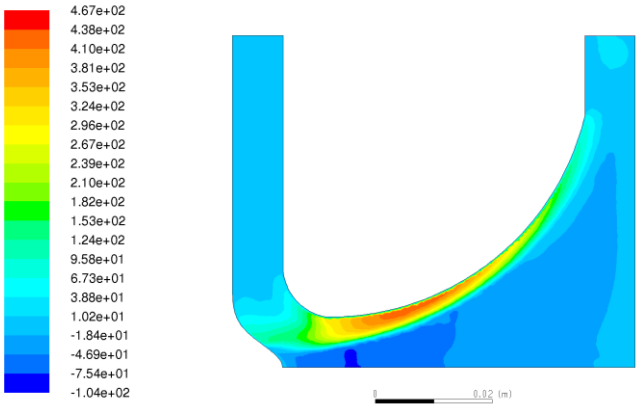

Figure 7-32: Axial velocity [m s^{-1}] in a 10 mm nozzle with bottom PEW.

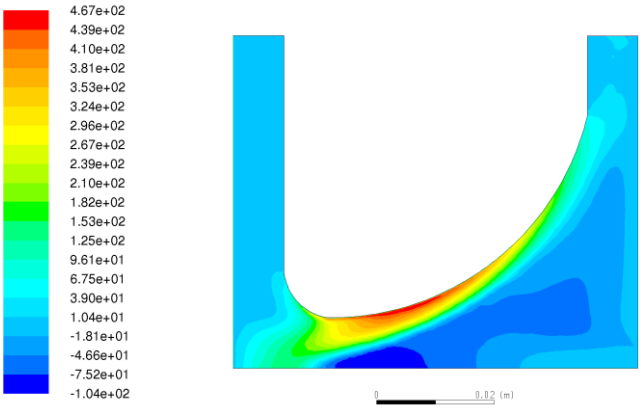

Figure 7-33: Axial velocity [m s^{-1}] in a 10 mm nozzle without PEW.

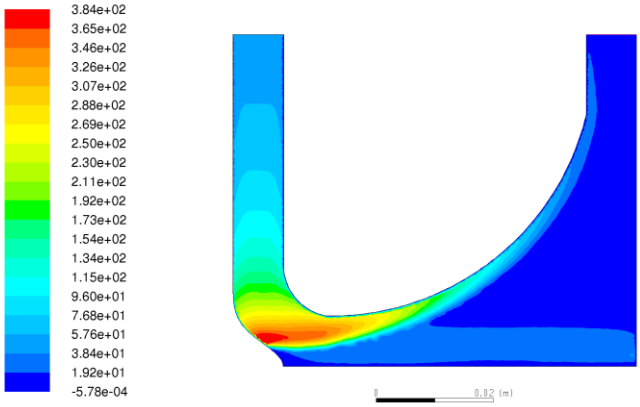

Figure 7-34: Swirl velocity [m s^{-1}] in a 10 mm nozzle with bottom PEW.

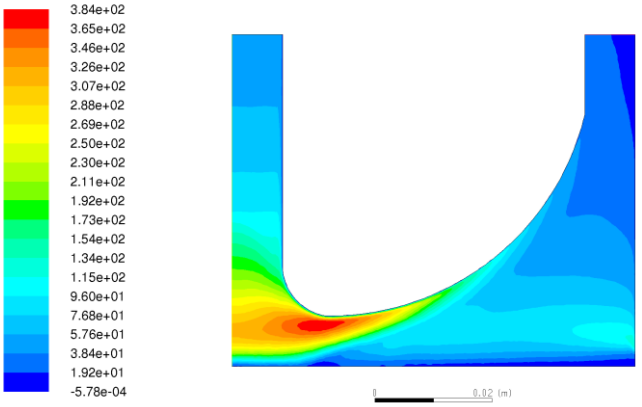

Figure 7-35: Swirl velocity [m s^{-1}] in a 10 mm nozzle without PEW.

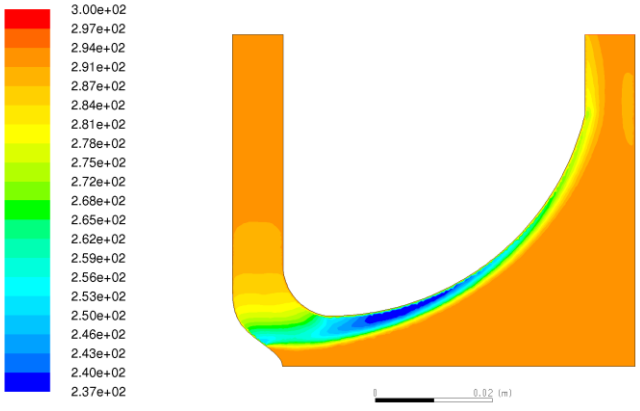

Figure 7-36: Temperature [K] in a 10 mm nozzle with bottom PEW.

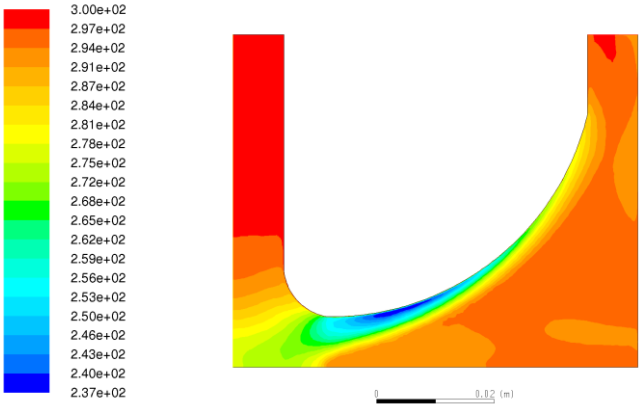

Figure 7-37: Temperature [K] in a 10 mm nozzle without PEW.

7.4.2.3 Axial Length

A final aspect of the geometry that is investigated is the axial length. In all previous simulations save the 5 mm nozzle, the high-velocity flow followed the outer wall very well and no flow separation was observed. Decreasing the axial length will result in a steeper side wall and potentially in flow separation. In the base case, the total axial length is 80.1 mm. Simulations will be performed using an axial length of 70.1 and 65.1 mm. The geometry with the PEW proved promising in section 7.4.2.2, therefore, the profiled end wall is retained in both cases. The case with an axial length of 65.1 mm is also simulated without a PEW. In addition to changing the axial length, the transition from the curved side wall to the straight outlet is smoothed, by arbitrarily extending the side wall with a gradual decrease in slope.

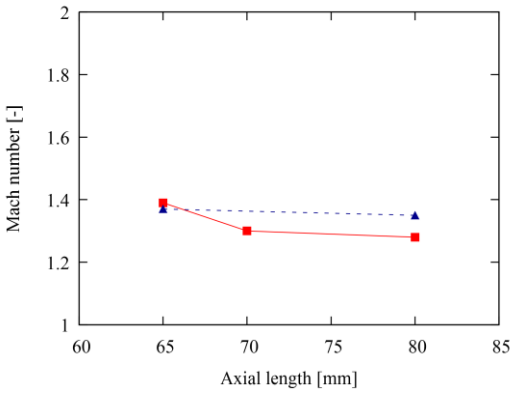

Figure 7-38: Maximal Mach number as function of the axial length, with (-■-) and without (-▲-) PEW.

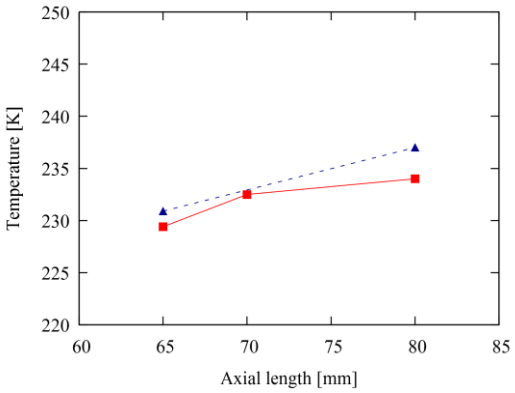

Figure 7-39: Minimal temperature as function of the axial length, with (-■-) and without (-▲-) PEW .

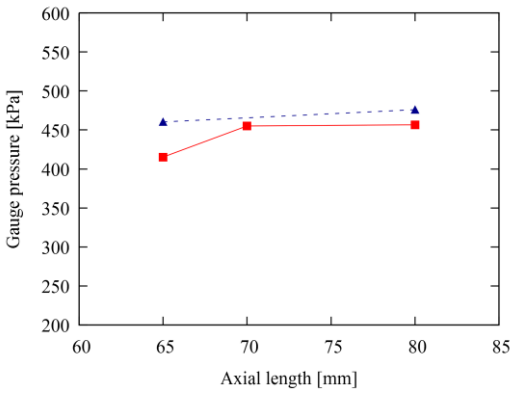

Figure 7-40: Inlet pressure as function of axial length, with (-■-) and without (-▲-) PEW .

Figure 7-38 to Figure 7-40 show the 0-dimensional results of maximal Mach number, minimal temperature and inlet pressure for the various cases. In general it is found that reducing the axial length is beneficial for the separation of water. The shorter the domain, the lower the temperature and the lower the required inlet pressure. It is important to note that no flow separation occurred in any of the cases, even for an axial length of 55 mm, the flow continues to follow the wall closely. Furthermore, some care should be taken when comparing absolute data from the cases with PEW with those without.

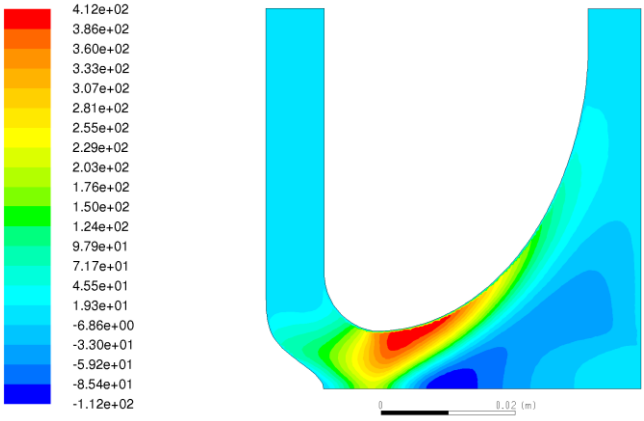

Figure 7-41: Axial velocity [m s^{-1}] in the case with PWE and axial length of 65 mm.

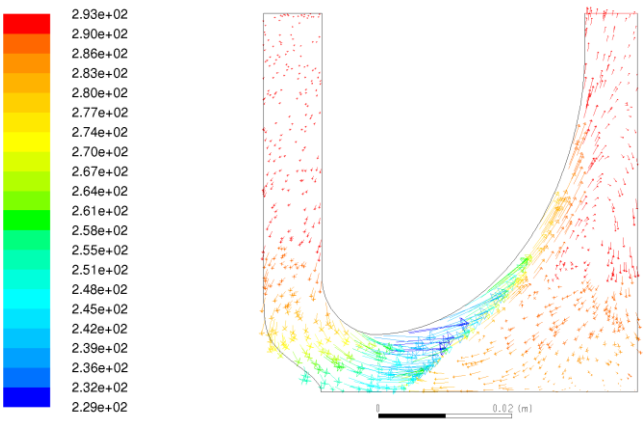

Figure 7-42: Velocity vectors coloured by temperature [K] in the case with PWE and axial length of 65 mm.

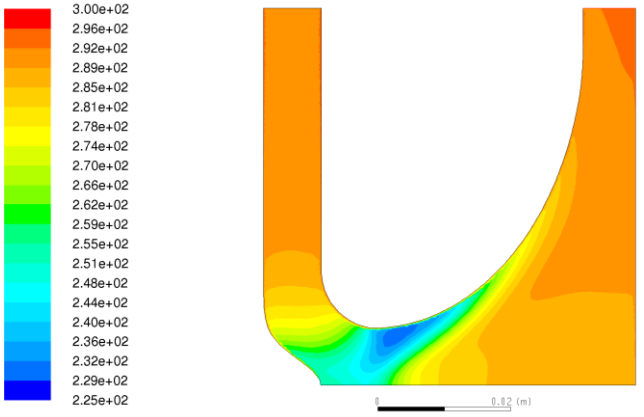

Figure 7-43: Temperature [K] in the case with PWE and axial length of 65 mm..

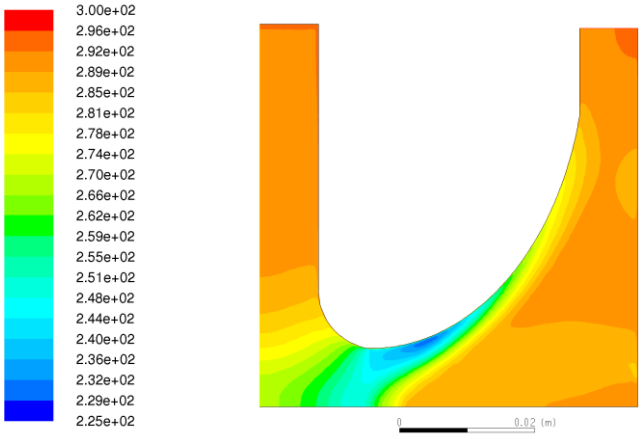

Figure 7-44: Temperature [K] in the case with PWE and axial length of 65 mm..

Due to the more complex geometry, the boundary layer in the PEW cases does not have a structured boundary layer. Simulations in the case without PEW showed that the lack of a high resolution boundary layer tends to underestimate parameters such as maximum Mach number and overestimate the minimum temperature. In the presence of a profiled end wall, a change in slope is noticed in the graphs. Related to Figure 7-32, it has been pointed out that the profiled end wall prevents the formation of a central zone with positive axial velocity, missing out on its goal to prevent the backflow zone from penetrating through the nozzle throat. However, when the length of the device becomes sufficiently low, this central zone is formed even in the presence of the PEW, blocking the throat to the negative axial velocity zone. As a result the cone of the backflow region is significantly pushed towards the outlet, as illustrated in Figure 7-41 and Figure 7-42. The disappearance of a backflow region through the nozzle throat leads to a decrease in pressure drop which in turn leads to a higher velocity, finally allowing greater expansion of the fluid and yielding a lower minimum temperature. In case no profiled end wall is present, the central zone is already present at an axial length of 80 mm, resulting in a fairly constant change of the parameters with the axial

length. Figure 7-36 and Figure 7-37 already pointed out a slightly broader low temperature zone in the case with a PEW. Figure 7-43 and Figure 7-44 show that the broader low temperature zone is now even more emphatically present just behind the nozzle throat region.

A final remark that must be made concerning the axial length of the device, is about the time a water droplet requires to impact the wall. First of all, shortening the domain will give the formed condensate droplets less time to move towards the side wall. Decreasing the length of the device too much will result in some droplets remaining in the gas flow, decreasing the separation efficiency. A similar reasoning applies to the location of the low temperature zone. Without a PEW, the low temperature zone is located very close to the wall, maximising the separation of formed condensate droplets. When a profiled end wall is present, the low temperature zone extends towards the device centreline. The droplets formed in this region will be separated less efficiently. Fortunately however, the low temperature zone covers a nearly equal fraction of the side wall as in the case without PEW. Therefore, the total separation efficiency is expected to be at least as high, if not higher, than without PEW.

7.4.3. Conclusion

Starting from the base case investigated by A. Malik [12], several different geometries have been investigated. First of all it became apparent that the base case as such cannot work efficiently as a supersonic swirling separator. The nozzle diameter is too large to accelerate the flow past a Mach number of one. A nozzle throat diameter of 10 mm is found to provide the best results compared to a diameter of 20 mm or 5 mm. In the narrowest nozzle shockwave like flow patterns are predicted, which is undesired as it significantly increases the pressure drop. Initially, the addition of a profiled end wall seemed to only marginally improve the performance, lowering the minimum temperature by 3 K and the inlet pressure by 0.2 bar. However, reducing the axial length of the SUSTOR separator proves to be highly beneficial, both with and without PEW, though the effects are most outspoken when a profiled end wall is present. Below a certain axial length, a major change in flow pattern is observed with the formation of a central high-velocity zone preventing backflow through the nozzle throat, greatly reducing the pressure drop. Without a PEW, this zone is already present at the longest axial lengths, explaining the less outspoken improvements. While decreasing the length improves performance based on pressure drop and temperature, it will decrease the separation efficiency as droplets have less time to travel to the wall in the centrifugal field. Investigating this is not possible with the current simulation set-up and requires additional modelling of nucleation phenomena. As optimal geometry of the simulated cases, the case with a nozzle diameter of 10 mm and an axial length of 65 mm and in which a profiled end wall is used on the left wall, is proposed.

7.5. SUSTOR-3D Simulations

7.5.1. Geometry and Mesh

The three dimensional geometry of the SUSTOR2 device is again based on the work of Shtern et al. [14, 15]. As opposed to the two dimensional case, an inlet and outlet section are added to the geometry. The geometry of the inlet section is shown in Figure 7-45. The outlet section is nearly identical, the only difference is that the outlet faces the positive x-axis instead of the negative axis. Three different layers can be discerned in the mesh of the geometry. The bottom disc of the geometry in Figure 7-46 joins with the inlet section on the middle layer. Analogously, the top disc joins with the outlet section on the middle layer as well. Using these extended inlet and outlet sections allows the prediction of the actual 'nozzle inlet' and 'nozzle outlet' conditions of the nozzle, rather than simply specifying a tangential component to the inlet velocity. They have large cross-sectional area to minimise the gas pressure drop in these sections. The inner part, shown in Figure 7-46 is a revolution by 360° of one of the 2D geometries discussed in section 7.4. The conclusion of that section pointed out that a geometry with a throat radius of 10 mm and a profiled end wall at the inlet shows the greatest potential. Therefore, this geometry is used as base for the 3D volume. The complex geometry of this region implies the use of an unstructured, tetrahedral grid. The added inlet and outlet sections have a tapered section. In this region, the grid is also unstructured, but only in the x-z plane. In the y-direction (height) the mesh is structured, implying the use of pyramidal cells. The entire grid comprises 4,769,718 cells, divided over 2,684,030 tetrahedral, 2,061,444 hexahedral and 24,244 pyramidal cells.The same conditions and settings as for the 2D simulations are used. The inlet mass flow rate is maintained at 0.14 kg s^{-1}. The outlet pressure is set at 202650 Pa. As a result, the outlet pressure of the central geometry will be slightly higher than in the 2D simulations due to the pressure drop in the outlet. However, the pressure drop is expected to be minimal, hence not significantly altering the nozzle outlet conditions. The inlet temperature is 293 K and methane is assumed to behave as an ideal gas. First order discretisation is used. The Courant number for the density-based solver is lowered to 0.5 as otherwise the simulation immediately diverges.

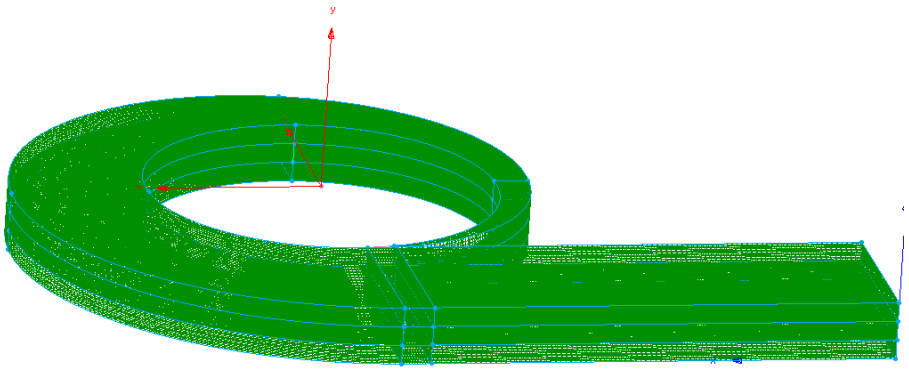

Figure 7-45: Mesh of the added inlet section.

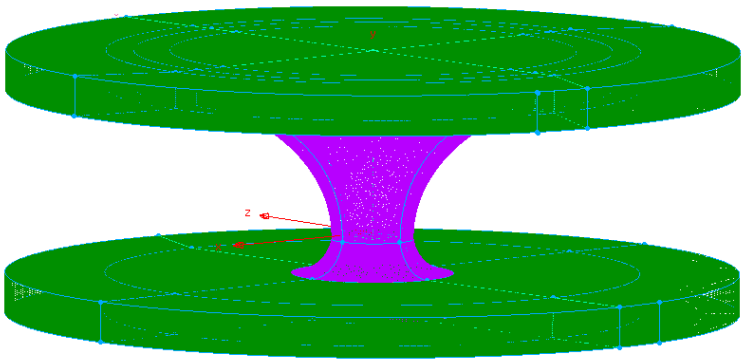

Figure 7-46: Mesh of the central region, corresponding to a revolution of the geometry used in Figure 7-41 to Figure 7-43. The purple zone is unstructured, the green areas are structured grids.

7.5.2. Results and Discussion

The 3D simulation with inlet conditions as specified before converges very poorly. In the results discussed below, there is still a mass imbalance between inlet and outlet of 15 %. The reason for this poor convergence is that, contrarily to the two-dimensional simulations, a shockwave is predicted. Consequentially, the discussed results for a flow rate of 0.14 kg s^{-1} are only useful for a qualitative analysis. The occurrence of a shockwave is illustrated by both the Mach number and temperature in the device, in respectively Figure 7-47 and Figure 7-48. The first iso-surface of unity Mach numbers is located nearly exactly in the throat of the device. Hence, a flow pattern similar to that in Figure 7-31 is observed. This is an important observation as it proves that, while the 2D simulations do not predict the occurrence of a shockwave, the 3D simulations do. Initially, the major drawback of such a shockwave was thought to be the high pressure drop. Upon analysing the results of the three dimensional simulations, it becomes clear that the shockwave prevents the device from working at all. From the stream lines in Figure 7-47, it is apparent that the flow loses most of its swirling character during the subsonic to supersonic transition. Hence there the centrifugal field which is responsible for the removal of the liquid droplets is no longer present. Additionally, the lowest temperatures (which are as low as 180 K), are present along the shock wave, instead of along the nozzle wall. This means that even in the presence of a centrifugal field, the separation efficiency of the water droplets is low. Another observation is that due to the asymmetric inlet and outlet, the assumption of axisymmetric flow in the nozzle is no longer valid.

As the shockwave prevents correct operation of the device, the flow rate is decreased. Simulations are performed for inlet mass flow rates of respectively 0.10, 0.07 and 0.035 kg s^{-1}. Figure 7-49 to Figure 7-51 illustrate the flow profiles for the different mass flow rates. The shockwave is no longer present for any of the reduced flow rates. In the 0.1 kg s^{-1} case, the flow appears to be in a transitional state, between shockwave flow and swirling flow. Figure 7-49 illustrates highly irregular iso-surfaces for unity Mach numbers. Additionally, a high degree of asymmetry is observed in the y-plane slices. This asymmetry is ascertained in all reduced flow rate cases. The asymmetrical outlet section is likely to be the main reason

for this flow pattern. The degree of asymmetry is increased as the mass flow rate increases. Once a shockwave is formed, the asymmetric character partially disappears as the upstream pressure no longer influences the flow downstream of the nozzle. For a mass flow rate of 0.07 kg s^1 or less, a flow pattern that resembles that from the two dimensional simulations is observed. The profiled end wall does not prevent the back flow region from penetration through the nozzle, in the 0.1 kg s^1 case, the back flow region even extends down one side of the PEW, into the inlet section. The inclusion of the PEW was based on the formation of a high velocity front in the 2D simulations. The absence of this phenomenon questions the use of the PEW.

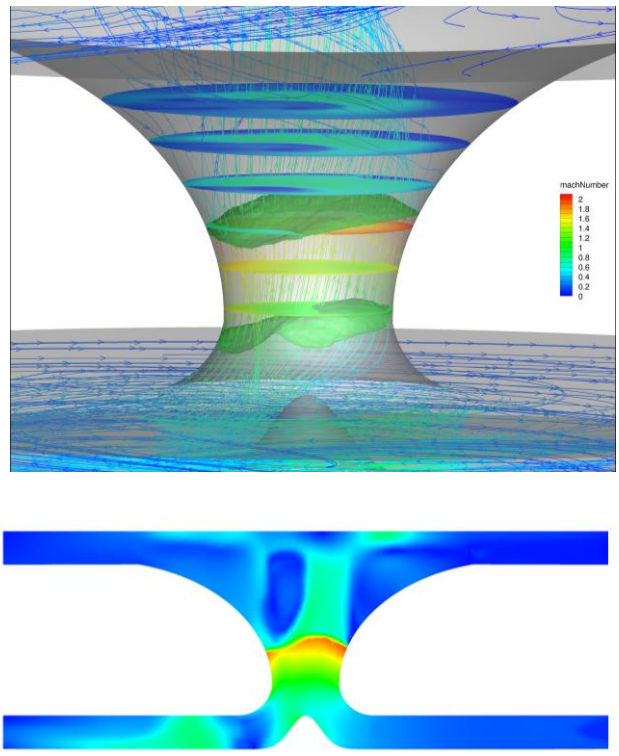

Figure 7-47: Mach number in the 3D SUSOR2 geometry, mass flow rate of 0.14 kg s^{-1}. Y-plane slices, stream lines and iso-surface of unity Mach number (top) and z-plane view of Mach number (bottom).

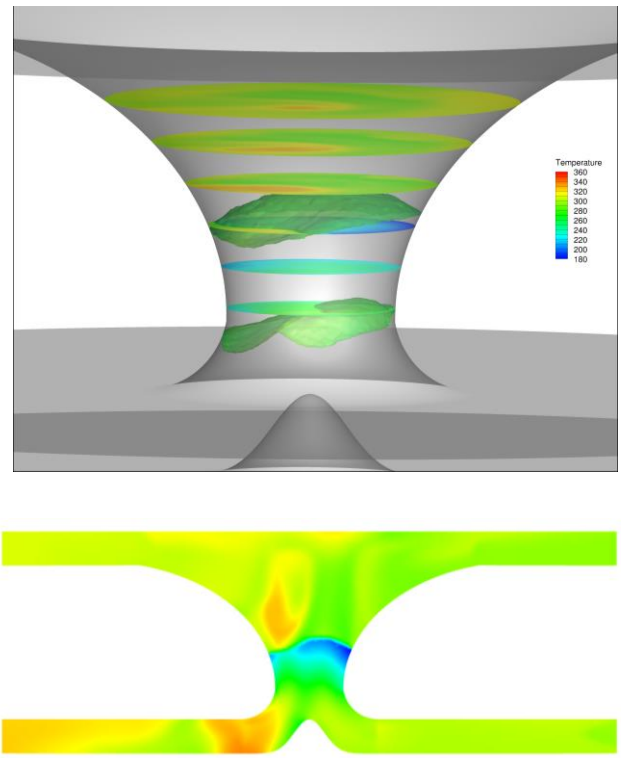

Figure 7-48: Temperature [K] in the 3D SUSOR2 geometry. Y-plane slices and iso-surface of unity Mach number (top) and z-plane view of Mach number (bottom).

The minimum temperature is predicted at or below 230 K in all cases, as shown in Figure 7-53. For the lowest mass flow rate, the temperature is 232 K, which is above the dew point temperature specification. By optimising the inlet section to achieve a more stable flow at higher mass flow rates, the temperature can be further decreased to ensure that the dew point specification is met to increase the fraction of the separator in which the temperature is below 230 K. Figure 7-54 indicates that the pressure drop in the three dimensional simulations is between 170 kPa and 180 kPa, or 46 % of the absolute inlet pressure. This close to reported pressure drops in other swirling flow devices. As long as no shockwave occurs, the pressure drop only increases slightly with increasing mass flow rate. A very abrupt increase in pressure drop is observed once a shockwave is formed, the pressure drop increases by 37 % to 245 kPa.

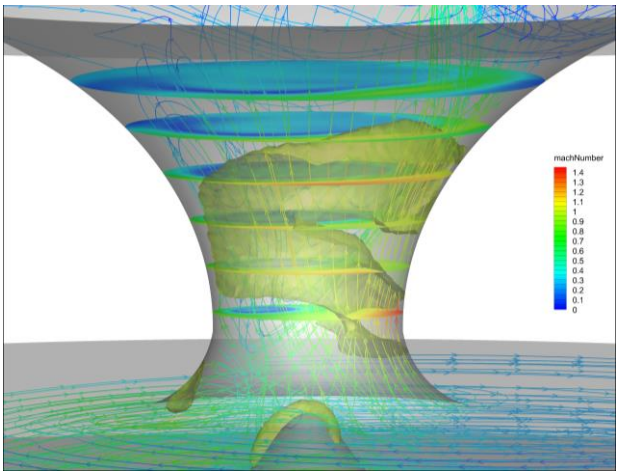

Figure 7-49: Mach number in the 3D SUSOR2 geometry, mass flow rate of 0.1 kg s^{-1}. Y-plane slices, stream lines and iso-surface of unity Mach number.

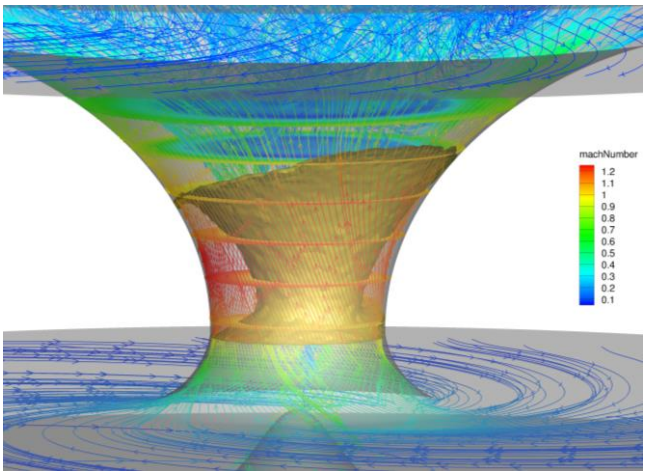

Figure 7-50: Mach number in the 3D SUSOR2 geometry, mass flow rate of 0.07 kg s^{-1}. Y-plane slices, stream lines and iso-surface of unity Mach number.

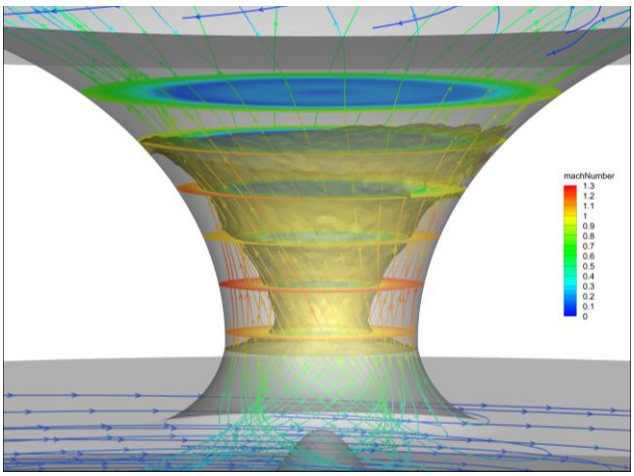

Figure 7-51: Mach number in the 3D SUSOR2 geometry, mass flow rate of 0.035 kg s^{-1}. Y-plane slices, stream lines and iso-surface of unity Mach number.

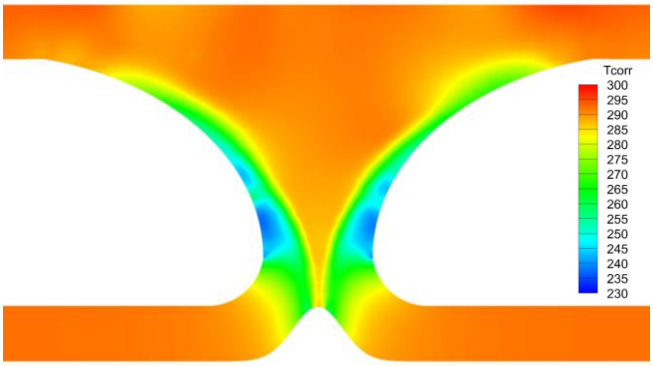

Figure 7-52: Temperature [K] in the 3D SUSOR2 , mass flow rate of 0.035 kg s^{-}, viewed in the z-plane.

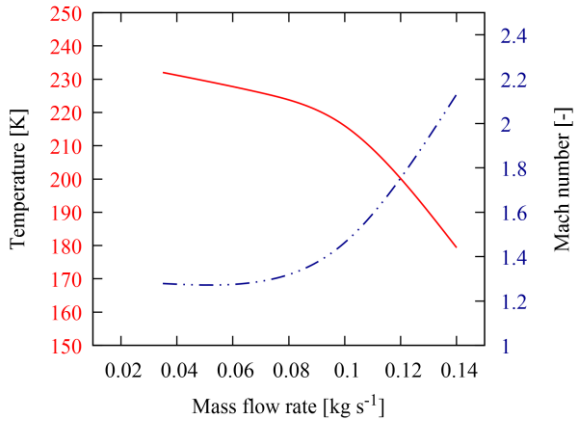

Figure 7-53: Minimum temperature (——) and maximum Mach number (· —), depending on the mass flowrate.

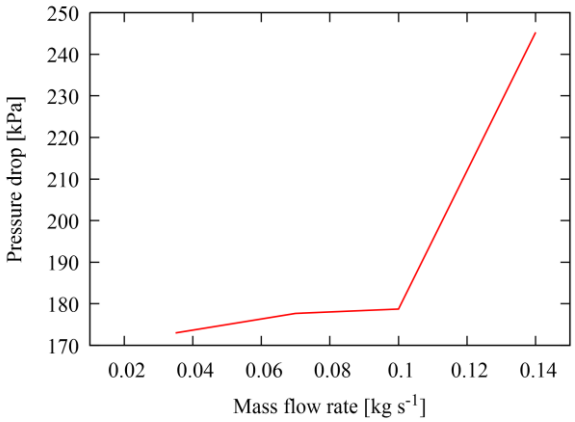

Figure 7-54: Pressure drop as function of the mass flow rate in the SUSTOR2 device.

7.6. Conclusions

The Joule-Thomson effect lowers the temperature of an expanding gas. This principle is exploited in SUSTOR2 for the dehydration of raw natural gas. To achieve sufficient expansion of the gas, the flow must be in the trans- or supersonic regime. These types of flows are numerically very challenging as they lead to discontinuities in the flow parameters in the form of a shockwave. To assess whether ANSYS Fluent is capable of calculating such flows, basic Laval-type nozzle simulations of Arina and Karimi et al. are reproduced. The results of Arina are reproduced with good accuracy. In the work of Karimi and Abdi several inconsistencies are found, making it difficult to judge the degree of agreement between the results.

An initial geometry is based on data from the SUSTOR2 patent, but indicates that the nozzle diameter is too large to achieve the required expansion. Based on three parameters, the geometry is optimised using two dimensional RANS simulations. The first parameter is the throat diameter. The axial length of the domain and the effect of a profiled end wall are also studied. Simulations show that reducing the nozzle diameter increases the maximum velocity and reduces the minimum temperature, improving the performance of the device. However, for a nozzle diameter of 10 mm, a shockwave is formed, nullifying the performance enhancement. The inclusion of a profiled end wall initially only yields minor performance enhancements, but combined with a reduction of the axial length of the domain, gives the best overall combination of high swirl velocity and low temperatures.

A three dimensional design is based on the two dimensional geometry with a profiled end wall, an axial length of 65 mm and a throat diameter of 10 mm. The 3D simulation using the exact same boundary conditions as in the two dimensional case predicts the formation of a shockwave, in contrast to the 2D case. Not only is this detrimental to the pressure drop, the tangential component of the velocity is practically reduced to nihil, eliminating the centrifugal forces required to separate formed water droplets. Simulations with lower inlet mass flow rates no longer predict the shock wave, though at 0.1 kg s^{-1}, an unstable, transitional regime is observed. Otherwise, the results are promising. The simulated minimum temperature is below 230 K except for the lowest mass flow rate. At 0.035 kg s^{-1}, the minimum temperature is 232 K. In the other two cases without shockwave behaviour, the temperature is sufficiently low to comply with the dew point specification of the natural gas. The predicted pressure drop is between 170 and 180 kPa, corresponding to 46 % of the total inlet pressure. It is possible that this pressure drop is rather independent of the total pressure, implying that at the actual dehydration operating pressure, the pressure drop could be below the acclaimed 5 %. Further performance gains can be achieved by optimising the inlet and outlet section which have been only modelled very basically in these simulations. This can result in both a reduction of the pressure drop and a potential reduction of the minimum temperature by stabilising the flow at higher mass flow rates.

7.7. References

1. Baehr, H. D., Stationäre Flieβprozesse. In *Thermodynamik: Eine Einführung in die Grundlagen und ihre Technischen Andwendungen*, Fünfte Auflage ed.; Springer-Verlag: Berlin, 1981; pp 232-292.
2. Welty, J. R.; Wicks, C. E.; Wilson, R. E.; Rorrer, G. L., Differential Equations of Fluid Flow. In *Fundamentals of Momentum, Heat, and Mass Transfer*, John Wiley and Sons, Inc.: , 2008; pp 99-112.
3. Geen, D. W.; Perry, R. H., Physical and Chemical Data. In *Perry's Chemical Engineers' Handbook*, 8 th ed.; McGraw-Hill Companies, Inc.: 2008; pp 2.1-2.517.
4. Borissov, A.; Mirzoev, G.; Shtern, V. Supersonic Swirling Separator 2 (Sustor2). US 20120180668 A1, 2012.
5. Lin, Z.; Junming, F.; Jia, Z.; Li, Q.; Luling, L., Formula calculation methods of water content in sweet natural gas and their adaptability analysis. *Natural Gas Industry B* **2014,** 1, (2), 144-149.
6. Arina, R., Numerical simulation of near-critical fluids. *Applied Numerical Mathematics* **2004,** 51, (4), 409-426.
7. Karimi, A.; Abdi, M. A., Selective dehydration of high-pressure natural gas using supersonic nozzles. *Chemical Engineering and Processing: Process Intensification* **2009,** 48, (1), 560-568.
8. Wen, C.; Cao, X.; Yang, Y., Swirling flow of natural gas in supersonic separators. *Chemical Engineering and Processing: Process Intensification* **2011,** 50, (7), 644-649.
9. Jassim, E.; Abdi, M. A.; Muzychka, Y., Computational Fluid Dynamics Study for Flow of Natural Gas through High-pressure Supersonic Nozzles: Part 1. Real Gas Effects and Shockwave. *Petroleum Science and Technology* **2008,** 26, (15), 1757-1772.
10. Xiao, Q.; Tsai, H.-M.; Papamoschou, D., Numerical investigation of supersonic nozzle flow separation. *AIAA Journal* **2007,** 45, (3), 532-541.
11. Papamoschou, D.; Zill, A.; Johnson, A., Supersonic flow separation in planar nozzles. *Shock waves* **2009,** 19, (3), 171-183.
12. Malik, A.; Van Geem, K. *Preliminary Comutational Fluid Dynamics Analysis of SUSTOR2*; Ghent University: Ghent, 10/8/2015, 2015; p 33.
13. Andersson, B.; Andersson, R.; Hakansson, L.; Mortensen, M.; Sudiyo, R.; Wachem, B. v., Turbulent-Flow Modelling. In *Computational Fluid Dynamics for Engineers*, Cambridge University Press: 2012; pp 62-112.
14. Shtern, V.; Borissov, A. *Cold Flow in a Vortex Nozzle*; SUSTOR: 2015.
15. Shtern, V.; Mirzoev, G.; Borissov, A. *SUSTOR-Business Plan*; 2013.

8

Conclusions and Future Work

8.1. Conclusions

In this work, turbulent flows have been investigated using both the Reynolds averaged Navier-Stokes (RANS) and the large eddy simulation (LES) principles for turbulence modelling. LES has been used to simulate reactive flow in different steam cracking coil geometries. RANS has been used to model the single phase, non-reactive flow in the SUSTOR2 natural gas dehydration device.

Modelling of turbulence is a topic which has received significant attention in the past, resulting in well-validated and widely used models. However, inevitably information concerning the turbulence is lost when adopting any modelling strategy. Direct numerical simulation (DNS) is the one method that does not model any aspect or scale of the turbulence. Currently DNS still has too high computational demands to be feasible on full-size geometries, but it is an excellent research tool on down-scaled systems. The specific demands of DNS require dedicated computational codes, focussing on minimising the numerical errors of the simulation. Several such codes exist, each tailored to certain types of flow. A first DNS-capable code, is OpenFOAM. It is based on the free volume discretisation method (FVM), in which the conservation equations in their weak formulation are solved in a discrete number of cells, determining one value for the flow parameters in each cell. The drawback of OpenFOAM is that it is not dedicated to DNS and has a low order of accuracy. A second FVM-based code is Gerris, which has been fine-tuned for multi-phase flows. An important characteristic in this context is the capacity to automatically refine the mesh, depending on the position of the fluid interface, via octree refinement. This allows for a larger average cell volume, reducing the computational cost of the simulation. The GPU accelerated code S3D is property of the Sandia National Laboratories and has been developed for reactive DNS in large geometries (exa-scale simulations). S3D is based on the finite differencing method (FDM), which is quite similar to the FVM, only that the flow equations are solved in their strong formulation. Contrary to OpenFOAM, S3D has a high, twelfth order accuracy. The two final codes – Nek5000 and SIMSON – are based on a different discretisation principle. Instead of solving the equations in each individual cell, the solution is represented as a weighted sum of base functions. The function value in a grid point, combined with the flow equations then determines the value of the weighting coefficients for the general solution. These methods are known as spectral methods (SM). The obtained solution is theoretically only correct in the grid points themselves, though it is assumed that the resulting values elsewhere in the domain are also valid. This is comparable to applying interpolation in the FVM or FDM. SIMSON uses a pure spectral method, giving it the highest single core performance of all mentioned codes. Its major disadvantage in the inability of fully spectral methods to represent complex geometries. This problem is solved in Nek5000, using spectral element methods (SEM). These combine the superior accuracy of spectral methods with the geometry flexibility of the finite volume method. In different discrete "elements" of the domain, the solution is represented by a different set of weighting coefficients.

Taking into account the distinctive characteristics of the different numerical codes, Nek5000 proves to be the code of choice for performing DNS. Besides excellent accuracy and the capability to handle complex geometries, it is open-source, has a considerable user base and is well supported and documented.

Wall-resolved large eddy simulations (WRLES) of butane steam cracking in different geometries are performed. A bare tube is used as reference, to compare heat transfer, pressure drop and light olefin yields and selectivities to those in two enhanced reactor geometries, *i.e.* a longitudinally finned tube and a helicoidally ribbed tube. In the finned geometry, the heat transfer is improved by increasing the heat transfer surface area, while in the ribbed geometry this is achieved by promoting turbulence and radial mixing. All other effects are directly or indirectly related to the aforementioned alterations. The wall-adaptive local eddy viscosity model (WALE) is used to determine the sub-grid scale stresses. As basic validation of the simulation, the results are compared to one dimensional simulations using CHEMKIN. Good qualitative agreement is observed, but since radial and tangential gradients are taken into account in the LES, there are important quantitative differences. The most important difference is the overall lower bulk temperature simulated in the three dimensional simulations. Since radial and tangential mixing improves from the bare reactor via the finned reactor to the ribbed reactor, the corresponding average bulk temperature is lowest in the bare reactor and highest in the ribbed reactor. The 1D simulations, being a case with perfect radial and tangential mixing, thus exhibits the highest average bulk temperature.

The average Reynolds number varies in the different cases, from 66,600 in the bare reactor to 52,200 in the finned reactor and 67,200 in the ribbed reactor. Ideally, the mass flow rates in the different cases should be adjusted to match Reynolds numbers. In the bare and finned geometries, the radial and tangential velocity components are rather small compared to the axial velocity component, while in the ribbed tube there is a clear swirling velocity component. This is the result of the flow impinging on the rib. The swirling flow increases the path length of fluid elements along the wall and combined with the momentum loss as a result of the impingement on the rib, the pressure drop in the ribbed tube equals 2.15 times the pressure drop in the bare reactor. In the finned tube, the larger internal surface area leads to an increase in pressure drop compared to the bare reactor. The pressure drop is 1.19 times that of the bare reactor. This undesired increase in pressure drop in the enhanced geometries is compensated for by a higher heat transfer coefficient. In the bare tube, the average heat transfer coefficient is 691.8 W m^{-2} K^{-1}. In the finned tube, the heat transfer rate (W m^{-1} K^{-1}) amounts to 1.25 times the rate in the bare rube, while in the ribbed the factor is 1.33. The increased heat transfer coefficient implies that, for an equal heat flux, the temperature difference between the wall and the fluid is lower. This is apparently contradicted by the wall temperature profiles, in which the finned reactor is observed to have the lowest wall temperature, though initially the difference with the ribbed tube is negligible. This is the result of slight differences in the imposed heat flux profiles. In all three geometries, the reactions proceed with significant rates only in proximity of the wall. Therefore, the reaction rates and corresponding selectivities are correlated with the tube wall temperature more strongly than with the average bulk temperature. Consequentially, the ethene selectivity is highest in

the reactor with the highest wall temperature, *i.e.* the bare reactor. The differences in selectivities in the ribbed and finned geometries are minimal, though a marginally higher selectivity towards ethene is observed in the ribbed reactor. The overall conversion is mainly affected by the average bulk temperature, rather than the wall temperature. Due to the increased uniformity of the radial temperature profiles in the enhanced geometries, the reactor volume is used more efficiently, compensating for the lower volumetric reaction rate due to the lower average wall temperature. The lower wall temperatures also affect the coking rate in the different coils. On average, the highest coking rates are predicted in the bare reactor. In the ribbed tube, the coking rates are low on the majority of the internal reactor wall, but on the trailing edge of the rib and on a portion of the wall in front of the rib, high coking rates are observed. At these locations, coking rates can be up to 70 times as high as the average. Due to these extremes, the local formation of cokes can potentially have a detrimental effect on the promotion of turbulence by the ribs, nullifying the advantage of the ribbed geometry compared to the bare reactor. These speculations require confirmation via run-length simulations, accounting for the growth of the coke layer.

The comparison of the results obtained in OpenFOAM to those obtained in AVBP was hampered due to the unavailability of raw data from the AVBP cases. Several inconsistencies between the simulations are observed, such as differences in the initialisation of turbulent fluctuations, lengths of the computational domain and averaging procedures. Overall, the results from both codes are found to be in decent agreement with each other, though further analysis is required to attribute the differences to specific causes.

A second industrial application in which turbulence is of importance, is the SUSTOR2 device for raw natural gas dehydration. The working principle of SUSTOR2 is the Joule-Thomson effect, which is a temperature drop of a gas due to expansion, and centrifugal separation of condensed water via swirling flow. The temperature drop should bring the temperature below the dew point specification on the natural gas, which is around 230 K.

For the flow simulations in the SUSTOR2 device, the RANS approach is applied to turbulence modelling. First, proof of concept simulations are performed to validate the capability of ANSYS Fluent to simulate trans- and supersonic flows in which shockwaves may occur. Via two dimensional simulations, the initial SUSTOR2 geometry is optimised. Three main parameters are identified as being of interest for optimisation, namely the throat diameter, the axial length of the device and the effect of a profiled end wall, both in the inlet and outlet region. The simulations show that the initial throat diameter of 40 mm is too large to achieve sufficient acceleration of the flow. The low acceleration does not permit the gas to expand behind the throat, hence no significant drop in temperature is observed. A diameter of 20 mm is shown to achieve an adequate temperature drop, while avoiding the formation of a shockwave. In the 10 mm throat diameter case shockwave formation is observed, which is detrimental to the dehydration potential of the device. The axial length of the separator is varied to determine the onset of flow separation at the wall. None of the investigated axial lengths (80, 70 and 65 mm) results in flow separation. Shorter axial lengths are not considered as it is assumed that below 65 mm, the formed condensate will have an insufficiently

long residence time to impinge on the wall due to the centrifugal forces. The addition of a profiled end wall in the inlet section is observed to reduce the pressure drop over the device by eliminating the recirculation zone in the inlet and by reducing the backflow region centred around the axis of the device. Based on the optimised design (profiled end wall at the inlet, throat diameter of 20 mm and axial length of 65 mm), a three dimensional case is constructed, accounting for the spiralling inlet and outlet sections. Simulations at an equal mass flow rate (0.14 kg s^{-1}) as in the two dimensional cases, predict shockwave flow in the proposed geometry. Reducing the mass flow rate eliminates the shockwave while preserving the supersonic velocities and the associated lower temperatures in the mass flow rate range of 0.035 kg s^{-1} to 0.10 kg s^{-1}. The minimum temperature is around 230 K for all reduced flow rates. The pressure drop is around 160 kPa. At 40 % of the inlet pressure, this is well above the acclaimed pressure drop of 5 % in the SUSTOR2 patent (US patent 20120180668 A1). It is possible that the relative pressure drop decreases with increasing operating pressure. These initial results are quite promising and are in line with reported values for existing separators based on swirling supersonic flow, potentially making the 5 % pressure drop achievable at the actual operating pressure of 100 bar. Additional simulations are required to determine whether SUSTOR2 is indeed capable of significantly outperforming existing swirling flow separators.

8.2. Future Work

The present LES simulations of butane steam cracking have proven to predict heat transfer and pressure drop fairly accurately. The theoretical comparison of heat transfer coefficients and pressure drops is biased somewhat by differences in Reynolds numbers in the different cases. For a consistent theoretical comparison, the simulations should be repeated, but with adapted mass rates, such that the average Reynolds numbers match. Due to the immense computational cost of the ribbed geometry, it is advised to adapt the bare and finned case flow rates to match the ribbed case Reynolds number. For an industrially relevant comparison, the differences in Reynolds number are not the issue, as the capacity of a steam cracking plant is a fixed parameter. From an industrial point of view, it is relevant to repeat the simulations with adapted coil inlet pressures (CIP), such that the coil outlet pressures (COP) are equal in the different cases. In the steam cracking process, the COP is fixed, while the CIP is a degree of freedom. Due to numerical instabilities induced by calculating the chemical source terms via the pseudo-steady state assumption, first order upwind schemes were necessary for temperature and species discretisation, while LES typically requires higher order central discretisation. Further improving the stability of the calculation of the chemical source terms to allow the use of at least central schemes is also a topic of interest. This will significantly reduce the diffusivity of the code as it was observed that small-scale fluctuations are not well resolved due to numerical diffusion.

An in-depth analysis of the differences between OpenFOAM and AVBP requires a consistent definition of the cases in the separate codes. Ideally, simulations in both codes are performed by the same user, to ensure identical settings.

Considering the relevance of LES for industrial steam cracking, it should be noted that CFD is only used in the design stage of the coils. During this design, the relative differences between the implemented and proposed technology is important. The achieved improvements are in the order of fractions of a percent. In this respect, there is a definitive advantage in using LES. Especially when assessing the economic impact of a new technology, knowing whether the gain in olefin selectivity is 0.1 % of 0.2 %, is of crucial importance. On the other hand, the computational cost of LES is very high. The present simulations consumed thousands of CPU hours on state-of-the-art HPC infrastructure. RANS expedites the design process significantly. Accurate RANS models exist, implying that decent average data can be attained using 3D RANS. In the present work, the importance of the near-wall flow has been indicated. The representation of the boundary layer is a significant short-coming of the RANS approach. A hybrid approach could therefore prove to be highly efficient. A final comment on the application of the LES approach for industrial steam cracking concerns the coke formation. The ultimate parameter determining the performance of a coil, is its run-length. Determining the run-length of a specific geometry requires dynamic simulations accounting for the growth of the coke layer. Considering the computational cost required to attain the "steady state" solution, it is highly questionable whether dynamic simulations of an industrial scale coil are feasible using LES. Hence it becomes debatable whether it is required to perform initial simulations using LES, when the run-length simulations are eventually performed at RANS level.

A final relevant prospect is continuing the development of the SUSTOR2 geometry. The current simulations show that there is industrial potential in the design. However, the acclaimed pressure drop of only 5 % appears to be unachievable based on the current results. There is still appreciable room for improvement of the geometry and reduction of the pressure drop, which is currently simulated between 30 – 50 % of the absolute inlet pressure. Further optimisation of the profile of the nozzle outer wall can potentially increase the performance of the separator. In the present work, the swirling inlet and outlet sections are modelled crudely. Refining and optimising the geometry of these sections could result in a significant decrease in pressure drop and increase in dehydration potential. Vanes in the inlet and outlet section are to be considered to stabilise the flow, though they induce an unavoidable increase in pressure drop. Also, performing the simulations at the actual operating pressure of 100 bar, could also give better insights into the actual pressure drop. If the pressure drop is a fixed value, independent of the total pressure, a pressure drop of 200 kPa on 10 MPa implies a relative pressure drop of only 2 %. Due to the numerical instability of trans- and supersonic flows with potential occurrence of shockwaves, large qualitative differences are observed between the two dimensional and three dimensional simulations, implying that the optimisation of the geometry will require 3D simulations as well. Experimental investigation of the flow in the device is indispensable to validate the numerical simulations. Overall, however, based on the results in the present work, SUSTOR2 may become a viable industrial method for the dehydration of raw natural gas.

A

Reaction model equations

A.1. Rate Equations

In this appendix, the full kinetic model is given, starting from the full model as used in CHEMKIN. The CHEMKIN kinetics input file is shown below.

```
!  This chemkin file was generated by RMG - Reaction Mechanism Generator (http://rmg.mit.edu)
!  The java code was compiled by ant at:
!    2012-08-09T12:04:51
!  The git repository was on the branch:
!    master
!  And at the commit with the hash:
!    1340a83f79b8bc9110decba6c27124b98f19bc2d
!
!  For details visit:
!   http://github.com/GreenGroup/RMG-Java/tree/1340a8
!To see changes since then visit:
!   http://github.com/GreenGroup/RMG-Java/compare/1340a8...master

ELEMENTS H C O N Ne Ar He Si S Cl END
SPECIES
    H2(23)
        CH4(11)
        C2H4(10) !C2H4
        C2H6(8) !C2H6
        C3H6(15) !C3H6
        C3H8(12) !C3H8
        C4H8(28) !1C4H8
        C4H8(29) !2C4H8
        C4H6(173) !13C4H6
        C4H10(1) !C4H10
        HJ(5) !H
        CH3J(2) !CH3
        C2H5J(6) !C2H5
        C3H7J(3) !1C3H7
        C3H7J(18) !2C3H7
        C4H9J(4) !1C4H9
        C4H9J(7) !2C4H9
        C4H7J(136) !1C4H7_4
        C4H7J(99) !1C4H7_3
        H2O
END
THERMO ALL
   300.000  1000.000  5000.000
! The first four sets of polynomial coefficients (Ar, N2, Ne, He) are from
! THIRD MILLENIUM IDEAL GAS AND CONDENSED PHASE THERMOCHEMICAL DATABASE FOR
! COMBUSTION WITH UPDATES FROM ACTIVE THERMOCHENICAL TABLES
! Authors: Alexander Burcat and Branko Ruscic
!
! The rest of the species are estimated by RMG (http://rmg.mit.edu/)
H2O                     C   0H   2O   1      G      300.     5000.   1000.      1
 0.28617966E+01 0.27417880E-02-0.69903300E-06 0.83739816E-10-0.38747362E-14    2
-0.29983447E+05 0.57924369E+01 0.39643913E+01-0.36069624E-03 0.19731396E-05    3
-0.36343313E-09-0.22898504E-12-0.30268709E+05 0.14771534E+00                   4

!Estimated by RMG using Group Additivity
C4H7J(99)               C   4H   7          G   250.000  5000.000   995.043    1
 9.30587932E+00 1.81664497E-02-6.26407184E-06 9.84132901E-10-5.79132700E-14    2
 1.20666362E+04-2.48404295E+01 3.57920944E+00 1.22166230E-02 4.63775625E-05    3
-6.35451306E-08 2.35062160E-11 1.46404979E+04 9.96573631E+00                   4

!Estimated by RMG using Group Additivity
C4H7J(136)              C   4H   7          G   250.000  5000.000   995.043    1
 9.06813694E+00 1.79475749E-02-6.17736805E-06 9.71267356E-10-5.72193042E-14    2
 2.02377598E+04-2.01308330E+01 3.60805455E+00 1.19094581E-02 4.51149543E-05    3
-6.16607785E-08 2.27807069E-11 2.27098861E+04 1.31459027E+01                   4

!Estimated by RMG using Group Additivity
C4H6(173)               C   4H   6          G   250.000  5000.000   995.043    1
 1.10283952E+01 1.28920777E-02-3.95448678E-06 5.66446112E-10-3.10025524E-14    2
 8.15102140E+03-3.56754561E+01 3.22147962E+00 1.05227964E-02 5.04981450E-05    3
-7.00058205E-08 2.62648333E-11 1.13755999E+04 1.03459015E+01                   4

!Estimated by RMG using Group Additivity
C4H10(1)                C   4H  10          G   250.000  5000.000   995.043    1
 9.55894461E+00 2.51112690E-02-8.70980376E-06 1.37678114E-09-8.14311852E-14    2
```

```
-2.01848471E+04-2.68629891E+01 3.59442147E+00 1.60364012E-02 5.47950347E-05    3
-7.45526578E-08 2.73825644E-11-1.73616090E+04 1.01047398E+01                   4

!Primary Thermo Library: GRIMech3.0 (Species ID: s00002703)
C2H5J(6)                C   2H   5          G   250.000  5000.000   995.043    1
 4.59320890E+00 1.18436237E-02-4.07290481E-06 6.40369771E-10-3.77359054E-14    2
 1.19693206E+04-8.17949459E-01 3.93585841E+00-1.41361383E-03 3.98804465E-05    3
-4.48664018E-08 1.54302743E-11 1.28872636E+04 6.30535006E+00                   4

!Primary Thermo Library: GRIMech3.0 (Species ID: s00009089)
CH3J(2)                 C   1H   3          G   250.000  5000.000   995.043    1
 3.29357244E+00 5.17342537E-03-1.59469094E-06 2.30721655E-10-1.27839589E-14    2
 1.64213935E+04 2.99099001E+00 3.95487471E+00-8.01537496E-05 1.02371184E-05    3
-1.03175622E-08 3.29596781E-12 1.64182649E+04 4.49456912E-01                   4

!Estimated by RMG using Group Additivity
C3H7J(3)                C   3H   7          G   250.000  5000.000   995.043    1
 6.95424497E+00 1.72816380E-02-5.92405012E-06 9.28115810E-10-5.45380465E-14    2
 8.39537670E+03-1.13350131E+01 3.74143322E+00 6.63085674E-03 4.56568982E-05    3
-5.74319432E-08 2.05881685E-11 1.02014031E+04 1.00112877E+01                   4

!Estimated by RMG using Group Additivity
C3H7J(18)               C   3H   7          G   250.000  5000.000   995.043    1
 5.33679302E+00 1.93426330E-02-6.91306521E-06 1.11583350E-09-6.69780006E-14    2
 7.64649051E+03-2.39416512E+00 4.00224620E+00 5.82500229E-03 4.19291210E-05    3
-5.06788648E-08 1.77377140E-11 8.84686013E+03 8.73482173E+00                   4

!Primary Thermo Library: GRIMech3.0 (Species ID: s00002577)
C2H4(10)                C   2H   4          G   250.000  5000.000   995.043    1
 4.53370569E+00 9.57308713E-03-3.23408854E-06 5.01623403E-10-2.92495620E-14    2
 4.05240745E+03-3.34571790E+00 3.90849430E+00-6.61973360E-03 4.93751261E-05    3
-5.36388906E-08 1.83200843E-11 5.10288607E+03 4.32080737E+00                   4

!Primary Thermo Library: GRIMech3.0 (Species ID: s00009800)
HJ(5)                   C   0H   1          G   250.000  5000.000   995.043    1
 2.50000000E+00-3.49466136E-16 1.88320877E-19-4.06176413E-23 3.19728232E-27    2
 2.54706576E+04-4.49305799E-01 2.50000000E+00-1.69371698E-15 4.40846916E-18    3
-4.33783649E-21 1.45212725E-24 2.54706576E+04-4.49305799E-01                   4

!Primary Thermo Library: GRIMech3.0 (Species ID: s00009809)
H2(23)                  C   0H   2          G   250.000  5000.000   995.043    1
 3.23597865E+00 3.41872004E-04 1.23407858E-07-4.57800734E-11 3.78637707E-15    2
-9.64700069E+02-2.79075150E+00 3.40255781E+00 1.01721558E-04-1.62009963E-07    3
 5.79222153E-10-2.62226797E-13-1.01911266E+03-3.70041102E+00                   4

!Estimated by RMG using Group Additivity
C4H9J(7)                C   4H   9          G   250.000  5000.000   995.043    1
 6.76177826E+00 2.59093186E-02-9.15278708E-06 1.46363455E-09-8.72805066E-14    2
 4.35496751E+03-6.90031400E+00 3.86622761E+00 1.63496182E-02 3.72160310E-05    3
-5.10142749E-08 1.84770645E-11 5.98070403E+03 1.23282829E+01                   4

!Estimated by RMG using Group Additivity
C3H6(15)                C   3H   6          G   250.000  5000.000   995.043    1
 6.43968377E+00 1.54389014E-02-5.30972083E-06 8.34510743E-10-4.91522454E-14    2
-9.10049185E+02-1.05529198E+01 3.79616984E+00 3.13592835E-03 4.78025900E-05    3
-5.79088422E-08 2.05283796E-11 7.51179506E+02 7.89137976E+00                   4

!Estimated by RMG using Group Additivity
C4H9J(4)                C   4H   9          G   250.000  5000.000   995.043    1
 9.30384551E+00 2.28213487E-02-7.94275649E-06 1.25861444E-09-7.45754905E-14    2
 4.76859908E+03-2.20613609E+01 3.62888761E+00 1.69600053E-02 4.41187344E-05    3
-6.25826380E-08 2.32414908E-11 7.31749820E+03 1.24218583E+01                   4

!Primary Thermo Library: GRIMech3.0 (Species ID: s00009193)
CH4(11)                 C   1H   4          G   250.000  5000.000   995.043    1
 1.30383064E+00 1.06312170E-02-3.63140341E-06 5.65079843E-10-3.30334874E-14    2
-9.84472024E+03 1.18953866E+01 4.13429347E+00-5.99159306E-03 2.93330551E-05    3
-2.68176503E-08 8.17758596E-12-1.01483723E+04-4.41255344E-01                   4

!Primary Thermo Library: GRIMech3.0 (Species ID: s00002784)
C2H6(8)                 C   2H   6          G   250.000  5000.000   995.043    1
 4.31432931E+00 1.47965141E-02-5.13777267E-06 8.13192623E-10-4.81447582E-14    2
-1.25000423E+04-2.38870767E+00 3.97360158E+00-3.06302033E-03 5.07725418E-05    3
-5.60673537E-08 1.91223516E-11-1.14802815E+04 4.03689134E+00                   4

!Estimated by RMG using Group Additivity
C4H8(28)                C   4H   8          G   250.000  5000.000   995.043    1
 9.32323605E+00 2.02374952E-02-6.94441532E-06 1.08943405E-09-6.40749989E-14    2
```

```
-4.71568639E+03-2.42393839E+01 3.57358840E+00 1.09858540E-02 5.57912545E-05    3
-7.36307984E-08 2.69217805E-11-1.96922106E+03 1.15218616E+01                   4

!Estimated by RMG using Group Additivity
C4H8(29)                C   4H   8          G   250.000  5000.000   995.043    1
 8.03147951E+00 2.18298992E-02-7.70855002E-06 1.23496273E-09-7.37535387E-14    2
-5.73117481E+03-1.80898899E+01 3.78420755E+00 1.33482456E-02 4.36013543E-05    3
-5.89526982E-08 2.15329317E-11-3.62079935E+03 8.73680911E+00                   4

!Primary Thermo Library: GRIMech3.0 (Species ID: s00003749)
C3H8(12)                C   3H   8          G   250.000  5000.000   995.043    1
 7.39040044E+00 1.93494966E-02-6.81221609E-06 1.09026926E-09-6.50630141E-14    2
-1.63822386E+04-1.71504126E+01 3.81651685E+00 4.45590583E-03 5.97486434E-05    3
-7.30573201E-08 2.59891448E-11-1.42224570E+04 7.35257278E+00                   4

END

REACTIONS      KCAL/MOL       MOLES
!! Kinetics Genesys
!! recombinations
C2H5J(6)+C2H5J(6)=C4H10(1)                              8.730e+14   -0.699  -0.0031
CH3J(2)+C3H7J(3)=C4H10(1)                               1.230e+15   -0.562   0.02
C4H9J(7)+HJ(5)=C4H10(1)                                 1.660e+13       0.22    0.00
C4H9J(4)+HJ(5)=C4H10(1)                                 5.440e+13       0.16    0.00

!! h abstractions
C4H10(1)+CH3J(2)=C4H9J(4)+CH4(11)                       2.280E+13    0.00    17.7   !4.560E13
0.00    17.7 preexp halved CMS
C4H10(1)+CH3J(2)=C4H9J(7)+CH4(11)                       1.630E+13    0.00    15.4   !3.260E13
0.00    15.4 preexp halved CMS
C4H10(1)+HJ(5)=C4H9J(4)+H2(23)                          3.515E+14    0.00    12.8   !7.030E14
0.00    12.8 preexp halved CMS
C4H10(1)+HJ(5)=C4H9J(7)+H2(23)                          2.440E+14    0.00    10.14  !4.880E14
0.00    10.14 preexp halved CMS
HJ(5)+CH4(11)=H2(23)+CH3J(2)                            4.270E14     0.00    15.87
C4H8(28)+CH3J(2)=C4H7J(99)+CH4(11)                      1.220E13     0.00    12.16
C4H8(28)+HJ(5)=C4H7J(99)+H2(23)                         1.590E14     0.00    7.29

!! additions
C2H4(10)+CH3J(2)=C3H7J(3)                               7.430E15     0.00    10.31
C2H4(10)+HJ(5)=C2H5J(6)                                 2.130E13     0.00    4.43 !preexp /10 CMS
C3H6(15)+HJ(5)=C3H7J(3)                                 9.690E13     0.00    5.38
C2H4(10)+C2H5J(6)=C4H9J(4)                              7.430E15     0.00    10.31
C4H6(173)+HJ(5)=C4H7J(99)                               2.010E14     0.00    2.75
C4H8(28)+HJ(5)=C4H9J(7)                                 3.340E14     0.00    3.85

!! Kinetics RMG

HJ(5)+HJ(5)=H2(23)                                      1.090e+11       0.00    1.50
       !R_Recombination exact:   [ H_rad , H_rad ]
HJ(5)+C2H5J(6)=H2(23)+C2H4(10)                          1.083e+13       0.00    0.00
       !Disproportionation exact:   [ H_rad , Cmethyl_Csrad ]
C2H5J(6)+C4H9J(7)=C2H4(10)+C4H10(1)                     6.330e+14      -0.70    0.00
       !Disproportionation exact:   [ Cmethyl_Csrad , C_rad/H/NonDeC ]
HJ(5)+C3H7J(3)=H2(23)+C3H6(15)                          3.620e+12       0.00    0.00
       !Disproportionation exact:   [ H_rad , C/H2/Nd_Csrad ]
C3H6(15)+CH3J(2)=C4H9J(7)                               3.100e+12       0.00    8.50
       !R_Addition_MultipleBond exact:   [ Cd/H2_Cd/H/Nd , C_methyl ]
C4H9J(7)+C3H7J(3)=C4H10(1)+C3H6(15)                     1.026e+14      -0.35    0.00
       !Disproportionation exact:   [ C_rad/H/NonDeC , C/H2/Nd_Csrad ]
C2H5J(6)+C4H9J(4)=C2H4(10)+C4H10(1)                     6.900e+13      -0.35    0.00
       !Disproportionation exact:   [ Cmethyl_Csrad , C_rad/H2/Cs ]
C4H9J(4)+C4H10(1)=C4H10(1)+C4H9J(7)                     6.160e+03       2.66    10.10
       !H_Abstraction exact:   [ C_rad/H2/Cs , C/H2/NonDeC ]
C4H9J(4)=C4H9J(7)                                       2.360e+10       0.82    35.10
       !intra_H_migration exact:   [ Others-R3H_SS , C_rad_out_2H , Cs_H_out_H/NonDeC ] pre-
exp doubled to account for duplicate (CMS)
C3H7J(3)+C4H9J(4)=C3H6(15)+C4H10(1)                     2.900e+12       0.00    0.00
       !Disproportionation exact:   [ C/H2/Nd_Csrad , C_rad/H2/Cs ]
CH3J(2)+C2H5J(6)=CH4(11)+C2H4(10)                       6.570e+14      -0.68    0.00
       !Disproportionation exact:   [ C_methyl , Cmethyl_Csrad ]
CH3J(2)+C3H7J(3)=CH4(11)+C3H6(15)                       2.300e+13      -0.32    0.00
       !Disproportionation exact:   [ C_methyl , C/H2/Nd_Csrad ]
HJ(5)+CH3J(2)=CH4(11)                                   1.930e+14       0.00    0.27
       !R_Recombination exact:   [ H_rad , C_methyl ]
C4H9J(4)+C2H6(8)=C4H10(1)+C2H5J(6)                      1.926e-05       5.28    7.78
       !H_Abstraction exact:   [ C_rad/H2/Cs , InChI=1/C2H6/c1-2/h1-2H3 ]
```

```
C4H10(1)+C2H5J(6)=C4H9J(7)+C2H6(8)                    6.160e+03       2.66    10.10
       !H_Abstraction estimate: (Average:)  [ C/H2/NonDeC , InChI=1/C2H5/c1-2/h1H2,2H3 ]
C2H5J(6)+C2H5J(6)=C2H6(8)+C2H4(10)                    6.900e+13      -0.35    0.00
       !Disproportionation exact:   [ C_rad/H2/Cs , Cmethyl_Csrad ]
CH3J(2)+CH3J(2)=C2H6(8)                               8.260e+17      -1.40    1.00
       !R_Recombination exact:   [ C_methyl , C_methyl ]
C2H5J(6)+C3H7J(3)=C2H6(8)+C3H6(15)                    2.900e+12       0.00    0.00
       !Disproportionation exact:   [ C_rad/H2/Cs , C/H2/Nd_Csrad ]
HJ(5)+C2H5J(6)=C2H6(8)                                1.000e+14       0.00    0.00
       !R_Recombination exact:   [ H_rad , C_rad/H2/Cs ]
HJ(5)+C2H6(8)=H2(23)+C2H5J(6)                         3.768e+08       1.75    7.51
       !H_Abstraction estimate: (Average:)  [ H_rad , InChI=1/C2H6/c1-2/h1-2H3 ]
CH3J(2)+C2H6(8)=CH4(11)+C2H5J(6)                      1.668e+06       1.90    11.05
       !H_Abstraction estimate: (Average:)  [ C_methyl , InChI=1/C2H6/c1-2/h1-2H3 ]
C2H5J(6)+C4H9J(7)=C2H6(8)+C4H8(28)                    6.900e+13      -0.35    0.00
       !Disproportionation exact:   [ C_rad/H2/Cs , Cmethyl_Csrad ]
CH3J(2)+C4H9J(7)=CH4(11)+C4H8(28)                     6.570e+14      -0.68    0.00
       !Disproportionation exact:   [ C_methyl , Cmethyl_Csrad ]
HJ(5)+C4H9J(7)=H2(23)+C4H8(28)                        1.083e+13       0.00    0.00
       !Disproportionation exact:   [ H_rad , Cmethyl_Csrad ]
C4H9J(7)+C4H9J(7)=C4H10(1)+C4H8(28)                   6.330e+14      -0.70    0.00
       !Disproportionation exact:   [ C_rad/H/NonDeC , Cmethyl_Csrad ]
C4H8(28)+HJ(5)=C4H9J(4)                               1.180e+13       0.00    3.80
       !R_Addition_MultipleBond exact:   [ Cd/H/Nd_Cd/H2 , H_rad ]
C2H5J(6)+C4H9J(4)=C2H6(8)+C4H8(28)                    2.900e+12       0.00    0.00
       !Disproportionation exact:   [ C_rad/H2/Cs , C/H2/Nd_Csrad ]
CH3J(2)+C4H9J(4)=CH4(11)+C4H8(28)                     2.300e+13      -0.32    0.00
       !Disproportionation exact:   [ C_methyl , C/H2/Nd_Csrad ]
HJ(5)+C4H9J(4)=H2(23)+C4H8(28)                        3.620e+12       0.00    0.00
       !Disproportionation exact:   [ H_rad , C/H2/Nd_Csrad ]
C4H9J(4)+C4H9J(7)=C4H10(1)+C4H8(28)                   6.900e+13      -0.35    0.00
       !Disproportionation exact:   [ C_rad/H2/Cs , Cmethyl_Csrad ]
C4H9J(4)+C4H9J(4)=C4H10(1)+C4H8(28)                   2.900e+12       0.00    0.00
       !Disproportionation exact:   [ C_rad/H2/Cs , C/H2/Nd_Csrad ]
C4H7J(136)+C2H6(8)=C4H8(28)+C2H5J(6)                  1.926e-05       5.28    7.78
       !H_Abstraction exact:   [ C_rad/H2/Cs , InChI=1/C2H6/c1-2/h1-2H3 ]
C4H8(28)+CH3J(2)=C4H7J(136)+CH4(11)                   8.340e+05       1.90    11.05
       !H_Abstraction exact:   [ C/H3/Cs , C_methyl ]
C4H8(28)+HJ(5)=C4H7J(136)+H2(23)                      1.884e+08       1.75    7.51
       !H_Abstraction exact:   [ C/H3/Cs , H_rad ]
C4H7J(136)+C4H10(1)=C4H8(28)+C4H9J(7)                 6.160e+03       2.66    10.10
       !H_Abstraction exact:   [ C_rad/H2/Cs , C/H2/NonDeC ]
C4H7J(136)+C4H10(1)=C4H8(28)+C4H9J(4)                 3.954e+03       2.71    12.92
       !H_Abstraction exact:   [ C_rad/H2/Cs , C/H3/Cs ]
C4H7J(136)+HJ(5)=C4H8(28)                             1.000e+14       0.00    0.00
       !R_Recombination exact:   [ C_rad/H2/Cs , H_rad ]
C2H5J(6)+C4H7J(136)=C2H4(10)+C4H8(28)                 6.900e+13      -0.35    0.00
       !Disproportionation exact:   [ Cmethyl_Csrad , C_rad/H2/Cs ]
C3H7J(3)+C4H7J(136)=C3H6(15)+C4H8(28)                 2.900e+12       0.00    0.00
       !Disproportionation exact:   [ C/H2/Nd_Csrad , C_rad/H2/Cs ]
C4H9J(7)+C4H7J(136)=C4H8(28)+C4H8(28)                 6.900e+13      -0.35    0.00
       !Disproportionation exact:   [ Cmethyl_Csrad , C_rad/H2/Cs ]
C4H9J(4)+C4H7J(136)=C4H8(28)+C4H8(28)                 2.900e+12       0.00    0.00
       !Disproportionation exact:   [ C/H2/Nd_Csrad , C_rad/H2/Cs ]
C4H8(28)+C2H5J(6)=C4H7J(99)+C2H6(8)                   3.120e-04       4.31    3.39
       !H_Abstraction estimate: (Average:)  [ InChI=1/C4H8/c1-3-4-2/h3H,1,4H2,2H3 ,
InChI=1/C2H5/c1-2/h1H2,2H3 ]
C4H8(28)+C4H9J(7)=C4H7J(99)+C4H10(1)                  1.936e+02       2.96    6.79
       !H_Abstraction estimate: (Average:)  [ InChI=1/C4H8/c1-3-4-2/h3H,1,4H2,2H3 ,
C_rad/H/NonDeC ]
C4H8(28)+C4H9J(4)=C4H7J(99)+C4H10(1)                  3.120e-04       4.31    3.39
       !H_Abstraction estimate: (Average:)  [ InChI=1/C4H8/c1-3-4-2/h3H,1,4H2,2H3 ,
C_rad/H2/Cs ]
C4H7J(99)+HJ(5)=C4H8(28)                              5.000e+13       0.00    0.00
       !R_Recombination estimate: (Average:)  [ C_rad/H/OneDeC , H_rad ]
C2H5J(6)+C4H7J(99)=C2H4(10)+C4H8(28)                  6.330e+14      -0.70    0.00
       !Disproportionation estimate: (Average:)  [ Cmethyl_Csrad , C_rad/H/OneDeC ]
C3H7J(3)+C4H7J(99)=C3H6(15)+C4H8(28)                  1.026e+14      -0.35    0.00
       !Disproportionation estimate: (Average:)  [ C/H2/Nd_Csrad , C_rad/H/OneDeC ]
C4H9J(7)+C4H7J(99)=C4H8(28)+C4H8(28)                  6.330e+14      -0.70    0.00
       !Disproportionation estimate: (Average:)  [ Cmethyl_Csrad , C_rad/H/OneDeC ]
C4H9J(4)+C4H7J(99)=C4H8(28)+C4H8(28)                  1.026e+14      -0.35    0.00
       !Disproportionation estimate: (Average:)  [ C/H2/Nd_Csrad , C_rad/H/OneDeC ]
C4H8(28)+C4H7J(136)=C4H7J(99)+C4H8(28)                3.120e-04       4.31    3.39
       !H_Abstraction estimate: (Average:)  [ InChI=1/C4H8/c1-3-4-2/h3H,1,4H2,2H3 ,
C_rad/H2/Cs ]
C4H7J(136)=C4H7J(99)                                  2.820e+08       1.28    27.90
       !intra_H_migration exact:   [ Others-R2H_S , C_rad_out_2H , Cs_H_out_H/OneDe ]
```

```
C4H6(173)+HJ(5)=C4H7J(136)                          5.700e+13       0.00    4.30
       !R_Addition_MultipleBond exact:   [ Cd/H/De_Cd/H2 , H_rad ]
C2H5J(6)+C4H7J(136)=C2H6(8)+C4H6(173)               1.099e+13       -0.06   2.47
       !Disproportionation estimate: (Average:)  [ C_rad/H2/Cs , C/H2/De_Csrad ]
CH3J(2)+C4H7J(136)=CH4(11)+C4H6(173)                1.099e+13       -0.06   2.47
       !Disproportionation estimate: (Average:)  [ C_methyl , C/H2/De_Csrad ]
HJ(5)+C4H7J(136)=H2(23)+C4H6(173)                   1.099e+13       -0.06   2.47
       !Disproportionation estimate: (Average:)  [ H_rad , C/H2/De_Csrad ]
C4H9J(7)+C4H7J(136)=C4H10(1)+C4H6(173)              1.099e+13       -0.06   2.47
       !Disproportionation estimate: (Average:)  [ C_rad/H/NonDeC , C/H2/De_Csrad ]
C4H9J(4)+C4H7J(136)=C4H10(1)+C4H6(173)              1.099e+13       -0.06   2.47
       !Disproportionation estimate: (Average:)  [ C_rad/H2/Cs , C/H2/De_Csrad ]
C4H7J(136)+C4H7J(136)=C4H8(28)+C4H6(173)            1.099e+13       -0.06   2.47
       !Disproportionation estimate: (Average:)  [ C_rad/H2/Cs , C/H2/De_Csrad ]
C2H5J(6)+C4H7J(99)=C2H6(8)+C4H6(173)                6.900e+13       -0.35   0.00
       !Disproportionation exact:   [ C_rad/H2/Cs , Cmethyl_Csrad ]
CH3J(2)+C4H7J(99)=CH4(11)+C4H6(173)                 6.570e+14       -0.68   0.00
       !Disproportionation exact:   [ C_methyl , Cmethyl_Csrad ]
HJ(5)+C4H7J(99)=H2(23)+C4H6(173)                    1.083e+13       0.00    0.00
       !Disproportionation exact:   [ H_rad , Cmethyl_Csrad ]
C4H9J(7)+C4H7J(99)=C4H10(1)+C4H6(173)               6.330e+14       -0.70   0.00
       !Disproportionation exact:   [ C_rad/H/NonDeC , Cmethyl_Csrad ]
C4H9J(4)+C4H7J(99)=C4H10(1)+C4H6(173)               6.900e+13       -0.35   0.00
       !Disproportionation exact:   [ C_rad/H2/Cs , Cmethyl_Csrad ]
C4H7J(99)+C4H7J(136)=C4H8(28)+C4H6(173)             1.099e+13       -0.06   2.47
       !Disproportionation estimate: (Average:)  [ C_rad/H/OneDeC , C/H2/De_Csrad ]
C4H7J(99)+C4H7J(99)=C4H8(28)+C4H6(173)              6.330e+14       -0.70   0.00
       !Disproportionation estimate: (Average:)  [ C_rad/H/OneDeC , Cmethyl_Csrad ]
C3H7J(3)=C3H7J(18)                                  1.938e+10       0.89    35.80
       !intra_H_migration exact:   [ Others-R2H_S , C_rad_out_2H , Cs_H_out_H/NonDeC ]
C3H6(15)+HJ(5)=C3H7J(18)                            2.010e+13       0.00    2.10
       !R_Addition_MultipleBond exact:   [ Cd/H2_Cd/H/Nd , H_rad ]
C3H7J(18)+C4H9J(4)=C3H6(15)+C4H10(1)                1.380e+14       -0.35   0.00
       !Disproportionation exact:   [ Cmethyl_Csrad , C_rad/H2/Cs ]
C3H7J(18)+C4H9J(7)=C3H6(15)+C4H10(1)                1.266e+15       -0.70   0.00
       !Disproportionation exact:   [ Cmethyl_Csrad , C_rad/H/NonDeC ]
C3H7J(18)+HJ(5)=C3H6(15)+H2(23)                     2.166e+13       0.00    0.00
       !Disproportionation exact:   [ Cmethyl_Csrad , H_rad ]
C3H7J(18)+CH3J(2)=C3H6(15)+CH4(11)                  1.314e+15       -0.68   0.00
       !Disproportionation exact:   [ Cmethyl_Csrad , C_methyl ]
C3H7J(18)+C2H5J(6)=C3H6(15)+C2H6(8)                 1.380e+14       -0.35   0.00
       !Disproportionation exact:   [ Cmethyl_Csrad , C_rad/H2/Cs ]
C3H7J(18)+C4H7J(99)=C3H6(15)+C4H8(28)               1.266e+15       -0.70   0.00
       !Disproportionation estimate: (Average:)  [ Cmethyl_Csrad , C_rad/H/OneDeC ]
C3H7J(18)+C4H7J(136)=C3H6(15)+C4H8(28)              1.380e+14       -0.35   0.00
       !Disproportionation exact:   [ Cmethyl_Csrad , C_rad/H2/Cs ]
C4H8(29)+HJ(5)=C4H9J(7)                             2.000e+13       0.00    2.90
       !R_Addition_MultipleBond estimate: (Average:)  [ Cd/H/Nd_Cd/H/Nd , H_rad ]
C2H5J(6)+C4H9J(7)=C2H6(8)+C4H8(29)                  2.900e+12       0.00    0.00
       !Disproportionation exact:   [ C_rad/H2/Cs , C/H2/Nd_Csrad ]
CH3J(2)+C4H9J(7)=CH4(11)+C4H8(29)                   2.300e+13       -0.32   0.00
       !Disproportionation exact:   [ C_methyl , C/H2/Nd_Csrad ]
HJ(5)+C4H9J(7)=H2(23)+C4H8(29)                      3.620e+12       0.00    0.00
       !Disproportionation exact:   [ H_rad , C/H2/Nd_Csrad ]
C4H9J(7)+C4H9J(7)=C4H10(1)+C4H8(29)                 1.026e+14       -0.35   0.00
       !Disproportionation exact:   [ C_rad/H/NonDeC , C/H2/Nd_Csrad ]
C4H9J(4)+C4H9J(7)=C4H10(1)+C4H8(29)                 2.900e+12       0.00    0.00
       !Disproportionation exact:   [ C_rad/H2/Cs , C/H2/Nd_Csrad ]
C4H7J(136)+C4H9J(7)=C4H8(28)+C4H8(29)               2.900e+12       0.00    0.00
       !Disproportionation exact:   [ C_rad/H2/Cs , C/H2/Nd_Csrad ]
C4H9J(4)+C4H8(29)=C4H10(1)+C4H7J(99)                3.360e+12       0.00    12.40
       !H_Abstraction estimate: (Average:)  [ C_rad/H2/Cs , InChI=1/C4H8/c1-3-4-2/h3-4H,1-
2H3/b4-3+ ]
C4H9J(7)+C4H8(29)=C4H10(1)+C4H7J(99)                1.722e+12       0.00    12.30
       !H_Abstraction estimate: (Average:)  [ C_rad/H/NonDeC , InChI=1/C4H8/c1-3-4-2/h3-4H,1-
2H3/b4-3+ ]
HJ(5)+C4H8(29)=H2(23)+C4H7J(99)                     2.598e+06       2.38    2.80
       !H_Abstraction estimate: (Average:)  [ H_rad , InChI=1/C4H8/c1-3-4-2/h3-4H,1-2H3/b4-3+
]
CH3J(2)+C4H8(29)=CH4(11)+C4H7J(99)                  4.824e+02       2.92    7.16
       !H_Abstraction estimate: (Average:)  [ C_methyl , InChI=1/C4H8/c1-3-4-2/h3-4H,1-2H3/b4-
3+ ]
C2H5J(6)+C4H8(29)=C2H6(8)+C4H7J(99)                 3.360e+12       0.00    12.40
       !H_Abstraction estimate: (Average:)  [ InChI=1/C2H5/c1-2/h1H2,2H3 , InChI=1/C4H8/c1-3-
4-2/h3-4H,1-2H3/b4-3+ ]
C4H8(28)+C4H7J(99)=C4H7J(99)+C4H8(29)               3.120e-04       4.31    3.39
       !H_Abstraction estimate: (Average:)  [ InChI=1/C4H8/c1-3-4-2/h3H,1,4H2,2H3 ,
InChI=1/C3H5/c1-3-2/h3H,1-2H2 ]
```

```
C4H7J(136)+C4H8(29)=C4H8(28)+C4H7J(99)                3.360e+12       0.00    12.40
       !H_Abstraction estimate: (Average:)  [ C_rad/H2/Cs , InChI=1/C4H8/c1-3-4-2/h3-4H,1-
2H3/b4-3+ ]
C4H7J(99)+HJ(5)=C4H8(29)                              5.000e+13       0.00    0.00
       !R_Recombination estimate: (Average:)  [ C_rad/H2/Cd , H_rad ]
C4H7J(99)+C2H5J(6)=C4H8(29)+C2H4(10)                  6.870e+13      -0.35   -0.13
       !Disproportionation exact:   [ C_rad/H2/Cd , Cmethyl_Csrad ]
C4H7J(99)+C3H7J(3)=C4H8(29)+C3H6(15)                  2.900e+12       0.00   -0.13
       !Disproportionation exact:   [ C_rad/H2/Cd , C/H2/Nd_Csrad ]
C4H7J(99)+C4H9J(7)=C4H8(29)+C4H8(28)                  6.870e+13      -0.35   -0.13
       !Disproportionation exact:   [ C_rad/H2/Cd , Cmethyl_Csrad ]
C4H7J(99)+C4H9J(7)=C4H8(29)+C4H8(29)                  2.900e+12       0.00   -0.13
       !Disproportionation exact:   [ C_rad/H2/Cd , C/H2/Nd_Csrad ]
C4H7J(99)+C4H9J(4)=C4H8(29)+C4H8(28)                  2.900e+12       0.00   -0.13
       !Disproportionation exact:   [ C_rad/H2/Cd , C/H2/Nd_Csrad ]
C4H7J(99)+C4H7J(136)=C4H8(29)+C4H6(173)               1.099e+13      -0.06    2.47
       !Disproportionation estimate: (Average:)  [ C_rad/H2/Cd , C/H2/De_Csrad ]
C4H7J(99)+C4H7J(99)=C4H8(29)+C4H6(173)                6.870e+13      -0.35   -0.13
       !Disproportionation exact:   [ C_rad/H2/Cd , Cmethyl_Csrad ]
C4H7J(99)+C3H7J(18)=C4H8(29)+C3H6(15)                 1.374e+14      -0.35   -0.13
       !Disproportionation exact:   [ C_rad/H2/Cd , Cmethyl_Csrad ]
CH3J(2)+C2H5J(6)=C3H8(12)                             3.370e+13       0.00    0.00
       !R_Recombination exact:   [ C_methyl , C_rad/H2/Cs ]
C4H9J(4)+C3H8(12)=C4H10(1)+C3H7J(3)                   3.954e+03       2.71    12.92
       !H_Abstraction exact:   [ C_rad/H2/Cs , C/H3/Cs ]
C4H10(1)+C3H7J(3)=C4H9J(7)+C3H8(12)                   6.160e+03       2.66    10.10
       !H_Abstraction exact:   [ C/H2/NonDeC , C_rad/H2/Cs ]
C3H7J(3)+C2H5J(6)=C3H8(12)+C2H4(10)                   6.900e+13      -0.35    0.00
       !Disproportionation exact:   [ C_rad/H2/Cs , Cmethyl_Csrad ]
C3H7J(3)+C3H7J(3)=C3H8(12)+C3H6(15)                   2.900e+12       0.00    0.00
       !Disproportionation exact:   [ C_rad/H2/Cs , C/H2/Nd_Csrad ]
HJ(5)+C3H7J(3)=C3H8(12)                               1.000e+14       0.00    0.00
       !R_Recombination exact:   [ H_rad , C_rad/H2/Cs ]
HJ(5)+C3H8(12)=H2(23)+C3H7J(3)                        3.768e+08       1.75    7.51
       !H_Abstraction exact:   [ H_rad , C/H3/Cs ]
C3H7J(3)+C4H9J(7)=C3H8(12)+C4H8(28)                   6.900e+13      -0.35    0.00
       !Disproportionation exact:   [ C_rad/H2/Cs , Cmethyl_Csrad ]
C3H7J(3)+C4H9J(7)=C3H8(12)+C4H8(29)                   2.900e+12       0.00    0.00
       !Disproportionation exact:   [ C_rad/H2/Cs , C/H2/Nd_Csrad ]
C3H7J(3)+C4H9J(4)=C3H8(12)+C4H8(28)                   2.900e+12       0.00    0.00
       !Disproportionation exact:   [ C_rad/H2/Cs , C/H2/Nd_Csrad ]
CH3J(2)+C3H8(12)=CH4(11)+C3H7J(3)                     1.668e+06       1.90    11.05
       !H_Abstraction exact:   [ C_methyl , C/H3/Cs ]
C2H5J(6)+C3H8(12)=C2H6(8)+C3H7J(3)                    3.954e+03       2.71    12.92
       !H_Abstraction estimate: (Average:)  [ InChI=1/C2H5/c1-2/h1H2,2H3 , C/H3/Cs ]
C4H8(28)+C3H7J(3)=C4H7J(99)+C3H8(12)                  3.120e-04       4.31    3.39
       !H_Abstraction estimate: (Average:)  [ InChI=1/C4H8/c1-3-4-2/h3H,1,4H2,2H3 ,
C_rad/H2/Cs ]
C4H7J(136)+C3H8(12)=C4H8(28)+C3H7J(3)                 3.954e+03       2.71    12.92
       !H_Abstraction exact:   [ C_rad/H2/Cs , C/H3/Cs ]
C3H7J(3)+C4H7J(136)=C3H8(12)+C4H6(173)                1.099e+13      -0.06    2.47
       !Disproportionation estimate: (Average:)  [ C_rad/H2/Cs , C/H2/De_Csrad ]
C3H7J(3)+C4H7J(99)=C3H8(12)+C4H6(173)                 6.900e+13      -0.35    0.00
       !Disproportionation exact:   [ C_rad/H2/Cs , Cmethyl_Csrad ]
C4H9J(4)+C3H8(12)=C4H10(1)+C3H7J(18)                  3.080e+03       2.66    10.10
       !H_Abstraction estimate: (Average:)  [ C_rad/H2/Cs , InChI=1/C3H8/c1-3-2/h3H2,1-2H3 ]
C4H10(1)+C3H7J(18)=C4H9J(7)+C3H8(12)                  6.080e+01       3.19    10.31
       !H_Abstraction estimate: (Average:)  [ C/H2/NonDeC , InChI=1/C3H7/c1-3-2/h3H,1-2H3 ]
HJ(5)+C3H8(12)=H2(23)+C3H7J(18)                       2.600e+08       1.69    4.78
       !H_Abstraction estimate: (Average:)  [ H_rad , InChI=1/C3H8/c1-3-2/h3H2,1-2H3 ]
CH3J(2)+C3H8(12)=CH4(11)+C3H7J(18)                    2.900e+06       1.77    8.53
       !H_Abstraction estimate: (Average:)  [ C_methyl , InChI=1/C3H8/c1-3-2/h3H2,1-2H3 ]
C2H5J(6)+C3H8(12)=C2H6(8)+C3H7J(18)                   3.080e+03       2.66    10.10
       !H_Abstraction estimate: (Average:)  [ InChI=1/C2H5/c1-2/h1H2,2H3 , InChI=1/C3H8/c1-3-
2/h3H2,1-2H3 ]
C4H8(28)+C3H7J(18)=C4H7J(99)+C3H8(12)                 1.936e+02       2.96    6.79
       !H_Abstraction estimate: (Average:)  [ InChI=1/C4H8/c1-3-4-2/h3H,1,4H2,2H3 ,
InChI=1/C3H7/c1-3-2/h3H,1-2H3 ]
C4H7J(136)+C3H8(12)=C4H8(28)+C3H7J(18)                3.080e+03       2.66    10.10
       !H_Abstraction estimate: (Average:)  [ C_rad/H2/Cs , InChI=1/C3H8/c1-3-2/h3H2,1-2H3 ]
C3H7J(18)+HJ(5)=C3H8(12)                              2.000e+13       0.00    0.00
       !R_Recombination exact:   [ C_rad/H/NonDeC , H_rad ]
C3H7J(18)+C2H5J(6)=C3H8(12)+C2H4(10)                  6.330e+14      -0.70    0.00
       !Disproportionation exact:   [ C_rad/H/NonDeC , Cmethyl_Csrad ]
C3H7J(18)+C3H7J(3)=C3H8(12)+C3H6(15)                  1.026e+14      -0.35    0.00
       !Disproportionation exact:   [ C_rad/H/NonDeC , C/H2/Nd_Csrad ]
C3H7J(18)+C4H9J(7)=C3H8(12)+C4H8(28)                  6.330e+14      -0.70    0.00
       !Disproportionation exact:   [ C_rad/H/NonDeC , Cmethyl_Csrad ]
```

```
C3H7J(18)+C4H9J(7)=C3H8(12)+C4H8(29)                1.026e+14       -0.35    0.00
        !Disproportionation exact:   [ C_rad/H/NonDeC , C/H2/Nd_Csrad ]
C3H7J(18)+C4H9J(4)=C3H8(12)+C4H8(28)                1.026e+14       -0.35    0.00
        !Disproportionation exact:   [ C_rad/H/NonDeC , C/H2/Nd_Csrad ]
C3H7J(18)+C4H7J(136)=C3H8(12)+C4H6(173)             1.099e+13       -0.06    2.47
        !Disproportionation estimate: (Average:)  [ C_rad/H/NonDeC , C/H2/De_Csrad ]
C3H7J(18)+C4H7J(99)=C3H8(12)+C4H6(173)              6.330e+14       -0.70    0.00
        !Disproportionation exact:   [ C_rad/H/NonDeC , Cmethyl_Csrad ]
C3H7J(18)+C3H7J(18)=C3H8(12)+C3H6(15)               1.266e+15       -0.70    0.00
        !Disproportionation exact:   [ C_rad/H/NonDeC , Cmethyl_Csrad ]
C4H8(29)+C3H7J(3)=C4H7J(99)+C3H8(12)                3.360e+12        0.00    12.40
        !H_Abstraction estimate: (Average:)  [ InChI=1/C4H8/c1-3-4-2/h3-4H,1-2H3/b4-3+ ,
C_rad/H2/Cs ]
C4H8(29)+C3H7J(18)=C4H7J(99)+C3H8(12)               1.722e+12        0.00    12.30
        !H_Abstraction estimate: (Average:)  [ InChI=1/C4H8/c1-3-4-2/h3-4H,1-2H3/b4-3+ ,
InChI=1/C3H7/c1-3-2/h3H,1-2H3 ]
C3H8(12)+C3H7J(3)=C3H7J(18)+C3H8(12)                3.080e+03        2.66    10.10
        !H_Abstraction estimate: (Average:)  [ InChI=1/C3H8/c1-3-2/h3H2,1-2H3 , C_rad/H2/Cs ]
END
```

To be useable in the LES, the model is simplified using the pseudo-steady-state assumption (PSSA). The corresponding equations can also be found in the 'sources.H' file of the QSSAPipeFoam solver. The model is split into three sections, corresponding to the reaction rates (forwards and backwards) for each of the reactions, the algebraic equations for the concentrations of the pseudo-steady-state (PSS) species and the differential equations for the non-PSS species. The numbering of the reactions (0-148) follows the same order as listed in the CHEMKIN file. The model takes into account 21 possible components, Table A-1 lists their respective number-IDs.

Table A-1: Component IDs used to construct equations.

Component	***Id***	***Component***	***Id***	***Component***	***Id***
Hydrogen	0	*Propene*	7	*Ethyl*	14
Methane	1	*1,3-Butadiene*	8	*n-Propyl*	15
Ethane	2	*1-Butene*	9	*iso-Propyl*	16
Propane	3	*2-Butene*	10	*t-1-Methylallyl*	17
n-Butane	4	*Water*	11	*t-3-Butene-1-yn*	18
Nitrogen	5	*Hydro*	12	*sec-Butyl*	19
Ethene	6	*Methyl*	13	*n-Butyl*	20

Equations (A-1) to (A-149) give the forward reaction rate on the left side and the backward reaction rate on the right side.

$$F[0] = kf[0] * Conc[14]^2 \qquad B[0] = kb[0] * Conc[4] \qquad \textbf{(A-1)}$$

$$F[1] = kf[1] * Conc[13] * Conc[15] \qquad B[1] = kb[1] * Conc[4] \qquad \textbf{(A-2)}$$

$$F[2] = kf[2] * Conc[12] * Conc[20] \qquad B[2] = kb[2] * Conc[4] \qquad \textbf{(A-3)}$$

$$F[3] = kf[3] * Conc[12] * Conc[19] \qquad B[3] = kb[3] * Conc[4] \qquad \textbf{(A-4)}$$

$$F[4] = kf[4] * Conc[4] * Conc[13] \qquad B[4] = kb[4] * Conc[1] * Conc[19] \qquad \textbf{(A-5)}$$

$$F[5] = kf[5] * Conc[4] * Conc[13] \qquad B[5] = kb[5] * Conc[1] * Conc[20] \qquad \textbf{(A-6)}$$

$$F[6] = kf[6] * Conc[4] * Conc[12] \qquad B[6] = kb[6] * Conc[0] * Conc[19] \quad \textbf{(A-7)}$$

$$F[7] = kf[7] * Conc[4] * Conc[12] \qquad B[7] = kb[7] * Conc[0] * Conc[20] \quad \textbf{(A-8)}$$

$$F[8] = kf[8] * Conc[1] * Conc[12] \qquad B[8] = kb[8] * Conc[0] * Conc[13] \quad \textbf{(A-9)}$$

$$F[9] = kf[9] * Conc[9] * Conc[13] \qquad B[9] = kb[9] * Conc[1] * Conc[17] \quad \textbf{(A-10)}$$

$$F[10] = kf[10] * Conc[9] * Conc[12] \qquad B[10] = kb[10] * Conc[0] * Conc[17] \quad \textbf{(A-11)}$$

$$F[11] = kf[11] * Conc[6] * Conc[13] \qquad B[11] = kb[11] * Conc[15] \quad \textbf{(A-12)}$$

$$F[12] = kf[12] * Conc[6] * Conc[12] \qquad B[12] = kb[12] * Conc[14] \quad \textbf{(A-13)}$$

$$F[13] = kf[13] * Conc[7] * Conc[12] \qquad B[13] = kb[13] * Conc[15] \quad \textbf{(A-14)}$$

$$F[14] = kf[14] * Conc[6] * Conc[14] \qquad B[14] = kb[14] * Conc[19] \quad \textbf{(A-15)}$$

$$F[15] = kf[15] * Conc[8] * Conc[12] \qquad B[15] = kb[15] * Conc[17] \quad \textbf{(A-16)}$$

$$F[16] = kf[16] * Conc[9] * Conc[12] \qquad B[16] = kb[16] * Conc[20] \quad \textbf{(A-17)}$$

$$F[17] = kf[17] * Conc[12]^2 \qquad B[17] = kb[17] * Conc[0] \quad \textbf{(A-18)}$$

$$F[18] = kf[18] * Conc[12] * Conc[14] \qquad B[18] = kb[18] * Conc[0] * Conc[6] \quad \textbf{(A-19)}$$

$$F[19] = kf[19] * Conc[14] * Conc[20] \qquad B[19] = kb[19] * Conc[4] * Conc[6] \quad \textbf{(A-20)}$$

$$F[20] = kf[20] * Conc[12] * Conc[15] \qquad B[20] = kb[20] * Conc[0] * Conc[7] \quad \textbf{(A-21)}$$

$$F[21] = kf[21] * Conc[7] * Conc[13] \qquad B[21] = kb[21] * Conc[20] \quad \textbf{(A-22)}$$

$$F[22] = kf[22] * Conc[15] * Conc[20] \qquad B[22] = kb[22] * Conc[4] * Conc[7] \quad \textbf{(A-23)}$$

$$F[23] = kf[23] * Conc[14] * Conc[19] \qquad B[23] = kb[23] * Conc[4] * Conc[6] \quad \textbf{(A-24)}$$

$$F[24] = kf[24] * Conc[4] * Conc[19] \qquad B[24] = kb[24] * Conc[4] * Conc[20] \quad \textbf{(A-25)}$$

$$F[25] = kf[25] * Conc[19] \qquad B[25] = kb[25] * Conc[20] \quad \textbf{(A-26)}$$

$$F[26] = kf[26] * Conc[15] * Conc[19] \qquad B[26] = kb[26] * Conc[4] * Conc[7] \quad \textbf{(A-27)}$$

$$F[27] = kf[27] * Conc[13] * Conc[14] \qquad B[27] = kb[27] * Conc[1] * Conc[6] \quad \textbf{(A-28)}$$

$$F[28] = kf[28] * Conc[13] * Conc[15] \qquad B[28] = kb[28] * Conc[1] * Conc[7] \quad \textbf{(A-29)}$$

$$F[29] = kf[29] * Conc[12] * Conc[13] \qquad B[29] = kb[29] * Conc[1] \quad \textbf{(A-30)}$$

$$F[30] = kf[30] * Conc[2] * Conc[19] \qquad B[30] = kb[30] * Conc[4] * Conc[14] \quad \textbf{(A-31)}$$

$$F[31] = kf[31] * Conc[4] * Conc[14] \qquad B[31] = kb[31] * Conc[2] * Conc[20] \quad \textbf{(A-32)}$$

$$F[32] = kf[32] * Conc[14]^2 \qquad B[32] = kb[32] * Conc[2] * Conc[6] \quad \textbf{(A-33)}$$

$$F[33] = kf[33] * Conc[13]^2 \qquad B[33] = kb[33] * Conc[2] \quad \textbf{(A-34)}$$

$$F[34] = kf[34] * Conc[14] * Conc[15] \qquad B[34] = kb[34] * Conc[2] * Conc[7] \quad \textbf{(A-35)}$$

$$F[35] = kf[35] * Conc[12] * Conc[14] \qquad B[35] = kb[35] * Conc[2] \quad \textbf{(A-36)}$$

$$F[36] = kf[36] * Conc[2] * Conc[12] \qquad B[36] = kb[36] * Conc[0] * Conc[14] \quad \textbf{(A-37)}$$

$$F[37] = kf[37] * Conc[2] * Conc[13] \qquad B[37] = kb[37] * Conc[1] * Conc[14] \quad \textbf{(A-38)}$$

$$F[38] = kf[38] * Conc[14] * Conc[20] \qquad B[38] = kb[38] * Conc[2] * Conc[9] \quad \textbf{(A-39)}$$

$$F[39] = kf[39] * Conc[13] * Conc[20] \qquad B[39] = kb[39] * Conc[1] * Conc[9] \quad \textbf{(A-40)}$$

$$F[40] = kf[40] * Conc[12] * Conc[20] \qquad B[40] = kb[40] * Conc[0] * Conc[9] \quad \textbf{(A-41)}$$

$$F[41] = kf[41] * Conc[20]^2 \qquad B[41] = kb[41] * Conc[4] * Conc[9] \quad \textbf{(A-42)}$$

$$F[42] = kf[42] * Conc[9] * Conc[12] \qquad B[42] = kb[42] * Conc[19] \quad \textbf{(A-43)}$$

$$F[43] = kf[43] * Conc[14] * Conc[19] \qquad B[43] = kb[43] * Conc[2] * Conc[9] \quad \textbf{(A-44)}$$

$$F[44] = kf[44] * Conc[13] * Conc[19] \qquad B[44] = kb[44] * Conc[1] * Conc[9] \quad \textbf{(A-45)}$$

$$F[45] = kf[45] * Conc[12] * Conc[19] \qquad B[45] = kb[45] * Conc[0] * Conc[9] \quad \textbf{(A-46)}$$

$$F[46] = kf[46] * Conc[19] * Conc[20] \qquad B[46] = kb[46] * Conc[4] * Conc[9] \quad \textbf{(A-47)}$$

$$F[47] = kf[47] * Conc[19]^2 \qquad B[47] = kb[47] * Conc[4] * Conc[9] \quad \textbf{(A-48)}$$

$$F[48] = kf[48] * Conc[2] * Conc[18] \qquad B[48] = kb[48] * Conc[9] * Conc[14] \quad \textbf{(A-49)}$$

$$F[49] = kf[49] * Conc[9] * Conc[13] \qquad B[49] = kb[49] * Conc[1] * Conc[18] \quad \textbf{(A-50)}$$

$$F[50] = kf[50] * Conc[9] * Conc[12] \qquad B[50] = kb[50] * Conc[0] * Conc[18] \quad \textbf{(A-51)}$$

$$F[51] = kf[51] * Conc[4] * Conc[18] \qquad B[51] = kb[51] * Conc[9] * Conc[20] \quad \textbf{(A-52)}$$

$$F[52] = kf[52] * Conc[4] * Conc[18] \qquad B[52] = kb[52] * Conc[9] * Conc[19] \quad \textbf{(A-53)}$$

$$F[53] = kf[53] * Conc[12] * Conc[18] \qquad B[53] = kb[53] * Conc[9] \quad \textbf{(A-54)}$$

$$F[54] = kf[54] * Conc[14] * Conc[18] \qquad B[54] = kb[54] * Conc[6] * Conc[9] \quad \textbf{(A-55)}$$

$$F[55] = kf[55] * Conc[15] * Conc[18] \qquad B[55] = kb[55] * Conc[7] * Conc[9] \quad \textbf{(A-56)}$$

$$F[56] = kf[56] * Conc[18] * Conc[20] \qquad B[56] = kb[56] * Conc[9]^2 \quad \textbf{(A-57)}$$

$$F[57] = kf[57] * Conc[18] * Conc[19] \qquad B[57] = kb[57] * Conc[9]^2 \quad \textbf{(A-58)}$$

$$F[58] = kf[58] * Conc[9] * Conc[14] \qquad B[58] = kb[58] * Conc[2] * Conc[17] \quad \textbf{(A-59)}$$

$$F[59] = kf[59] * Conc[9] * Conc[20] \qquad B[59] = kb[59] * Conc[4] * Conc[17] \quad \textbf{(A-60)}$$

$$F[60] = kf[60] * Conc[9] * Conc[19] \qquad B[60] = kb[60] * Conc[4] * Conc[17] \quad \textbf{(A-61)}$$

$$F[61] = kf[61] * Conc[12] * Conc[17] \qquad B[61] = kb[61] * Conc[9] \quad \textbf{(A-62)}$$

$$F[62] = kf[62] * Conc[14] * Conc[17] \qquad B[62] = kb[62] * Conc[6] * Conc[9] \quad \textbf{(A-63)}$$

$$F[63] = kf[63] * Conc[15] * Conc[17] \qquad B[63] = kb[63] * Conc[7] * Conc[9] \quad \textbf{(A-64)}$$

$$F[64] = kf[64] * Conc[17] * Conc[20] \qquad B[64] = kb[64] * Conc[9]^2 \quad \textbf{(A-65)}$$

$$F[65] = kf[65] * Conc[17] * Conc[19] \qquad B[65] = kb[65] * Conc[9]^2 \quad \textbf{(A-66)}$$

$$F[66] = kf[66] * Conc[9] * Conc[18] \qquad B[66] = kb[66] * Conc[9] * Conc[17] \quad \textbf{(A-67)}$$

$$F[67] = kf[67] * Conc[18] \qquad B[67] = kb[67] * Conc[17] \quad \textbf{(A-68)}$$

$$F[68] = kf[68] * Conc[8] * Conc[12] \qquad B[68] = kb[68] * Conc[18] \quad \textbf{(A-69)}$$

$$F[69] = kf[69] * Conc[14] * Conc[18] \qquad B[69] = kb[69] * Conc[2] * Conc[8] \quad \textbf{(A-70)}$$

$$F[70] = kf[70] * Conc[13] * Conc[18] \qquad B[70] = kb[70] * Conc[1] * Conc[8] \quad \textbf{(A-71)}$$

$$F[71] = kf[71] * Conc[12] * Conc[18] \qquad B[71] = kb[71] * Conc[0] * Conc[8] \quad \textbf{(A-72)}$$

$$F[72] = kf[72] * Conc[18] * Conc[20] \qquad B[72] = kb[72] * Conc[4] * Conc[8] \quad \textbf{(A-73)}$$

$$F[73] = kf[73] * Conc[18] * Conc[19] \qquad B[73] = kb[73] * Conc[4] * Conc[8] \quad \textbf{(A-74)}$$

$$F[74] = kf[74] * Conc[18]^2 \qquad B[74] = kb[74] * Conc[8] * Conc[9] \quad \textbf{(A-75)}$$

$$F[75] = kf[75] * Conc[14] * Conc[17] \qquad B[75] = kb[75] * Conc[2] * Conc[8] \quad \textbf{(A-76)}$$

$$F[76] = kf[76] * Conc[13] * Conc[17] \qquad B[76] = kb[76] * Conc[1] * Conc[8] \quad \textbf{(A-77)}$$

$$F[77] = kf[77] * Conc[12] * Conc[17] \qquad B[77] = kb[77] * Conc[0] * Conc[8] \quad \textbf{(A-78)}$$

$$F[78] = kf[78] * Conc[17] * Conc[20] \qquad B[78] = kb[78] * Conc[4] * Conc[8] \quad \textbf{(A-79)}$$

$$F[79] = kf[79] * Conc[17] * Conc[19] \qquad B[79] = kb[79] * Conc[4] * Conc[8] \quad \textbf{(A-80)}$$

$$F[80] = kf[80] * Conc[17] * Conc[18] \qquad B[80] = kb[80] * Conc[8] * Conc[9] \quad \textbf{(A-81)}$$

$$F[81] = kf[81] * Conc[17]^2 \qquad B[81] = kb[81] * Conc[8] * Conc[9] \quad \textbf{(A-82)}$$

$$F[82] = kf[82] * Conc[15] \qquad B[82] = kb[82] * Conc[16] \quad \textbf{(A-83)}$$

$$F[83] = kf[83] * Conc[7] * Conc[12] \qquad B[83] = kb[83] * Conc[16] \quad \textbf{(A-84)}$$

$$F[84] = kf[84] * Conc[16] * Conc[19] \qquad B[84] = kb[84] * Conc[4] * Conc[7] \quad \textbf{(A-85)}$$

$$F[85] = kf[85] * Conc[16] * Conc[20] \qquad B[85] = kb[85] * Conc[4] * Conc[7] \quad \textbf{(A-86)}$$

$$F[86] = kf[86] * Conc[12] * Conc[16] \qquad B[86] = kb[86] * Conc[0] * Conc[7] \quad \textbf{(A-87)}$$

$$F[87] = kf[87] * Conc[13] * Conc[16] \qquad B[87] = kb[87] * Conc[1] * Conc[7] \quad \textbf{(A-88)}$$

$$F[88] = kf[88] * Conc[14] * Conc[16] \qquad B[88] = kb[88] * Conc[2] * Conc[7] \quad \textbf{(A-89)}$$

$$F[89] = kf[89] * Conc[16] * Conc[17] \qquad B[89] = kb[89] * Conc[7] * Conc[9] \quad \textbf{(A-90)}$$

$$F[90] = kf[90] * Conc[16] * Conc[18] \qquad B[90] = kb[90] * Conc[7] * Conc[9] \quad \textbf{(A-91)}$$

$$F[91] = kf[91] * Conc[10] * Conc[12] \qquad B[91] = kb[91] * Conc[20] \quad \textbf{(A-92)}$$

$$F[92] = kf[92] * Conc[14] * Conc[20] \qquad B[92] = kb[92] * Conc[2] * Conc[10] \quad \textbf{(A-93)}$$

$$F[93] = kf[93] * Conc[13] * Conc[20] \qquad B[93] = kb[93] * Conc[1] * Conc[10] \quad \textbf{(A-94)}$$

$$F[94] = kf[94] * Conc[12] * Conc[20] \qquad B[94] = kb[94] * Conc[0] * Conc[10] \quad \textbf{(A-95)}$$

$$F[95] = kf[95] * Conc[20]^2 \qquad B[95] = kb[95] * Conc[4] * Conc[10] \quad \textbf{(A-96)}$$

$$F[96] = kf[96] * Conc[19] * Conc[20] \qquad B[96] = kb[96] * Conc[4] * Conc[10] \quad \textbf{(A-97)}$$

$$F[97] = kf[97] * Conc[18] * Conc[20] \qquad B[97] = kb[97] * Conc[9] * Conc[10] \quad \textbf{(A-98)}$$

$$F[98] = kf[98] * Conc[10] * Conc[19] \qquad B[98] = kb[98] * Conc[4] * Conc[17] \quad \textbf{(A-99)}$$

$$F[99] = kf[99] * Conc[10] * Conc[20] \qquad B[99] = kb[99] * Conc[4] * Conc[17] \quad \textbf{(A-100)}$$

$$F[100] = kf[100] * Conc[10] * Conc[12] \qquad B[100] = kb[100] * Conc[0] * Conc[17] \quad \textbf{(A-101)}$$

$$F[101] = kf[101] * Conc[10] * Conc[13] \qquad B[101] = kb[101] * Conc[1] * Conc[17] \quad \textbf{(A-102)}$$

$$F[102] = kf[102] * Conc[10] * Conc[14] \qquad B[102] = kb[102] * Conc[2] * Conc[17] \quad \textbf{(A-103)}$$

$$F[103] = kf[103] * Conc[9] * Conc[17] \qquad B[103] = kb[103] * Conc[10] * Conc[17] \quad \textbf{(A-104)}$$

$$F[104] = kf[104] * Conc[10] * Conc[18] \qquad B[104] = kb[104] * Conc[9] * Conc[17] \quad \textbf{(A-105)}$$

$$F[105] = kf[105] * Conc[12] * Conc[17] \qquad B[105] = kb[105] * Conc[10] \quad \textbf{(A-106)}$$

$$F[106] = kf[106] * Conc[14] * Conc[17] \qquad B[106] = kb[106] * Conc[6] * Conc[10] \quad \textbf{(A-107)}$$

$$F[107] = kf[107] * Conc[15] * Conc[17] \qquad B[107] = kb[107] * Conc[7] * Conc[10] \quad \textbf{(A-108)}$$

$$F[108] = kf[108] * Conc[17] * Conc[20] \qquad B[108] = kb[108] * Conc[9] * Conc[10] \quad \textbf{(A-109)}$$

$$F[109] = kf[109] * Conc[17] * Conc[20] \qquad B[109] = kb[109] * Conc[10]^2 \quad \textbf{(A-110)}$$

$$F[110] = kf[110] * Conc[17] * Conc[19] \qquad B[110] = kb[110] * Conc[9] * Conc[10] \quad \textbf{(A-111)}$$

$$F[111] = kf[111] * Conc[17] * Conc[18] \qquad B[111] = kb[111] * Conc[8] * Conc[10] \quad \textbf{(A-112)}$$

$$F[112] = kf[112] * Conc[17]^2 \qquad B[112] = kb[112] * Conc[8] * Conc[10] \quad \textbf{(A-113)}$$

$$F[113] = kf[113] * Conc[16] * Conc[17] \qquad B[113] = kb[113] * Conc[7] * Conc[10] \quad \textbf{(A-114)}$$

$$F[114] = kf[114] * Conc[13] * Conc[14] \qquad B[114] = kb[114] * Conc[3] \quad \textbf{(A-115)}$$

$$F[115] = kf[115] * Conc[3] * Conc[19] \qquad B[115] = kb[115] * Conc[4] * Conc[15] \quad \textbf{(A-116)}$$

$$F[116] = kf[116] * Conc[4] * Conc[15] \qquad B[116] = kb[116] * Conc[3] * Conc[20] \quad \textbf{(A-117)}$$

$$F[117] = kf[117] * Conc[14] * Conc[15] \qquad B[117] = kb[117] * Conc[3] * Conc[6] \quad \textbf{(A-118)}$$

$$F[118] = kf[118] * Conc[15]^2 \qquad B[118] = kb[118] * Conc[3] * Conc[7] \quad \textbf{(A-119)}$$

$$F[119] = kf[119] * Conc[12] * Conc[15] \qquad B[119] = kb[119] * Conc[3] \quad \textbf{(A-120)}$$

$$F[120] = kf[120] * Conc[3] * Conc[12] \qquad B[120] = kb[120] * Conc[0] * Conc[15] \quad \textbf{(A-121)}$$

$$F[121] = kf[121] * Conc[15] * Conc[20] \qquad B[121] = kb[121] * Conc[3] * Conc[9] \quad \textbf{(A-122)}$$

$$F[122] = kf[122] * Conc[15] * Conc[20] \qquad B[122] = kb[122] * Conc[3] * Conc[10] \quad \textbf{(A-123)}$$

$$F[123] = kf[123] * Conc[15] * Conc[19] \qquad B[123] = kb[123] * Conc[3] * Conc[9] \quad \textbf{(A-124)}$$

$$F[124] = kf[124] * Conc[3] * Conc[13] \qquad B[124] = kb[124] * Conc[1] * Conc[15] \quad \textbf{(A-125)}$$

$$F[125] = kf[125] * Conc[3] * Conc[14] \qquad B[125] = kb[125] * Conc[2] * Conc[15] \quad \textbf{(A-126)}$$

$$F[126] = kf[126] * Conc[9] * Conc[15] \qquad B[126] = kb[126] * Conc[3] * Conc[17] \quad \textbf{(A-127)}$$

$$F[127] = kf[127] * Conc[3] * Conc[18] \qquad B[127] = kb[127] * Conc[9] * Conc[15] \quad \textbf{(A-128)}$$

$$F[128] = kf[128] * Conc[15] * Conc[18] \qquad B[128] = kb[128] * Conc[3] * Conc[8] \quad \textbf{(A-129)}$$

$$F[129] = kf[129] * Conc[15] * Conc[17] \qquad B[129] = kb[129] * Conc[3] * Conc[8] \quad \textbf{(A-130)}$$

$$F[130] = kf[130] * Conc[3] * Conc[19] \qquad B[130] = kb[130] * Conc[4] * Conc[16] \quad \textbf{(A-131)}$$

$$F[131] = kf[131] * Conc[4] * Conc[16] \qquad B[131] = kb[131] * Conc[3] * Conc[20] \quad \textbf{(A-132)}$$

$$F[132] = kf[132] * Conc[3] * Conc[12] \qquad B[132] = kb[132] * Conc[0] * Conc[16] \quad \textbf{(A-133)}$$

$$F[133] = kf[133] * Conc[3] * Conc[13] \qquad B[133] = kb[133] * Conc[1] * Conc[16] \quad \textbf{(A-134)}$$

$$F[134] = kf[134] * Conc[3] * Conc[14] \qquad B[134] = kb[134] * Conc[2] * Conc[16] \quad \textbf{(A-135)}$$

$$F[135] = kf[135] * Conc[9] * Conc[16] \qquad B[135] = kb[135] * Conc[3] * Conc[17] \quad \textbf{(A-136)}$$

$$F[136] = kf[136] * Conc[3] * Conc[18] \qquad B[136] = kb[136] * Conc[9] * Conc[16] \quad \textbf{(A-137)}$$

$$F[137] = kf[137] * Conc[12] * Conc[16] \qquad B[137] = kb[137] * Conc[3] \quad \textbf{(A-138)}$$

$$F[138] = kf[138] * Conc[14] * Conc[16] \qquad B[138] = kb[138] * Conc[3] * Conc[6] \quad \textbf{(A-139)}$$

$$F[139] = kf[139] * Conc[15] * Conc[16] \qquad B[139] = kb[139] * Conc[3] * Conc[7] \quad \textbf{(A-140)}$$

$$F[140] = kf[140] * Conc[16] * Conc[20] \qquad B[140] = kb[140] * Conc[3] * Conc[9] \quad \textbf{(A-141)}$$

$$F[141] = kf[141] * Conc[16] * Conc[20] \qquad B[141] = kb[141] * Conc[3] * Conc[10] \quad \textbf{(A-142)}$$

$$F[142] = kf[142] * Conc[16] * Conc[19] \qquad B[142] = kb[142] * Conc[3] * Conc[9] \quad \textbf{(A-143)}$$

$$F[143] = kf[143] * Conc[16] * Conc[18] \qquad B[143] = kb[143] * Conc[3] * Conc[8] \quad \textbf{(A-144)}$$

$$F[144] = kf[144] * Conc[16] * Conc[17] \qquad B[144] = kb[144] * Conc[3] * Conc[8] \quad \textbf{(A-145)}$$

$$F[145] = kf[145] * Conc[16]^2 \qquad B[145] = kb[145] * Conc[3] * Conc[7] \quad \textbf{(A-146)}$$

$$F[146] = kf[146] * Conc[10] * Conc[15] \qquad B[146] = kb[146] * Conc[3] * Conc[17] \quad \textbf{(A-147)}$$

$$F[147] = kf[147] * Conc[10] * Conc[16] \qquad B[147] = kb[147] * Conc[3] * Conc[17] \quad \textbf{(A-148)}$$

$$F[148] = kf[148] * Conc[3] * Conc[15] \qquad B[148] = kb[148] * Conc[3] * Conc[16] \quad \textbf{(A-149)}$$

A.2. PSS Species Equations

To reduce the number of differential equations that has to be solved, the pseudo-steady-state assumption is applied to all radical species. This means that the concentrations of these species can be determined via algebraic equations, which are given by eqs. (A-150) to (A-167).

$$R[12] = 0.0 + B[2] + B[3] + B[6] + B[7] + B[8] + B[10] + B[12] + B[13] + B[15] + B[16] + 2 * B[17] + B[18] + B[20] + B[29] + B[35] + B[36] + B[40] + B[42] + B[45] + B[50] + B[53] + B[61] + B[68] + B[71] + B[77] + B[83] + B[86] + B[91] + B[94] + B[100] + B[105] + B[119] + B[120] + B[132] + B[137] \quad \textbf{(A-150)}$$

$$R[21] = 0.0 - F[2] - F[3] - F[6] - F[7] - F[8] - F[10] - F[12] - F[13] - F[15] - F[16] - 2 * F[17] - F[18] - F[20] - F[29] - F[35] - F[36] - F[40] - F[42] - F[45] - F[50] - F[53] - F[61] - F[68] - F[71] - F[77] - F[83] - F[86] - F[91] - F[94] - F[100] - F[105] - F[119] - F[120] - F[132] - F[137] \quad \textbf{(A-151)}$$

$$R[13] = 0.0 + B[1] + B[4] + B[5] + F[8] + B[9] + B[11] + B[21] + B[27] + B[28] + B[29] + 2 * B[33] + B[37] + B[39] + B[44] + B[49] + B[70] + B[76] + B[87] + B[93] + B[101] + B[114] + B[124] + B[133] \quad \textbf{(A-152)}$$

$$R[22] = 0.0 - F[1] - F[4] - F[5] - B[8] - F[9] - F[11] - F[21] - F[27] - F[28] - F[29] - 2 * F[33] - F[37] - F[39] - F[44] - F[49] - F[70] - F[76] - F[87] - F[93] - F[101] - F[114] - F[124] - F[133] \quad \textbf{(A-153)}$$

$$R[14] = 0.0 + 2 * B[0] + F[12] + B[14] + B[18] + B[19] + B[23] + B[27] + F[30] + B[31] + 2 * B[32] + B[34] + B[35] + F[36] + F[37] + B[38] + B[43] + F[48] + B[54] + B[58] + B[62] + B[69] + B[75] + B[88] + B[92] + B[102] + B[106] + B[114] + B[117] + B[125] + B[134] + B[138] \quad \textbf{(A-154)}$$

$$R[23] = 0.0 - 2 * F[0] - B[12] - F[14] - F[18] - F[19] - F[23] - F[27] - B[30] - F[31] - 2 * F[32] - F[34] - F[35] - B[36] - B[37] - F[38] - F[43] - B[48] - F[54] - F[58] - F[62] - F[69] - F[75] - F[88] - F[92] - F[102] - F[106] - F[114] - F[117] - F[125] - F[134] - F[138] \quad \textbf{(A-155)}$$

$$R[15] = 0.0 + B[1] + F[11] + F[13] + B[20] + B[22] + B[26] + B[28] + B[34] + B[55] + B[63] + B[82] + B[107] + F[115] + B[116] + B[117] + 2 * B[118] + B[119] + F[120] + B[121] + B[122] + B[123] + F[124] + F[125] + B[126] + F[127] + B[128] + B[129] + B[139] + B[146] + B[148] \quad \textbf{(A-156)}$$

$$R[24] = 0.0 - F[1] - B[11] - B[13] - F[20] - F[22] - F[26] - F[28] - F[34] - F[55] - F[63] - F[82] - F[107] - B[115] - F[116] - F[117] - 2 * F[118] - F[119] - B[120] - F[121] - F[122] - F[123] - B[124] - B[125] - F[126] - B[127] - F[128] - F[129] - F[139] - F[146] - F[148] \quad \textbf{(A-157)}$$

$$R[16] = 0.0 + F[82] + F[83] + B[84] + B[85] + B[86] + B[87] + B[88] + B[89] + B[90] + B[113] + F[130] + B[131] + F[132] + F[133] + F[134] + B[135] + F[136] + B[137] + B[138] + B[139] + B[140] + B[141] + B[142] + B[143] + B[144] + 2 * B[145] + B[147] + F[148] \quad \textbf{(A-158)}$$

$$R[25] = 0.0 - B[82] - B[83] - F[84] - F[85] - F[86] - F[87] - F[88] - F[89] - F[90] - F[113] - B[130] - F[131] - B[132] - B[133] - B[134] - F[135] - B[136] - F[137] - F[138] - F[139] - F[140] - F[141] - F[142] - F[143] - F[144] - 2 * F[145] - F[147] - B[148] \quad \textbf{(A-159)}$$

$$R[17] = 0.0 + F[9] + F[10] + F[15] + F[58] + F[59] + F[60] + B[61] + B[62] + B[63] + B[64] + B[65] + F[66] + F[67] + B[75] + B[76] + B[77] + B[78] + B[79] + B[80] + 2 * B[81] + B[89] + F[98] + F[99] + F[100] + F[101] + F[102] + B[103] + F[103] + F[104] + B[105] + B[106] + B[107] + B[108] + B[109] + B[110] + B[111] + 2 * B[112] + B[113] + F[126] + B[129] + F[135] + B[144] + F[146] + F[147] \quad \textbf{(A-160)}$$

$$R[26] = 0.0 - B[9] - B[10] - B[15] - B[58] - B[59] - B[60] - F[61] - F[62] - F[63] - F[64] - F[65] - B[66] - B[67] - F[75] - F[76] - F[77] - F[78] - F[79] - F[80] - 2 * F[81] - F[89] - B[98] - B[99] - B[100] - B[101] - B[102] - F[103] - B[103] - B[104] - F[105] - F[106] - F[107] - F[108] - F[109] - F[110] - F[111] - 2 * F[112] - F[113] - B[126] - F[129] - B[135] - F[144] - B[146] - B[147] \quad \textbf{(A-161)}$$

$$R[18] = 0.0 + B[48] + F[49] + F[50] + B[51] + B[52] + B[53] + B[54] + B[55] + B[56] + B[57] + B[66] + B[67] + F[68] + B[69] + B[70] + B[71] + B[72] + B[73] + 2 * B[74] + B[80] + B[90] + B[97] + B[104] + B[111] + B[127] + B[128] + B[136] + B[143] \quad \textbf{(A-162)}$$

$$R[27] = 0.0 - F[48] - B[49] - B[50] - F[51] - F[52] - F[53] - F[54] - F[55] - F[56] - F[57] - F[66] - F[67] - B[68] - F[69] - F[70] - F[71] - F[72] - F[73] - 2 * F[74] - F[80] - F[90] - F[97] - F[104] - F[111] - F[127] - F[128] - F[136] - F[143] \quad \textbf{(A-163)}$$

$$R[19] = 0.0 + B[3] + F[4] + F[6] + F[14] + B[23] + B[24] + B[25] + B[26] + B[30] + F[42] + B[43] + B[44] + B[45] + B[46] + 2 * B[47] + F[52] + B[57] + B[60] + B[65] + B[73] + B[79] + B[84] + B[96] + B[98] + B[110] + B[115] + B[123] + B[130] + B[142] \quad \textbf{(A-164)}$$

$$R[28] = 0.0 - F[3] - B[4] - B[6] - B[14] - F[23] - F[24] - F[25] - F[26] - F[30] - B[42] - F[43] - F[44] - F[45] - F[46] - 2 * F[47] - B[52] - F[57] - F[60] - F[65] - F[73] - F[79] - F[84] - F[96] - F[98] - F[110] - F[115] - F[123] - F[130] - F[142] \quad \textbf{(A-165)}$$

$$\begin{aligned} R[20] = 0.0 &+ B[2] + F[5] + F[7] + F[16] + B[19] + F[21] + B[22] + F[24] + F[25] + F[31] \\ &+ B[38] + B[39] + B[40] + 2 * B[41] + B[46] + F[51] + B[56] + B[59] + B[64] \\ &+ B[72] + B[78] + B[85] + F[91] + B[92] + B[93] + B[94] + 2 * B[95] + B[96] \\ &+ B[97] + B[99] + B[108] + B[109] + F[116] + B[121] + B[122] + F[131] \\ &+ B[140] + B[141] \end{aligned} \quad \textbf{(A-166)}$$

$$\begin{aligned} R[29] = 0.0 &- F[2] - B[5] - B[7] - B[16] - F[19] - B[21] - F[22] - B[24] - B[25] - B[31] \\ &- F[38] - F[39] - F[40] - 2 * F[41] - F[46] - B[51] - F[56] - F[59] - F[64] \\ &- F[72] - F[78] - F[85] - B[91] - F[92] - F[93] - F[94] - 2 * F[95] - F[96] \\ &- F[97] - F[99] - F[108] - F[109] - B[116] - F[121] - F[122] - B[131] \\ &- F[140] - F[141] \end{aligned} \quad \textbf{(A-167)}$$

The concentrations of the PSS species are determined iteratively by correcting the old concentration with the square root of the old ratio between forward and backward net formation rate of the PSS species, until a certain tolerance is fulfilled or a maximum number of iterations is exceed.

$$C[i]^{new} = \sqrt{\frac{-R[i]}{R[i+9]}} C[i]^{old} \quad \textbf{(A-168)}$$

The square root of the ratio of forward and backward net formation rates is taken as this is found to improve the stability of the method [1, 2].

A.3. Source Term Non-PSS Species

For all species on which the PSSA is not applicable, a conservation equation must be solved. This equation was given in eq. (4-4). As stated there, the source term depends on the concentrations of the various species. For the non-PSS species, the source terms are given by eqs. (A-169) to (A-180).

$$\begin{aligned} R[0] = 0.0 &+ F[6] + F[7] + F[8] + F[10] + F[17] + F[18] + F[20] + F[36] + F[40] + F[45] \\ &+ F[50] + F[71] + F[77] + F[86] + F[94] + F[100] + F[120] + F[132] - B[6] \\ &- B[7] - B[8] - B[10] - B[17] - B[18] - B[20] - B[36] - B[40] - B[45] \\ &- B[50] - B[71] - B[77] - B[86] - B[94] - B[100] - B[120] - B[132] \end{aligned} \quad \textbf{(A-169)}$$

$$\begin{aligned} R[1] = 0.0 &+ F[4] + F[5] + B[8] + F[9] + F[27] + F[28] + F[29] + F[37] + F[39] + F[44] + F[49] \\ &+ F[70] + F[76] + F[87] + F[93] + F[101] + F[124] + F[133] - B[4] - B[5] \\ &- F[8] - B[9] - B[27] - B[28] - B[29] - B[37] - B[39] - B[44] - B[49] \\ &- B[70] - B[76] - B[87] - B[93] - B[101] - B[124] - B[133] \end{aligned} \quad \textbf{(A-170)}$$

$$\begin{aligned} R[2] = 0.0 &+ B[30] + F[31] + F[32] + F[33] + F[34] + F[35] + B[36] + B[37] + F[38] + F[43] \\ &+ B[48] + F[58] + F[69] + F[75] + F[88] + F[92] + F[102] + F[125] + F[134] \\ &- F[30] - B[31] - B[32] - B[33] - B[34] - B[35] - F[36] - F[37] - B[38] \\ &- B[43] - F[48] - B[58] - B[69] - B[75] - B[88] - B[92] - B[102] - B[125] \\ &- B[134] \end{aligned} \quad \textbf{(A-171)}$$

$$\begin{aligned}R[3] = 0.0 &+ F[114] + B[115] + F[116] + F[117] + F[118] + F[119] + B[120] + F[121] + F[122] \\ &+ F[123] + B[124] + B[125] + F[126] + B[127] + F[128] + F[129] + B[130] \\ &+ F[131] + B[132] + B[133] + B[134] + F[135] + B[136] + F[137] + F[138] \\ &+ F[139] + F[140] + F[141] + F[142] + F[143] + F[144] + F[145] + F[146] \\ &+ F[147] + B[148] + F[148] - B[114] - F[115] - B[116] - B[117] - B[118] \\ &- B[119] - F[120] - B[121] - B[122] - B[123] - F[124] - F[125] - B[126] \\ &- F[127] - B[128] - B[129] - F[130] - B[131] - F[132] - F[133] - F[134] \\ &- B[135] - F[136] - B[137] - B[138] - B[139] - B[140] - B[141] - B[142] \\ &- B[143] - B[144] - B[145] - B[146] - B[147] - F[148] - B[148]\end{aligned} \quad \textbf{(A-172)}$$

$$\begin{aligned}R[4] = 0.0 &+ F[0] + F[1] + F[2] + F[3] + B[4] + B[5] + B[6] + B[7] + F[19] + F[22] + F[23] \\ &+ B[24] + F[24] + F[26] + F[30] + B[31] + F[41] + F[46] + F[47] + B[51] \\ &+ B[52] + F[59] + F[60] + F[72] + F[73] + F[78] + F[79] + F[84] + F[85] \\ &+ F[95] + F[96] + F[98] + F[99] + F[115] + B[116] + F[130] + B[131] - B[0] \\ &- B[1] - B[2] - B[3] - F[4] - F[5] - F[6] - F[7] - B[19] - B[22] - B[23] \\ &- F[24] - B[24] - B[26] - B[30] - F[31] - B[41] - B[46] - B[47] - F[51] \\ &- F[52] - B[59] - B[60] - B[72] - B[73] - B[78] - B[79] - B[84] - B[85] \\ &- B[95] - B[96] - B[98] - B[99] - B[115] - F[116] - B[130] - F[131]\end{aligned} \quad \textbf{(A-173)}$$

$$R[5] = 0.0 \quad \textbf{(A-174)}$$

$$\begin{aligned}R[6] = 0.0 &+ B[11] + B[12] + B[14] + F[18] + F[19] + F[23] + F[27] + F[32] + F[54] + F[62] \\ &+ F[106] + F[117] + F[138] - F[11] - F[12] - F[14] - B[18] - B[19] - B[23] \\ &- B[27] - B[32] - B[54] - B[62] - B[106] - B[117] - B[138]\end{aligned} \quad \textbf{(A-175)}$$

$$\begin{aligned}R[7] = 0.0 &+ B[13] + F[20] + B[21] + F[22] + F[26] + F[28] + F[34] + F[55] + F[63] + B[83] \\ &+ F[84] + F[85] + F[86] + F[87] + F[88] + F[89] + F[90] + F[107] + F[113] \\ &+ F[118] + F[139] + F[145] - F[13] - B[20] - F[21] - B[22] - B[26] - B[28] \\ &- B[34] - B[55] - B[63] - F[83] - B[84] - B[85] - B[86] - B[87] - B[88] \\ &- B[89] - B[90] - B[107] - B[113] - B[118] - B[139] - B[145]\end{aligned} \quad \textbf{(A-176)}$$

$$\begin{aligned}R[8] = 0.0 &+ B[15] + B[68] + F[69] + F[70] + F[71] + F[72] + F[73] + F[74] + F[75] + F[76] \\ &+ F[77] + F[78] + F[79] + F[80] + F[81] + F[111] + F[112] + F[128] \\ &+ F[129] + F[143] + F[144] - F[15] - F[68] - B[69] - B[70] - B[71] - B[72] \\ &- B[73] - B[74] - B[75] - B[76] - B[77] - B[78] - B[79] - B[80] - B[81] \\ &- B[111] - B[112] - B[128] - B[129] - B[143] - B[144]\end{aligned} \quad \textbf{(A-177)}$$

$$\begin{aligned}R[9] = 0.0 &+ B[9] + B[10] + B[16] + F[38] + F[39] + F[40] + F[41] + B[42] + F[43] + F[44] \\ &+ F[45] + F[46] + F[47] + F[48] + B[49] + B[50] + F[51] + F[52] + F[53] \\ &+ F[54] + F[55] + 2 * F[56] + 2 * F[57] + B[58] + B[59] + B[60] + F[61] \\ &+ F[62] + F[63] + 2 * F[64] + 2 * F[65] + B[66] + F[66] + F[74] + F[80] \\ &+ F[81] + F[89] + F[90] + F[97] + B[103] + F[104] + F[108] + F[110] \\ &+ F[121] + F[123] + B[126] + F[127] + B[135] + F[136] + F[140] + F[142] \\ &- F[9] - F[10] - F[16] - B[38] - B[39] - B[40] - B[41] - F[42] - B[43] \\ &- B[44] - B[45] - B[46] - B[47] - B[48] - F[49] - F[50] - B[51] - B[52] \\ &- B[53] - B[54] - B[55] - 2 * B[56] - 2 * B[57] - F[58] - F[59] - F[60] \\ &- B[61] - B[62] - B[63] - 2 * B[64] - 2 * B[65] - F[66] - B[66] - B[74] \\ &- B[80] - B[81] - B[89] - B[90] - B[97] - F[103] - B[104] - B[108] \\ &- B[110] - B[121] - B[123] - F[126] - B[127] - F[135] - B[136] - B[140] \\ &- B[142]\end{aligned} \quad \textbf{(A-178)}$$

$$\begin{aligned}R[10] = 0.0 &+ B[91] + F[92] + F[93] + F[94] + F[95] + F[96] + F[97] + B[98] + B[99] + B[100] \\ &+ B[101] + B[102] + F[103] + B[104] + F[105] + F[106] + F[107] + F[108] \\ &+ 2 * F[109] + F[110] + F[111] + F[112] + F[113] + F[122] + F[141] \\ &+ B[146] + B[147] - F[91] - B[92] - B[93] - B[94] - B[95] - B[96] - B[97] \\ &- F[98] - F[99] - F[100] - F[101] - F[102] - B[103] - F[104] - B[105] \\ &- B[106] - B[107] - B[108] - 2 * B[109] - B[110] - B[111] - B[112] \\ &- B[113] - B[122] - B[141] - F[146] - F[147]\end{aligned} \quad \textbf{(A-179)}$$

$$R[11] = 0.0 \quad \textbf{(A-180)}$$

A.4. References

1. Reyniers, P. A.; Schietekat, C. M.; Van Cauwenberge, D. J.; Vandewalle, L. A.; Van Geem, K. M.; Marin, G. B., Necessity and Feasibility of 3D Simulations of Steam Cracking Reactors. *Industrial & Engineering Chemistry Research* **2015,** 54, (49), 12270-12282.
2. Lu, T.; Law, C. K., Systematic approach to obtain analytic solutions of quasi steady state species in reduced mechanisms. *The Journal of Physical Chemistry A* **2006,** 110, (49), 13202-13208.

B

Structure of OpenFOAM

B.1. File Structure

OpenFOAM uses a well-defined file structure. Each case should have its own folder, though the location or name of this folder are not of importance. This folder should contain at least three sub-folders. The first is the "0" folder. This file contains all initial and boundary conditions for the different parameters of the flow. The second folder is the "constant" folder. Here, one should place all property input files as well as all files concerning the mesh. The latter are placed in a sub-folder named "polyMesh". This name also illustrates a common practice in OpenFOAM, in which the first word of a variable name starts with a lower case letter and all following words with an uppercase letter. The final mandatory folder is the "system" folder, which contains all files linked to computational aspects and (most of) the so-called dictionary files. These files contain the necessary input for various tools. This structure is illustrated in Figure B-1.

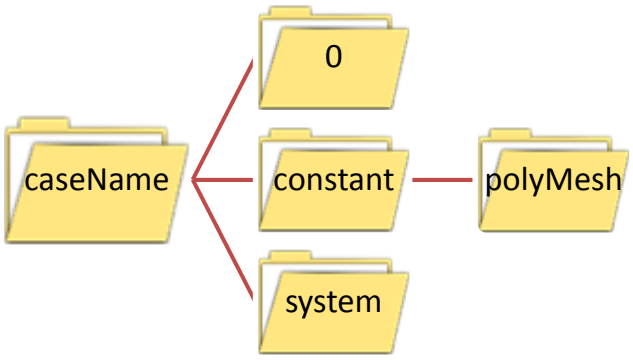

Figure B-1: File structure of OpenFOAM.

B.2. Input Files

Each of the folders mentioned above may contain several input files. The "0" folder contains the files with field initialisations and boundary conditions. An example for the pressure is given in Figure B-2. The dimensions of the input are defined by the exponents of the S.I. unit in the row [kg m s K mol A cd].

```
/*--------------------------------*- C++ -*----------------------------------*\
| =========                 |                                                 |
| \\      /  F ield         | OpenFOAM: The Open Source CFD Toolbox           |
|  \\    /   O peration     | Version:  2.2.0                                 |
|   \\  /    A nd           | Web:      www.OpenFOAM.org                      |
|    \\/     M anipulation  |                                                 |
\*---------------------------------------------------------------------------*/
FoamFile
{
    version     2.0;
    format      ascii;
    class       volScalarField;
    location    "0";
    object      p;
}
// * * * * * * * * * * * * * * * * * * * * * * * * * * * * * * * * * * * * //

dimensions      [1 -1 -2 0 0 0 0];
```

```
internalField   uniform 235680;

boundaryField
{
    outlet
    {
        type            cyclic;
    }
    inlet
    {
        type            cyclic;
    }
    wall
    {
        type            zeroGradient;
    }
}

// ************************************************************************* //
```

Figure B-2: Example of input file for pressure initial - and boundary conditions.

The “constant” folder contains input concerning general fluid and flow properties, such as the parameters for the turbulence models, thermodynamic data, and transport properties. The “system” folder contains important files for the simulation. The discretisation schemes that are used for the simulation are listed in `fvSchemes`. The file `fvSolution` allows input on which type of solver is used, maximum number of iterations, the number of correction steps in the PISO-loop, etc. The file `fvOptions` makes it possible to specify other input. Here, a constraint is imposed on the temperature. In some cases, it is possible that convergence is not attained in a very limited number of cells. This could result in too high or too low temperatures. The constraints on the temperature will limit the deviation of these cells. If the number of cells in which this must be done is low, a correct solution can still be obtained. If a multiple cells start exceeding these temperature limits though, the solution will no longer be correct. The only obligatory dictionary file is the `controlDict`, which contains the settings for start-stop of the simulation, post-processing, solver, check-pointing and so on.

C

Solvers, Utilities and Case Files

C.1. Utilities

The following OpenFOAM utilities have been used during this work. Changes to these utilities were purely cosmetic or resolved version related issues between the 2.2.2 version on the local computers and the 2.2.0 version running on the HPC infrastructure.

Utility	*File location*
`perturbUCyl`	ir12sw3a.UGent.be/users/pplehier/OpenFOAM/LES/Utilities/perturbUCyl
`plehiersCoking`	ir12sw3a.UGent.be/users/pplehier/OpenFOAM/LES/Utilities/plehiersCoking
`twoPointCorrelate`	ir12sw3a.UGent.be/users/pplehier/OpenFOAM/LES/Utilities/twoPointCorrelate

C.2. Libraries

The files in the libraries "Libs" folder contain data that is required by the solver or built-in utilities.

Library	*File location*
`blockMesh`	ir12sw3a.UGent.be/users/pplehier/OpenFOAM/LES/Libs/blockMesh
`cuttingPlane`	ir12sw3a.UGent.be/users/pplehier/OpenFOAM/LES/Libs/sampling/cuttingPlane
`diffusivityModels`	ir12sw3a.UGent.be/users/pplehier/OpenFOAM/LES/Libs/diffusivityModels
`extrudeModel`	ir12sw3a.UGent.be/users/pplehier/OpenFOAM/LES/Libs/extrudeModel
`WALE`	ir12sw3a.UGent.be/users/pplehier/OpenFOAM/LES/Libs/LES/WALE

C.3. Solvers

The following OpenFOAM solver has been used in this work. Some minor changes were made to the original solver. Input data such as PSSA loop tolerances and iterations were mare run-time modifiable. A post-processing step was implemented in the solver as well, automatically writing only the necessary fields (temperature, pressure, species etc.) at certain positions in the reactor. The tool works on the local infrastructure, but an unresolved version issue interfered with its correct working on the HPC infrastructure.

Solver	*File location*
`QSSAPipeFoam`	ir12sw3a.UGent.be/users/pplehier/OpenFOAM/LES/Solver/QSSAPipeFoamr

C.4. Case Files

C.4.1. Large Eddy Simulations

Case Description	*Case location*
Bare tube, pre-reactive simulation	ir12sw3a.UGent.be/users/pplehier/OpenFOAM/LES/barePreReactiveData
Finned tube, pre-reactive simulation	ir12sw3a.UGent.be/users/pplehier/OpenFOAM/LES/finnedPreReactiveData
Ribbed tube, pre-reactive simulation	ir12sw3a.UGent.be/users/pplehier/OpenFOAM/LES/ribbedPreReactiveData
Bare tube, reactive, with interpolation schemes: `limitedLinear`	ir12sw3a.UGent.be/users/pplehier/OpenFOAM/LES/Other/bare
Finned tube, reactive, with interpolation schemes: `limitedLinear`	ir12sw3a.UGent.be/users/pplehier/OpenFOAM/LES/Other/finned
Ribbed tube reactive, with interpolation schemes: `limitedLinear`	ir12sw3a.UGent.be/users/pplehier/OpenFOAM/LES/Other/ribbed
Bare tube, reactive, with interpolation schemes: `skewCorrected`	ir12sw3a.UGent.be/users/pplehier/OpenFOAM/LES/bareReactiveData
Finned tube, reactive, with interpolation schemes: `skewCorrected`	ir12sw3a.UGent.be/users/pplehier/OpenFOAM/LES/finnedReactiveData
Ribbed tube reactive, with interpolation schemes: `skewCorrected`	ir12sw3a.UGent.be/users/pplehier/OpenFOAM/LES/finnedReactiveData

C.4.2. RANS in Trans- and Supersonic Flows

Case Description	*Case location*
Non-converged and backup of proof-of-concept nozzle flow	ir12sw3a.UGent.be/users/pplehier/SUSTOR2/Shockwaves/xxx.cas
Arina, with axial symmetry and inviscid flow assumption at 300 K	ir12sw3a.UGent.be/users/pplehier/SUSTOR2/Shockwaves/Converged/ArinaSymInviscid.cas

Case Description	*Case location*
Arina, with axial symmetry and inviscid flow assumption, at 288 K	ir12sw3a.UGent.be/users/pplehier/SUSTOR2/Shockwaves/Converged/ArinaSymInviscid288K.cas
Arina, with axial symmetry and realisable k-epsilon turbulence model, at 300 K	ir12sw3a.UGent.be/users/pplehier/SUSTOR2/Shockwaves/Converged/ArinaSymRKE.cas
Arina, with axial symmetry and realisable k-epsilon turbulence model, at 288 K	ir12sw3a.UGent.be/users/pplehier/SUSTOR2/Shockwaves/Converged/ArinaSymRKE288K.cas
Arina, with axial symmetry and Reynolds stress turbulence model, at 300 K	ir12sw3a.UGent.be/users/pplehier/SUSTOR2/Shockwaves/Converged/ArinaSymRSM.cas
Arina, with axial symmetry and Reynolds stress turbulence model, at 288 K, first order discretisation	ir12sw3a.UGent.be/users/pplehier/SUSTOR2/Shockwaves/Converged/ArinaSymRSM288K1order.cas
Arina, with axial symmetry and realisable k-epsilon turbulence model, at 288 K, second order discretisation	ir12sw3a.UGent.be/users/pplehier/SUSTOR2/Shockwaves/Converged/ArinaSymRSM288K2order.cas
Karimi, case A, with axial symmetry, inviscid, first order discretisation, using methane	ir12sw3a.UGent.be/users/pplehier/SUSTOR2/Shockwaves/Converged/KarimiNarrowMethaneInviscid.cas
Karimi, case A, with axial symmetry, inviscid, second order discretisation, using methane	ir12sw3a.UGent.be/users/pplehier/SUSTOR2/Shockwaves/Converged/KarimiNarrowMethaneInviscid2Order.cas
Karimi, case A, with axial symmetry, realisable k-epsilon turbulence model, first order discretisation, using methane	ir12sw3a.UGent.be/users/pplehier/SUSTOR2/Shockwaves/Converged/KarimiNarrowMethaneRKE.cas
Karimi, case B, with axial symmetry, realisable k-epsilon turbulence model, first order discretisation	ir12sw3a.UGent.be/users/pplehier/SUSTOR2/Shockwaves/Converged/KarimiAxiSym1order.cas
Karimi, case B, with axial symmetry, Reynolds stress turbulence model, first order discretisation, using nitrogen	ir12sw3a.UGent.be/users/pplehier/SUSTOR2/Shockwaves/Converged/KarimiAxiSym1orderRSM.cas
Karimi, case B, with axial symmetry, realisable k-epsilon turbulence model, second order discretisation, using nitrogen	ir12sw3a.UGent.be/users/pplehier/SUSTOR2/Shockwaves/Converged/KarimiAxiSym2order.cas

Case Description	*Case location*
Karimi, case B, with axial symmetry, Reynolds stress turbulence model, second order discretisation, using nitrogen	ir12sw3a.UGent.be/users/pplehier/SUSTOR2/Shockwaves/Converged/KarimiAxiSym2orderRSM.cas
2D SUSTOR, initial simulations	ir12sw3a.UGent.be/users/pplehier/SUSTOR2/2D/Presim/xxx.cas
2D SUSTOR, first order, 5 mm nozzle radius, axial length 80 mm	ir12sw3a.UGent.be/users/pplehier/SUSTOR2/2D/1stOrder/SUSTOR_5mm_nozzle_1storder.cas
2D SUSTOR, first order, 10 mm nozzle radius, axial length 80 mm	ir12sw3a.UGent.be/users/pplehier/SUSTOR2/2D/1stOrder/SUSTOR_10mm_nozzle_highMass_1storder.cas
2D SUSTOR, first order, 20 mm nozzle radius, axial length 80 mm	ir12sw3a.UGent.be/users/pplehier/SUSTOR2/2D/1stOrder/SUSTOR_20mm_nozzle__highMass_1storder.cas
2D SUSTOR, first order, 10 mm nozzle radius, axial length 65 mm	ir12sw3a.UGent.be/users/pplehier/SUSTOR2/2D/1stOrder/SUSTOR_10mm_nozzle_-15mmtop1storder.cas
2D SUSTOR, first order, 10 mm nozzle radius, axial length 55 mm	ir12sw3a.UGent.be/users/pplehier/SUSTOR2/2D/1stOrder/SUSTOR_10mm_nozzle_-25mmtop1storder.cas
2D SUSTOR, first order, 10 mm nozzle radius, axial length 80 mm, with PEW at inlet	ir12sw3a.UGent.be/users/pplehier/SUSTOR2/2D/1stOrder/SUSTOR_10mm_nozzle_bottomcone_1storder.cas
2D SUSTOR, first order, 10 mm nozzle radius, axial length 65 mm, with PEW at inlet	ir12sw3a.UGent.be/users/pplehier/SUSTOR2/2D/1stOrder/SUSTOR_10mm_nozzle_bottomcone_-15mmtop1storder.cas
2D SUSTOR, first order, 10 mm nozzle radius, axial length 65 mm, with PEW at inlet, without planar symmetry	ir12sw3a.UGent.be/users/pplehier/SUSTOR2/2D/1stOrder/SUSTOR_10mm_nozzle_bottomcone_-15mmtopnosym1storder.cas
2D SUSTOR, first order, 10 mm nozzle radius, axial length 70 mm, with PEW at inlet	ir12sw3a.UGent.be/users/pplehier/SUSTOR2/2D/1stOrder/SUSTOR_10mm_nozzle_bottomcone_narrowtop_1storder.cas
2D SUSTOR, first order, 10 mm nozzle radius, axial length 70 mm, with PEW at inlet, without planar symmetry	ir12sw3a.UGent.be/users/pplehier/SUSTOR2/2D/1stOrder/SUSTOR_10mm_nozzle_bottomcone_narrowtop_nosym_1storder.cas
2D SUSTOR, first order, 10 mm nozzle radius, axial length 80 mm, with PEW at inlet and outlet	ir12sw3a.UGent.be/users/pplehier/SUSTOR2/2D/1stOrder/SUSTOR_10mm_nozzle_bottomtopcone1storder.cas

Case Description	*Case location*
2D SUSTOR, first order, 10 mm nozzle radius, axial length 80 mm, with PEW at inlet and outlet (reduced height)	ir12sw3a.UGent.be/users/pplehier/SUSTOR2/2D/1stOrder/SUSTOR_10mm_nozzle_bottomtopconesmall1storder.cas
2D SUSTOR, first order, 10 mm nozzle radius, axial length 80 mm, with PEW at inlet and outlet (reduced height), without planar symmetry	ir12sw3a.UGent.be/users/pplehier/SUSTOR2/2D/1stOrder/SUSTOR_10mm_nozzle_bottomtopconesmallnosym1storder.cas
2D SUSTOR, second order, 5 mm nozzle radius, axial length 80 mm	ir12sw3a.UGent.be/users/pplehier/SUSTOR2/2D/2ndOrder/SUSTOR_5mm_nozzle_2ndorder.cas
2D SUSTOR, second order, 10 mm nozzle radius, axial length 80 mm	ir12sw3a.UGent.be/users/pplehier/SUSTOR2/2D/2ndOrder/SUSTOR_10mm_nozzle_2ndorder.cas
2D SUSTOR, second order, 20 mm nozzle radius, axial length 80 mm	ir12sw3a.UGent.be/users/pplehier/SUSTOR2/2D/2ndOrder/SUSTOR_20mm_nozzle_2ndorder.cas
2D SUSTOR, second order, 10 mm nozzle radius, axial length 65 mm, PEW at inlet	ir12sw3a.UGent.be/users/pplehier/SUSTOR2/2D/2ndOrder/SUSTOR_10mm_nozzle_bottomcone_-15mmtop2ndorder.cas
2D SUSTOR, second order, 10 mm nozzle radius, axial length 70 mm, PEW at inlet	ir12sw3a.UGent.be/users/pplehier/SUSTOR2/2D/2ndOrder/SUSTOR_5mm_nozzle_bottomcone_-narrowtop2ndorder.cas
2D SUSTOR, first order, 10 mm nozzle radius, axial length 80 mm, with PEW at inlet and outlet (reduced height)	ir12sw3a.UGent.be/users/pplehier/SUSTOR2/2D/2ndOrder/SUSTOR_10mm_nozzle_bottomtopconesmall2norder.cas
3D SUSTOR, first order, mass flow rate 0.035 kg s^{-1}	ir12sw3a.UGent.be/users/pplehier/SUSTOR2/3D/m0.035/SUSTOR3D_m0.035_50.cas
3D SUSTOR, first order, mass flow rate 0.07 kg s^{-1}	ir12sw3a.UGent.be/users/pplehier/SUSTOR2/3D/m0.035/SUSTOR3D_m0.07_50.cas
3D SUSTOR, first order, mass flow rate 0.1 kg s^{-1}	ir12sw3a.UGent.be/users/pplehier/SUSTOR2/3D/m0.035/SUSTOR3D_m0.10_50.cas
3D SUSTOR, first order, mass flow rate 0.14 kg s^{-1}	ir12sw3a.UGent.be/users/pplehier/SUSTOR2/3D/m0.035/SUSTOR3D_m0.14_50.cas